

**Structural and functional analysis of MscS-like
channels from *Nanoarchaeum equitans***



DISSERTATION

ZUR ERLANGUNG DES

DOKTORGRADES DER NATURWISSENSCHAFTEN (DR. RER. NAT.)

DER FAKULTÄT FÜR BIOLOGIE UND VORKLINISCHE MEDIZIN

DER UNIVERSITÄT REGENSBURG

vorgelegt von

PIA BERLIK

(geb. Wiegmann)

aus Lübbecke

im Jahr 2018

Das Promotionsgesuch wurde eingereicht am:
09.05.2018

Die Arbeit wurde angeleitet von:
Prof. Dr. Christine Ziegler

Unterschrift:

“Be (like) water, my friend!”

Bruce Lee

Für M.

Table of contents

List of abbreviations	VI
List of figures	X
List of tables.....	XII
ABSTRACT	XIV
I INTRODUCTION.....	1
1 Mechanosensitive channels	1
1.1 Mechanosensitive channels of large conductance (MscL)	3
1.2 Mechanosensitive channels of small conductance (MscS).....	5
1.2.1 MscS superfamily	5
1.2.2 Structure and function of MscS	7
1.2.3 Protein-lipid interactions	11
1.2.4 Physiological functions of MscS-like channels.....	13
1.3 Mechanosensitive channels in archaea	15
2 <i>Nanoarchaeum equitans</i> and <i>Ignicoccus hospitalis</i>: the unusual intimate association of two archaea	16
2.1 The “intimate association”	16
2.2 <i>I. hospitalis</i> : current knowledge	17
2.3 <i>N. equitans</i> : a putative ectoparasite?	18
3 Aim of this work	21
II MATERIALS AND METHODS	22
1 Materials.....	22
1.1 Instruments	22
1.2 Chemicals	23

Table of contents

1.3	Detergents	23
1.4	Enzymes and inhibitors	24
1.5	Molecular weight markers	24
1.6	Reagent kits	24
1.7	Column materials.....	25
1.8	Antibodies.....	25
1.9	Media and antibiotics.....	26
1.9.1	LB media	26
1.9.2	2YT media	26
1.9.3	TB media	26
1.9.4	SOC media.....	27
1.9.5	CP minimal media	27
1.9.6	Antibiotics	28
1.10	Bacterial <i>E. coli</i> strains	28
1.11	Plasmids and oligonucleotide primers	29
1.12	Archaeal strains	30
2	Molecular methods	31
2.1	Polymerase chain reaction (PCR).....	31
2.2	Fusion PCR.....	32
2.3	Agarose gel electrophoresis	32
2.4	Digestion with restriction enzymes	33
2.5	Ligation.....	33
2.6	Preparation of chemical competent <i>E. coli</i> cells.....	34
2.7	Transformation of <i>E. coli</i>	35
2.8	Colony PCR	35
2.9	Isolation of plasmid DNA.....	36
2.10	Determination of DNA concentration	36
3	Biochemical methods.....	36
3.1	Determination of protein concentration.....	36
3.1.1	BCA assay	36
3.1.2	Bradford assay	36

3.1.3	Photometrical determination.....	37
3.2	SDS-Polyacrylamide gel electrophoresis (SDS-Page)	37
3.3	Blue Native Electrophoresis (BNE).....	38
3.4	Western blot.....	39
3.5	Heterologous protein expression in <i>E. coli</i>	40
3.5.1	Expression	40
3.5.2	Cell disruption and membrane preparation.....	41
3.6	Protein purification	41
3.6.1	Solubilization	41
3.6.1.1	Detergent screening	41
3.6.1.2	Solubilization for purification.....	42
3.6.2	Immobilized metal affinity chromatography (IMAC)	42
3.6.2.1	Flow through-based purification.....	42
3.6.2.2	Gravity flow based method in batch	43
3.6.2.3	Proteolytic cleavage of histidine tag	43
3.6.3	Desalting and concentrating of protein samples	43
3.6.4	Size exclusion chromatography (SEC).....	44
3.7	Reconstitution into membrane-mimicking environments	44
3.7.1	Reconstitution into nanodiscs	44
3.7.1.1	Expression and purification of the membrane scaffold protein MSP1E3D1	44
3.7.1.2	Reconstitution procedure	46
3.7.2	Reconstitution into amphipol A8-35	47
3.8	Lipid analysis by thin layer chromatography (TLC)	47
4	Electrophysiological analyses	48
4.1	Preparation of liposomes	48
4.2	Patch clamp recordings of proteoliposomes	49
4.3	Preparation of <i>E. coli</i> spheroplasts	49
4.4	Patch clamp recordings of <i>E. coli</i> spheroplasts	51
4.5	Hypoosmotic down-shock assay	51
5	Biophysical methods	52
5.1	Negative stain electron microscopy.....	52

Table of contents

5.1.1	Preparation of carbon coated copper grids	52
5.1.2	Negative staining and electron microscopy	52
5.2	Cryo electron microscopy (cryo-EM).....	53
5.3	Image-processing and single particle analysis.....	53
5.4	Map visualization and analysis	53
6	Bioinformatical analyses	54
6.1	Sequence alignments	54
6.2	Topology prediction	54
6.3	Homology modeling	54
III	RESULTS	56
1	Biochemical analysis of Neq198 and Neq531	56
1.1	Heterologous expression and purification	56
1.2	Reconstitution into membrane-mimicking environments	62
1.3	Lipid analysis by thin layer chromatography	68
2	Structural analysis of the MscS-like channels from <i>N. equitans</i>	70
2.1	Sequence analysis	70
2.2	Single particle analysis	73
2.3	Negative stain single particle analysis	73
2.3.1	Neq198 reconstituted into amphipol A8-35	73
2.3.2	Neq531 reconstituted into amphipol A8-35	77
2.3.3	Neq198 reconstituted into nanodiscs	80
2.4	Single particle analysis of a cryo-EM data set.....	84
2.5	Neq198: Fitting of atomic coordinates into cryo-EM density	92
3	Functional analysis of Neq198 and Neq531	96
3.1	Hypoosmotic down-shock assay	96
3.2	Patch clamp analysis	97
IV	DISCUSSION	102
1	Heterologous expression and purification of MscS-like channels from <i>N. equitans</i>.....	102

2	The role of lipids in mechanosensation	105
2.1	Bacteria and archaea: membranes and lipids	105
2.2	Towards a functional understanding of Neq198 and Neq531	108
3	Single particle analysis using RELION	111
3.1	Protein quality and sample preparation challenges	111
3.2	Nanodiscs versus amphipol reconstitution	113
3.3	Preferred orientation and neighbouring particles	117
3.4	Heterogeneity within a data set.....	118
4	Structure of the first archaeal MscS-like channel	119
5	Conclusions and future directions.....	122
V	REFERENCES.....	125
VI	APPENDIX	148
1	Protein characteristics.....	148
1.1	General characteristics of Neq198 and Neq531	148
1.2	Protein sequences of relevant MS channels.....	149
1.3	Accession numbers of relevant MS channels	151
1.4	Sequence alignments	151
2	Single particle data sets	155
2.1	Negative stain data sets.....	155
2.2	Cryo-EM data sets	155
3	Cryo-EM data sets: experimental set-up	156
3.1	Experimental set-up for “Feb2016” data set.....	156
3.2	Experimental set-up for “Jun2016” data set	157
	ACKNOWLEDGMENTS	158

List of abbreviations

2D	two-dimensional
3D	three-dimensional
Å	Angström (s)
Aa	amino acids
Amp	ampicillin
APS	ammonium persulfate
AU	arbitrary unit (absorption unit)
BCA	bicinchoninic acid
BCIP	5-bromo-4-chloro-3-indolyl-phosphate
BSA	bovine serum albumin
CD	cytoplasmic domain
Cfu	colony forming units
Cm	chloramphenicol
Cmc	critical micelle concentration
CIP	alkaline phosphatase, calf intestinal
CTF	contrast transfer function
CV	column volume
CYMAL-5	5-Cyclohexyl-1-Pentyl- β -D-Maltoside
CYMAL-6	6-Cyclohexyl-1-Hexyl- β -D-Maltoside
DDM	<i>n</i> -dodecyl- β -D-maltoside
DM	<i>n</i> -decyl- β -D-maltoside
DNA	deoxyribonucleic acid
<i>e.g.</i>	<i>exempli gratia</i> , for example
EM	electron microscope/ microscopy
EMDB	electron microscopy data bank
EPL	<i>E. coli</i> polar lipids
<i>et al.</i>	<i>et alia</i> , <i>et alii</i>
forw	forward

Fos14	Fos-Choline-14 (n-Tetradecylphosphocholine)
Fos12	Fos-Choline-12 (n-Dodecylphosphocholine)
<i>xg</i>	acceleration of gravity
GOF	gain-of-function
His ₆	hexa-histidine tag
HMW	high molecular weight
<i>i.e.</i>	<i>id est</i> , that is
IPTG	isopropyl- β -D-thiogalactopyranosid
IMAC	immobilized metal affinity chromatography
K _m	kanamycin
LMNG	Lauryl Maltose Neopentyl Glycol
LOF	loss-of-function
MS	mechanosensitive
MSP	membrane scaffold protein
MWCO	molecular weight cut-off
NBT	nitro blue tetrazolium
NG	n-Nonyl- β -D-Glucopyranoside
OD	optical density
OG	n-Octyl- β -D-Glucopyranoside
o/N	overnight
PC	phosphatidylcholine
PD	periplasmic domain
PDB	protein data base
PE	Phosphatidylethanolamine
PELDOR	Pulsed electron-electron double resonance
PG	phosphatidylglycerol
pI	isoelectric point
POPC	1-palmitoyl-1,2-oleoyl- <i>sn</i> -glycero-3-phosphocholine
POPG	1-palmitoyl-1,2-oleoyl- <i>sn</i> -glycero-3-phospho-(1'-rac-glycerol)
PTA	phosphotungstic acid
rev	reverse
rpm	revolutions per minute

List of abbreviations

RT	room temperature
SDS	sodiumdodecylsulfate
SEC	size exclusion chromatography
SEM	scanning electron microscopy
SNR	signal-to-noise ratio
TEM	transmission electron microscope/ microscopy
TM	transmembrane
TMD	transmembrane domain
Tris	2-amino-2-hydroxymethyl-propane-1,3-diol
UAc	uranyl acetate
UDM	n-Undecyl- β -D-Maltoside
v/v	volume per volume
w/	with
w/o	without
w/v	weight per volume

Amino acid	One-letter code	Three-letter code
alanine	A	Ala
cysteine	C	Cys
aspartic acid	D	Asp
glutamic acid	E	Glu
phenylalanine	F	Phe
glycine	G	Gly
histidine	H	His
isoleucine	I	Ile
lysine	K	Lys
leucine	L	Leu
methionine	M	Met
asparagine	N	Asn
proline	P	Pro
glutamine	Q	Gln
arginine	R	Arg
serine	S	Ser
threonine	T	Thr
valin	V	Val
tryptophan	W	Trp
tyrosin	Y	Tyr
variable	X	-

List of figures

Figure 1: Physiological function of mechanosensitive channels in bacteria.	2
Figure 2: 3D crystal structure of MscL from <i>M. tuberculosis</i>	4
Figure 3: Comparison of MscS homologues in <i>E. coli</i>	6
Figure 4: 3D crystal structure of MscS from <i>E. coli</i>	7
Figure 5: Proposed selectivity mechanism in MscS-like channels.	10
Figure 6: Lipid effect on membrane curvature.	11
Figure 7: Lipid exchange between the pockets and the lipid bilayer in MscS.	13
Figure 8: “Intimate association” of <i>I. hospitalis</i> and <i>N. equitans</i>	16
Figure 9: Transmission electron micrographs of <i>N. equitans</i>	19
Figure 10: Structure of amphipol A8-35.	47
Figure 11: Formation of <i>E. coli</i> spheroplasts.	50
Figure 12: Negative stain transmission electron micrograph of Neq531.	57
Figure 13: Western blot analysis of homogenized membranes.	58
Figure 14: Solubilization test of Neq198.	58
Figure 15: Buffer conditions for IMAC purification.	59
Figure 16: Immobilized metal affinity chromatography (IMAC) of Neq198.	60
Figure 17: Immobilized metal affinity chromatography (IMAC) of Neq531.	60
Figure 18: Homogeneity and oligomeric state of Neq198 in Fos14.	61
Figure 19: Membrane-mimicking systems for membrane protein stabilization.	62
Figure 20: Determination of the optimal MP:APol ratio for Neq198.	63
Figure 21: Reconstitution of Neq198 into amphipol A8-35.	64
Figure 22: Reconstitution of Neq531 into amphipol A8-35.	65
Figure 23: Reconstitution of Neq198 into nanodiscs.	66
Figure 24: Quality control of Neq198 reconstituted into nanodiscs.	66
Figure 25: 1D thin layer chromatograms.	69
Figure 26: 2D thin layer chromatograms.	69
Figure 27: Prediction of TM helices of Neq198.	71
Figure 28: Prediction of TM helices of Neq531.	71

Figure 29: Sequence alignment of <i>EcMscS</i> , Neq198 and Neq531	72
Figure 30: Protein surface of <i>EcMscS</i> in different orientations.....	73
Figure 31: Representative 2D class-averages in negative stain of Neq198 reconstituted into APol.	74
Figure 32: Putative domain organization of Neq198.....	75
Figure 33: RELION-2.1 workflow overview of Neq198 reconstituted into APol in negative stain.	76
Figure 34: Representative 2D class-averages of Neq531 reconstituted into APol.	78
Figure 35: RELION-2.1 workflow overview of Neq531 reconstituted into APol in negative stain.	79
Figure 36: Surface representation of Neq531 reconstituted into APol.	80
Figure 38: RELION-2.1 workflow overview of Neq198 reconstituted into nanodiscs in negative stain.	82
Figure 39: Surface representation of Neq198 reconstituted into nanodiscs.....	83
Figure 40: Cryo-EM micrographs of Neq198 reconstituted into nanodiscs.	85
Figure 41: Comparison of different data sets during 2D classification in RELION-2.1.	86
Figure 42: Representative 2D class-averages showing “defective” particles.	87
Figure 43: Representative 2D class-averages.	88
Figure 44: Representative final 3D volumes.....	91
Figure 45: Surface representation of cryo-EM density with fitted atomic model of Neq198.	94
Figure 46: Profile of ion permeation pathway.	95
Figure 47: Hypoosmotic down-shock assay of Neq198 in MJF465 <i>E. coli</i> cells.	96
Figure 48: Patch clamp currents of Neq198 reconstituted into azolectin liposomes.	100
Figure 49: Patch clamp currents of Neq531 reconstituted into azolectin liposomes.....	100
Figure 50: Comparison of archaeal and bacterial lipids and membranes.	105
Figure 51: Effect of internal pressure on the lipid membrane.	106
Figure 52: Structural comparison of Neq198 and <i>EcMscS</i>	121
Figure 53: Electrostatic potential surface of Neq198 and <i>EcMscS</i>	122

List of tables

Table I.1: Solved structures for mechanosensitive channels of large conductance	4
Table I.2: Solved structures of mechanosensitive channels of small conductance	9
Table I.3: Annotated transporter classes and families in the genome of <i>N. equitans</i>	20
Table II.1: Detergents and their characteristics	23
Table II.2: Enzymes	24
Table II.3: Protease inhibitors	24
Table II.4: Molecular weight markers	24
Table II.5: Reagent kits	25
Table II.6: Column materials	25
Table II.7: Primary and secondary antibodies	25
Table II.8: Antibiotics and their working concentrations	28
Table II.9: Bacterial strains for general cloning/subcloning and their characteristics	28
Table II.10: Bacterial strains for expression and their characteristics	29
Table II.11: General plasmids and their properties	29
Table II.12: Plasmid constructs for protein expression	30
Table II.13: Oligonucleotides	30
Table II.14: Archaeal strains	30
Table II.15: PCR mixture	31
Table II.16: Thermocycler program for PCR	31
Table II.17: Thermocycler program for Fusion PCR	32
Table II.18: Setup for digestion with restriction enzymes	33
Table II.19: Mixture for ligation of digested plasmids and DNA inserts	34
Table II.20: Transformation buffer for preparation of chemical competent <i>E. coli</i> cells	34
Table II.21: Colony PCR mixture	35
Table II.22: Thermocycler program for colony PCR	35
Table II.23: Separation and stacking gel buffer for SDS-Page	37
Table II.24: Laemmli running buffer and 6x loading buffer	37
Table II.25: SDS-Page gel composition	38

Table II.26: Composition of staining and destaining solution for SDS-Page	38
Table II.27: Blue Native gel buffer	39
Table II.28: Blue Native gel composition	39
Table II.29: Composition of Blue Native cathode and anode buffer	39
Table II.30: IMAC purification buffer	42
Table II.31: Buffers and columns used for size exclusion chromatography	44
Table III.1: Liposome preparations	98
Table III.2: Reconstitution of Neq198 into <i>E. coli</i> spheroplast	101
Table IV.1: Representative membrane proteins that have been reconstituted into nanodiscs for structure determination in cryo-EM	114
Table IV.2: Commonly used membrane scaffold protein constructs (Ritchie <i>et al.</i> , 2009)	115

ABSTRACT

Mechanosensitive (MS) channels are found throughout all domains of life since maintaining the intracellular homeostasis is crucial for all living cells. Bacterial MS channels represent the best-characterized force-sensing system. They mainly act as “emergency relief valves” by directly sensing elevated membrane tension as a consequence of osmotic down-shock. Upon opening, the channels release osmotically active solutes and ions from the cell and therefore prevent cell lysis.

In this thesis, two putative archaeal MscS-like channels from *N. equitans* - Neq198 and Neq531 - were investigated with respect to their structure and function. Major bottlenecks for the analysis of membrane proteins are the expression, solubilization, and purification that should yield sufficient amount of biologically active protein. Both channels were heterologously expressed in *E. coli* and successfully purified. Here, the N-terminal localization of the tag for purification turned out to be crucial. For Neq198 an optimized purification protocol was established. However, Neq531 is challenging to purify and the purification protocol still requires further optimization.

Membrane-mimicking systems such as lipid nanodiscs and amphipols are highly favored for the analysis of membrane proteins since they provide more native-like environments compared to detergents. Both MscS-like channels were reconstituted into amphipols or lipid nanodiscs for electron microscopy single particle analysis. Single particle analysis of negative-stained channels already gave a rough idea about the channel organization. The resulting 3D volume can be compared to *EcMscS*, whose structure was solved in 2002 by X-ray crystallography. Here, lipid nanodiscs were highly favored over amphipol for the structural analysis of Neq198. In amphipol reconstituted channels provided less detail than in lipid nanodisc reconstituted channels.

Neq198 reconstituted into lipid nanodiscs was further analyzed in cryo-EM single particle that led to the first putative structure of an archaeal mechanosensitive channel at intermediate resolution so far. The heptameric channel organization was confirmed. While the cytoplasmic domain of the channel is hardly changed compared to *EcMscS*, the membrane domain exhibits major differences. Two additional helices are located on top of the membrane domain building up a cap-like structure of unknown function. Whether this structural feature takes actively part in tension sensing and e.g. provides interaction with the S-layer of *N. equitans* is open for speculation. The electrostatic potential surfaces indicate that the channel from *N. equitans* exhibits higher anion selectivity than its homologue in *E. coli* (*EcMscS*).

The functional analyses by patch clamping highlighted that these channels are highly dependent on their native environment. A proper characterization with respect to conductance, activation threshold and ion selectivity failed in liposomes and *E. coli* spheroplasts. So far, channels reconstituted into liposomes exhibited spontaneous and constitutive activity, although no pressure was applied. These difficulties were mainly contributed to the lipid environment, which is clearly different in *N. equitans*. To characterize the channels, native lipids from *N. equitans* are required for future reconstitution and patch clamp analysis. However, hypoosmotic down-shock assays indicate that the channels are purified in active form and do not lose their functionality upon purification.

This thesis provides first structural insights into a MscS-like channel from *N. equitans* representing the first structure of an archaeal mechanosensitive channel from the MscS family. To increase the resolution of the membrane domain and cap-like structure and to refine the proposed model, more single particle analysis cryo-EM data is required.

I INTRODUCTION

1 Mechanosensitive channels

Mechanosensation as a physiological process describes the ability to convert a mechanical stimulus into electrical or biochemical signals and is believed to be one of the most ancient signal transduction mechanisms (Kloda and Martinac, 2001b). Mechanosensory transduction is involved in a wide range of physiological processes, such as touch, pain, hearing, proprioception, blood pressure control in animals, turgor control and gravitaxis in plants as well as regulation of cell shape and cell volume in bacteria (Hamill and Martinac, 2001; Martinac, 2004). As force-transducing molecules the so-called mechanosensitive (MS) channels have been identified. They can be found throughout all domains of life: archaea, bacteria (Pivetti *et al.*, 2003; Kung, 2005), and eukarya (Árnadóttir and Chalfie, 2010), thus suggesting their early appearance during evolution on earth. This is further supported by the assumption that all aspects of cellular dynamics as growth, cell division, and differentiation involve changes in cell volume and shape (Kung *et al.*, 1990; Martinac and Kloda, 2003).

Bacterial MS channels represent one of the best-characterized force-sensing systems and serve as model systems for mechanosensation (Kung, 2005). MS channels represent a structurally diverse group of proteins that have been classified according to their function rather than their sequence similarity or topology. In prokaryotes two families of MS channels have been identified. Those are classified according to their conductance: the mechanosensitive channels of large conductance (MscL) and the mechanosensitive channels of small conductance (MscS). Originally, three groups of mechanosensitive channel activities have been identified in *Escherichia coli*: MscL, MscS and MscM

(mechanosensitive channels of mini conductance) (Berrier *et al.*, 1996). However, channels that exhibit MscM activity are structurally classified as members of the MscS family. Prokaryotic MS channels were first discovered 1987 in giant *E. coli* spheroplasts using patch clamp technique (Hamill *et al.*, 1981; Martinac *et al.*, 1987). Maintaining the intracellular homeostasis is imperative for all living cells so that the major function of MS channels can be assigned to act as an “emergency relief valve” upon hypoosmotic down-shock. The immediate release of solutes enables growth and survival even at changing external osmolarities (Figure 1) (Booth and Blount, 2012).

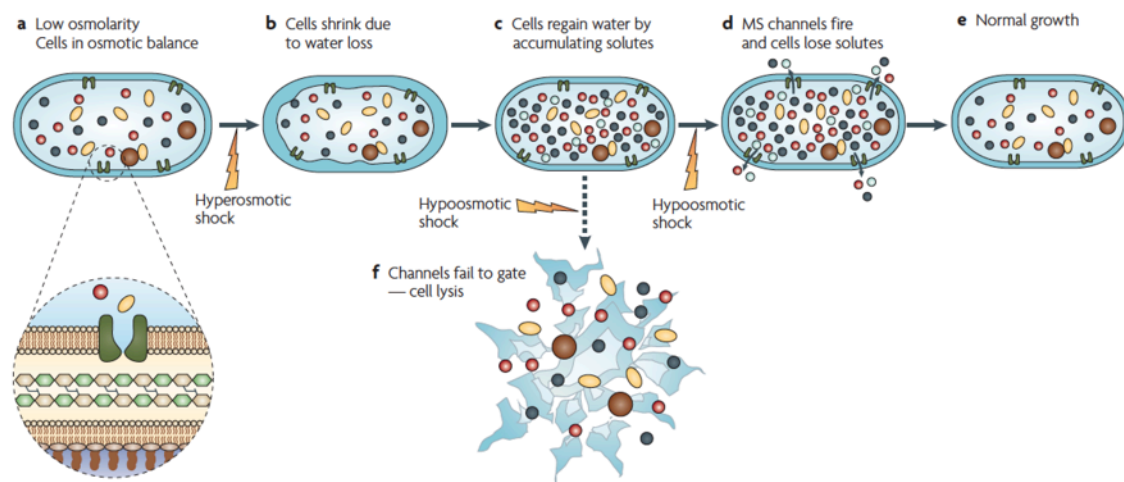


Figure 1: Physiological function of mechanosensitive channels in bacteria.

(a) At low osmolarity conditions, cells build up an outwardly directed turgor pressure, which is balanced by the cell wall and outer membrane; (b) upon hyperosmotic shock, cells shrink due to rapid water loss (c) but recover to full size by the accumulation of compatible solutes in the cytoplasm; MS channels remain closed; (d) in response to a reduction in external osmolarity (hypoosmotic shock), water floods into bacterial cells, resulting in swelling of the cell with a corresponding rise of cellular turgor and membrane tension. The rapid water entry is accompanied by the immediate activation of MS channels, allowing the efflux of intracellular osmolytes and relieving the membrane tension; (e) subsequently allowing normal growth; (f) in absence or fail in function of MS channels, the rise of membrane tension results in cell lysis as soon as the pressure exceeds the mechanical strength of the cell wall (Booth *et al.*, 2007).

MS channels directly respond to changes in membrane tension. Osmotic down shift results in water influx into the cell causing the cell to swell. By the interaction with the surrounding lipid bilayer MS channels sense the increased membrane tension and temporarily open large pores in the membrane, by which compatible solutes and ions are released. By this, the pressure is relieved and cell integrity is preserved. Booth and co-workers showed that $\Delta mscL$ and $\Delta mscS$ double mutants were not able to maintain their cell integrity resulting in cell lysis upon down-shock (Levina *et al.*, 1999). MscL and MscS have complementary function. They respond in a coordinated way to osmotic stress indicating a relationship between their activation threshold and their conductance (Berrier *et al.*, 1989; Levina *et*

al., 1999; Perozo and Rees, 2003). MS channels exhibit a step-wise response to osmotic stress, where MscS open first and MscL remains closed as backup, opening just before the lytic limit of the cell. By this, as much metabolites as possible are retained within the cell sustaining their membrane gradients (Haswell *et al.*, 2011). MS channels differ significantly with respect to their conductance ranging from 10-3,500 pS (Martinac *et al.*, 1987; Sukharev *et al.*, 1993) and their selectivity ranging from non-selective to potassium- and cation- or anion-selective channels (Sukharev *et al.*, 1993; Li *et al.*, 2002; Zhang *et al.*, 2012).

1.1 Mechanosensitive channels of large conductance (MscL)

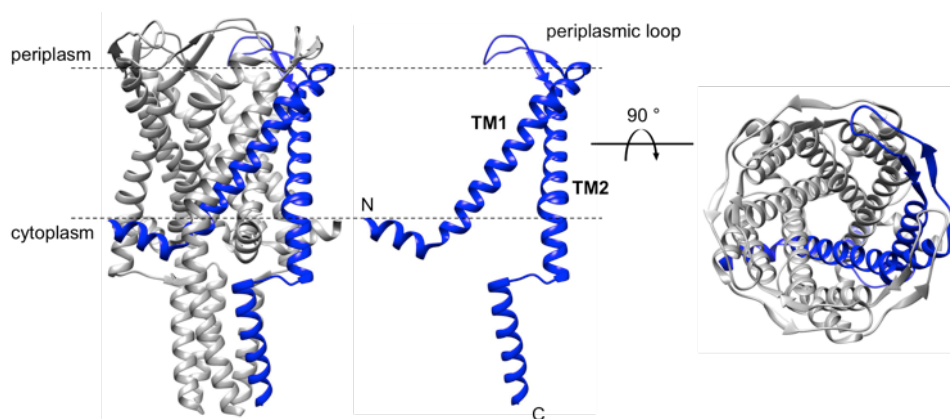
Since its first discovery in *E. coli* in 1993 by Kung's laboratory (Sukharev *et al.*, 1993; Sukharev *et al.*, 1994), the mechanosensitive channel of large conductance, MscL, was extensively studied and characterized. Compared to MscS, the MscL family is highly conserved with respect to structure and function. In general, the MscL family consists of non-selective ion channels, that exhibit an elevated conductance of ~3 nS. Members of the MscL family are pressure-activated and open at high membrane tension close to lytic limit of the bilayer (Berrier *et al.*, 1989; Sukharev *et al.*, 1993). Interestingly, the *TbMscL* – a MscL homologue from *Mycobacterium tuberculosis* – exhibits an opening threshold that is significantly larger than that of *EcMscL* and even exceeds the membrane breaking point (Moe *et al.*, 2000). This might be a result of the different lipid environments and underscores the importance of lipid-protein interactions in MS channel function (Perozo and Rees, 2003). However, in *E. coli* the *mscL* gene is not essential for growth and survival under hypoosmotic down-shock conditions. The MscL activity can be compensated by other mechanosensitive channels (Sukharev *et al.*, 1994). MscL is commonly absent from marine organisms (Booth *et al.*, 2015) and cannot be found in plants (Haswell, 2007).

To date, three MscL structures, two from bacterial and only one from an archaeal organism, have been solved by X-ray crystallography (Table I.1). As the first structure, the MscL from *M. tuberculosis* was solved in a closed conformation at a resolution of 3.5 Å (Chang *et al.*, 1998). This 136-amino-acid protein exhibits a transmembrane (TM) domain and a cytoplasmic domain assembled to a homopentameric complex (Figure 2). Each subunit consists of two membrane-spanning α -helices (TM1 and TM2) connected by a periplasmic loop resulting in the location of N- and C-terminus in the cytoplasm. At the C-terminus a short α -helix forms a bundle below the pore that reaches into the cytoplasm (Chang *et al.*, 1998; Steinbacher *et al.*, 2007). Deletion experiments showed that the cytoplasmic bundle is not essential for channel activity (Blount *et al.*, 1996).

Table I.1: Solved structures for mechanosensitive channels of large conductance

Organism	Characteristics	Resolution (Å)	Method	Reference/ PDB
<i>M. acetivorans</i> / <i>M. jannashii</i> (<i>MaMscL-MjRS</i>)	chimera, pentameric open/closed	3.5/4.1	X-ray	Li <i>et al.</i> , 2015 4y7k, 4y7j
<i>S. aureus</i> (<i>SaMscL</i>)	tetrameric, expanded intermediate state	3.82	X-ray	Liu <i>et al.</i> , 2009 3hzq
<i>M. tuberculosis</i> (<i>TbMscL</i>)	pentameric, closed	3.5	X-ray	Steinbacher <i>et al.</i> , 2007 Chang <i>et al.</i> , 1998 2oar

The TM1 helix of each subunit lines the pore and forms a tightly packed bundle with its adjacent TM1 helices, whereas the TM2 helices interact with the surrounding lipid bilayer (Chang *et al.*, 1998). The homo-pentameric complex forms a pore with a diameter of 30 Å, which can vary between 2 and 30 Å during gating (Perozo *et al.*, 2002).

**Figure 2: 3D crystal structure of MscL from *M. tuberculosis*.**

Crystal structure of the pentameric *TbMscL* in closed conformation at 3.5 Å resolution (Chang *et al.*, 1998), showing the overall structure (left) with one subunit highlighted in blue, a monomer (middle), and the top view from the periplasmic side of the membrane with one subunit highlighted in blue (right); N- and C-terminus are located in the cytoplasm; TM1 and TM2 helices are connected by a periplasmic loop. Structure was visualized in Chimera 1.12 (Pettersen *et al.*, 2004), 2oar.pdb.

Deletion mutants lacking the cytoplasmic α -helical bundle were used for structure determination of the first archaeal MS channel, which also adopts a pentameric fold. The archaeal channel protein comprised only limited hydrophilic regions; therefore riboflavin synthetase from *Methanocaldococcus jannashii* (*MjRS*) was fused to the C-terminus of the MscL channel protein from *Methanosarcina acetivorans* (*MaMscL*) to increase potential crystal contacts (Table I.1) (Li *et al.*, 2015). Surprisingly, the structure of the MscL homologue from *Staphylococcus aureus* (*SaMscL*) suggested a tetrameric

stoichiometry (Liu *et al.*, 2009). Further experiments demonstrated that the detergents used in purification and crystallization caused the variable stoichiometry of SaMscL *in vitro*. *In vivo* studies suggested a pentameric oligomeric state (Dorwart *et al.*, 2010).

1.2 Mechanosensitive channels of small conductance (MscS)

1.2.1 MscS superfamily

In contrast to the MscL family, the MscS family is relatively diverse with respect to structure and function. Members of the MscS superfamily show great diversity in sequence, size, and topology. They are classified into 15 subfamilies according to their unique functional domains. Those can be further divided into larger subfamilies (~50 to 645 members each) like MscK, DUF3772-MscS, bCNG, BON-MscS, EF-MscS and smaller subfamilies (one to only few members) like MscCG, extended C-terminus MscS, MscS-DEP, YjeP, Glucose Transporter MscS, PBD-1-MscS, Cu-Heme-MscS, and concatenated MscS (Malcolm and Maurer, 2012). For the overall and most-common architecture of MscS applies the following: a large water-filled cytoplasmic domain that opens to the cytoplasm follows the transmembrane domain. Several members exhibit additional N- and/or C-terminal extensions/domains, which are assumed to affect the tension sensing mechanism or create additional regulatory sites. MscS subtypes exhibit varying numbers of transmembrane helices ranging from at least three (e.g. *EcMscS*) to 11 (e.g. MscK) (Booth *et al.*, 2011; Malcolm and Maurer, 2012). The pore lining helix TM3a is highly conserved within the MscS superfamily (Pivetti *et al.*, 2003; Balleza and Gómez-Lagunas, 2009). The ion selectivity that distinguishes different family members is mediated by the cytoplasmic domain (Gamini *et al.*, 2011; Cox *et al.*, 2014). Single organisms might encode multiple MscS members in their genome. In *E. coli* for example, six MscS-like channels of variable size are present in total: MscS (286 aa, *EcMscS*), MscK (1120 aa), YbdG (415 aa), YnaI (343 aa), YbiO (741 aa), and YjeP (1107 aa) (Figure 3) (Levina *et al.*, 1999; Schumann *et al.*, 2010; Edwards *et al.*, 2012). The *EcMscS* represents the MscS archetype (cf. I1.2.2). YbdG has a larger cytoplasmic domain than the other homologues due to an insertion of ~50 amino acids between the middle β and the $\alpha\beta$ domains (cf. Figure 4). Moreover, YbdG exhibits five putative TM helices. The expression level of YbdG in the membrane of *E. coli* is not sufficient to protect against severe hypoosmotic shock. Interestingly, overexpression of YbdG provides complete protection. YbdG is characterized to have MscM activity with a conductance of 350-400 pS (Schumann *et al.*, 2010). YbdG comprising five putative TM helices belongs like *EcMscS* and YnaI to the smaller topological

class of channels, while YbiO, YjeP, and MscK comprising 11 putative TM helices and extensive periplasmic domains form the larger topological class (Pivetti *et al.*, 2003). The potassium-dependent MscK represents the largest MscS-like channel in *E. coli* and has a conductance of ~ 0.875 nS (Li *et al.*, 2002). YbiO, YnaI, and YjeP are only present in low levels in the membrane and therefore do not provide protection against hypoosmotic shock as well. NaCl especially induces YbiO, which exhibits a conductance of ~ 1000 pS. YnaI and YjeP have MscM activity with a conductance of ~ 100 pS and ~ 300 pS, respectively (Edwards *et al.*, 2012).

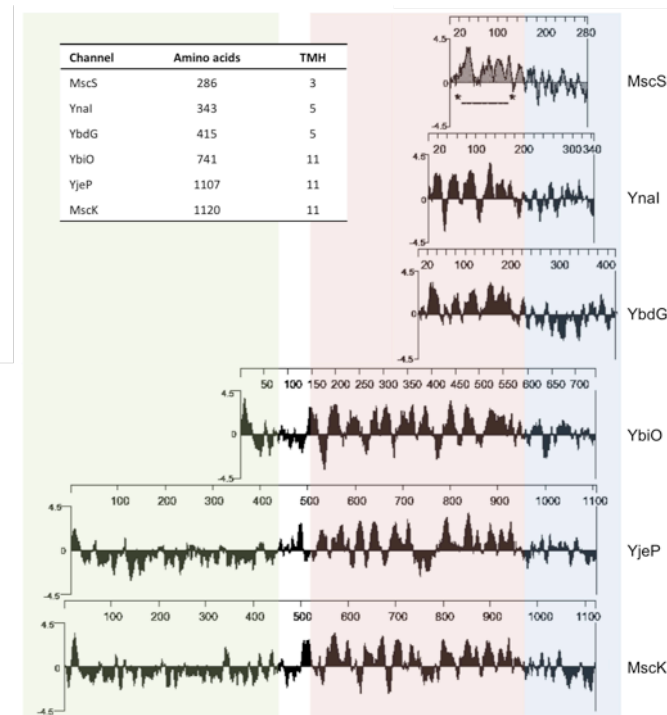


Figure 3: Comparison of MscS homologues in *E. coli*.

Hydrophobicity blots (Kyte-Doolittle, $w = 9$) of the six MscS homologues in *E. coli*, aligned by the last three predicted transmembrane (TM) helices for each homolog with the three TM helices of MscS (*-----*). Highlighted sequences: periplasmic region – green, membrane region – red; cytoplasmic domain – blue (adapted from Schumann *et al.*, 2010 and Naismith and Booth, 2012); inset: overview of amino acid length and predicted TM helices of each homolog.

Besides the six homologues in *E. coli*, various other members have been characterized electrophysiological, e.g. MscMJ and MscMJLR from *M. jannashii* (Kloda and Martinac, 2001d), MscSP from *Silicibacter pomeroyi* (Petrov *et al.*, 2013), MSL10 from *Arabidopsis thaliana* (Maksaev and Haswell, 2013), and Ng-MscS from *N. gonorrhoeae* (Wang *et al.*, 2018).

1.2.2 Structure and function of MscS

MscS fold as homo-heptamers with a sevenfold rotational axis perpendicular to the membrane normal through the center of the pore. The channel can be divided in a transmembrane domain and a large water-filled cytoplasmic domain (Figure 4) (Bass *et al.*, 2002; Steinbacher *et al.*, 2007).

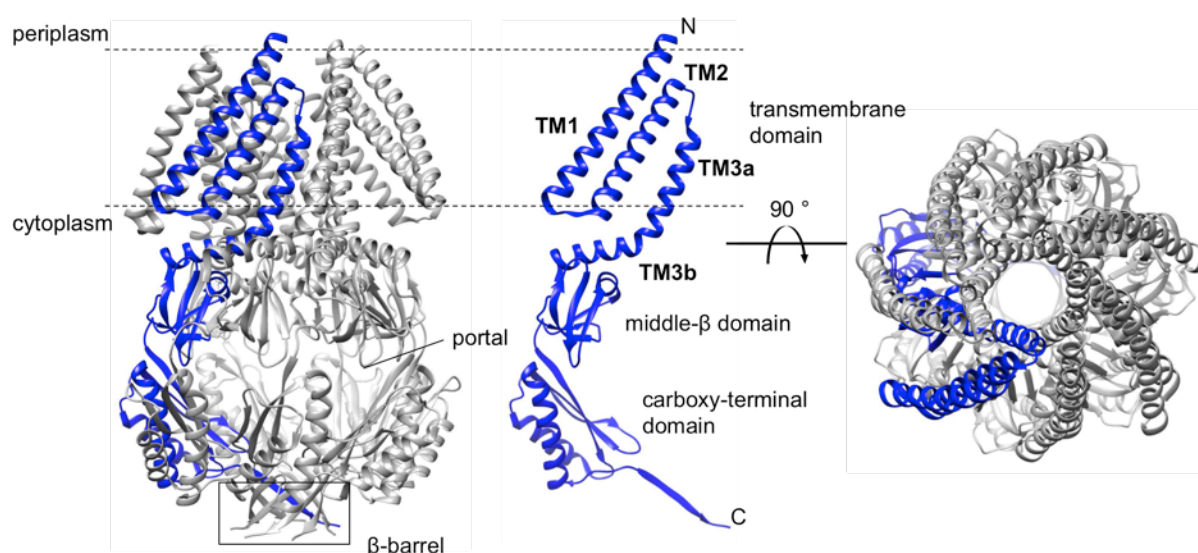


Figure 4: 3D crystal structure of MscS from *E. coli*.

Crystal structure of the homo-heptameric *EcMscS* in a closed conformation at a resolution of 3.7 Å (Bass *et al.*, 2002; Steinbacher *et al.*, 2007), showing an overall structure (left) with one subunit highlighted in blue, a channel monomer (middle) and the top view of the channel (right) from the periplasmic side of the membrane with one subunit highlighted in blue; N-terminus is located in the periplasm, whereas the C-terminus is located in the cytoplasm. Structure was visualized in Chimera 1.12 (Pettersen *et al.*, 2004), 2oau.pdb.

Each subunit of WT *EcMscS* consists of 286 amino acids and exhibits three transmembrane helices (TM1 29-57, TM2 68-91, TM3 96-127) with the N-terminus facing the periplasm (Bass *et al.*, 2002). The membrane-spanning helices TM1 and TM2 form a closely packed hairpin. They are tilted by 27° to 35° with respect to the sevenfold axis, which results in the displacement of the helices TM1 and TM2 from the core of TM3 helices. A kink at Gly113 divides the TM3 helix into the pore-lining helix TM3a (residues 96-112) and the helix TM3b (residues 114-127) and marks the membrane boundary. Seven TM3a helices are arranged in a helical barrel, which creates the central axis of the pore and thereby lines the route of ions through the membrane. Adjacent TM3a helices from neighboring subunits are tightly packed. A pattern of highly conserved alanine and glycine residues enables these tight helix-helix interactions by packing the glycines of one helix to the alanines of the neighboring helix (knob and hole mechanism). Especially glycines are known to facilitate conformational changes during gating (Bass *et al.*, 2002; Anishkin and Sukharev, 2004; Edwards *et al.*, 2005). Two rings of

hydrophobic residues (Leu105 and Leu109) line the permeation pathway. In addition to the hydrophobic nature of the TM3a, these residues create a hydrophobic seal (Bass *et al.*, 2002) that was also termed as “vapor lock” (Anishkin and Sukharev, 2004). The narrowest point is constricted to ~ 11 Å (Bass *et al.*, 2002). TM3b connects the membrane-embedded channel part to the cytoplasmic domain and is orientated almost parallel to the membrane surface (Booth *et al.*, 2011). The membrane channel opens to a large water-filled chamber with a diameter of 40 Å and is formed predominantly by β -sheets and $\alpha\beta$ -sheet domains. Seven lateral portals with a diameter of ~ 14 Å between the interfaces of the single subunits connect the chamber to the cytoplasm. The last ~ 18 C-terminal amino acids of each subunit form a seven-stranded β -barrel as a distal pore with a diameter of ~ 8 Å (Bass *et al.*, 2002). Deletion experiments have shown that a loss of the β -barrel does not influence channel assembly or gating mechanisms but severely impairs stability (Schumann *et al.*, 2004). The overall structure of *EcMscS* is determined to dimensions of 120 Å in length parallel to the sevenfold axis and 80 Å in width parallel to the membrane (Bass *et al.*, 2002).

To date, nine different structures of MscS were solved, among those six of *EcMscS* in distinct conformations and at different resolutions (Table I.2). The first crystal structure for the WT *EcMscS* was obtained at a resolution of 3.9 Å by Bass and co-workers in 2002 (Bass *et al.*, 2002). They captured the protein in a non-conducting, closed conformation. For the subsequently solved structures, the cytoplasmic domain remained essentially unchanged whereas distinct conformations could be observed for the transmembrane region. The Ala106Val variant resulted in an open conformation at a resolution of 3.45 Å (Wang *et al.*, 2008). Compared to the closed state, the helices TM1 and TM2 rotate clockwise as a rigid body by approximately 45° along the sevenfold axis. Moreover, the helices TM1 and TM2 increase their tilt by $\sim 15^\circ$ with respect to the sevenfold axis. The TM3a helices rotate clockwise around their axis by $\sim 15^\circ$ and move out from the central axis of the channel. As a result, the TM3a helices are parallel to each other, to the sevenfold axis, and to the membrane normal in the open structure. In the closed structure the TM3a helices arrange diagonal to the sevenfold axis, instead. It is proposed that the open-close-transition of the channel is enabled by an iris-like motion of the three TM helices (Wang *et al.*, 2008). Intriguingly, the DDM solubilized WT *EcMscS* adopts an open conformation as observed for the Ala106Val *EcMscS* variant, which was solubilized in Fos14. This highlighted the general sensitivity of membrane proteins and their conformational states to variations in detergents, crystallization conditions, and point mutations (Lai *et al.*, 2013). In 2015 the structure of another low-conductance MscS channel from *E. coli*, YnaI, was solved by cryo-electron microscopy to a resolution of 12.6 Å (Böttcher *et al.*, 2015) - to date, the first and only structure of a

mechanosensitive channel of small conductance solved by cryo-EM. Furthermore, the structure of a MscS homologue from *Helicobacter pylori* (Lai *et al.*, 2013), a gram-negative bacterium with potential pathogenicity, is currently available as well as a structure from *Thermoanaerobacter tengcongensis*, characterized as an anion-selective channel (Zhang *et al.*, 2012) (Table I.2).

Table I.2: Solved structures of mechanosensitive channels of small conductance

Organism	Characteristics	Resolution (Å)	Method	Reference EMDB/PDB
<i>E. coli</i> (YnaI)	DDM	12.6	cryo-EM	Böttcher <i>et al.</i> , 2015 3035
<i>E. coli</i> (<i>EcMscS</i>)	D67R1 (R1 = MTSSL cysteine adduct), open	2.99	X-ray	Pliotas <i>et al.</i> , 2015 5aji
<i>E. coli</i> (<i>EcMscS</i>)	WT, open, DDM	4.4	X-ray	Lai <i>et al.</i> , 2013 4hwa, 4hw9
<i>H. pylori</i> (<i>HpMscS</i>)	WT, closed, DDM	4.2	X-ray	Zhang <i>et al.</i> , 2012 3udc, 3t9n
<i>E. coli</i> (<i>EcMscS</i>)	spin labeled D67C mutant, open, DDM	4.84	X-ray	Pliotas <i>et al.</i> , 2012 4agf, 4age
<i>E. coli</i> (<i>EcMscS</i>)	spin labeled L124C mutant, open, DDM	4.70	X-ray	Wang <i>et al.</i> , 2008 2vv5
<i>T. tengcongensis</i> (<i>TiMscS</i>)	WT, w/o ligand, w/ ligand LMT closed, DDM	3.36/3.46	X-ray	Steinbacher <i>et al.</i> , 2007 Bass <i>et al.</i> , 2002 2oau
<i>E. coli</i> (<i>EcMscS</i>)	Ala106Val variant, open, Fos14	3.45	X-ray	
<i>E. coli</i> (<i>EcMscS</i>)	WT, closed, Fos14 desensitized/inactive	3.7/3.9	X-ray	

The helices TM1 and TM2 of *EcMscS* are thought to act as sensors for membrane tension by interacting with the surrounding lipid bilayer and therefore directly coupling changes in membrane tension to conformational rearrangements (Bass *et al.*, 2002; Wang *et al.*, 2008) (I1.2.3). PELDOR studies of *EcMscS* in proteoliposomes confirmed basic findings of the first crystal structure: the pronounced gap between the outer helices (TM1, TM2) and the pore lining helix TM3 is preserved in lipid environment and probably contributes to the gating mechanism (Pliotas *et al.*, 2012; Ward *et al.*, 2014). Moreover, the presence of charged residues (arginines) in this region suggest that the helices TM1 and TM2 act as voltage sensor as well (Bass *et al.*, 2002; Bezanilla and Perozo, 2002).

In addition to its importance for stabilization and oligomerization (Schumann *et al.*, 2004; Rasmussen *et al.*, 2007), the cytoplasmic vestibule domain is involved in selectivity and gating. This domain is thought to act as a selectivity filter or sieve by controlling, which ions can enter through the portals and therefore exit the cells (Gamini *et al.*, 2011). Interestingly, the filter function of the cytoplasmic domain stands in contrast to voltage-gated Cl^- , Ca^{2+} , K^+ and Na^+ channels, whose selectivity filters are located within the transmembrane region (Cox *et al.*, 2014). For *E. coli* it is assumed that electronegative regions on the bottom of the cytoplasmic vestibule trap cations resulting in an environment that is more conducive to anion conduction (Figure 5) (Cox *et al.*, 2014). In *T. tengcongensis* the lateral portals seem to be missing. Here, electronegative regions on the bottom of the cytoplasmic vestibule together with a residue outside the β -barrel result even in higher anion selectivity compared to *E. coli* (Zhang *et al.*, 2012). The significant role of the β -barrel for anion selectivity in *TtMscS* was confirmed by Song *et al.*, 2017.

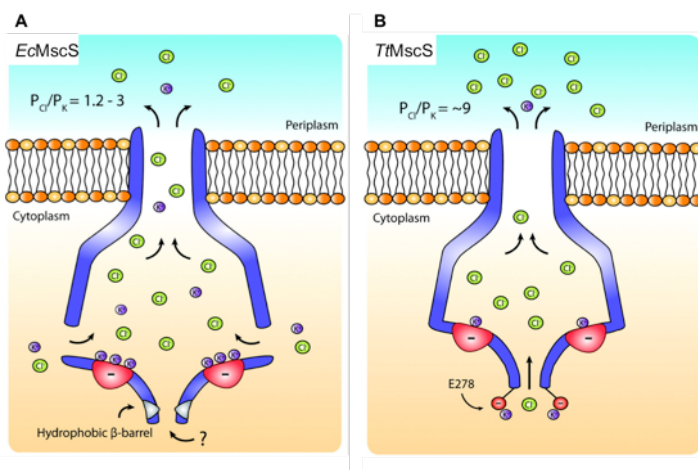


Figure 5: Proposed selectivity mechanism in MscS-like channels.

Electronegative regions on the bottom of the cytoplasmic domains create an environment conducive to anion conduction. (A) Residues around E187 and E227 trap cations resulting in easier transit for anions; (B) in addition to the electronegative region on the bottom of the cytoplasmic domain, a residue on the outside of the β -barrel (E278) likely traps cations resulting in a higher anion selectivity in *TtMscS* compared to *EcMscS* (adapted from Cox *et al.*, 2014).

Electrophysiological experiments characterize the *EcMscS* to exhibit a conductance of ~ 1 nS and a slight preference for anions over cations: ($P_{\text{Cl}}/P_{\text{K}}$) of 1.2-3.0. The channel is activated by membrane tensions 1.4 times lower compared to *MscL* and shows additional voltage dependency (Martinac *et al.*, 1987; Sukharev *et al.*, 1993; Sukharev, 1997). Furthermore, *EcMscS* shows a complex inactivation/desensitization mechanism while sustaining membrane tension (Levina *et al.*, 1999). *EcMscS* reacts to sudden changes in membrane tension; however, if lateral pressure is applied slowly, the channel remains closed suggesting a relation between gating and pressure rate (Akitake *et al.*, 2005). *EcMscS* measurements of gating transitions show that the channel opens within milliseconds to around two-thirds of its conductance and then opens slower to full conductance (Booth *et al.*, 2007).

1.2.3 Protein-lipid interactions

Protein-lipid interactions have moved to the center of interest lately. Direct or indirect interactions with the surrounding membrane and thus conformational changes of the proteins have been investigated. Recently, a general model for tension sensing in MS channels was introduced (Pliotas and Naismith, 2017). Bacterial MS channels were first described to directly sense membrane tension in the lipid bilayer. This “bilayer model” or force-from-lipids (FFL) principle applies to both prokaryotic and eukaryotic ion channels (Hamill and Martinac, 2001; Perozo *et al.*, 2002; Teng *et al.*, 2015). An explanation towards the understanding of channel gating was established with the observation that an incorporation of conical lipids in the lipid bilayer results in the opening of MscS and MscL (Martinac *et al.*, 1990; Perozo *et al.*, 2002). The incorporation of conical lipids alters the curvature of the membrane and therefore changes intrinsic forces (Figure 6). Regardless of whether conical lipids are incorporated, or the internal pressure rises as a result of hypoosmotic shock, the membrane is dilated so that the membrane curvature decreases. Thereby the lateral pressure on the mechanosensitive channels is relieved resulting in channel opening.

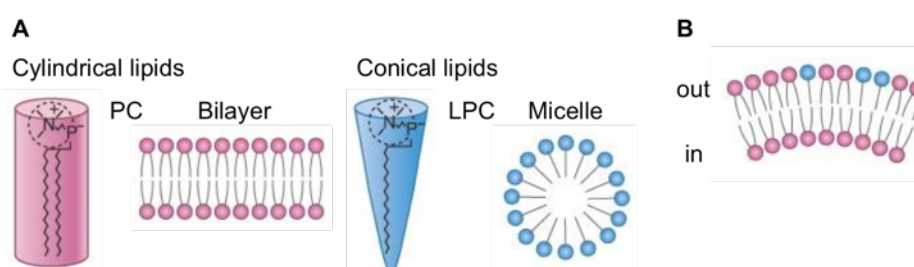


Figure 6: Lipid effect on membrane curvature.

(A) Bilayer-forming phospholipids (shown in red), such as phosphatidylcholine (PC), can be approximated as rods. Micelle-forming lysophospholipids (blue), such as lysophosphatidylcholine (LPC) with only one fatty acid chain, can be regarded as cones. (B) The addition of cone-shaped lipids (or other amphipaths) into one of the leaflets of the bilayer can alter the shape/curvature, and therefore the intrinsic forces (modified from Kung, 2005).

These findings suggested that changes in the membrane tension alone or lateral pressure are sufficient for channel gating. Furthermore, prokaryotic MscS and MscL maintain their mechanosensitivity after purification and reconstitution into liposomes suggesting that the mechanical force is directly transmitted from the lipid bilayer to the protein (Sukharev *et al.*, 1993; Sukharev, 2002; Nomura *et al.*, 2006). MscS channels that have been studied in different lipid environments (giant *E. coli* spheroplasts, liposomes) exhibited different channel behavior (Shaikh *et al.*, 2014). Hence, the lipid-protein interface plays a crucial role in membrane tension sensation. This is further supported by the fact that the mechanosensitivity of MscL increases dramatically along with the thickness reduction of

the hydrophobic core of the membrane (Perozo *et al.*, 2002). Since changes of lipids determine MS channel activity, the interaction of MS channels with their surrounding lipid bilayer was identified as an important aspect of their function. Among membrane proteins, the MscS family offers probably the most dynamic set of interactions with the lipid bilayer (Booth *et al.*, 2011).

EcMscS provides three principal lipid-protein interfaces. Originally, the TM1-TM2 helix pair was determined to sense membrane tension (Bass *et al.*, 2002). These helices form a rigid sensor paddle that moves independently upon channel gating whereupon the tension is transmitted to the pore through the linker between TM2 and TM3a (Wang *et al.*, 2008). Sukharev and co-workers showed that the inter-helical contact is inevitable for force transmission from the lipid-facing helices TM1/TM2 to the pore-lining helix TM3. The uncoupling of TM2 and TM3 appears to result in inactivation of the channels (Belyy *et al.*, 2010). The extreme asymmetry with respect to their amino acid composition of TM1 and TM2 might additionally contribute to lipid tension sensing: whereas the residues in the periplasmic half of the helices are of low polarity, polar residues are observed in the cytoplasmic half. Thus, different interactions with lipid head groups on both sides of the membrane are induced (Booth *et al.*, 2011). Scanning mutagenesis identified residues located at both ends of the helices TM1 and TM2 as essential for channel function (Nomura *et al.*, 2006). In another study, lipid-facing hydrophobic residues, that are located within the TM1 and TM2 helices, were determined to be involved in tension sensing. Those residues interact with lipid tail groups in the closed state and are rotated inwards to form intra-protein hydrophobic interactions in the open state of the channel (Malcolm *et al.*, 2011). Another lipid-protein interface is located within TM3b helix, which is proposed to lie along the inner membrane presenting a hydrophobic surface to the bilayer. Conserved basic residues (Arg128 and Arg131) at the C-terminal end of TM3b are proposed to build an anchor by the interaction with phospholipid head groups (Nomura *et al.*, 2008; Booth *et al.*, 2011). Finally, the N-terminal sequence (residues 1-26) seems to have a significant impact on gating characteristics. Especially, the tryptophan residue (Trp16), which is located upstream of TM1 facing the periplasm, is proposed to have an anchoring function by the interaction with lipid head groups (Rasmussen *et al.*, 2007).

The *EcMscS* crystal structure revealed that the helices TM1 and TM2 are displaced from the core of TM3 helices creating an apparent void in between (Bass *et al.*, 2002; Pliotas *et al.*, 2012; Ward *et al.*, 2014). These voids have also been observed in other organisms (Zhang *et al.*, 2012; Lai *et al.*, 2013). Intriguingly, alkyl chains inside this hydrophobic cleft have been identified in a new high-resolution structure (Pliotas *et al.*, 2015). Moreover, it was shown that the void between TM3 and TM1/TM2 is

reversibly filled with lipids (lipid interdigitation) upon channel gating. The number of lipids decreases upon channel opening. Thus, the degree of lipid interdigitation determines open/closed conformations of MscS (Figure 7) (Pliotas *et al.*, 2015). How lipids move in and out of a binding site and by this create sensitivity to membrane tension, was already shown for the human TRAAK K⁺ channel (Brohawn *et al.*, 2014). Thus, reversible lipid interdigitation is proposed to represent an universal model for tension sensing by MS channels (Pliotas *et al.*, 2015; Pliotas and Naismith, 2017).

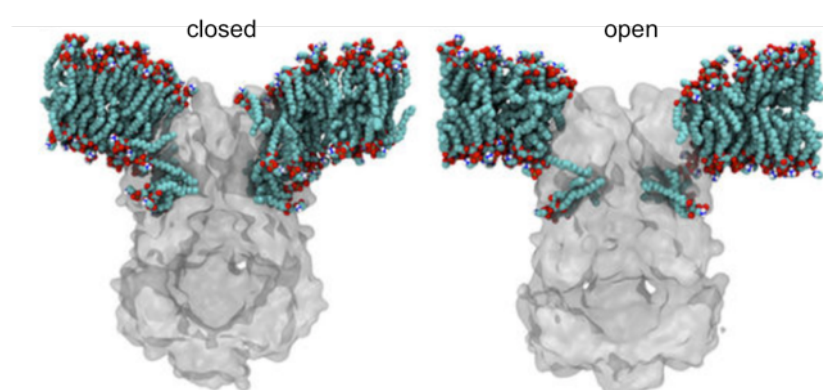


Figure 7: Lipid exchange between the pockets and the lipid bilayer in MscS.

Multiscale molecular dynamics (MD) simulations of the closed and open conformation of MscS in POPE/POPG (4:1) phospholipid bilayers. During simulations lipids migrated to fill the TM pockets and a strong local membrane curvature around MscS was observed (Pliotas *et al.*, 2015).

The question of lipid-protein interaction for larger members of the MscS family is more complex. Several homologues exhibit multiple additional N-terminal transmembrane helices, which result in isolating the aforementioned TM1-TM2 sensor domain from the surrounding lipid bilayer. Possibly, here the tension sensor is not constituted by the adjacent helices of the TM3a domain. Therefore, larger homologous channels require a more complex mechanism for tension sensing and transmission to the channel pore than it was described so far for MS channels exhibiting only three transmembrane helices (Booth *et al.*, 2011). For a larger family member, YnaI from *E. coli*, lipid interdigitation into cavities and extended sensor paddles, i.e. four TM helices instead of two as in *EcMscS*, have already been discussed (Böttcher *et al.*, 2015).

1.2.4 Physiological functions of MscS-like channels

Besides its well-known and characterized function as emergency relief valve upon hypoosmotic down-shock (Levina *et al.*, 1999), there is emerging evidence that MS channels are not only limited to osmoregulation. Especially members of the MscS family play additional roles in bacterial and plant cell physiology. Those physiological functions range from osmoregulation to more specialized activities in Ca²⁺ regulation, signal transduction pathways, amino acid efflux, and cell division and survival (Haswell *et al.*, 2011; Cox *et al.*, 2015).

MscK from *E. coli* represents an example for a highly specialized and tightly regulated channel, which is more sensitive to membrane tension than *EcMscS* but is also regulated by the ionic environment. Its activation requires external potassium ions and the channel is proposed to be essential for the survival at high potassium concentrations (Li *et al.*, 2002).

In *E. coli* the interaction of FtsZ with the α/β domain of the cytoplasmic domain of MscS was identified as a possible non-channel function (Koprowski *et al.*, 2015). FtsZ, a bacterial tubulin-like protein, is involved in the Z-ring formation that initiates cell division (Buddelmeijer and Beckwith, 2002; Adams and Errington, 2009). Overexpression of the soluble α/β domain as well as a deletion mutant missing the last 20 amino acids disabled cell division resulting in elongated (filamentous) cells. Moreover, mutations in the α/β domain reduced its binding to FtsZ and its interaction was identified to play a crucial role in cell protection against antibiotic stress. Therefore, it was hypothesized that the α/β domain binds FtsZ and modulates FtsZ-dependent processes like cell wall synthesis and repair (Koprowski *et al.*, 2015). This is further supported by the involvement of MSL2 and MSL3, two MscS-like channels from *A. thaliana*, in chloroplast division (Wilson *et al.*, 2011; Wilson and Haswell, 2012).

With the cyanobacterial MscS homologue PamA, a protein was identified that is independent of osmotic shock but instead implicated in cellular signal transduction pathways. Here, the C-terminus of PamA interacts with the signaling protein PII, that coordinates several signal transduction pathways associated with carbon and nitrogen metabolism. Moreover, a deletion of *pamA* results in glucose sensitive mutants that show abnormal expression of genes involved in sugar and nitrogen signaling (Osanai *et al.*, 2005).

Two MscS-like homologues from the fission yeast *Schizosaccharomyces pombe* are localized within the membrane of the endoplasmatic reticulum and have a putative EF-hand motif. They play a crucial role in regulation of cell volume and intracellular Ca^{2+} concentrations (Nakayama *et al.*, 2012). Furthermore, new findings suggest that *EcMscS* is not only involved in osmotic shock response but also in the regulation of intracellular Ca^{2+} concentrations (Cox *et al.*, 2013).

In microbial biotechnology the MscS-like channel from *Corynebacterium glutamicum* (MscCG) is of high interest. This channel plays a crucial role in the industrial production of amino acids, e.g. glutamate or lysine. Under production conditions like biotin limitation or the treatment with penicillin, MscCG mediates the passive efflux of negatively charged glutamate down its electrochemical gradient (Nakamura *et al.*, 2007; Becker *et al.*, 2013). Interestingly, MscCG was also reported to act under

hyperosmotic stress conditions by fine-tuning the steady state concentration of compatible solutes (betaine) in the cytoplasm of *C. glutamicum* (Börngen *et al.*, 2010).

Two putative MS channels from *Campylobacter jejuni*, responsible for bacterial gastroenteritis in humans, provide first evidence for the role of MS channels in pathogenicity. Especially one channel turned out to be essential for the survival upon hypoosmotic stress that is experienced during environmental transmission (Kakuda *et al.*, 2012). With Ng-MscS another MscS-like channel from the human-specific bacterial pathogen *Neisseria gonorrhoeae* was identified and characterized. Ng-MscS contributes to *in vivo* colonization of the mucosal epithelia of the urogenital tract and survival. Here, gain-of-function mutations in Ng-MscS inhibited bacterial growth. Moreover, the survival of Ng-*mscS* deletion mutants was significantly reduced in hypoosmotic shock assays (Wang *et al.*, 2018). Recently, MscS-like channels have been repeatedly discussed as potential targets for antibiotics (Booth and Blount, 2012). In this regard, it is particularly advantageous that MscS-like channels have no homologues in humans or animals, are more widely distributed than MscL and can be numerous found among pathogenic bacteria, for example like *H. pylori*, *Vibrio cholera*, *Neisseria meningitides* and *Haemophilus influenza* (Lai *et al.*, 2013; Cox *et al.*, 2015).

1.3 Mechanosensitive channels in archaea

Archaea are adapted to extreme habitats, where they are exposed to high temperatures, extreme salinity or low pH. Therefore, it is not surprising that mechanosensitive channels are found within the archaea, since maintaining the intracellular homeostasis is imperative for all living cells for their growth and survival.

The existence of MS channels in archaea was first documented using patch clamp technique with the identification of two types of MS channels located in the cell membrane of *Haloferax volcanii* (Le Dain *et al.*, 1998). Since then other archaeal mechanosensitive channels have been characterized electrophysiological, e.g. MscTA from the cell wall-less *Thermoplasma acidophilum* (Kloda and Martinac, 2001a), and MscMJ/MscMJLR from *M. jannashii* (Kloda and Martinac, 2001d; Kloda and Martinac, 2001c). Archaeal MS channels share structural and functional homology with bacterial MS channels regarding ion selectivity, voltage dependence and mechanism of activation. They are expected to carry out similar cellular functions (Kloda and Martinac, 2001a). However, archaeal lipids differ significantly from bacterial lipids, which should be considered for protein-lipid interactions and will be discussed later (IV2.1). In contrast to their bacterial homologues, archaeal mechanosensitive channels have not been studied as extensively yet but it is discussed whether they represent a missing

link or an evolutionary intermediate between bacterial and eukaryotic MS channels (Kloda and Martinac, 2001b; Kloda and Martinac, 2002; Martinac and Kloda, 2003; Balleza, 2011). So far, only one structure of the mechanosensitive channel chimera of large conductance (MscL) from *M. acetivorans* has been solved by X-ray crystallography (Li *et al.*, 2015) (Table I.1).

2 *Nanoarchaeum equitans* and *Ignicoccus hospitalis*: the unusual intimate association of two archaea

2.1 The “intimate association”

Ignicoccus hospitalis (“the friendly fire sphere”) and *Nanoarchaeum equitans* (“the riding dwarf”) represent the first described (meanwhile two further biocoenoses are known) cultivable natural biocoenosis of two archaea that is also designated as “intimate association” (Huber *et al.*, 2002; Jahn *et al.*, 2008). The strictly anaerobic and hyperthermophilic organisms were isolated from hydrothermal vents at the Kolbeinsey Ridge at the northern coast of Iceland (Huber *et al.*, 2000).

In contrast to its host, the symbiotic partner *N. equitans* can only be cultivated in co-culture, at least under laboratory conditions, depending vitally on a direct cell-cell contact with an actively growing *I. hospitalis* cell (Figure 8) (Huber *et al.*, 2002). So far, the explicit nature and mechanism of this relationship remains still unclear, although no beneficial effects for *I. hospitalis* have been found yet.

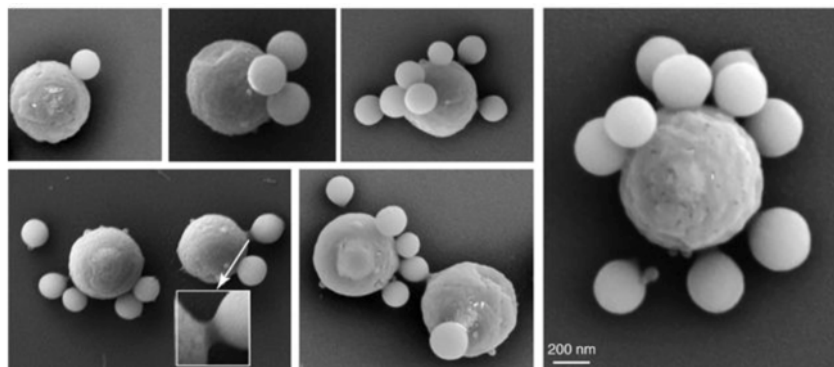


Figure 8: “Intimate association” of *I. hospitalis* and *N. equitans*.

SEMs illustrating different stages of *N. equitans* colonization of *I. hospitalis*; depending on the growth stage of the co-culture a variable number of *N. equitans* cells is attached to the surface of *I. hospitalis* ranging from one (exponential growth) to many (stationary phase); the close-up shows the interspecies membrane contact (Giannone *et al.*, 2015).

Currently, the genus *Ignicoccus* includes three species: *I. hospitalis* (Paper *et al.*, 2007), *I. islandicus*, and *I. pacificus* (Huber *et al.*, 2000). Moreover, another species was isolated: *Ignicoccus* sp. MEX13A (“*I. morulus*”, Lange, 2009). Whereas a highly unusual cell anatomy can be seen as a common structural feature within this genus, cross infection studies have demonstrated that only *I. hospitalis* can serve as a host for *N. equitans* (Jahn *et al.*, 2008). Related *Nanoarchaea* are widespread in marine and terrestrial thermal environments around the world (Hohn *et al.*, 2002; McCliment *et al.*, 2006; Casanueva *et al.*, 2008; Clingenpeel *et al.*, 2013; Munson-McGee *et al.*, 2015; Wurch *et al.*, 2016). Recently, a new terrestrial representative of the *Nanoarchaeota* was isolated at the Yellowstone National Park, which is assumed to live in a similar association with an archaeon (*Acidolobus* sp.) (Podar *et al.*, 2013).

2.2 *I. hospitalis*: current knowledge

The genus *Ignicoccus* belongs to the *Desulfurococcaceae* within the Crenarchaeota. These strictly anaerobic and obligate chemolithoautotrophs have an optimal growth temperature at 90 °C. As energy source, elemental sulfur is reduced using molecular hydrogen as electron donor (Paper *et al.*, 2007). CO₂, the sole carbon source, is fixed by the dicarboxylate/4-hydroxybutyrate pathway (Jahn *et al.*, 2007; Huber *et al.*, 2008). Due to its unique relationship to *N. equitans*, *I. hospitalis* represents the best known and most studied species. Still, general characteristics are believed to be applicable to all members of the genus *Ignicoccus* (Huber *et al.*, 2012).

I. hospitalis forms cocci with a cell diameter of 1.5-5 μm and exhibit a new type of cell surface appendages. Those fibers (Ø 14 nm) are anchored by spherical structures located beneath the inner membrane in the cell and show features as in type IV pilus-like structures (Müller *et al.*, 2009; Meyer *et al.*, 2014). Intriguingly, *I. hospitalis* cells exhibit unusual cell architecture for a prokaryote. Unlike most other archaea, they lack an S-layer and are instead surrounded by two membranes: the inner and the outer cellular membrane (IM, OCM respectively) (Näther and Rachel, 2004; Huber *et al.*, 2012). Both membranes form a large inter-membrane compartment (IMC), which is completely separated from the cytoplasm (Figure 9B) (Rachel *et al.*, 2002). The localization of different membrane proteins involved in energy conservation in the OCM leads to an energization of the outer cellular membrane, which is highly unusual. In contrast to other prokaryotes, the H₂:sulfur oxidoreductase (primary proton pump) and the A₁A₀ ATP synthase complex (secondary proton pump) are not localized in the inner membrane but in the OCM (Küper *et al.*, 2010). As ATP is synthesized within the IMC and ribosomes and DNA are localized in the cytoplasm, energy conservation is separated from protein biosynthesis

(Küper *et al.*, 2010). This results in a structural as well as in a functional compartmentalization. With the Acetyl-CoA synthetase, which is associated with the OCM, a first ATP-consuming process in the IMC was identified (Mayer *et al.*, 2012). Recently, another novel membrane-associated octa-heme cytochrome *c* was characterized, which is believed to be involved in detoxification or in respiratory energy conservation due to its nitrite reductase activity (Parey *et al.*, 2016).

Both membranes differ in their lipid composition: whereas the OCM consists mainly of archaeol, the IM is made up of archaeol and caldarchaeol (Jahn *et al.*, 2004). Moreover, a novel pore-forming complex Ihomp1 was identified in the OCM of *I. hospitalis*. It represents the most abundant protein in the OCM, for which no recognizable homologues have been found in other archaea (Burghardt *et al.*, 2007; Burghardt *et al.*, 2008). In earlier studies, numerous vesicles of different shape and size were observed within the IMC. Those vesicles were either budding from the IMC or undergoing fusion with the IMC or OCM (Rachel *et al.*, 2002; Näther and Rachel, 2004). Recent studies for *I. hospitalis* identified a complex and highly dynamic endomembrane system, which consists of cytoplasmic protrusions and might have secretory function. Moreover, filamentous structures, similar to a cytoskeleton, were observed in the IMC (Heimerl *et al.*, 2017).

The genome of *I. hospitalis* is the most minimal organized genome known to date that guarantees an independent way of living. With only a size of 1.3 Mbp it encodes for 1,444 genes, whereas less than 3 % of the proteome encodes for transport proteins (Podar *et al.*, 2008). Interestingly, comparative analysis of the proteome of *I. hospitalis* in single and co-culture with *N. equitans* showed that the relative abundance of membrane proteins increases up to 50 % in co-culture. This up-regulation affected especially protein complexes involved in energy conservation as well as proteins involved in membrane stabilization and transporters (Giannone *et al.*, 2015).

If the eukaryotic cell originated from an archaeal ancestor, as many believe, then an organism like *I. hospitalis*, with its large ATP-rich intermembrane compartment, is an ideal candidate for such an ancestor; providing easy ATP and other metabolites to an incorporated symbiont.

2.3 *N. equitans*: a putative ectoparasite?

N. equitans forms tiny cocci with cell diameters of only 0.35-0.5 μm and exhibits a typical archaeal cell architecture: cytoplasm, cytoplasmic membrane and S-Layer (Figure 9A) (Huber *et al.*, 2002; Huber *et al.*, 2003). The cytoplasmic membrane consists of archaeol and caldarchaeol like the IM of *I. hospitalis*. The interaction between both organisms is mediated by filamentous structures or a direct cell-cell contact and is limited to a relatively small contact area of only 40-170 nm in diameter (Figure

9B) (Junglas *et al.*, 2008). Recently, the direct contact or fusion of the cytoplasm from *N. equitans* with the endomembrane system of *I. hospitalis* was observed, involving the degeneration of the S-layer from *N. equitans* (Heimerl *et al.*, 2017). Moreover, Ihomp1 is believed to play a crucial role for the interaction of *I. hospitalis* and *N. equitans*, since only this species exhibits Ihomp1 within the genus *Ignicoccus* (Burghardt *et al.*, 2007; Huber *et al.*, 2012).

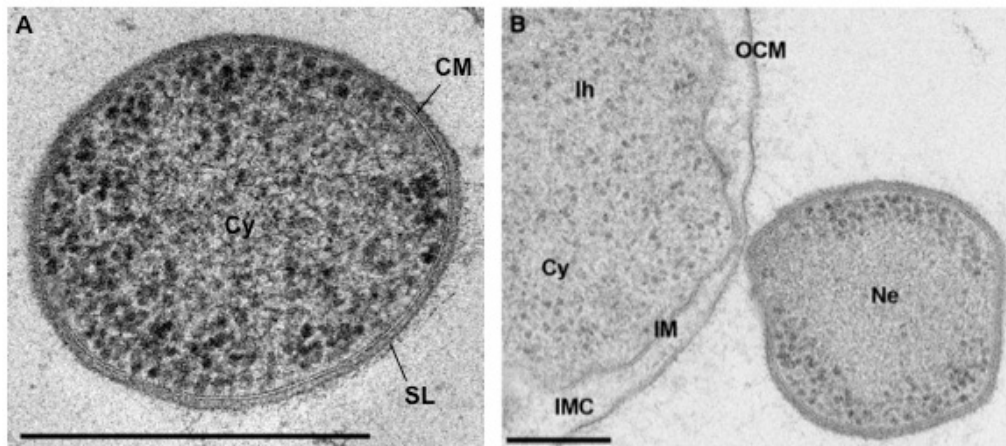


Figure 9: Transmission electron micrographs of *N. equitans*.

(A) Ultra-thin section of a single *N. equitans* cell, prepared by high-pressure freezing, freeze-substitution, and embedding in Epon, Cy cytoplasm, CM cytoplasmic membrane, and SL S-Layer, bar corresponds to 0.5 μm (adapted from Huber *et al.*, 2003); (B) *N. equitans* (Ne) attached to the surface of *I. hospitalis* (Ih), Cy cytoplasm, IM inner membrane, IMC inter membrane compartment, OCM outer cellular membrane, OCM and IM are in direct contact to *N. equitans* cell; ultra-thin section, platinum shadowed, bar corresponds to 1 μm (Huber *et al.*, 2012).

The genome of *N. equitans* with a size of 0.49 Mbp is one of the smallest amongst archaea and encodes for only 563 genes. Interestingly, it lacks genes for the synthesis of lipids, amino acids, nucleotides and cofactors as well as the genes for metabolic activity like glycolysis, pentose (P)-cycle, assimilation of CO_2 , TCA cycle or primary proton pumps (Waters *et al.*, 2003). This highly reduced genome emphasizes the strong dependency of *N. equitans* on *I. hospitalis*. In fact, the transport of amino acids and lipids from *I. hospitalis* to *N. equitans* was observed (Jahn *et al.*, 2004; Jahn *et al.*, 2008). On the contrary, the genome encodes genes for DNA replication, transcription, translation, DNA repair, and recombination. Moreover, several membrane proteins were identified and a rudimentary ATP synthase is also present (Waters *et al.*, 2003). Whether this ATP synthase is functional or whether energy is imported from *I. hospitalis*, is still debated. However, *in vivo* the enzyme may contribute to the generation of an electrochemical gradient in free *N. equitans* cells (Kreuter, 2014).

Extensive genomic analyses showed that only 85 % of the annotated proteins could actually be detected in *N. equitans* (for *I. hospitalis*: 80 %). Moreover, about 30 % (20 % in *I. hospitalis*) represent hypothetical proteins with unknown function (Giannone *et al.*, 2011; Giannone *et al.*, 2015). Although a number of putative transporters have been identified in the genome, this set of transporter types is unlikely to be sufficient for the import of metabolites, which *N. equitans* requires. Eight different types of transporters were identified belonging for example to the Ca²⁺:cation antiporter (CaCA) family, tellurite-resistance/dicarboxylate transporter (TDT) family, amino acid-polyamine-organocation (APC) family or CorA metal ion transporter (MIT) family and MscS superfamily (Waters *et al.*, 2003; Podar *et al.*, 2008). In contrast, according to the Transporter Protein Analysis Database (Elbourne *et al.*, 2017), 22 transporter proteins are annotated for *N. equitans* (Table I.3). However, it should be considered that each subunit of a larger protein complex is counted individually here.

Table I.3: Annotated transporter classes and families in the genome of *N. equitans*.

Transporter class	Family	Proteins
ATP-dependent	ABC	NEQ074, NEQ129, NEQ175, NEQ421
	F-ATPase	NEQ103, NEQ166, NEQ217, NEQ263, NEQ410
Ion channels	MIT	NEQ501
	MscS	NEQ198, NEQ531
Secondary transporters	AI-2E	NEQ162
	APC	NEQ273
	CaCA	NEQ164, NEQ486
	MOP	NEQ090
	RND	NEQ436, NEQ437
	TDT	NEQ014
Unclassified	FeoB	NEQ157
	HCC	NEQ189

ABC = ATP-binding cassette superfamily; F-ATPase = H⁺- or Na⁺-translocating F-type, V-type and A-type ATPase superfamily; MIT = CorA metal ion transporter family; MscS = mechanosensitive channel of small conductance family; AI-2E = autoinducer-2 exporter family; APC = amino acid-polyamine-organocation family; CaCA = Ca²⁺:cation antiporter family; MOP = multidrug/oligosaccharidyl-lipid/polysaccharide flippase superfamily; RND = resistance-nodulation-cell division superfamily; TDT = tellurite-resistance/dicarboxylate transporter family; FeoB = ferrous ion uptake family; HCC = HlyC/CorC family.

In total, three ion channels are annotated, two of them belonging to the MscS superfamily: Neq198 and Neq531 (Podar *et al.*, 2008).

3 Aim of this work

This work will focus on *N. equitans*. Its reduced genome with only 22 encoded transporter proteins is intriguing. The abundance of channels in *N. equitans* raises the question, whether one or all these channels are involved in the interaction, transport and communication between *I. hospitalis* and its symbiotic partner *N. equitans*. Since archaeal MS channels are expected to carry out similar cellular functions to their bacterial homologues, the MscS-like channels from *N. equitans* might play crucial roles in cell integrity and symbiosis exhibiting most likely unique yet unknown functions. The channel structures from *N. equitans* would describe the first structure of an archaeal homologue to *EcMscS* providing important insights to lipid-protein interactions and evolutionary aspects.

Previous experiments concerning the heterologous expression in *E. coli* and preliminary purification tests have already shown that one of the MscS-like channels, Neq531, can be expressed and purified (Wiegmann, 2014). Therefore, an optimized expression and purification protocol for both MscS-like channels, Neq198 and Neq531, should be established to analyze the channels with respect to their structure and function. The structure analysis should be addressed by single particle analysis in negative stain as well as cryo-electron microscopy (cryo-EM). Since with the beginning of this thesis, no pipeline for the structure analysis of membrane proteins by single particle was established in our group, these channels served as a “proof of principle” project. Moreover, the channels should be characterized electrophysiological by patch clamp technique.

II MATERIALS AND METHODS

1 Materials

1.1 Instruments

ÄKTA Chromatography System (pure, purifier) (GE Healthcare, Little Chalfont, UK)

Cell disruptor TS 0.75 (Constant Systems Ltd., Daventry, GB)

Digidata 1140A Low-Noise Data Acquisition System (Molecular Devices, San José, US)

EM Grid Plunger (Leica Microsystems, Wetzlar)

Micropipette puller PP-83, vertical (Narishige, Tokyo, J)

Multitron Pro shaker (Infors AG, Bottmingen, CH)

Nanodrop Spectrophotometer ND-1000 (Peqlap Biotechnologies GmbH, Erlangen)

High Vacuum Carbon Coater 208carbon (Cressington Scientific Instruments, Watford, UK)

OLYMPUS IMT-2 Inverted Microscope (Olympus Optical Co., Ltd., Nagano, J)

Micromanipulator MO-103, three-dimensional (Narishige, Tokyo, J)

Patch Clamp Amplifier AXOPATCH 1D (Molecular Devices, San José, US)

Patch Clamp Headstage holder CV-4 (Molecular Devices, San José, US)

Plasma Cleaner/Sterilizer PDC-3XG (Harrick Plasma, Ithaca, US)

TECAN Infinite M200 Pro (Platereader) (Tecan Austria GmbH, Görding, AT)

Transmission electron microscope CM12 (FEI, Oregon, US)

Transmission electron microscope JEOL F2100 (Jeol, Eching)

Transmission electron microscope Tecnai F30 Polara (FEI, Oregon, US)

Ultracentrifuge Optima Max-XP (Beckman Coulter, Palo Alto, US)

Ultracentrifuge Optima XPN-100 (Beckman Coulter, Palo Alto, US)

1.2 Chemicals

If not declared specifically, general chemicals used in this work were purchased from Anatrace (Maumee, US), AppliChem GmbH (Darmstadt), Avanti[®] Polar Lipids Inc. (Alabaster, US), Bio-Rad (Hercules, US), Gerbu (Wieblingen), Glycon Biochemicals (Luckenwalde), Merck (Darmstadt), New England Biolabs (Frankfurt/Main), QIAGEN (Hilden), Roche (Mannheim), Carl Roth GmbH (Karlsruhe), Serva Electrophoresis GmbH (Heidelberg), Sigma-Aldrich[®] (St. Louis, US) and Thermo Scientific Molecular Biology (Dreieich).

1.3 Detergents

Detergents were purchased from Anatrace or Glycon Biochemicals. Their characteristics are listed in the table below. For the extensively used detergents DDM and Fos-Choline-14 (Fos14) the micelle size is determined to 72 kDa and 47 kDa, respectively. The critical micelle concentration (cmc) in H₂O of each detergent is listed below (Table II.1).

Table II.1: Detergents and their characteristics

Detergent	Detergent class	Cmc (H ₂ O)	
CYMAL-5, Anagrade	Nonionic, maltoside	~2.4-5.0 mM	(0.12 %)
CYMAL-6, Anagrade	Nonionic, maltoside	~0.56 mM	(0.028 %)
DDM, >99 % highly purified	Nonionic, maltoside	~0.17 mM	(0.0087 %)
DM, Anagrade	Nonionic, maltoside	~1.8 mM	(0.087 %)
Fos-Choline-12, Anagrade	Zwitterionic, lipid-like	~1.5 mM	(0.047 %)
Fos-Choline-14, Anagrade	Zwitterionic, lipid-like	~0.12 mM	(0.0046 %)
LDAO, Anagrade	Zwitterionic, amine oxide	~1-2 mM	(0.023 %)
LMNG	Nonionic, neopentyl glycol	~0.01 mM	(0.001 %)
NG, Sol-Grade	Nonionic, glycoside	~6.5 mM	(0.20 %)
OG, Anagrade	Nonionic, glycoside	~18-20 mM	(0.53 %)
UDM, >99 % highly purified	Nonionic, maltoside	~0.59 mM	(0.029 %)

1.4 Enzymes and inhibitors

Table II.2: Enzymes

Enzymes	Manufacturer
Alkaline Phosphatase, calf intestinal (CIP)	New England Biolabs GmbH, Frankfurt (Main)
DNase I	Roche Diagnostics GmbH, Mannheim
Lysozyme, from chicken egg white	Sigma Aldrich Chemie GmbH, Taufkirchen
Phire Hot Start II Polymerase	New England Biolabs GmbH, Frankfurt (Main)
Phusion® High-Fidelity DNA Polymerase (2,000 U/ml)	New England Biolabs GmbH, Frankfurt (Main)
Restriction endonucleases	New England Biolabs GmbH, Frankfurt (Main)
T4 DNA Ligase (400,000 U/ml)	New England Biolabs GmbH, Frankfurt (Main)
TEV protease	Kindly provided by Katrin Rohde, MPI Frankfurt (Main)
Thrombin (Coagulation Factor IIa, Bovine)	BIOPUR AG, Reinach (CH)

Table II.3: Protease inhibitors

Inhibitors	Manufacturer
Pefabloc® SC	Roche Diagnostics GmbH, Mannheim
cComplete™ EDTA-free Protease Inhibitor Cocktail	Roche Diagnostics GmbH, Mannheim

1.5 Molecular weight markers

Table II.4: Molecular weight markers

Molecular weight markers	Manufacturer
GeneRuler™ 1 kb Plus DNA Ladder (75-20,000 bp)	Thermo Fisher Scientific Inc., Rockford (US)
High Molecular Weight Calibration Kit for Native Electrophoresis	GE Healthcare, Little Chalfont (UK)
PageRuler Prestained Protein Ladder (10-170 kDa)	Thermo Fisher Scientific Inc., Rockford (US)

1.6 Reagent kits

The following reagent kits were used according to manufacturer's instructions.

Table II.5: Reagent kits

Reagent kit	Manufacturer
BCA Protein Assay Kit Pierce™	Thermo Fisher Scientific Inc., Rockford (US)
Bradford reagent	Sigma-Aldrich Chemie GmbH, Taufkirchen
innuPREP Plasmid Mini Kit	Analytik Jena AG, Jena
PCR clean-up & NucleoSpin Gel clean-up Kit	MACHEREY-NAGEL, Düren
QIAprep Spin Miniprep Kit	QIAGEN, Hilden
QIAquick Gel Extraction Kit	QIAGEN, Hilden
QIAquick PCR Purification Kit	QIAGEN, Hilden

1.7 Column materials

Table II.6: Column materials

Column materials	Manufacturer
His-Select HF Nickel Affinity Gel	Sigma-Aldrich Chemie GmbH, Taufkirchen
HiTrap Chelating HP (5 ml)	GE Healthcare, Little Chalfont (UK)
Ni-NTA agarose	QIAGEN, Hilden
PD-10 Desalting Columns	GE Healthcare, Little Chalfont (UK)
Superose 6 10/300 GL	GE Healthcare, Little Chalfont (UK)
Superose 6 Increase 10/300 GL	GE Healthcare, Little Chalfont (UK)
Superdex 200 10/300 GL	GE Healthcare, Little Chalfont (UK)
TALON Metal Affinity Resin	Clontech Laboratories Inc., Mountain View (US)

1.8 Antibodies

Table II.7: Primary and secondary antibodies

Antibody	Species	Manufacturer
Anti-His (C-Term), monoclonal	Mouse	Life Technologies (Invitrogen), Carlsbad (US)
Anti-His (poly-His), monoclonal	Mouse	Sigma-Aldrich Chemie GmbH, Taufkirchen
Anti-Mouse IgG (whole molecule)-alkaline phosphatase	Rabbit	Sigma-Aldrich Chemie GmbH, Taufkirchen

The primary antibodies anti-His (C-term) and anti-His (poly-His) were used in ratios of 1:10,000 and 1:5,000, respectively. The secondary antibody anti-mouse IgG (whole molecule)-alkaline phosphatase was used in a ratio of 1:2,000 for colorimetric detection.

1.9 Media and antibiotics

Unless stated otherwise, all chemicals for media were dissolved in ddH₂O and the pH was adjusted with NaOH or HCl, respectively.

1.9.1 LB media

LB media (Lysogeny Broth), pH 7.0 (Bertani, 1951)

Bacto Tryptone	1 % (w/v)
Bacto Yeast Extract	0.5 % (w/v)
NaCl	1 % (w/v)

For LB agar plates the media was additionally supplemented with 1.5 % (w/v) agar.

1.9.2 2YT media

2YT media (2x Yeast Extract-Tryptone), pH 7.0

Bacto Tryptone	1.6 % (w/v)
Bacto Yeast Extract	1 % (w/v)
NaCl	0.5 % (w/v)

1.9.3 TB media

TB media (Terrific Broth), pH 7.0 (Tartoff and Hobbs, 1987)

Bacto Tryptone	1.2 % (w/v)
Bacto Yeast Extract	2.4 % (w/v)
10x TB phosphate	1x

10x TB phosphates (0.17 M KH₂PO₄, 0.72 M K₂HPO₄ · 3 H₂O) were prepared and autoclaved separately to prevent precipitation of hardly soluble phosphates. They were added to the media just before usage.

1.9.4 SOC media

SOC media was used in the standard transformation protocol of *E. coli*. In particular, the presence of the various cations was shown to increase the transformation efficiency whereas glucose is thought to act as stabilizer (Hanahan, 1983).

SOC media (Super Optimal Broth with Catabolite Repression), pH 7.0	
Bacto Tryptone	2 % (w/v)
Bacto Yeast Extract	0.5 % (w/v)
NaCl	0.05 % (w/v)
KCl	2.5 mM
MgCl ₂	10 mM
MgSO ₄	10 mM
Glucose	20 mM

KCl, MgCl₂, MgSO₄ and glucose were prepared separately as 1 M stock solutions and added after autoclaving.

1.9.5 CP minimal media

CP minimal media (citrate-phosphate defined medium), pH 7.0	
Na ₂ HPO ₄	8.58 g
K ₂ HPO ₄	0.87 g
Citrate acid	1.34 g
NH ₄ SO ₄	1.0 g
Thiamine	0.001 g
MgSO ₄ · 7H ₂ O	0.1 g
(NH ₄) ₂ SO ₄ · FeSO ₄ · 6H ₂ O	0.002 g
ddH ₂ O	ad 1000 ml

CP minimal media was used for the hypoosmotic down-shock assay. For growth under hyperosmotic conditions prior to shock, the medium was supplemented with 0.5 M NaCl. NaCl was added separately from a 5 M stock solution after autoclaving.

1.9.6 Antibiotics

Antibiotics used for selection are listed in the table below.

Table II.8: Antibiotics and their working concentrations

Antibiotic	Stock solution	Working concentration
Ampicillin	100 mg/ml	100 μ g/ml
Carbenicillin	50 mg/ml	50-100 μ g/ml
Chloramphenicol	34 mg/ml in Ethanol p.a.	34 μ g/ml
Kanamycin sulfate	50 mg/ml	50 μ g/ml

1.10 Bacterial *E. coli* strains

Bacterial strains used in this work were either purchased from manufacturers as chemical competent cells or prepared as chemical competent cells following the corresponding protocol (II.2.6).

Table II.9: Bacterial strains for general cloning/subcloning and their characteristics

Bacterial strain	Genotype	Reference
DH5 α TM -T1 ^R	F Φ 80 <i>lacZ</i> Δ M15 Δ (<i>lacZYA-argF</i>) U169 <i>recA1 endA1 hsdR17</i> (r_k^- , m_k^+) <i>phoA supE44 thi-1 gyrA96 relA1 tonA</i> (confers resistance to phage T1)	Thermo Fisher Scientific, Waltham (US) Killmann <i>et al.</i> , 1996
Top10	F <i>mrcA</i> Δ (<i>mrr-hsdRMS-mcrBC</i>) Φ 80 <i>lacZ</i> Δ M15 Δ <i>lacX74 recA1 araD139</i> Δ (<i>araleu</i>) 7697 <i>galU galK rpsL</i> (StrR) <i>endA1 nupG</i>	Thermo Fisher Scientific, Waltham (US)

The hereinafter-mentioned *E. coli* strains were tested for heterologous expression or were used for hypoosmotic down-shock assay. C41 (DE3) and C43 (DE3) Δ AcrB strains have at least one non-characterized mutation that prevents cell death upon expression of numerous recombinant and toxic proteins. This is the reason why they are particularly favored for the expression of membrane proteins (Miroux and Walker, 1996; Dumon-Seignovert *et al.*, 2004). MJF641 (Δ 7) represents a sevenfold *E. coli* knock-out strain lacking all mechanosensitive channels that are present in *E. coli*: MscL, MscS and 5 further paralogues (YnaI, YbdG, YbiO, MscK and YjeP) (Edwards *et al.*, 2012). MJF465 represents a triplicate knock-out strain which lacks the *mscL*, *mscS* and the *mscK* gene (Levina *et al.*, 1999).

Table II.10: Bacterial strains for expression and their characteristics

Bacterial strain	Genotype	Reference
BL21 (DE3)	F ⁻ <i>ompT hsdS_B(r_B⁻ m_B⁻) gal dcm</i>	Life Technologies (Invitrogen), Carlsbad (US)
BL21 (DE3) pLysS	F ⁻ <i>ompT hsdS_B(r_B⁻ m_B⁻) gal dcm rne131</i> (DE3) pLysS (Cam ^R)	Life Technologies (Invitrogen), Carlsbad (US)
BL21 Star TM (DE3)	F ⁻ <i>ompT hsdS_B(r_B⁻ m_B⁻) gal dcm rne131</i> (DE3)	Life Technologies (Invitrogen), Carlsbad (US)
C41 (DE3)	F ⁻ <i>ompT gal dcm hsdS_B(r_B⁻ m_B⁻)</i> (DE3)	Lucigen Corp., Middleton (US)
C43 (DE3) ΔAcrB	F ⁻ <i>ompT gal dcm hsdS_B(r_B⁻ m_B⁻)</i> (DE3) Δ <i>acrB</i>	Kindly provided by Prof. M. Pos (Goethe-University, Frankfurt/Main)
MJF641 (Δ7)	F ⁻ <i>rha thi gal lacZ ΔmscL::cm ΔyggB ΔkefA::kan ΔybdG ΔybiO ΔyjeP ΔynaI</i>	Kindly provided by Prof. B. Martinac (VCCRI, Sydney, AUS); Edwards <i>et al.</i> , 2012
MJF465	F ⁻ <i>rha thi gal lacZ ΔmscL::cm ΔyggB ΔkefA::kan</i>	Levina <i>et al.</i> , 1999
Rosetta TM 2 (DE3)	F ⁻ <i>ompT hsdS_B(r_B⁻ m_B⁻) gal dcm</i> (DE3) pRARE2 (Cam ^R)	Merck KgaA, Darmstadt

1.11 Plasmids and oligonucleotide primers

Table II.11: General plasmids and their properties

Plasmids	Resistance	Properties	Reference
pBAD/HisA, B, C	Amp ^R	<i>araBAD</i> promotor, N-terminal His6-tag, <i>araC</i> gene	Life Technologies (Invitrogen), Carlsbad (US)
pBAD24	Amp ^R	<i>araBAD</i> promotor	Guzman <i>et al.</i> , 1995
pET26b(+)	Kan ^R	T7promotor, lacI, N-terminal pelB signal sequence for potential periplasmic localization, optional C-terminal His6-tag	Merck KgaA, Darmstadt
pET28a(+)	Kan ^R	T7promotor, lacI, thrombin cleavage site, N-terminal His6-tag	Merck KgaA, Darmstadt

All genes used in this work for the heterologous expression in *E. coli* were codon optimized for this purpose. Oligonucleotide primers used for PCR and DNA sequencing were purchased from Metabion (Planegg/Steinkirchen). Eurofins Genomics (Ebersberg) performed sequencing of cloned products using the corresponding primers (Table II.13).

Table II.12: Plasmid constructs for protein expression

Plasmids	Properties	Reference
pBAD24_MscL	MscL gene subcloned, pBAD24 cut with NheI and SalI, no useful restriction sites created, C-terminal His6-tag	Kindly provided by Prof. B. Martinac (VCCRI, Sydney, AUS)
pBAD24_Neq198_w/o 6his	Neq198 gene subcloned, pBAD cut with NheI and SalI, no useful restriction sites created, without thrombin cleavage site and N-terminal His6-tag	This work
pBAD24_Neq198_w/ 6his	Neq198 gene subcloned, pBAD cut with NheI and SalI, pET28a(+)_Neq198 cut with XbaI and XhoI, compatible sticky ends, no useful restriction sites created, thrombin cleavage site, N-terminal His6-tag	This work
pET26b(+)_Neq531	Neq531 gene subcloned with NdeI and XhoI, C-terminal His6-tag	Wiegmann, 2014
pET28a(+)_Neq198	Neq198 gene subcloned with NheI and XhoI, N-terminal His6-tag	This work
pET28a(+)_Neq531_A	Neq531 gene subcloned with NcoI and HindIII, frame shift resulting in loss of stop codon, N-terminal His6-tag, construct originated from pET26b(+)_Neq531	This work
pET28a(+)_Neq531_B	Neq531 gene subcloned with NcoI and HindIII, corrected stop, N-terminal His6-tag	This work
pMSP1E3D1	pET28a(+), “extended” MSP1D1, contains repeats of helices 4, 5 and 6, N-terminal His7-tag followed by spacer sequence and TEV protease cleavage site	Denisov <i>et al.</i> , 2007 (Addgene plasmid 20066)

Table II.13: Oligonucleotides

Label	Sequence (5' → 3')	Description
pBAD forward	ATGCCATAGCATTTTTATCC	General used pBAD plasmid primers
pBAD reverse	GATTTAATCTGTATCAGG	
NEQ531_NcoI_forw	CCATGGGCAGCAGCCAT	pET28a(+)_Neq531_B insert primer
NEQ531_Stop_HindIII_rev	CAAGCTTTCATTATTGCAGACCG	
T7 forward	TAATACGACTCACTATAGG	General used pET plasmid primers
T7 reverse (T7 Term)	CTAGTTATTGCTCAGCGGT	

1.12 Archaeal strains

Table II.14: Archaeal strains

Archaeal strain	Origin	Reference
<i>Nanoarchaeum equitans</i> KIN4/M	Kolbeinsey Ridge	Huber <i>et al.</i> , 2002
<i>Ignicoccus hospitalis</i> KIN4/I	Kolbeinsey Ridge	Paper <i>et al.</i> , 2007

2 Molecular methods

2.1 Polymerase chain reaction (PCR)

The polymerase chain reaction (PCR) is a technique for *in vitro* amplification (Mullis and Faloona, 1987) of a specific DNA segment by using two synthetic DNA oligonucleotides (primers) complementary to the desired sequence (Saiki *et al.*, 1988). PCR is performed in a cyclic repetitive three-step reaction: (1) denaturation of the DNA, (2) annealing of the oligonucleotide primers to the single-stranded DNA template and (3) an elongation step in which the DNA polymerase synthesizes a new complementary DNA strand at the 3'-OH end. The PCR mixture and thermocycler settings are listed below.

Table II.15: PCR mixture

	Volume	Final concentration
5x Phusion HF buffer	10 μ l	1x
10 mM dNTPs	1 μ l	200 μ M each
Primer A (forward)	2 μ l	0.5 μ M
Primer B (reverse)	2 μ l	0.5 μ M
Template DNA	1 μ l	5-10 ng
Phusion High-Fidelity DNA Polymerase	0.5 μ l	0.02 U/ μ l
ddH ₂ O	ad 50 μ l	-

Table II.16: Thermocycler program for PCR

Step	Temperature (°C)	Time (s)	Cycle
Initial denaturation	98	30	1 x
Denaturation	98	5	} 30 x
Annealing	60	30	
Elongation	72	30/1 kb	
Final elongation	72	300	1 x

QIAquick PCR Purification Kit was used according to manufacturer's instruction to purify amplified DNA. The DNA concentration and quality was determined with a Nanodrop Spectrophotometer (II2.10).

2.2 Fusion PCR

To combine two PCR products, DNA in equimolar amounts was used in a Fusion PCR. 5 ng of each PCR product were added to the PCR mixture as described in Table II.15. Fusion PCR was performed in two consecutive steps; in the second step the primers were added. The products were analyzed by a preparative agarose gel electrophoresis (II2.3).

Table II.17: Thermocycler program for Fusion PCR

Step	Temperature (°C)	Time (s)	Cycle
Initial denaturation	98	30	1 x
Denaturation	98	5	} 3-5 x
Annealing	58	30	
Elongation	72	30/1 kb (largest fragment)	
Addition of primers	72	120	1 x
Denaturation	98	5	} 30 x
Annealing	60	30	
Elongation	72	30/1 kb (total fragment)	
Final elongation	72	300	

2.3 Agarose gel electrophoresis

Amplified DNA or cleaved vectors and inserts were analyzed by agarose gel electrophoresis. For visualization of the DNA fragments ethidium bromide was added to the agarose gel. Ethidium bromide is a substituted phenanthridine derivate, an isomer of the fluorescent dye acridine, that intercalates with the nucleotides of the DNA and can be illuminated at the excitation wavelength of 312 nm.

For analytical agarose gel electrophoresis, 1 % (w/v) agarose was dissolved in 1x TAE (Tris-acetate-EDTA) buffer (40 mM Tris/HCl, 40 mM acetic acid, 4 mM EDTA, pH 8.0) and ethidium bromide added. DNA samples were mixed with 6x DNA loading dye and loaded onto an agarose gel together

with a molecular weight standard. The separation of DNA samples was carried out for 20 min at 200 V. The preparative agarose gel electrophoresis was performed in 0.8 % (w/v) agarose. Under UV inspection the corresponding DNA bands were cut out and purified with QIAquick Gel Extraction Kit according to manufacturer's instruction. The quality and concentration of DNA was determined with a Nanodrop Spectrophotometer (II2.10).

2.4 Digestion with restriction enzymes

Plasmid and insert DNA were cleaved with restriction endonucleases to get linearized and prepared for ligation. The appropriate reaction conditions were determined with the "Double Digest Finder" (New England Biolabs). The reaction was carried out for at least 2 h at 37 °C. To prevent re-ligation of linearized plasmid DNA, CIP (1 μ l CIP/20 μ l reaction mixture) was added to the reaction. Alkaline phosphatase nonspecifically catalyzes the dephosphorylation of 5' and 3' ends of DNA. The reaction products were purified in a preparative agarose gel electrophoresis (II2.3).

Table II.18: Setup for digestion with restriction enzymes

	Volume
Cut Smart Buffer 10x	5 μ l
Restriction enzyme 1	2 μ l
Restriction enzyme 2	2 μ l
DNA (2-4 μ g)	x μ l
ddH ₂ O	ad 50 μ l

2.5 Ligation

Ligation of digested plasmids and DNA inserts was carried out by addition of T4 DNA Ligase. The T4 DNA Ligase was added in a molar plasmid-insert ratio of 1:1 to 1:3 to a total volume of 20 μ l. The final concentration of plasmid was adjusted to 50-100 ng. Ligation was carried out o/N for 16-18 h at 16 °C. Subsequently, the T4 DNA Ligase was heat inactivated for 10 min at 65 °C. The ligation product was transformed in competent *E. coli* TOP10 or DH5 α cells (II2.7).

Table II.19: Mixture for ligation of digested plasmids and DNA inserts

	Volume
Plasmid DNA	x μ l
Insert DNA	x μ l
10x T4 DNA Ligase Buffer	2 μ l
T4 DNA Ligase	1.5 μ l
ddH ₂ O	ad 20 μ l

2.6 Preparation of chemical competent *E. coli* cells

Chemical competent *E. coli* cells were produced with the CaCl₂ method that increases the permeability of membranes and their ability to take up extracellular DNA (competence) due to an excess of Ca²⁺ ions by a so far unknown mechanism.

For preparation of the transformation buffer, PIPES was dissolved in ddH₂O and the pH was adjusted to 6.7 with KOH. Subsequently, salts were added in the order stated below (Table II.20) and dissolved completely in between. 20 ml LB media supplemented with 10 mM MgCl₂ was inoculated with a single colony of an o/N agar plate and incubated o/N at 37 °C, 80-100 rpm. Subsequently, 250 ml SOB media (corresponds to SOC media without glucose) supplemented with 10 mM MgCl₂ were inoculated with 1 ml of this pre-culture and incubated at 20 °C and 150 rpm up to an OD₆₀₀ of 0.5-0.6. The cells were incubated on ice-cooled water for 10 min and centrifuged for 10 min at 2,500 *xg* and 4 °C. The cell pellet was carefully resuspended under shaking in ice-cold transformation buffer, centrifuged again and finally resuspended in 20 ml ice-cold transformation buffer. The cells were supplemented with 1.5 ml DMSO and incubated on ice for additional 10 min. The chemical competent cells were aliquoted to 100 μ l, frozen in liquid N₂ and stored at -80 °C.

Table II.20: Transformation buffer for preparation of chemical competent *E. coli* cells

Transformation buffer (Inoue *et al.*, 1990), pH 6.7

KCl	250 mM
CaCl ₂ · 2 H ₂ O	15 mM
MnCl ₂ · 4 H ₂ O	55 mM
PIPES	10 mM

2.7 Transformation of *E. coli*

For transformation, 100 μl of competent *E. coli* cells were thawed on ice before 5 μl of ligation reaction or 1 pg-100 ng of plasmid DNA was added. Cells were incubated on ice for additional 30 min followed by heat shock for 45 s at 42 °C. After 5 min incubation on ice, the cells were supplemented with 800 μl pre-warmed SOC media and incubated for 1 h at 37 °C, shaking. The cells were pelleted by centrifugation, resuspended in 100 μl media and plated on LB-agar plates containing the corresponding antibiotics. The agar plates were incubated o/N at 37 °C.

2.8 Colony PCR

To evaluate cloning experiments transformed *E. coli* cells were used for colony PCR. For this purpose, cell material was resuspended in a 20- μl -colony PCR mixture.

Table II.21: Colony PCR mixture

	Volume	Final concentration
5x Phusion HF buffer	4 μl	1x
10 mM dNTPs	0.4 μl	200 μM each
Primer A (forward)	1 μl	0.5 μM
Primer B (reverse)	1 μl	0.5 μM
Phire Hot Start II DNA Polymerase	0.4 μl	-
ddH ₂ O	ad 20 μl	-

Table II.22: Thermocycler program for colony PCR

Step	Temperature (°C)	Time (s)	Cycle
Initial denaturation	98	120	1 x
Denaturation	98	5	} 30 x
Annealing	60	10	
Elongation	72	30	
Final elongation	72	120	1 x

Subsequently, the plasmid DNA of clones with positive results was isolated (II.2.9) and sequenced (II.2.11).

2.9 Isolation of plasmid DNA

Plasmid DNA was isolated from a fresh o/N culture of a single colony of transformed *E. coli* cells with the innuPREP Plasmid Mini Kit (Analytik Jena AG) according to manufacturer's instructions. The plasmid DNA was eluted with H₂O (nuclease-free).

2.10 Determination of DNA concentration

Plasmid DNA concentration and quality was determined with a ND 1000 Spectrophotometer (software ND-1000 V 3.8.0, Peqlab Biotechnologies GmbH). Here, only 1-2 μ l of plasmid DNA was needed.

3 Biochemical methods

3.1 Determination of protein concentration

3.1.1 BCA assay

Due to interference of most detergents with protein concentration determination assays, the BCA assay with its detergent-compatible formulation was used as standard determination method. For quantification of total protein this colorimetric method is based on the reduction of Cu⁺² to Cu⁺¹ when binding to peptide bonds in alkaline medium (biuret reaction). Bicinchoninic acid (BCA) as a component of the reagent chelates the reduced cuprous ions resulting in a purple-colored reaction product that can be measured at 562 nm. The complex formation is nearly linear with increasing protein concentrations (20-2,000 μ g/ml) (Smith *et al.*, 1985).

For this, 10 μ l of protein sample or standard were mixed in duplicate with 200 μ l of test reagent in a 96-well plate. The test reagent was composed of 1 volume reagent A and 1/50 volume reagent B. As protein standard BSA (bovine serum albumin) in concentrations of 0-2.0 mg/ml was used. After incubation at 37 °C for 30 min the complex formation was measured photometrically with a TECAN plate reader and evaluated with Magellan software (V 7.1).

3.1.2 Bradford assay

Bradford assay was used for quick determination of protein concentrations during purification. This assay is based on an absorbance shift of Coomassie Brilliant Blue dye in acidic solution from 465 nm to 595 nm by binding primarily to basic and aromatic amino acid residues (Bradford, 1976).

For this, 25 μl H_2O and 5 μl protein sample or 28 μl H_2O and 2 μl of protein sample were mixed with 150 μl Bradford reagent and visually controlled for the blue-colored reaction to identify protein-containing fractions.

3.1.3 Photometrical determination

For quick concentration determination of the purified protein an ND 1000 Spectrophotometer was used. The provided software (ND-1000 V 3.8.0) uses the extinction coefficient in conjunction with Lambert-Beer's law to calculate the sample concentration without a standard curve. The extinction coefficients of Neq198 and Neq531 were calculated and determined as 40,340 $\text{M}^{-1}\text{cm}^{-1}$ and 50,880 $\text{M}^{-1}\text{cm}^{-1}$, respectively (Gill and von Hippel, 1989).

3.2 SDS-Polyacrylamide gel electrophoresis (SDS-Page)

For protein sample analysis SDS-Page under denaturing conditions with a Laemmli buffer system was used (Laemmli, 1970). 12 % polyacrylamide gels with a size of 10 x 8 cm and 1 mm thick were used in a Mini-Protean Tetra System (Bio-Rad). Samples were mixed with 6x loading sample buffer. As molecular weight standard 5 μl of Page Ruler Prestained (10-170 kDa) (Thermo Fisher Scientific Inc.) was loaded next to the protein samples onto the gel.

Table II.23: Separation and stacking gel buffer for SDS-Page

	Separation gel buffer, pH 8.8	Stacking gel buffer, pH 6.8
Tris/HCl	1.5 M	0.5 M
SDS	0.4 % (w/v)	0.4 % (w/v)

Table II.24: Laemmli running buffer and 6x loading buffer

	Laemmli running buffer, pH 8.3	Laemmli loading buffer (6x), pH 6.8
Tris/HCl	250 mM	350 mM
Glycine	1.92 M	-
Glycerol	-	30 % (v/v)
SDS	1 % (w/v)	10 % (w/v)
β -Mercaptoethanol	-	10 % (v/v)
Bromophenol blue	-	0.02 % (w/v)

Table II.25: SDS-Page gel composition

	Separation gel (12 %)	Stacking gel (5.7 %)
Separation gel buffer	5 ml	-
Stacking gel buffer	-	1.5 ml
Acrylamide 30 %	8 ml	1.5 ml
ddH ₂ O	7 ml	4.8 ml
APS 10 % (w/v)	200 μ l	100 μ l
TEMED	20 μ l	10 μ l

The electrophoresis was started with 10 mA/gel to let the samples enter the stacking gel. Subsequently, the current was increased up to 30 mA/gel. Proteins were detected by staining with Coomassie for 20 min. Destaining was performed for several hours. Buffer and gel compositions are listed in the tables II.23-II.26.

Table II.26: Composition of staining and destaining solution for SDS-Page

	Staining solution	Destaining solution
Ethanol	30 % (v/v)	25 % (v/v)
Acetic acid	10 % (v/v)	5 % (v/v)
Coomassie Brilliant Blue R250	0.1 % (w/v)	-

3.3 Blue Native Electrophoresis (BNE)

Native Page allows the separation of protein complexes under native conditions, by which their endogenous subunit composition is maintained (Wittig and Schägger, 2009). In BN-Page, Coomassie Blue G250 binds on the surface of proteins and therefore provides negative charge. By this, even basic proteins migrate to the anode at neutral pH. It is used to determine the native mass and oligomeric state of membrane proteins (Schägger *et al.*, 1994).

The BNE was performed according to Wittig *et al.*, 2006 with minor modifications. The gels with a size of 20 x 20 cm and 1.5 mm thick were prepared with gradient mixing device (home-made, mechanics shop, Universität Regensburg) under constant stirring of the solutions resulting in a gradient from 5 % to 13 %. The acrylamide solution (AB-Mix: 48.5 % (w/v) acrylamide, 1.5 % (w/v) bis-acrylamide) was prepared separately. Protein samples were mixed with 10x Native loading buffer (50 % (v/v) glycerol, 0.1 % (w/v) Ponceau S). Maximal 30 μ g of protein was loaded per gel pocket.

As molecular weight marker 10 μ l of HMW Native Marker Kit (GE Healthcare) were used. The electrophoresis started with a voltage of 50 V for 30 min to let the samples enter the gel. That was followed for 18 h with 300 V, 50 W and 5 mA/gel. After electrophoresis, the proteins were detected by staining for 30 min with Coomassie staining solution (Table II.26). Buffer and gel compositions are listed in the tables II.27-II.29 below.

Table II.27: Blue Native gel buffer

Blue Native gel buffer, pH 7.0	
Imidazole	75 mM
ϵ -Aminocaproic acid	1.5 M
DDM	0.05 % (w/v)

Table II.28: Blue Native gel composition

	Separation gel (13 %)	Separation gel (5 %)	Stacking gel (4 %)
AB-Mix	5.5 ml	2.1 ml	1.2 ml
Native gel buffer (3x)	7 ml	7 ml	4 ml
Glycerol 50 % (v/v)	8.4 ml	-	-
ddH ₂ O	-	11.8 ml	6.7 ml
APS 10 % (w/v)	100 μ l	100 μ l	100 μ l
TEMED	10 μ l	10 μ l	10 μ l

Table II.29: Composition of Blue Native cathode and anode buffer

	Cathode buffer, pH 7.0	Anode buffer, pH 7.0
Imidazole	7.5 mM	25 mM
Tricine	50 mM	-
Coomassie Blue G250	0.02 % (w/v)	-

3.4 Western blot

For western blot analysis, proteins separated on a polyacrylamide gel were transferred in a continuous buffer system to a polyvinylidene difluoride (PVDF) membrane by electro blotting. The transfer was carried out in a wet-blot procedure using a Mini Trans Blot apparatus (Bio-Rad).

Whatman paper and sponges were soaked in transfer buffer and a PVDF membrane (Immobilon-P Transfer Membrane, 0.45 μm pore size, Millipore) was activated with methanol. The SDS-gel was equilibrated for 20 min in Towbin transfer buffer (25 mM Tris, 192 mM glycine, 20 % (v/v) methanol p.a.) (Towbin *et al.*, 1979). All components were stacked according to the prescribed order:

CATHODE
Sponge
2 x Whatman filter paper
Gel
PVDF membrane
2 x Whatman filter paper
Sponge
ANODE

The transfer was carried out at 30 V (constant), 95 mA (max) and 4 °C o/N. This was followed by immunodetection. To block unspecific binding sites the membrane was incubated at RT in 2 % BSA (w/v) in TBS-T buffer (10 mM Tris/HCl, 150 mM NaCl, 0.05 % (v/v) Tween-20, pH 7.5) for 1 h under gentle shaking. Subsequently, the membrane was incubated for 2 h with the primary antibody (in 0.3 % (w/v) BSA in TBS-T) followed by washing three times for 10 min in TBS-T and incubation for 2 h at RT with the secondary antibody (in 2 % (w/v) BSA in TBS-T). The corresponding antibody concentrations are listed in Table II.7. The membrane was washed twice with TBS-T for 10 min, equilibrated for 10 min in AP buffer (100 mM Tris, 100 mM NaCl, 5 mM MgCl₂, 0.05 % (v/v) Tween-20, pH 9.5) and incubated with 0.5 mg/ml NBT and 0.25 mg/ml BCIP (in 10 ml AP buffer) for colorimetric signal detection (Blake *et al.*, 1984). The addition of ddH₂O stopped the reaction.

3.5 Heterologous protein expression in *E. coli*

3.5.1 Expression

The protein expression was carried out like in Löw *et al.*, 2013 with some modifications. 2 L TB media in 5 L conical flasks were supplemented with the respective antibiotic. High phosphate concentrations in the media induce resistance to kanamycin; hence, a twofold kanamycin quantity (100 $\mu\text{g}/\text{ml}$) was added. The media was inoculated with an overnight LB culture to an OD₆₀₀ of 0.05

and incubated at 37 °C and 110 rpm. Once the culture had reached an OD₆₀₀ of 0.7-1.0, the temperature was reduced to 20 °C for 1 h. The protein expression was induced with 200-400 μM IPTG followed by incubation for 16 h at 20 °C and 110 rpm. The final OD₆₀₀ of each flask was measured and the cells were harvested by centrifugation at 4,000 rpm (Beckman Avanti J-26-XP, rotor JLA 8.1) and 4 °C for 20 min. The resulting cell pellet was resuspended in ice-cold membrane buffer (50 mM NaP_i pH 7.5 + 0.01 % (w/v) PefaBloc® SC + 1 tablet cOmplete™ EDTA-free Protease Inhibitor Cocktail) and homogenized. The required buffer volume was based on the final OD₆₀₀ of the cell culture: per 1 L culture with an OD₆₀₀ of 1.0, the cell pellet was resuspended in 10 ml membrane buffer.

3.5.2 Cell disruption and membrane preparation

Homogenized cells were disrupted using a high-pressure cell disruptor from Constant Systems Ltd. The system was washed with ice-cold ddH₂O and equilibrated with ice-cold 50 mM NaP_i buffer (pH 7.5). To the cell suspension 0.05 % (w/v) DNase I and 0.01 % (w/v) PefaBloc® SC were added, which was followed by three passages through the cell disrupter at 1.8 kbar. The resulting lysate was cleared from unbroken cells and cell debris by low speed centrifugation at 13,000 rpm for 30 min (Beckman Avanti J-26-XP, rotor JLA 16.250). To pellet the membranes, the supernatant was then further processed by high-speed centrifugation at 45,000 rpm for 1 h (Optima XPro-100, rotor Ti45). Depending on the wet weight of the resulting pellet, the membranes were resuspended in 2.5 ml NaP_i buffer per mg of membranes and homogenized. The total protein concentration was determined by BCA assay. The membrane suspension was aliquoted, frozen in liquid N₂ and stored at -80 °C until further usage for protein purification.

3.6 Protein purification

3.6.1 Solubilization

3.6.1.1 Detergent screening

A broad variety of detergents were tested to determine which has the highest solubilization efficiency for the aforementioned MscS-like channels of *N. equitans*. For this purpose, 1 ml of homogenized membranes was diluted 1:10 in membrane buffer. 200 μl of a 10 % (w/v) detergent stock solution was added to obtain a final concentration of 1.67 % (w/v) detergent and solubilized rotating for 1 h at RT. Subsequently, 1 ml fractions were centrifuged for 1 h at 62,400 rpm and 4 °C (Optima Max-XP UC, rotor MLA-130). The resulting pellets were resuspended in an equivalent volume of the membrane

buffer and homogenized. Supernatants/solubilizates and homogenized pellets were compared upon analysis with SDS-Page (II3.2) and western blot (II3.4).

3.6.1.2 Solubilization for purification

The protein was either solubilized in 1.5 % (w/v) Fos-Choline 14 for 1 h (structure determination) or in 2 % (w/v) DDM for 2 h (functional analyses). Subsequently, the solubilizate was centrifuged for 40 min at 70,000 rpm and 4 °C (Optima Max XP UC, rotor TLA110). The resulting supernatant was further used for affinity chromatography (II3.6.2).

3.6.2 Immobilized metal affinity chromatography (IMAC)

3.6.2.1 Flow through-based purification

For the flow through-based purification a 5 ml HiTrap Chelating HP column (GE Healthcare) was used. The matrix consists of highly cross-linked agarose beads to which iminodiacetic acid has been coupled and that can be charged with metal ions of choice. Here, nickel ions were used as standard. For this purpose, the column was washed with 3-5 CV ddH₂O to remove the storing buffer (20 % (v/v) ethanol). The matrix was charged with 2.5 ml of 100 mM NiSO₄ solution and equilibrated with 5 CV purification buffer. After usage, the column was regenerated by stripping of the nickel ions with 3-5 CV 50 mM EDTA, pH 7.5. Thereupon, it was thoroughly washed with 5 CV ddH₂O, charged with Ni⁺ and stored in 20 % (v/v) ethanol.

Table II.30: IMAC purification buffer

Protein sample	Purification buffer
Neq198	50 mM NaP _i pH 7.5, 300 mM NaCl, 0.02 % (w/v) Fos14
Neq531	50 mM NaP _i pH 7.5, 300 mM NaCl, 10 % (v/v) glycerol, 0.02 % (w/v) Fos14

The purification was performed on a ÄKTA chromatography system (ÄKTA purifier). The system, equipped with an UV detector (280 nm), conductivity device, and a fraction collector, was operated using the UNICORN software (GE Healthcare). After washing and equilibrating the system with purification buffer (Table II.30), the column was connected. The supernatant was loaded with a flow rate of 1 ml/min and 1 % (v/v) buffer B (purification buffer supplemented with 1 M imidazole = 10 mM imidazole) to reduce unspecific binding. This was followed by two washing steps with 3 CV 2 % (v/v) buffer B (20 mM imidazole) and 4 CV 15 % (v/v) buffer B (150 mM imidazole), respectively. The protein was eluted with 60 % (v/v) buffer B (600 mM imidazole) at a flow rate of

0.5 ml/min and fractionated to 500 μ l. The optimal washing and elution conditions were determined in a step-gradient ranging from 20-700 mM in a former experiment. The protein containing fractions were analyzed in SDS-PAGE (II3.2) and western blot (II3.4).

3.6.2.2 Gravity flow based method in batch

For patch clamp recordings, the protein was purified in a batch- and gravity flow-based method with Talon. Talon is an IMAC resin charged with cobalt, which binds his-tagged proteins with higher specificity compared to nickel-charged resins. DDM was used for solubilization of the membranes as detergent. For purification, ~1 ml Talon slurry (Clontech) was used to obtain a column volume of about 800 μ l. The slurry was first washed with ddH₂O and then equilibrated with the appropriate buffer (50mM NaP_i, 300 mM NaCl, 10 % (v/v) glycerol, 0.1 % (w/v) DDM). The solubilizate was mixed with the talon resin in presence of 10 mM imidazole to reduce unspecific binding. The binding occurred rotating for 3 h at 4 °C. The mixture was then transferred to a column. After the resin had settled down, it was successively washed with 10 CV buffer with increasing imidazole concentrations (40 mM, 60 mM, 80 mM). The protein was either eluted with 10 CV buffer containing 600 mM imidazole or cleaved off proteolytically with thrombin as described in II3.6.2.3. If eluted with imidazole, the protein was desalted upon concentrating in centrifugal spin filters with a molecular weight cut-off (MWCO) of 100 kDa. The protein was analyzed in SDS-Page (II3.2).

3.6.2.3 Proteolytic cleavage of histidine tag

Alternatively to imidazole elution, the protein was cleaved off the Talon resin by addition of thrombin. For this purpose, the resin was thoroughly washed with purification buffer to remove present imidazole of earlier washing steps. The Talon slurry (1:1 slurry to buffer) was then transferred to a 2 ml Eppendorf-Cup. Thrombin was added and incubated rotating o/N at 4 °C and additional 4 h at RT. Subsequently, the resin was removed by centrifugal spin filters/centrifugation at 700 \times g and the protein concentration was measured (II3.1.3).

3.6.3 Desalting and concentrating of protein samples

After IMAC, the protein containing fractions were desalted using PD10 columns to remove the high concentrations of imidazole. Before size exclusion chromatography (II3.6.4), the protein samples were concentrated up to 300-600 μ l using centrifugal filter units with 100 kDa MWCO.

3.6.4 Size exclusion chromatography (SEC)

Size exclusion chromatography was carried out on a ÄKTA pure or ÄKTA purifier system that was equipped with a UV detector (280 nm), conductivity device and a fraction collector and operated with the UNICORN software (GE Healthcare). The columns were washed with ddH₂O and equilibrated with 1.5 CV of buffer. 300-600 μ l of concentrated protein samples were loaded with a flow rate of 0.5 ml/min and fractionated in 500 μ l. Protein samples were optionally centrifuged for 30 min at 63,000 rpm (Optima Max XP UC, rotor MLA-130) and filtered before loading onto the column.

Table II.31: Buffers and columns used for size exclusion chromatography

Protein sample	Column	Buffer
in detergent	Superose 6 Increase 10/300 GL	50 mM NaP _i pH 7.5, 300 mM NaCl, w/ or w/o 10 % (v/v) glycerol, 0.02-0.05 % (w/v) detergent
in amphipol	Superose 6 Increase 10/300 GL	50 mM Tris pH 7.5, 100 mM NaCl
in nanodiscs	Superdex 200 10/300 GL	20 mM Tris pH 7.5, 100 mM NaCl

For quality control in negative stain the protein samples were diluted in buffer to 10-20 mAU (Neq198) and 20 mAU (Neq531) to obtain a good distribution of particles on the grid.

3.7 Reconstitution into membrane-mimicking environments

3.7.1 Reconstitution into nanodiscs

Nanodiscs provide a discoidal phospholipid bilayer that is encircled by an amphipathic helical protein belt, termed as membrane scaffold protein (MSP). The size of the nanodiscs is defined and controlled by the length of the MSP. For the reconstitution into nanodiscs, the membrane protein of interest is transiently solubilized with detergent in the presence of phospholipids and the MSP. Upon removal of the detergent by the absorption to hydrophobic beads, the target protein together with the phospholipids assembles into nanodiscs. The membrane protein is stabilized in a native-like environment that is rendered soluble by the surrounding MSP belt (Bayburt *et al.*, 2002; Bayburt and Sligar, 2003; Denisov *et al.*, 2004; Ritchie *et al.*, 2009; Bayburt and Sligar, 2010).

3.7.1.1 Expression and purification of the membrane scaffold protein MSP1E3D1

The plasmid pMSP1E3D1 was transformed in *E. coli* BL21 (DE3) cells for expression as described in Glück *et al.*, 2011. 1 L LB media supplemented with kanamycin in 5 L conical shaking flasks was inoculated with an o/N culture to a final OD of 0.1 and incubated at 37 °C and 110 rpm to an OD of

0.7. The expression was induced by addition of 1 mM IPTG for 3 hours. Subsequently, the cells were harvested by centrifugation at 4 °C and 4,000 rpm for 20 min (Beckman Avanti J-26 XP, rotor 8.1) and washed once with 1x PBS. After determining the wet weight of the resulting pellet, the pellets were stored at -20 °C until further usage. MSP1E3D1 was purified as described in Bayburt and Sligar, 2003 with modifications. For this purpose, 20 g wet weight cell pellet were resuspended in 100 ml lysis buffer (20 mM NaP_i pH 7.4, 0.05 % (w/v) DNase I, 1 tablet cOmplete™ EDTA-free Protease Inhibitor Cocktail). This was followed by three passages through the cell disrupter at 1.8 kbar and a centrifugation at 45,000 rpm (Beckman Optima Max-XP, rotor Ti45) and 4 °C for 1 h. For IMAC, the supernatant was applied to a 10 ml Ni-NTA (QIAGEN) column that was equilibrated with lysis buffer. The column was washed with 4 CV of the following buffers:

1. 40 mM Tris/HCl pH 8.0, 300 mM NaCl, 1 % (v/v) Triton X-100
2. 40 mM Tris/HCl pH 8.0, 300 mM NaCl, 50 mM Na-Cholate
3. 40 mM Tris/HCl pH 8.0, 300 mM NaCl
4. 40 mM Tris/HCl pH 8.0, 300 mM NaCl, 10 mM imidazole

The protein was eluted with 1 CV elution buffer I (40 mM Tris/HCl pH 8.0, 300 mM NaCl, 300 mM imidazole) followed by 3 CV elution buffer II (40 mM Tris/HCl pH 8.0, 300 mM NaCl, 750 mM imidazole), each fractionated in 1 ml. The protein containing fractions were combined and dialyzed for 1 h at RT against 1 L dialysis buffer (50 mM Tris/HCl pH 8.0, 0.5 mM EDTA, 1 mM DTT) with a dialysis membrane with 3,500 MWCO. TEV protease was added in a ratio of 1:20 (TEV:MSP) directly to the MSP into the dialysis bag to remove the histidine tag. The dialysis/cleavage was continued for 48 h at RT in 4 L fresh dialysis buffer. In a final step the MSP was dialyzed against 20 mM Tris/HCl pH 8.0, 150 mM NaCl for 2 h at RT. To remove the histidine tag and the TEV protease from the cleaved MSP, a second IMAC was performed. 15 ml Ni-NTA (QIAGEN) were equilibrated with IMAC buffer II (20 mM Tris/HCl pH 8.0, 150 mM NaCl, 50 mM Na-Cholate) and incubated for 1 h with the protein solution. Transferred to a column, the flow through was collected and the column washed with 4 CV IMAC buffer II. The MSP containing flow through and washing step were combined and dialyzed against 4 L nanodisc assembly buffer (20 mM Tris/HCl pH 8.0, 100 mM NaCl, 0.5 mM EDTA) for 48 h at 4 °C. The protein concentration was determined. The MSP was aliquoted in 1 mg fractions, frozen in liquid nitrogen and stored at -80 °C.

3.7.1.2 Reconstitution procedure

For nanodisc assembly purified Neq198, POPC and MSP, resulting in nanodiscs with 12-13 nm in diameter, were used. Calculations help to estimate the optimal ratios. The number of lipid molecules per nanodisc can be calculated as follows:

$$N_{lip} = 2 \times \frac{S_{ND} - S_{prot}}{S_{lip}}$$

N_{lip} is the number of lipids per nanodisc, S_{ND} refers to the surface area of the lipid nanodisc, S_{prot} applies to the area of the protein's transmembrane section, and S_{lip} is the area occupied by one phospholipid molecule. The factor two refers to the membrane as lipid bilayer.

The surface area of the lipid nanodisc S_{ND} can be estimated accordingly to the number of amino acids (M) of the used MSP (Denisov *et al.*, 2004):

$$S_{ND} = (0.423 \times M - 9.75)^2 (\text{\AA}^2)$$

For the estimation of the membrane cross-section of a membrane protein, an area of $\sim 140 \text{\AA}^2$ can be assumed for each transmembrane helix (Ritchie *et al.*, 2009). For N_{TM} transmembrane helices applies the following:

$$S_{prot} = 140 \times N_{TM} (\text{\AA}^2)$$

The optimal protein:lipid:MSP ratio was determined in small scale based upon the calculated number of lipids per nanodisc. Reconstitution in large scale was performed to obtain cryo-EM samples. In brief, lipids stored in chloroform were dried under a continuous nitrogen stream and dissolved in lipid buffer (20 mM Tris/HCl pH 7.4, 100 mM Na-Cholate, 10 mM Fos14) to a final concentration of 50 mM. For complete solubilization of the lipid-detergent-mixture a short incubation at 37 °C followed. For assembly, lipids and protein were combined in the desired molar ratio of 0.1:45 (protein:lipid) and incubated on ice for 10 min. 1 mg of MSP (II3.7.1.1) was thawed on ice and added to the lipid-protein mixture in a molar ratio of 0.1:1:45 (protein:MSP:lipid). This was followed by a cycling incubation of three times for 20 min on ice and 20 min at 4 °C (according to the phase transition temperature of the lipid POPC). The final Na-Cholate concentration was adjusted to 15-40 mM if necessary. The self-assembly was induced by the addition of Bio-BeadsTM SM-2 resin (Bio-Rad) and therefore removing of the detergent. For this purpose, 0.65 mg wet weight Bio-Beads (in Tris/HCl, pH 7.4) were added per ml assembly mixture and incubated o/N at RT under gentle rotation. The Bio-Beads were removed and the nanodiscs assembly was concentrated (MWCO 100 kDa), centrifuged (30 min at 63,000 rpm, Optima Max XP UC, rotor MLA-130), and filtered before applying to a gel filtration column (II3.6.4).

3.7.2 Reconstitution into amphipol A8-35

Amphipols (APol) are polymers that biochemically stabilize membrane proteins in aqueous solutions. After purification, the detergent is substituted by amphipols, which therefore keep membrane proteins soluble in a detergent-free environment. Due to their amphipathic character they absorb onto the hydrophobic transmembrane surface of proteins, stabilize the native structure and preserve the protein's functionality (Tribet *et al.*, 1996; Popot *et al.*, 2003; Zoonens and Popot, 2014a).

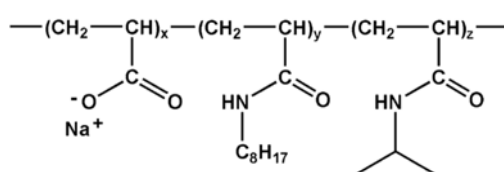


Figure 10: Structure of amphipol A8-35.

Molar percentage of each type unit, randomly distributed along the chain: $x = 35\%$, $y = 25\%$, and $z = 40\%$ (Tribet *et al.*, 1996).

After IMAC the concentration of purified protein in detergent was determined by BCA assay and the total protein amount in mg was calculated. Amphipol A8-35 (Figure 10) was added at a 5- to 6-fold excess (w/w) (for Neq198 and Neq531, respectively) and incubated rotating at RT for 4 h. To remove the detergent ~ 30 mg activated Bio-BeadsTM SM-2 Resin (Bio-Rad) was added per 1 ml protein-detergent-amphipol mixture and incubated rotating at RT o/N. Subsequently, the Bio-Beads were removed and the sample was washed three times upon concentrating (MWCO 100 kDa). This was followed by a centrifugation step (30 min at 63,000 rpm, Optima Max XP UC, rotor MLA-130). Finally, the sample was filtered and applied to a gel filtration column for SEC (II3.6.4).

3.8 Lipid analysis by thin layer chromatography (TLC)

Thin layer chromatography (TLC) was performed to analyze the lipid content of purified protein samples. To extract lipids from purified protein samples a chloroform-methanol-extraction was performed. 250 μl methanol and 125 μl chloroform were added to 100 μg proteins and mixed vigorously for 2 min (Vortex-Genie2, Scientific Industries Inc.). The mixture was incubated at RT for 10 min. Then, another 125 μl chloroform were added and the sample was mixed again for 30 sec. This was followed by the addition of 125 μl ddH₂O and mixing for 30 sec. By centrifugation for 5 min at 13,000 rpm a phase separation was induced. The lipid containing chloroform phase (bottom phase) was transferred to a new tube and dried under a continuous nitrogen stream. The lipids were re-dissolved in 5 μl 1% (w/v) DDM.

Pre-coated Silica 60 TLC plates (10 x 10 cm², Merck) were pre-treated in a closed tank filled with 20 ml of a 1:1 (v/v) mixture of chloroform:methanol and run twice with fresh buffer until 1 mm to the end of the plate. The plate dried at RT in between. Finally, the plates were dried for 2 h at 180 °C.

5 µg of purified protein sample was loaded onto a TLC plate by pipetting 5 x 1 µl sample and drying in between. Lipids standards (e.g. *E. coli* Polar Lipid extract, POPC, POPG, POPE) and detergent references were treated accordingly. The TLC was performed in a closed tank with a saturated atmosphere of a solvent mixture of chloroform:methanol:water = 69 %:27 %:4 % (v/v/v). Removing the plate from the tank when the buffer had reached 1 mm to the end of the plate stopped the chromatography. After drying, the lipids were visualized with iodine vapor, which stains lipids non-specifically by binding to carbon-carbon double bonds (C=C) of unsaturated fatty acids. Stained lipids were identified by yellow areas on the plates. For 2D TLC the plates were air dried, turned by 90° degree and run again.

4 Electrophysiological analyses

Patch clamping represents a valuable tool to characterize ion channels. In 1991 the Nobel Prize in Physiology or Medicine was awarded to Erwin Neher and Bert Sakman for their discoveries “concerning the function of single ion channels in cells” (Neher and Sakmann, 1976; Hamill *et al.*, 1981).

4.1 Preparation of liposomes

Liposomes were formed by the dehydration-rehydration method, as described in Häse *et al.*, 1995 and Delcour *et al.*, 1989. In brief, 200 µl of a 10 mg/ml lipid stock solution in chloroform were dried under a continuous stream of nitrogen and re-dissolved in 200 µl D/R buffer (5 mM HEPES/KOH pH 7.2, 200 mM NaCl). Subsequently, the solution was vortexed and sonicated for 15 min at 100 % to form a liposome suspension. The purified protein was added in a ratio of 1:1000-1:50 and incubated for several minutes. After adding 800 µl of D/R buffer, the lipid-protein mixture was transferred into a 15 ml falcon tube, to which additional 2 ml of D/R buffer were added. The mixture was incubated for 1 h at RT followed by an optional incubation at 4 °C for 30 min. The detergent was removed by adding Bio-BeadsTM SM-2 Resin (Bio-Rad), gently rocking for 3 h at RT. Then, the mixture was centrifuged at 40,000 rpm for 30 min (rotor Ti50.2). The resulting proteoliposome pellet was

resuspended in 60 μl D/R buffer and spotted with 3 x 20 μl on a glass slide. The spots were dried at vacuum o/N. The spots could be stored several weeks in the fridge. For patch clamp experiments, the spots were re-hydrated by adding 30 μl D/R buffer and incubating for 3 h at 4 °C.

4.2 Patch clamp recordings of proteoliposomes

Patch clamp recordings were performed at RT according to Hamill *et al.*, 1981. Pipettes for micromanipulation were made from borosilicate glass (Drummond Scientific Co.) using a vertical Micropipette puller (PP-83, Narishige). The pipette diameter was determined by measuring the pipette bubble number. A bubble number of approximately 6-7 corresponded to an average resistance of 1-2.5 M Ω in a recording solution containing 5 mM HEPES/KOH (pH 7.2), 200 mM KCl, and 40 mM MgCl₂ (bath solution). The pipettes were filled with recording solution free from any air bubbles. The proteoliposome sample was diluted 1:1000 in bath solution in the recording chamber and incubated for 5-30 min (in exceptional cases up to 3 h) to allow unilamellar blisters to be formed. These blisters were used to establish a giga- Ω -seal (G Ω) between micropipette and membrane. Here, an inside-out-patch was already obtained by just contacting the membrane with the pipette. A piezoelectric pressure manometer (World Precision Instruments) measured negative pressure in mmHg (suction) that was applied to the patch-clamp pipette. Currents were filtered at 1 kHz, digitized at 5 kHz, and analyzed using AXON™ pCLAMP™ 10 electrophysiology data acquisition and analysis software (Molecular Devices).

4.3 Preparation of *E. coli* spheroplasts

Additionally to patch clamp recordings in proteoliposomes, the MscS-like channel Neq198 was investigated in *E. coli* spheroplasts according to Martinac *et al.*, 1987. For this purpose, the protein with and without N-terminal 6x histidine tag was cloned in pBAD24 and transformed in *E. coli* MJF461 $\Delta 7$ strain, which lacks all seven encoded mechanosensitive channels. As positive control *E. coli* MscL was used. 40 ml LB media supplemented with 100 $\mu\text{g/ml}$ ampicillin was inoculated 1:100 with an overnight culture and incubated at 37 °C and 140 rpm up to exponential phase with an OD of 0.4-0.5. This culture was diluted 1:10 in 54 ml fresh LB media supplemented with ampicillin in a 200 ml flask. The addition of cephalexin (final concentration 60 $\mu\text{g/ml}$) inhibited the septation of growing *E. coli* cells and resulted in elongation of the cells to snakes (Figure 11). At low rpm the elongation growth was checked regularly. After elongation growth for either 1 h 15 min, 1 h 30 min or

1 h 45 min, the protein expression was induced with 0.02 % (w/v) arabinose for 1 h 20 min or 3 h at 37 °C. Optionally, the elongated *E. coli* cells were stored for 5 h at 4 °C and subsequently induced with 0.01 % (w/v) arabinose o/N at 20 °C. Then, the expression culture was evenly transferred in 2 x 50 ml falcon tubes, centrifuged for 5 min at 3,500 rpm and the resulting supernatant was discarded completely. Each pellet was resuspended in 5 ml 0.8 M sucrose by swirling, centrifuged and the supernatant was discarded again. Finally, the pellets were resuspended in 2.5 ml 0.8 M sucrose each by swirling. For spheroplast formation, the following solutions were added in the prescribed order:

1. 150 μ l 1 M Tris, pH 7.2
2. 120 μ l 5 mg/ml lysozyme
3. 50 μ l 5 mg/ml DNase I
4. 150 μ l 0.125 M EDTA (final concentration 6.3 mM)

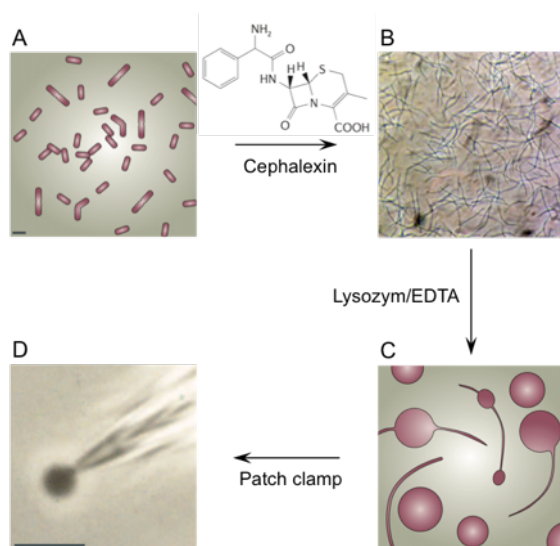


Figure 11: Formation of *E. coli* spheroplasts.

(A) Schematic view of normal growing *E. coli* cells, scale bar: 2 μ m; (B) live imaged *E. coli* $\Delta 7$ cells containing the plasmid with encoded Neq198 after treatment with cephalaxin. Cephalaxin prevents the cells from dividing completely. This causes bacteria to form long "snakes" (up to 100 μ m in length) that share a single membrane and cytoplasm; (C) schematic view of spheroplast formation: treatment with lysozyme and EDTA weakens the outer membrane, permitting rupture of this membrane by the differential between internal and external pressure, the cell walls of the "snakes" are digested, and the bacteria collapse into very large spheres (up to 10 μ m in diameter) surrounded by a single lipid bilayer; (D) patch clamping of spheroplasts, scale bar: 10 μ m (modified from Perozo, 2006).

The time after the addition of EDTA is critical. Therefore, the spheroplasts formation was continuously observed under the microscope. Usually, the spheroplast formation was stopped at two different time points (2-3 min + 5-7 min) to assure obtaining patchable spheroplasts. Thereto, 1 ml of stop solution (700 mM sucrose, 20 mM $MgCl_2$, 10 mM Tris pH 7.2) was added, swirled immediately and stored on ice. Followed by dilution in 7 ml cushion solution (700 mM sucrose, 10 mM $MgCl_2$, 10 mM Tris pH 7.2), the spheroplasts were aliquoted in 100 μ l and stored at -20 °C until further usage.

4.4 Patch clamp recordings of *E. coli* spheroplasts

The patch clamp recordings in spheroplast were performed analogously to those described in II4.2. Pipettes for patch clamping exhibited a slightly smaller pipette bubble number of 3.4-4.2, i.e. smaller diameter. This corresponded to an average resistance of 4-5 M Ω . As bath solution 5 mM HEPES/KOH (pH 7.2), 200 mM KCl, 90 mM MgCl₂, and 300 mM sucrose was used. The spheroplast sample was diluted 1:1000 in bath solution in the recording chamber. The pipette solution instead contained 5 mM HEPES/KOH (pH 7.2), 200 mM KCl, and 300 mM sucrose. To establish a G Ω -seal, suction was applied slowly, constantly and with care. As soon as a G Ω -seal was established, the pipette was carefully flipped with the finger to remove the spheroplast from the pipette resulting in an excised patch (inside-out) for recording.

4.5 Hypoosmotic down-shock assay

The survival rate after hypoosmotic shock was examined using a method based on that of Levina *et al.*, 1999. MJF465 cells, which lack the *mscL*, *mscS* and *mscK* gene, were used for expression of the MscS-like channels Neq198. Additionally, *E. coli* MscL served as positive control, whereas the MJF465 cells without any plasmid corresponded to the negative control. The expression was tightly regulated with the *araBAD* promoter. Cells were grown aerobically in citrate-phosphate defined medium (CP medium, II1.9.5) at 37 °C and 180 rpm. For o/N culture CP medium was supplemented with 0.2 % (w/v) glucose and the corresponding antibiotics for selection and inoculated with cells from a fresh transformation plate. The following morning the culture was supplemented with another 0.2 % (w/v) glucose for additional 1 h. CP medium supplemented with 0.5 M NaCl, 0.2 % (w/v) glucose and the corresponding antibiotics was inoculated to OD₆₀₀ of 0.02 for expression. The culture was incubated to OD₆₀₀ 0.14, which was followed by induction with 0.05 % (w/v) arabinose for 1 h. Subsequently, the culture was diluted to OD₆₀₀ 0.006 in pre-warmed identical CP medium supplemented with (control) and without 5 M NaCl (down-shock) and incubated for 5 min. To determine cell viability, the cultures were serially diluted and 15 μ l plated in triplicate on agar plates containing the corresponding antibiotics and 0.05 % (w/v) arabinose. After o/N incubation the survival rate ($n_{\text{down}}/n_{\text{control}}$) was calculated by counting the number of colony forming units (cfu) of cells that experienced the osmotic down-shock (n_{down}) compared to those that did not experience the down-shock (n_{control}). The down-shock experiment was repeated three times.

5 Biophysical methods

5.1 Negative stain electron microscopy

Negative staining was mainly used as quality control of freshly purified protein samples. Especially the evaluation with respect to protein heterogeneity, aggregates and protein concentration was of high interest.

5.1.1 Preparation of carbon coated copper grids

For analysis and quality control of protein samples with electron microscopy, carbon coated copper grids were prepared in-house. The carbon film was generated using a High Vacuum Carbon Coater 208carbon (Cressington Scientific Instruments), by which carbon is evaporated under vacuum as a 10-15 nm thin, fine-grained film over freshly cleaved mica plates. The carbon covered mica plates were settled for 24 h. Subsequently, glow-discharged copper grids (400 mesh) were placed on a filter paper under water and the carbon film was floated off the mica plates on the water surface. By lowering the water level, the copper grids were covered with the carbon film. Coated grids were dried o/N at 120 °C and stored at RT until usage.

5.1.2 Negative staining and electron microscopy

For negative staining 3 μ l of protein (protein concentration: 10-20 mAU after SEC, corresponding to \sim 0.01 mg/ml) were applied to a glow-discharged carbon coated copper grid (400 mesh) for 60 s. The grid was blotted with Whatman filter paper, washed once with 2 % (w/v) uranyl acetate (pH 4.5) (UAc) followed by staining for 30 s with 2 % (w/v) UAc. For quality control, negative-stained grids were imaged on a Philips CM12 operated at 120 kV. Images were recorded at a nominal magnification of 6,300x, 13,000x or 22,000x using a 1k x 1k digital camera (TVIPS, Gauting).

For single particle analysis, negative-stained grids were imaged on a JEOL 2100F electron microscope operated at 200 kV. Images were recorded at a nominal magnification of 30,000x using a 4k x 4k F416 camera with CMOS chip/detector (TVIPS, Gauting), corresponding to a pixel size of 3.7 Å on the specimen.

Electron microscopy images were recorded in collaboration with Veronika Heinz (Institute of Biophysics and Physical Biochemistry, University of Regensburg).

5.2 Cryo electron microscopy (cryo-EM)

Protein samples and freezing conditions were screened on a JEOL-2100F TEM operated at 200 kV; additional screening was conducted on a Tecnai F30 Polara (FEI), operated at 300 kV and equipped with a Gatan K2 summit direct electron detector. 3 μ l aliquots of purified protein (protein concentration: \sim 200 mAU after SEC, corresponding to \sim 0.1 mg/ml) were applied to a glow-discharged Quantifoil holey carbon grid (R2/4, 400 mesh). Grids were blotted with Whatman No. 1 filter paper for 1.2 - 4.5 s at \sim 88 % humidity and RT (pre-blotting for 15 s, post-blotting for 1 s), and plunge-frozen in liquid ethane using an EM Grid Plunger (Leica). Cryo-EM data were recorded on a Tecnai F30 Polara electron microscope (FEI) at the VBCF in Vienna under supervision of Thomas Heuser. Data were collected at a nominal magnification of 31,000x, corresponding to a physical pixel size of 1.273 Å on the specimen. Images were recorded with the automated EM data acquisition software SerialEM with a defocus range of -2.5 to -3.0 μ m. A total exposure of 10 s was used with 0.2 s per subframes (50 frames) to give a total dose of 70.89 electrons per Å² (1.4178 electrons per Å² per sub-frame). The experimental set-up of major data sets can be found in the appendix (VI3).

Cryo-electron microscopy images were recorded in collaboration with Veronika Heinz (Institute of Biophysics and Physical Biochemistry, University of Regensburg) and Thomas Heuser (VBCF, Vienna).

5.3 Image-processing and single particle analysis

Electron beam-induced sample motion in cryo-EM images was corrected with MotionCor2 (Zheng *et al.*, 2017). If possible, motion-corrected sums without dose-weighting were used for CTF correction using CTFFIND3 (Mindell and Grigorieff, 2003) or CTFFIND4 (Rohou and Grigorieff, 2015). Motion-corrected sums with dose-weighting were used for all other image processing in RELION 1.4 or 2.1beta. RELION (REGularized LIkelihood OptimizatiON) is an open-source computer program for the refinement of macromolecular structures by single-particle analysis (Scheres, 2012b). Data were processed up to 3D refinement and further analyzed (II5.4).

5.4 Map visualization and analysis

Negative stain and cryo-EM volumes were visualized and atomic models were fitted into the densities using Chimera 1.12 (Pettersen *et al.*, 2004). The homology model of Neq198 missing the two

additional TM helices served as starting point for fitting. The cytoplasmic domain was fitted separately into the cryo-EM volume using the segmentation option in Chimera (Pettersen *et al.*, 2004) and MD simulation using FlexEM (Topf *et al.*, 2008). Single segments were combined and the membrane domain was fitted manually into the cryo-EM density using Coot (Emsley *et al.*, 2010). The two additional TM helices were predicted with ROSETTA (<https://www.rosettacommons.org>). The best scoring models were fitted into the density; the best fitting model was evaluated visually and finally linked manually to the rest of the model.

6 Bioinformatical analyses

6.1 Sequence alignments

Protein sequence alignments were generated with the server with Clustal O (1.2.4) (Larkin *et al.*, 2007) and further processed with ESPript3.0 (Robert and Gouet, 2014). The archaeal protein sequences were taken from the UCSC Archaeal Genome Browser (<http://archaea.ucsc.edu>). Alignments can be found in the appendix (VII.4).

6.2 Topology prediction

For prediction of the topology of the MscS-like channels from *N. equitans* the following servers have been used: TMHMM2.0 (Krogh *et al.*, 2001; <http://www.cbs.dtu.dk/services/TMHMM/>), TOPCONS (Tsirigos *et al.*, 2015; <http://topcons.cbr.su.se/pred/>), OCTOPUS (Viklund and Elofsson, 2008; <http://octopus.cbr.su.se/index.php>), TMPred (Hoffmann and Stoffel, 1993; https://embnet.vital-it.ch/software/TMPRED_form.html) and PSIPRED (Jones, 1999; Buchan *et al.*, 2013; <http://bioinf.cs.ucl.ac.uk/psipred/>).

6.3 Homology modeling

The homology model of Neq198 was provided by Dr. M. Gregor Madej (Institute of Biophysics and Physical Biochemistry, University of Regensburg).

The Neq198 model was generated based on the X-ray structure of *E. coli* MscS (2oau.pdb, Bass *et al.*, 2002; Steinbacher *et al.*, 2007) as template using a standard ‘automodel’ class of MODELLER-v9-14 (Šali and Blundell, 1993). Evaluation was performed using Z-DOPE, a normalized atomic distance-

dependent statistical potential based on known protein structures. The finite model was selected based on the assessed scoring functions.

III RESULTS

1 Biochemical analysis of Neq198 and Neq531

1.1 Heterologous expression and purification

In previous experiments, the Neq531 gene encoding for one of the two MscS-like channels from *N. equitans* was codon optimized and fused with a C-terminal 6x histidine tag for the heterologous expression in *E. coli*. Conditions for expression and initial purification have already been screened (Wiegmann, 2014). After up scaling immobilized metal affinity chromatography (IMAC), immediate and complete precipitation of Neq531 was observed. Inappropriate purification conditions, e.g. unsuitable buffer compositions, are well-known reasons for protein instability. In literature several suggestions with respect to stabilizing additives can be found (e.g. Bondos and Bicknell, 2003; Lebendiker and Danieli, 2014). Buffers at various pH values ranging from pH 5.0-10.0 were tested. Moreover, different salts like NaCl, KCl and monopotassium glutamate were tested in various concentrations and combinations. Stabilizing additives such as sucrose and glycerol in changing concentrations were examined as well. None of these variations led to stable protein preparation. Furthermore, different column materials for IMAC were screened: TALON Metal Affinity Resin (Clontech), HiTrap Chelating HP column (QIAGEN), Ni-NTA Agarose (QIAGEN), Ni-NTA Agarose (Sigma). Since nickel ions have already been observed to leak off IMAC columns, protein was eluted into EDTA-containing buffer in order to chelate those ions. The effect of detergents (DDM, Fos14, LMNG, LDAO) on stability during purification was also screened, but did not have a positive effect. The quality control of negative stained samples shows a high extent of unfolded channel protein on

electron micrographs (Figure 12). Therefore, the histidine tag for detection and purification was exchanged from C-terminus to N-terminus to overcome channel instability issues.

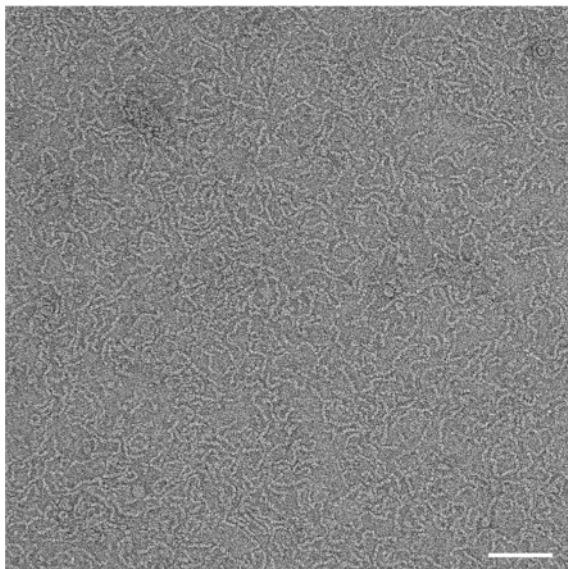


Figure 12: Negative stain transmission electron micrograph of Neq531.

Neq531 with C-terminal 6x histidine tag was solubilized in 2 % (w/v) Fos14, followed by detergent exchange to 0.1 % (w/v) LMNG during IMAC in 50 mM Tris, 300 mM NaCl, 10 % (v/v) glycerol, 0.1 % (w/v) LMNG; protein sample after IMAC showed unfolded protein; negative stain with 2.5 % PTA, magnification 50,000x; bar corresponds to 90 nm.

The genes for Neq198 and Neq531 that exhibited an N-terminal 6x histidine tag for detection were both codon-optimized for the expression in *E. coli*. Functional mechanosensitive channels form homo-heptamers (Bass *et al.*, 2002). The Neq198 monomer has a predicted molecular weight of 38.596 kDa that corresponds to 270 kDa for a heptamer. The Neq531 monomer has a predicted molecular weight of 37.245 kDa that corresponds to 260 kDa for a heptamer. Other specifications of both proteins can be found in the appendix (VII.1). The protein expression was tested in different *E. coli* strains like BL21 (DE3), BL21 StarTM (DE3), RosettaTM 2 (DE3) and C43 (DE3) Δ AcrB. The latter has at least one non-characterized mutation that prevents cell death upon expression of numerous recombinant and toxic proteins. It is especially preferred for the expression of membrane proteins (Miroux and Walker, 1996; Dumon-Seignovert *et al.*, 2004) and was therefore favored for the expression of both MscS-like channels. Moreover, the expression and its conditions in LB media, 2YT media and TB media were compared. The expression in TB media at low temperatures (20 °C) overnight shows sufficient quantity and quality of channel protein for structural and functional studies. Expression in 6 L TB media results in ~55 ml membranes with a total membrane protein concentration of 30 mg/ml for Neq198 expressing *E. coli*, and 70 ml membranes with a total membrane protein concentration of 38 mg/ml for Neq531. A western blot of homogenized membranes against the N-terminal histidine tag using a polyclonal antibody (Figure 13) detects a distinct band at approximately 35 kDa for Neq531 (A) and Neq198 (B).

III Results

For Neq531 multiple bands below the signal of interest are observed and a single band at 50 and 70 kDa. Besides the signal around 35 kDa, multiple faint signals are detected above for Neq198. Neq531 shows approximately two times higher expression yield compared to Neq198 in membranes.

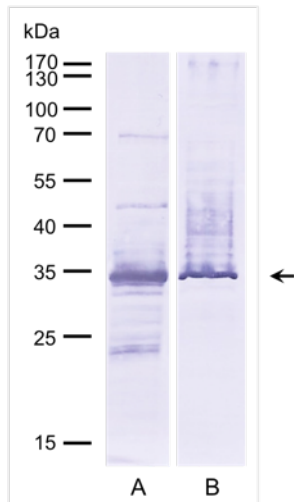


Figure 13: Western blot analysis of homogenized membranes.

Membrane blot, 10 μ g of total membrane proteins were applied to SDS-Page, protein expressed in TB media, (A) Neq531, (B) Neq198; semi-dry western blot with antibodies against N-terminal 6x histidine tag.

The detergents CYMAL-5, CYMAL-6, DDM, DM, Fos12, Fos14, LDAO, LMNG, NG, OG, UDM were screened for solubilization of Neq531 and Neq198. Neq198 is successfully solubilized within a range of detergents (Figure 14). A western blot with antibodies against the N-terminal histidine tag detects bands around 30-35 kDa as expected. Additionally, for all detergents more or less intense signals for higher oligomers above 130 kDa are visible. For NG, OG and CYMAL-5 the solubilization efficiency is lower compared to other detergents. In addition, the channel is not stable in NG and OG, which resulted in progressing precipitation. The maltosides DM, DDM, UDM, CYMAL-6 and LMNG show a solubilization efficiency of around 50 %. LDAO and the Fos-Cholines show efficiencies higher than 50 %. Based on recent test for Neq531 (Wiegmann, 2014) and literature (Bass *et al.*, 2002; Wang *et al.*, 2008; Petrov *et al.*, 2013), Fos14 is favored for structural analyses and DDM for functional analyses for both channels.

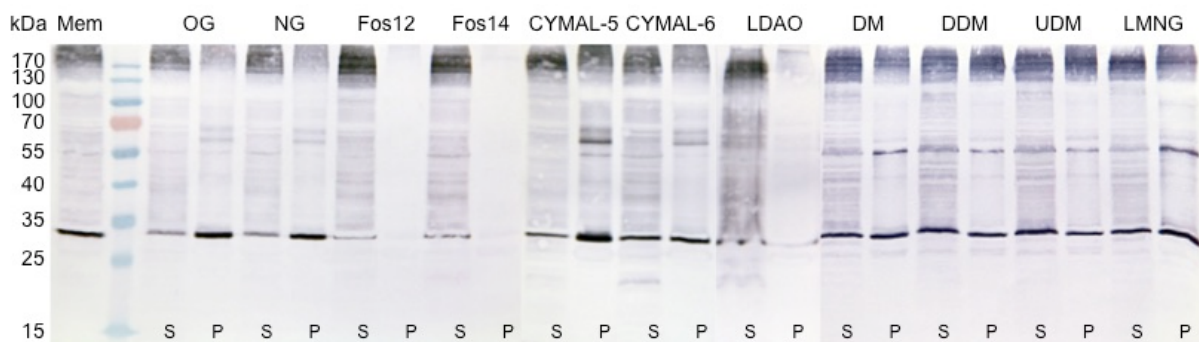


Figure 14: Solubilization test of Neq198.

Solubilization of homogenized membranes with 1.67 % (w/v) detergent, *Mem* membranes, diluted 1:10 in solubilization buffer, *S* solubilize, *P* pellet after ultra-centrifugation; western blot with antibodies against N-terminal 6x histidine tag.

For solubilization and purification NaP_i buffer is favored over Tris buffer. The latter results in contaminations with *E. coli* host cell proteins (Figure 15). Using NaP_i buffer for solubilization and

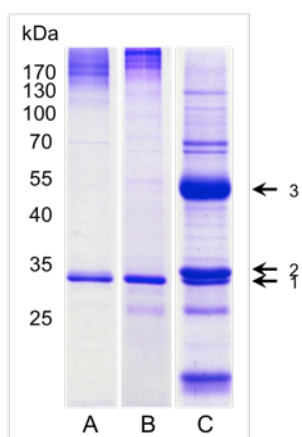


Figure 15: Buffer conditions for IMAC purification.

SDS-Page of elution peak after IMAC purification using different buffer-detergent combinations; (A) buffer: NaP_i , solubilization + purification: Fos14; (B) buffer: NaP_i , solubilization + purification: DDM; (C) buffer: Tris, solubilization + purification: DDM; 1 - Neq198; 2 - *E. coli* cytochrome o ubiquinol oxidase, subunit II, 3 - *E. coli* cytochrome o ubiquinol oxidase, subunit I.

purification results in a less contaminated elution peak (Figure 15A and B). The solubilization with DDM and purification with Tris buffer results in massive contamination with the cytochrome o ubiquinol oxidase from *E. coli* (Figure 15C) that cannot be eliminated during purification procedure. Similar results are obtained if the buffer is exchanged from NaP_i to Tris during IMAC. Therefore, solubilization and the first purification step in IMAC were carried out with 50 mM NaP_i , pH 7.5 supplemented with 300 mM NaCl. Neq531 requires additionally 10 % (v/v) glycerol for stabilization.

Different column materials have been tested for optimized binding: TALON Metal Affinity Resin (Clontech), Ni-NTA Agarose (QIAGEN), and Ni-NTA Agarose (Sigma) and HiTrap Chelating HP column (GE Healthcare); the latter showing best binding behavior (Figure 16A and Figure 17A). The solubilize, supplemented with 10 mM imidazole to prevent unspecific binding, is loaded onto a

HiTrap Chelating HP column using a ÄKTA pure/purifier system (I). Subsequently, in a first washing step with 20 mM imidazole (II), loosely bound protein was removed followed by a washing step with 150 mM imidazole (III) that removes most of the contaminants. Finally, the channel was eluted with 600 mM imidazole in a monodispersed peak (IV) (Figure 16A and Figure 17A). The optimal concentration of imidazole for washing and elution was determined in a previous step-gradient experiment. The elution peak was pooled, applied to SDS-Page, and analyzed further. Neq198 elutes in a relatively small peak with maximal ~1,900 mAU. In SDS-Page a distinct band around 30-35 kDa (monomer) and multiple bands above 130-170 kDa (higher oligomers) are detected (Figure 16B). Neq531 elutes in a comparable broader peak with up to 2,800 mAU. In SDS-Page a dominant band around 35 kDa (monomer), a faint band around 70 kDa (dimer) as well as a band above 170 kDa (higher oligomers) are detected (Figure 17B).

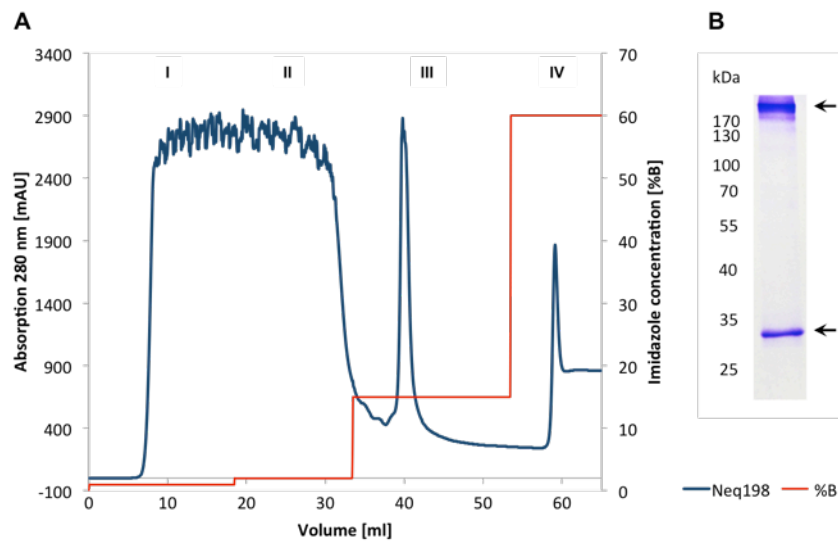


Figure 16: Immobilized metal affinity chromatography (IMAC) of Neq198.

Neq198 was solubilized with 2 % (w/v) Fos14 for 1 h at RT, 50 mM NaP_i, 300 mM NaCl, pH 7.5; (A) IMAC chromatogram, HiTrap Chelating HP column, (I) loading with 10 mM imidazole, (II) wash 1 with 20 mM imidazole, (III) wash 2 with 150 mM imidazole, (IV) elution with 600 mM imidazole; (B) SDS-Page of elution peak (IV), Coomassie stain.

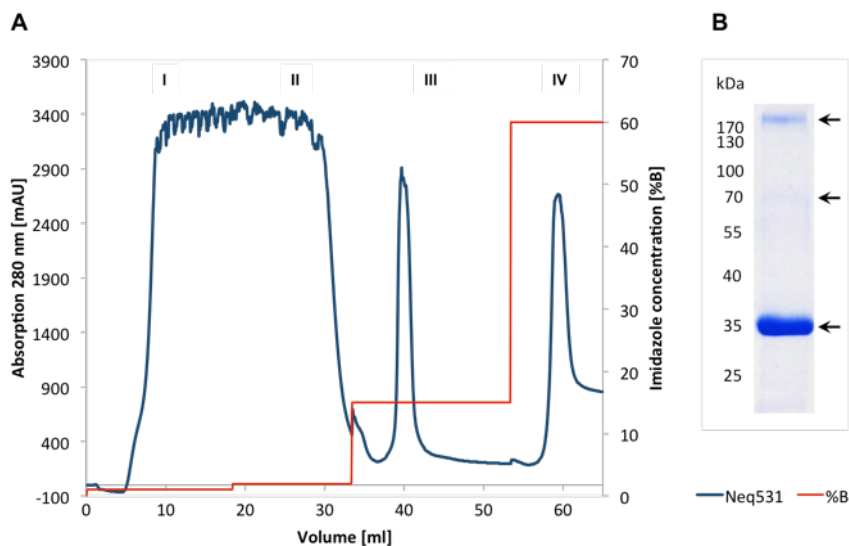


Figure 17: Immobilized metal affinity chromatography (IMAC) of Neq531.

Neq531 was solubilized with 1.5 % (w/v) Fos14 for 1 h at RT, 50 mM NaP_i, 300 mM NaCl, 10 % (v/v) glycerol, pH 7.5; (A) IMAC chromatogram, HiTrap Chelating HP column (5 ml), (I) loading with 10 mM imidazole, (II) wash 1 with 20 mM imidazole, (III) wash 2 with 150 mM imidazole, (IV) elution with 600 mM imidazole; (B) SDS-Page of elution peak (IV), Coomassie stain.

SDS-Page confirms that both protein samples are of relatively high purity with only few contaminations after the first purification step and are not degraded. A single IMAC purification of Neq198 results in a total protein amount of 0.7-1 mg target protein whereas that of Neq531 results in 1.5-2.0 mg. This corresponds to an extrapolated protein quantity of ~7 mg for Neq198 and the three-fold quantity of ~24 mg for Neq531 from 6 L expression culture.

In a second purification step the channel was analyzed regarding its homogeneity by size exclusion chromatography. Neq198, solubilized and purified with Fos14, elutes at approximately 13.3 ml in a monodispersed peak that results in a distinct signal around 390 kDa in Blue Native Page (Figure 18). In size exclusion chromatography only a small aggregation peak (v_0) is observed.

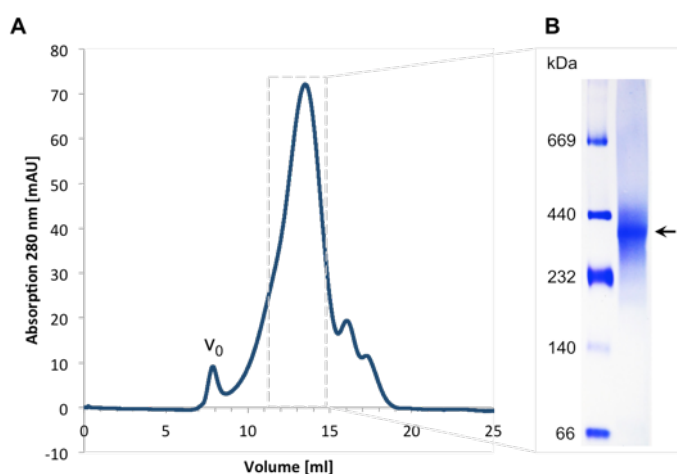


Figure 18: Homogeneity and oligomeric state of Neq198 in Fos14.

(A) Size exclusion chromatography of Neq198 in Fos14, Superose 6 GL 10/300, 50 mM NaP_i , 300 mM NaCl, 0.02 % (w/v) Fos14, pH 7.5; (B) Blue Native Page, Coomassie stain, arrow indicates the band of interest.

The purity and homogeneity (further denominated as quality control) of Neq198 solubilized and purified with Fos14/ NaP_i was performed by the visualization of negative-stained channel protein in the electron microscope. As NaP_i interacts with stains such as uranyl acetate or PTA resulting in aggregation of the channel on the grid, the buffer was exchanged to Tris (III1.2). Neq531 is less stable in Fos14 than Neq198 and suffers constant degradation. Therefore, Neq531 was solubilized in Fos14, while the final purification was carried out in amphipols (III1.2).

1.2 Reconstitution into membrane-mimicking environments

For stabilization after solubilization and first purification steps both channels were either reconstituted into amphipols (Tribet *et al.*, 1996; Popot *et al.*, 2003) or lipid nanodiscs (Bayburt *et al.*, 2002). The extraction of membrane proteins with detergents leads to the loss of the native lipid environment (Figure 19A). Consequently, the protein might be destabilized since important interactions with lipids or other proteins are missing. In contrast to lipid bilayers, detergent micelles exhibit very different physicochemical properties. Besides others, the lateral pressure profile differs significantly, which might be of special interest for membrane proteins in general and mechanosensitive channels in particular. Amphipols represent a promising alternative (II3.7.2; Figure 19B). A8-35 has a polyacrylate backbone that is modified with varying octylamine and isopropylamine groups (Tribet *et al.*, 1996). In contrast to detergents, those amphipathic polymers have a higher affinity to the surface of the protein resulting in low exchange rates of protein-bound amphipols and free molecules in solution (<http://www.ibpc.fr/amphipol/>). Lipid nanodiscs represent a reconstitution system that mimics the native membrane better than detergents and amphipols (II3.7; Figure 19C). Here, the membrane protein is reconstituted into small lipid bilayer patches, stabilized by the encircling amphipathic helical proteins derived from the human apolipoprotein A-1 (membrane scaffold protein) (Bayburt *et al.*, 2002). The scaffold protein shields the hydrophobic lipid acyl groups and thereby increases the solubility of the lipid nanodiscs. The lateral pressure provided by amphipols and lipid nanodiscs might have positive and stabilizing effects on the mechanosensitive channels.

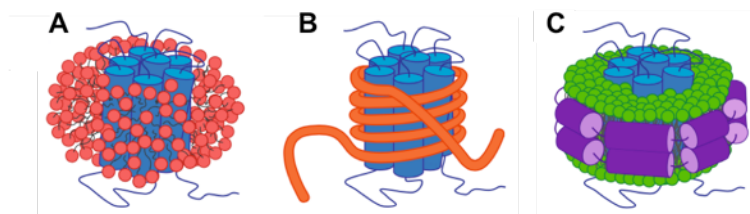


Figure 19: Membrane-mimicking systems for membrane protein stabilization.

Simplified representation of (A) a membrane protein in detergent (red) micelle, (B) in amphipol (orange), and stabilized in (C) lipid nanodisc by MSP (purple); the protein is indicated in blue, lipids in green (modified from Dörr *et al.*, 2016)

The mass ratio of membrane protein (MP):amphipol (APol) was optimized for each channel individually. The ratio depends on the size of the transmembrane region. Furthermore, the propensity of the protein to self-associate, and the ability of the amphipol to prevent the oligomerization should

be taken into account (Zoonens and Popot, 2014a). The optimized mass ratio is determined to at least 1:5 for Neq198 in small scale in previous experiments according to Zoonens *et al.*, 2014b. However, due to insufficient protein amount, the optimal ratio was estimated visually only by SDS-Page instead of size exclusion chromatography (Figure 20).

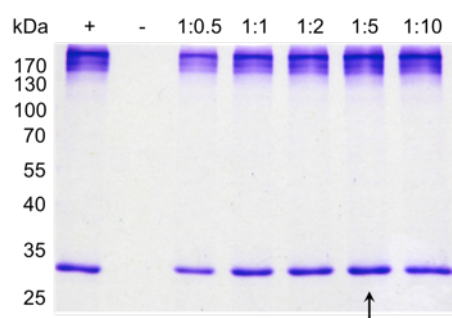


Figure 20: Determination of the optimal MP:APol ratio for Neq198.

Several MP:APol ratios have been tested, Neq198 was incubated for 20 min at RT with APols; after detergent removal by the absorption onto hydrophobic beads for 2 h at RT, the samples were centrifuged for 30 min at 70,000 rpm; protein samples before and after centrifugation were compared in SDS-Page; + positive control = protein sample without APol and biobeads, - negative control = without APol but biobeads were added; arrow indicates the optimal MP:APol ratio.

A heat shock of the protein sample for 20 min at 60 °C before applying to size exclusion chromatography is found to be beneficial. This step can successfully eliminate protein contaminants from the *E. coli* host. Moreover, higher temperatures might help the channel to oligomerize correctly considering its origin from a hyperthermophilic organism. An ultra-centrifugation step removes successfully aggregated protein prior to sample application to size exclusion chromatography. The size exclusion chromatogram shows a main peak containing the reconstituted channels (Neq198) with a preceding shoulder. The main peak elutes at approximately 13.6 ml. SDS-Page confirms that the shoulder also consists of target protein (Figure 21A and B).

Negative staining and electron microscopy was extensively used to monitor the quality of the purified channels. In negative stain, proteins are absorbed to a continuous carbon support and embedded in a thin layer of heavy metal stain that results in high-contrast images. This approach allows quickly accessing the protein sample's quality with respect to e.g. shape, size, oligomeric state, the presence and degree of contaminants, aggregation, and heterogeneity. Still, there are several drawbacks. Negative staining might introduce artifacts such as specimen flattening and the resolution is limited to ~20 Å (Ohi *et al.*, 2004; Cheng *et al.*, 2015). Buffer compositions and the type of detergent are crucial for the MscS-like channels from *N. equitans*. Furthermore, it is not recommended to use some of the popular buffers like phosphate buffer for negative staining. Uranyl salts, in particular, form crystalline precipitates with phosphate ions and obscure the particles. This contamination with salt residues needs to be washed off after staining, which in turn results in a loss of contrast. Moreover, some detergents might be incompatible with negative staining solutions. Therefore, a genuine quality control in negative stain of Neq531 (and later also of Neq198), solubilized with Fos14 in sodium-phosphate

III Results

buffer, was not possible. Neither with uranyl acetate nor with PTA a satisfying grid preparation was achieved. With PTA the channels aggregate on the grid. Due to detergent and phosphate buffer incompatibility, the channels are therefore stabilized in Tris buffer with amphipols or lipid nanodiscs. In general, it is recommended to establish a library of detergent and buffers for background effects in negative stain. This allows the visualization of the background with different detergents for an evaluation of the protein sample and its improvement. Especially in single particle analysis, signals that result from detergents might be mistaken for protein particles (false-positive particles) (Rubinstein, 2007). Micrographs of negative-stained Neq198 reconstituted into amphipols display separated particles in different orientations (Figure 21C), which were analyzed further in single particle analysis (III2.3.1). Smaller particles of at least one third in size are observed in the background of negative stain electron micrographs that are probably induced by buffer composition or excess of APol aggregates (Figure 21C). In Blue Native Page a broad signal above 440 kDa and a faint signal above 669 kDa is detected (Figure 21D). Compared to protein in Fos14 the signal is shifted to higher molecular mass (Figure 18B).

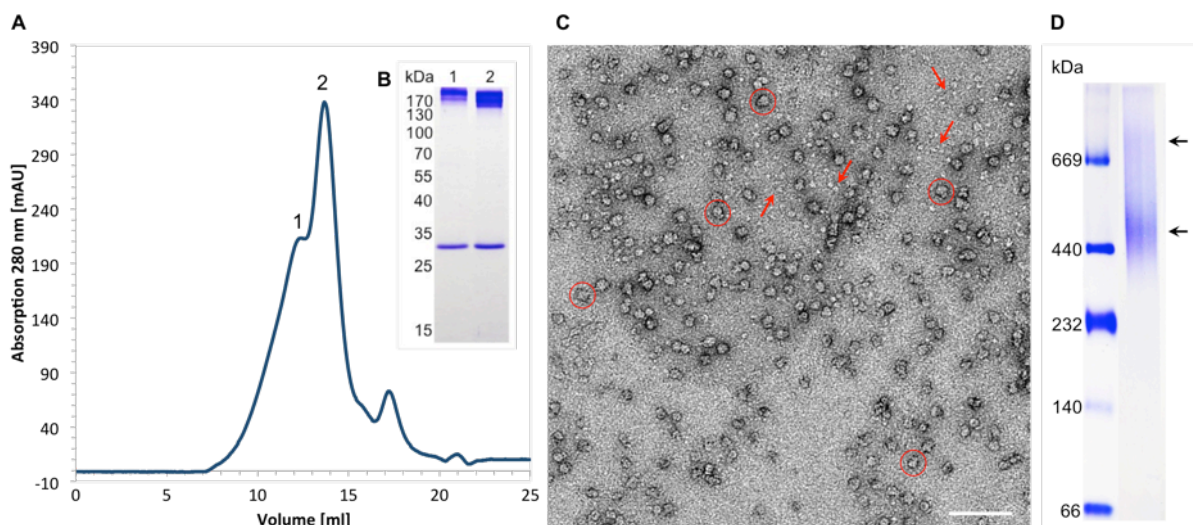


Figure 21: Reconstitution of Neq198 into amphipol A8-35.

(A) Size exclusion chromatography, Superose 6 Increase 10/300 GL, 20 mM Tris pH 7.5, 100 mM NaCl, v_0 – void volume, 1 - shoulder, 2 - main peak; (B) SDS-Page of shoulder (1) and main peak (2), Coomassie stain; (C) negative stain with 2 % (w/v) UAc, magnification 22,000x, bar corresponds to 90 nm, representative particles are encircled in red, red arrows indicate buffer-induced background; (D) Blue Native Page of main peak (2), Coomassie stain, arrows indicate bands of interest.

Neq531 reconstituted into amphipols shows slightly different results. In size exclusion chromatography, a main peak shows two preceding shoulders (Figure 22A). The main peak elutes at

approximately 14.1 ml. Approximately 10 % of the total protein elutes in the void volume, although the protein sample was subjected to ultra-centrifugation prior to sample application. SDS-Page confirms that the shoulder consists of target protein too: a strong signal at 35 kDa is detected. Additionally, there is a signal around 70 kDa as well as above 170 kDa and some minor degradation (Figure 22A and B). In negative stain with uranyl acetate nicely separated particles are visualized, but compared to Neq198 the sample seems to be more heterogeneous with respect to shape and size of the particles. Moreover, aggregation is observed (Figure 22C). The particles were analyzed further in single particle analysis (III2.3.2). The sample heterogeneity is also reflected in Blue Native Page: a broad strong band at approximately 380 kDa, a weaker band around 580 kDa and a third faint band above 669 kDa are detected. Examining the shoulder fraction (1) in Blue Native Page the ratio is shifted to the signals above 580 kDa (data not shown). These observations are in line with those for Neq98 reconstituted into amphipols.

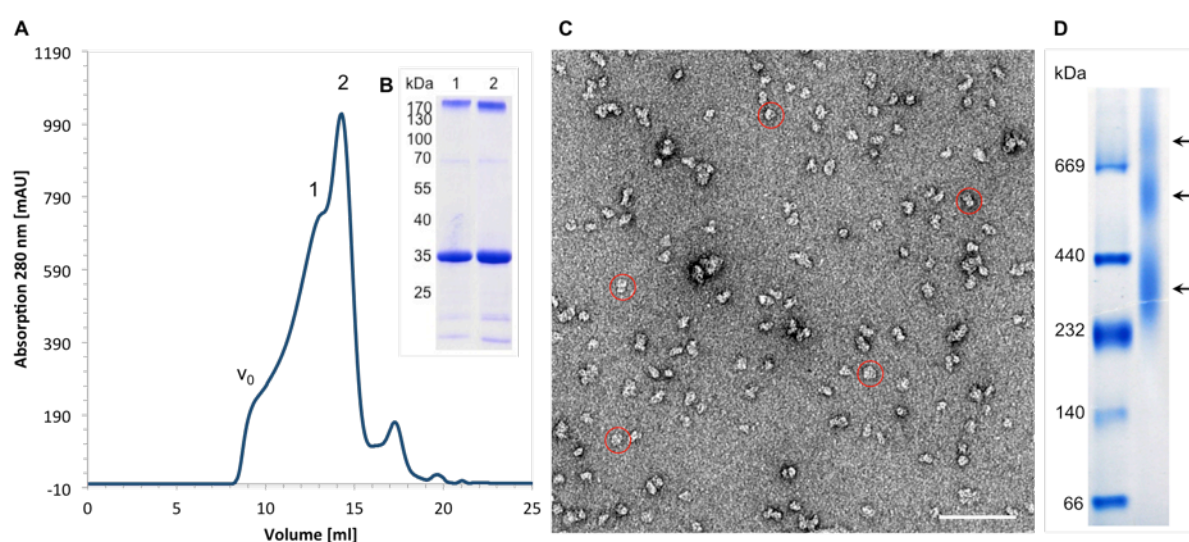


Figure 22: Reconstitution of Neq531 into amphipol A8-35.

(A) Size exclusion chromatography, Superose 6 Increase 10/300 GL, 20 mM Tris pH 7.5, 100 mM NaCl, v_0 – void volume, 1 - shoulder, 2 - main peak; (B) SDS-Page of shoulder (1) and main peak (2), Coomassie stain; (C) negative stain with 2 % (w/v) UAc, magnification 22,000x, bar corresponds to 90 nm, representative particles are encircled in red; (D) Blue Native Page of main peak (2), Coomassie stain, arrows indicate bands of interest.

For the reconstitution into nanodiscs, the membrane scaffold protein MSP1E3D1, which forms nanodiscs with a diameter of about 12 nm, was used. The optimal ratio of protein:lipid:MSP was determined in previous reconstitution experiments. For empty nanodiscs a ratio of 1:75 (MSP:POPC) shows the best reconstitution. The size exclusion chromatogram identifies a peak at a retention volume of ~11.25 ml (Figure 23A).

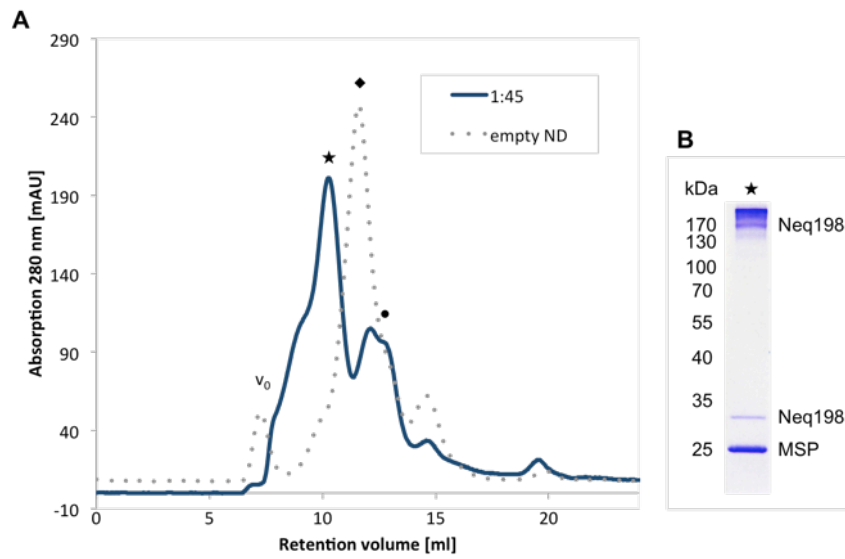


Figure 23: Reconstitution of Neq198 into nanodiscs.

(A) Size exclusion chromatography, channels reconstituted with POPC in MSP1E3D1; ratio protein:lipid:MSP = 0.1:45:1, buffer: 20 mM Tris, 100 mM NaCl, pH 7.4; Superdex 200 10/300 GL; v_0 - void volume; ★ - Neq198 incorporated into nanodiscs; ♦ - empty nanodiscs (1:75 = MSP:POPC); • - MSP protein/ empty nanodiscs; (B) SDS-Page of main peak, ★ - fraction of (A) showed a band for MSP and a band for lower and higher oligomers of Neq198.

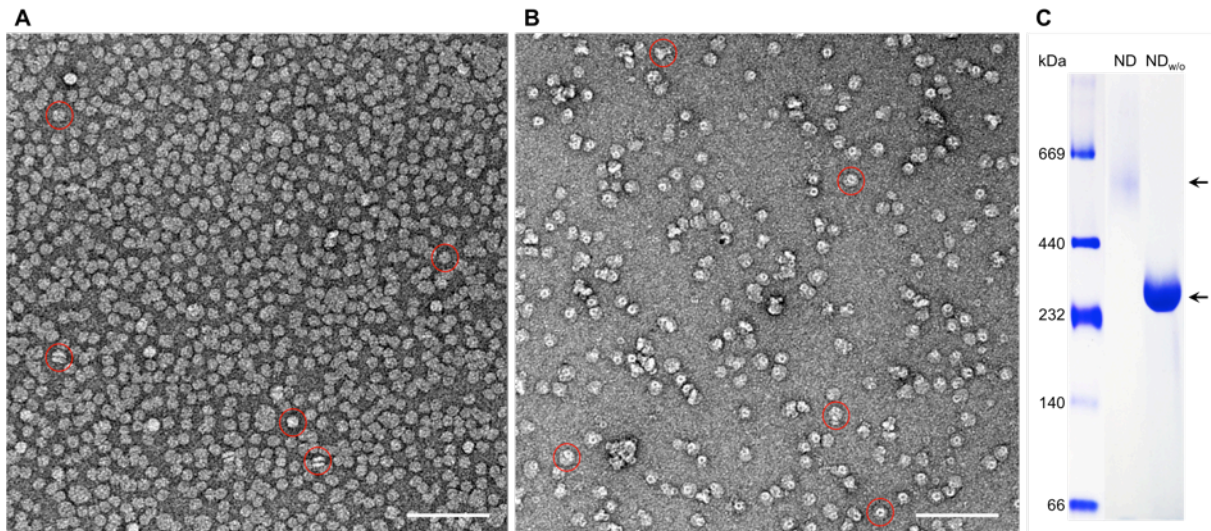


Figure 24: Quality control of Neq198 reconstituted into nanodiscs.

Negative stain with 2 % (w/v) UAc, magnification 22,000x, bar corresponds to 90 nm, representative particles are encircled in red, (A) empty nanodiscs MSP:POPC 1:75, (B) Neq198 incorporated into nanodiscs Neq198:MSP:POPC 0.1:1:45; (C) Blue Native Page, showing empty nanodiscs ($ND_{w/o}$) compared to nanodiscs with incorporated Neq198 (ND).

A control with empty nanodiscs is necessary for the final evaluation of the reconstitution by comparison of size exclusion chromatography, SDS-Page, Blue Native Page, and negative stain (Figure 23A; Figure 24A and C). For Neq198 a ratio of 0.1:1:45 (protein:MSP:POPC) results in a reasonable amount of reconstituted channels, although more than half of the protein is lost during reconstitution procedure due to aggregation upon removal of the detergent. The size exclusion chromatogram shows a peak fraction with a retention volume at approximately 10 ml that contains the channels incorporated into nanodiscs as judged from SDS-Page (Figure 23). MSP protein either isolated or from empty nanodiscs elutes in a second peak with a retention volume of 12.5 ml. Moreover, when comparing empty nanodiscs (retention volume 11.25 ml) with protein-loaded nanodiscs (retention volume 10 ml) a shift of the main peak is observed, indicating an increase in size and therefore the proper incorporation of Neq198 into nanodiscs (Figure 23A).

In negative stain the nanodisc sample shows separated particles in different orientations with only few aggregates (Figure 24B). Reconstituted channels were analyzed further by electron microscopy single particle analysis both negative stained (III2.3.3) and cryo-preserved (III2.4). In Blue Native Page a weak signal is detected at approximately 580 kDa for nanodiscs with incorporated channels (Figure 24C), while empty nanodiscs show a signal at around 310 kDa. The shift in size indicates a proper reconstitution as well.

Since Neq531 is susceptible with respect to protein stability, a direct reconstitution into nanodiscs without previous solubilization and purification (Shirzad-Wasei *et al.*, 2015) was tested. So far, this procedure was not successful and requires further optimization. Due to the high amount of detergent needed, the method was not pursued. Either an optimized direct reconstitution into nanodiscs or purification in the presence of lipids might help to stabilize Neq531.

1.3 Lipid analysis by thin layer chromatography

Lipids have strong impact on the stability of membrane proteins and can be added during purification. Thin layer chromatography (TLC) identifies lipids from the expression host that are bound to purified Neq198 and Neq531. Consequently, promising candidates can be determined that might improve the channel's stability during purification.

In a 1D TLC, lipids extracted from purified Neq198 and Neq531 were loaded together with lipid standards and references (Figure 25). Lipids from Neq198 and Neq531 were either extracted from protein samples that have been solubilized and purified with Fos14 or from protein samples that have been stabilized in amphipols after solubilization and purification. As references amphipols, Fos14 and DDM were used. For the lipid standard, EPL were either solved in chloroform or in DM. The lipid pattern for EPL differs significantly depending on the used solvent. EPL solved in chloroform is considered to be more reliable. Here, two distinct spots are identified: a lower spot that represents PG and CL, which run at the same height, and another spot that runs above representing PE (Figure 25). Interestingly, for Neq198 and Neq531 a different lipid pattern is observed. The spots near the baseline correspond to the detergent and/or the amphipol used for purification. The large middle spots correspond either to PG/CL or to the detergent as well, since the lipids were solved in DM after extraction. For the extracted lipids from purified Neq531 an additional signal is identified. The lipid spots could not be assigned unambiguously after staining with iodine vapour. However, 1D TLC indicates that purified Neq198 and Neq531 have bound a different set of lipids (Figure 25).

Also 2D TLC was not successful in identifying the nature of the channel associated lipids. Different migration patterns of single lipids compared to those of EPL are even contradictory. For Neq198 and Neq531 only the different lipid pattern as observed in 1D is confirmed in 2D as well (Figure 26), so far. 2D TLC requires further optimization.

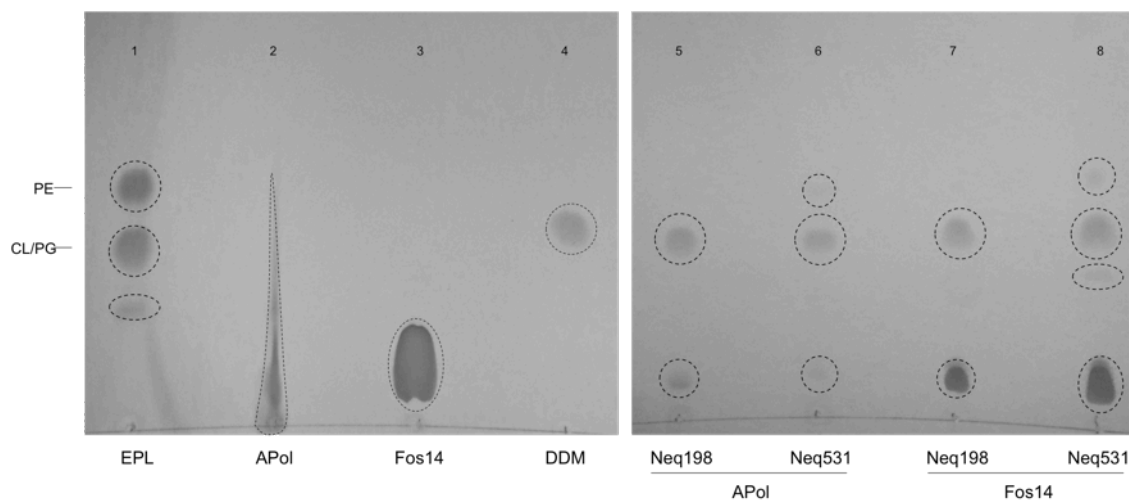


Figure 25: 1D thin layer chromatograms.

Lipid spots were originally stained with iodine vapor, for better visualization the chromatograms were colored in black/white, visible spots are marked; (1) EPL solved in chloroform, (2) 100 $\mu\text{g}/\mu\text{l}$ amphipols, (3) 10 % (w/v) Fos14, (4) 10 % (w/v) DDM, (5) extracted lipids from Neq198 reconstituted into amphipols, (6) extracted lipids from Neq531 reconstituted into amphipols, (7) extracted lipids from Neq198 purified in Fos14, (8) extracted lipids from Neq531 purified in Fos14.

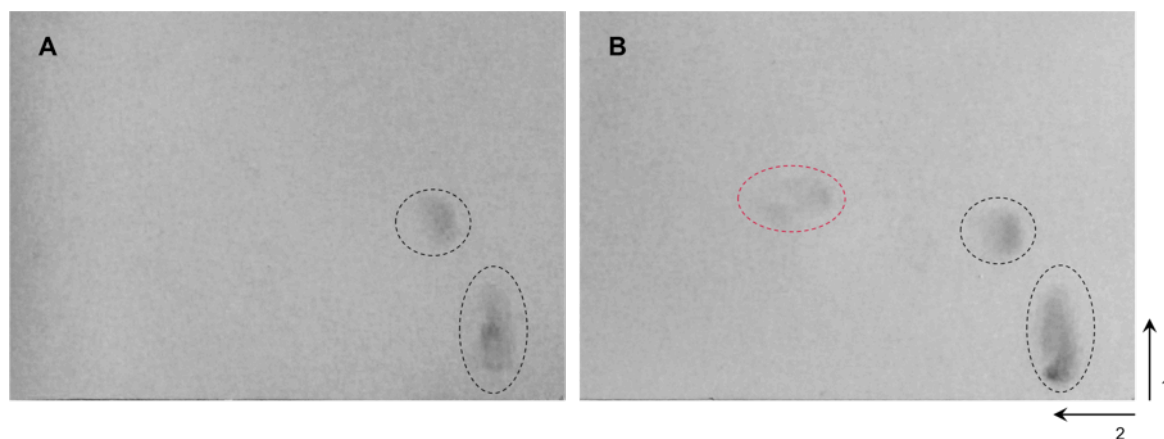


Figure 26: 2D thin layer chromatograms.

Lipid spots were originally stained with iodine vapor, for better visualization the chromatograms were colored in black/white, visible spots are marked; first and second migration directions are indicated; (A) Neq198 solubilized and purified in Fos14, lipids extracted and solved in 1 % (w/v) DM, (B) Neq531 solubilized and purified in Fos14, lipids extracted and solved in 1 % (w/v) DM.

2 Structural analysis of the MscS-like channels from *N. equitans*

2.1 Sequence analysis

The proteins Neq198 and Neq531 consist of 337 and 323 amino acids, respectively. According to their size, they rank between *EcMscS* (283 aa, 3 TM helices) and YnaI (343 aa, 5 TM helices) from *E. coli* (cf. II.2.1). Compared to *EcMscS*, both channels are predicted to exhibit two additional TM helices at the N-terminus resulting in a total of five TM helices (Figure 27, Figure 28). Both channels are predicted to have β -strands at the C-terminus. For Neq531 an additional helix downstream of the β -strand is predicted (Figure 28A). For the topology prediction several servers have been used. The program TMHMM2.0 predicts the orientation of the channels in the membrane and displays the N best prediction at the top of the plot (between 1 and 1.2) (Figure 27B, Figure 28B). The plot is obtained by calculating the total probability for a residue to reside inside or outside in the helix, respectively, summed over all possible paths through the model. Plot and predictions are sometimes contradictory (Figure 28B). Whereas the plot shows probabilities for each residue, the prediction is the over-all most probable structure. Therefore, the plot should be considered as a complementary source of information. One of the most common mistakes generated by the program is to reverse the direction of proteins with one TM segment (Sonnhammer *et al.*, 1998). According to the prediction, Neq531 exhibits an N_{in} - C_{out} topology in contrast to the expected N_{out} - C_{in} topology predicted for Neq198. The total probability that the N-terminus is located on the cytoplasmic side of the membrane (N_{in} - C_{out}) was calculated to only 0.19357 for Neq531. This value stands in contrast to the plot of posterior probabilities of inside/outside/TM helix (Figure 28B) highlighting that predictions require careful interpretation. Servers such as TOPCONS, OCTOPUS and TMPred (II.6.2) predicted an N_{out} - C_{in} topology for Neq531 as well. Therefore, the reverse incorporation of Neq531 in the membrane, i.e. N_{in} - C_{out} orientation, can be disregarded. According to the pairwise alignment with Clustal O (1.2.4) (Goujon *et al.*, 2010; Sievers *et al.*, 2011), Neq198 and Neq531 share a sequence identity of 28.73 % and 23.30 %, respectively, to the homologous *EcMscS*. The highest sequence identity is found in the pore-lining helices TM3 (Figure 29). Moreover, both channels share a sequence identity of 30.43 %. Additional sequence alignments (VII.4) and further protein characteristics with respect to e.g. amino acid composition (VII.1) are shown in the appendix.

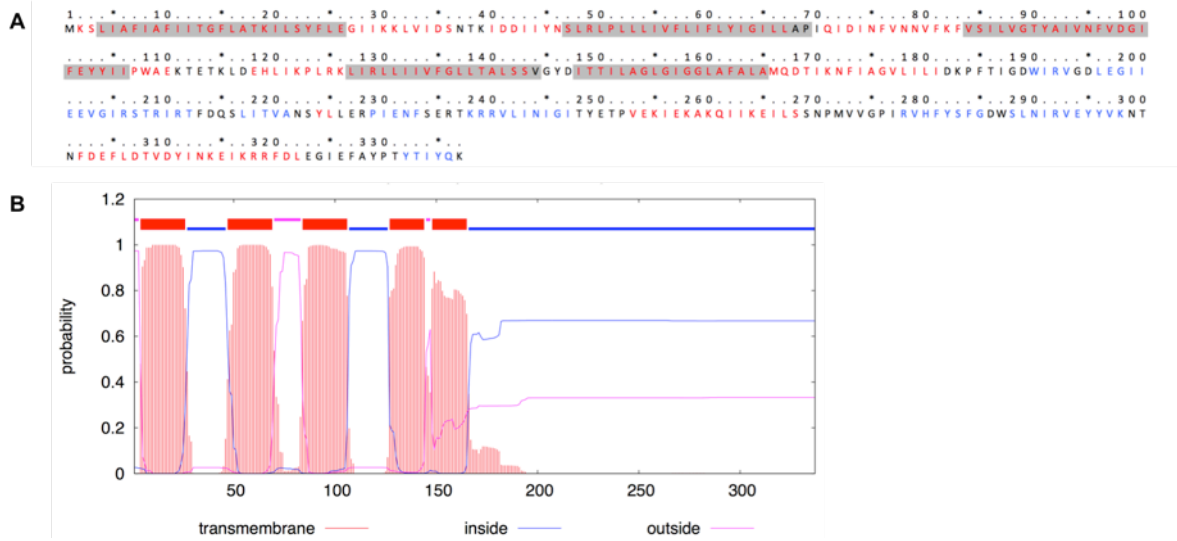


Figure 27: Prediction of TM helices of Neq198.

(A) Protein sequence of Neq198, with highlighted structural features; secondary structure depiction: LOOP, HELIX, STRAND predicted with PSIPRED v3.3 (Jones, 1999; Buchan *et al.*, 2013); TM helices highlighted in grey, predicted with TMHMM2.0 (Krogh *et al.*, 2001); (B) plot of posterior probabilities of inside/outside/TM helix, created with TMHMM2.0.

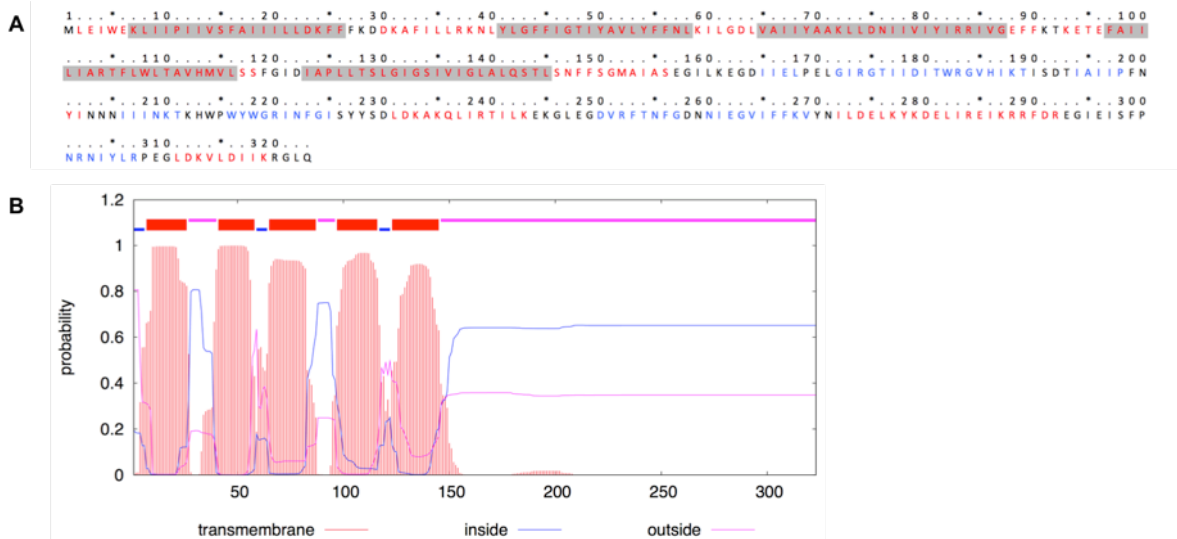


Figure 28: Prediction of TM helices of Neq531.

(A) Protein sequence of Neq531, with highlighted structural features; secondary structure depiction: LOOP, HELIX, STRAND predicted with PSIPRED v3.3 (Jones, 1999; Buchan *et al.*, 2013); TM helices highlighted in grey, predicted with TMHMM2.0 (Krogh *et al.*, 2001); (B) plot of posterior probabilities of inside/outside/TM helix, created with TMHMM2.0.

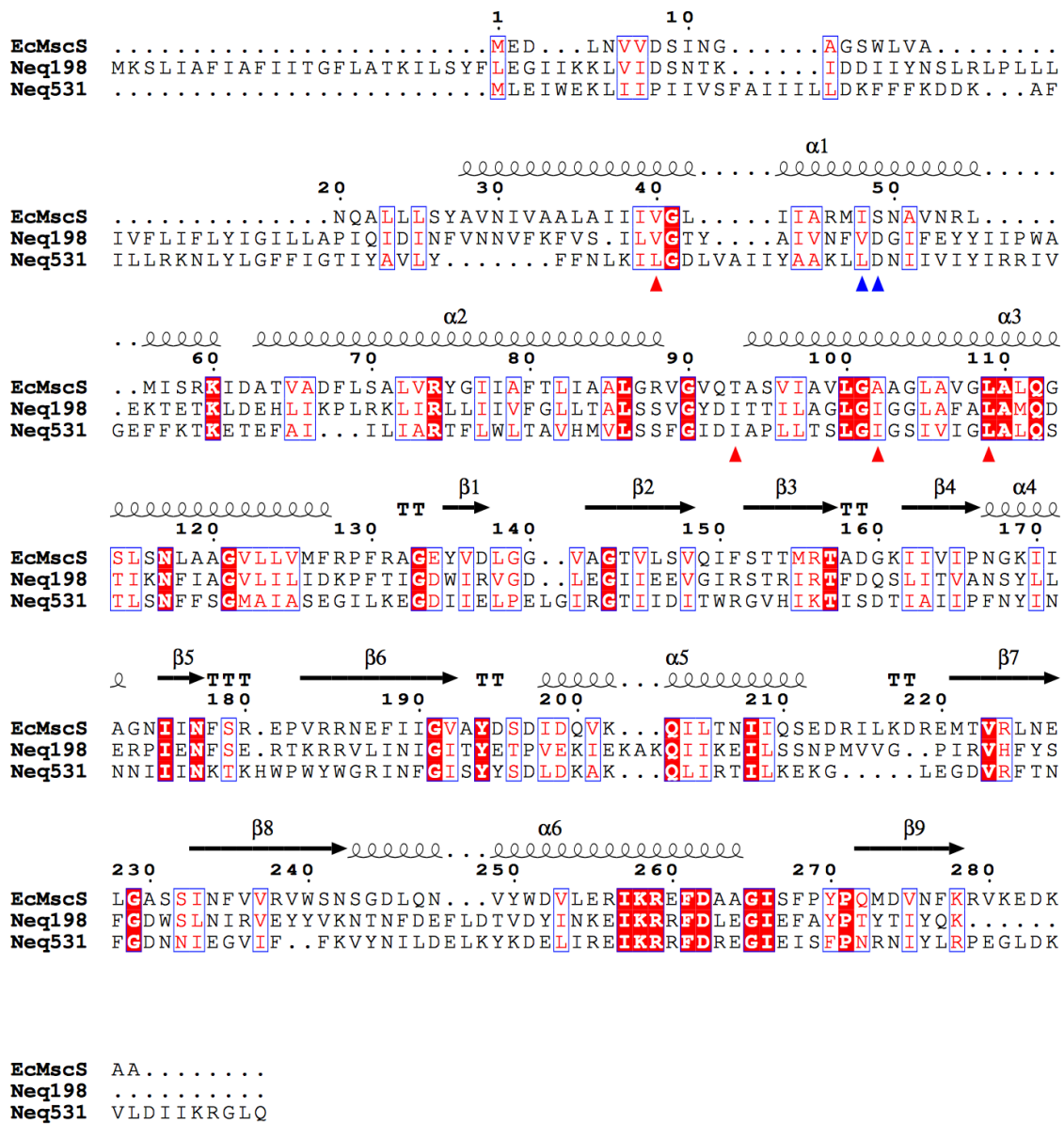


Figure 29: Sequence alignment of *EcMscS*, *Neq198* and *Neq531*.

Sequence alignment performed with Clustal O (1.2.4); secondary structure elements displayed above sequence blocks refer to *EcMscS* (2oau.pdb); a column is framed in blue if more than 70 % of its residues are similar according to physicochemical properties, identical residues are marked red; residues that have been identified to result in GOF (\blacktriangle) or LOF (\blacktriangleleft) (Miller *et al.*, 2003) are marked.

2.2 Single particle analysis

For structural analysis by single particle analysis different view orientations are required to construct a 3D model of the target protein. For the identification of the channel's envelope seen in different orientations, the protein surface of the *E. coli* MscS (2oau.pdb) is shown in tilted views from side to top and bottom view (Figure 30). Distinct structural features from different view angles helped to further analyze the individual data sets.

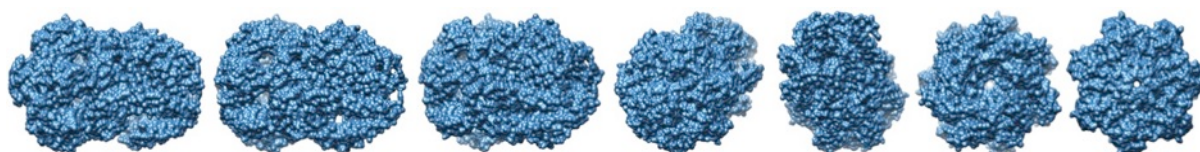


Figure 30: Protein surface of *EcMscS* in different orientations.

2oau.pdb, *EcMscS* shown in different orientations, side views, tilted views and top and bottom view, generated with Chimera 1.12 (Pettersen *et al.*, 2004).

2.3 Negative stain single particle analysis

2.3.1 Neq198 reconstituted into amphipol A8-35

In amphipol reconstituted Neq198 was negative-stained and the micrographs were recorded on a JEOL F2100 transmission electron microscope equipped with a 4k x 4k F416 camera with CMOS chip/detector, TVIPS.

The CTF was estimated using CTFFIND3 (Mindell and Grigorieff, 2003). Micrographs, for which the CTF estimation showed astigmatism or the thin rings of the model did not converge, were deleted from the data set. For Neq198 in total 38,237 particles were picked from 153 images using the autopicking option of RELION-1.4 (Scheres, 2012b). For the autopicking procedure a picking threshold of 0.3 and a minimum inter-particle distance of 210 Å were chosen. Here, a picking threshold of 0 results in large numbers of selected particles, whereas a picking threshold of 1 leads to the selection of only few particles. Before starting with 2D classification, the autopicked and extracted particles were visually controlled and the number was reduced to 32,374 particles. About 85 % of all autopicked particles served as input for 2D classification. Following the RELION-2.1 workflow (Scheres, 2012b) the data set was successively cleaned from corrupted particles during 2D classification. The cleaning results in a data set predominantly consisting of side views in 2D class-averages (Figure 31). Only few of them represent putative top views or slightly tilted views. The

“mushroom-like” head of the particles corresponds to the membrane domain of the channel, while the “mushroom-like” foot represents the cytoplasmic domain. Within the cytoplasmic domain, dark black areas are identified, indicating compartments where uranyl acetate penetrates the protein. This observation, as expected for the cytoplasmic domain, is consistent with the presence of a hollow compartment of the channel (cf. Figure 32).

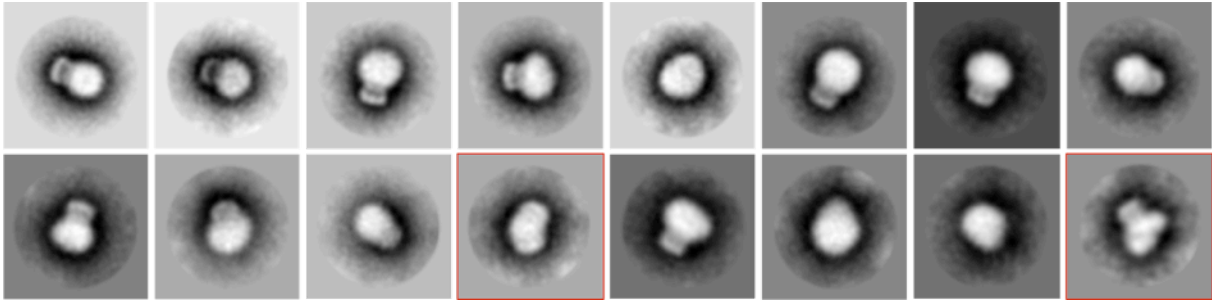


Figure 31: Representative 2D class-averages in negative stain of Neq198 reconstituted into APol.

Negative stain micrographs with a pixel size of 2.1 Å, particle mask diameter 300 Å, 2D class-averages ordered from higher to lower classes, showing different orientations of particles, predominantly side views, red marked boxes: channels of questionable quality.

The membrane part appears blurry due to the non-ordered and varying number of bound amphipol molecules. 2D class-averages of negative-stained particles already visualized the approximate organization of the channel’s membrane and cytoplasmic domain. Particles of minor quality are identified by their irregular shape and are excluded from further processing (Figure 31, red boxes). In total 18,900 particles, i.e. only about 49 % of all autopicked particles, served as input for 3D classification and were further processed (Figure 33). An initial model was generated *de novo* from the data set using the Stochastic Gradient Descent (SGD) algorithm on a subset of 3,200 particles with applied C7 symmetry. The best 2D class-averages, which represented different views of the particles, served as input for the initial model. Subsequently, the initial reference map was low-pass filtered to 40 Å to avoid bias. Here, the generation of a reliable initial model strongly relied on the chosen 2D class-averages, the total number of particles, and the particle mask diameter. For 3D classification, C1 symmetry was applied on the data set. It was found useful to start the classification with a higher degree in angular sampling for 10-25 iterations (15 degree angular sampling) followed by successively decreasing it (7.5-3.7 degree angular sampling). Various conditions for processing in 3D have been tested. The tests included for example different numbers of classes in each run or varying the combinations of 3D class-averages selected for the next run. Two consecutive 3D classifications with six classes each led to the best achieved result. For each run the best classes were selected after

evaluating each 3D volume in Chimera, arriving at 9,724 particles for refinement (Figure 33C). Moreover, those particles were classified in two classes in 3D again and subjected to 3D refinement (Figure 33A and B). In 3D refinement the C7 symmetry was applied that resulted in a final resolution (without masking) of 26.25 Å for 3D volume A and 24.71 Å for 3D volume B and C.

Taken together, an increasing number of particles does not necessarily implicate an increase in resolution. This data set is limited to a resolution of 24.71 Å, which represents a decent resolution of such a small particle in negative stain. The final 3D volumes do not show high level of details. Fitting the model from *EcMscS* into a final volume confirms the assumed domain organization (Figure 32). Only one orientation provides enough space for two additional TM helices and bound amphipol molecules. Moreover, the domain organization is supported by the putative cytoplasmic cavity that is also observed (Figure 32).

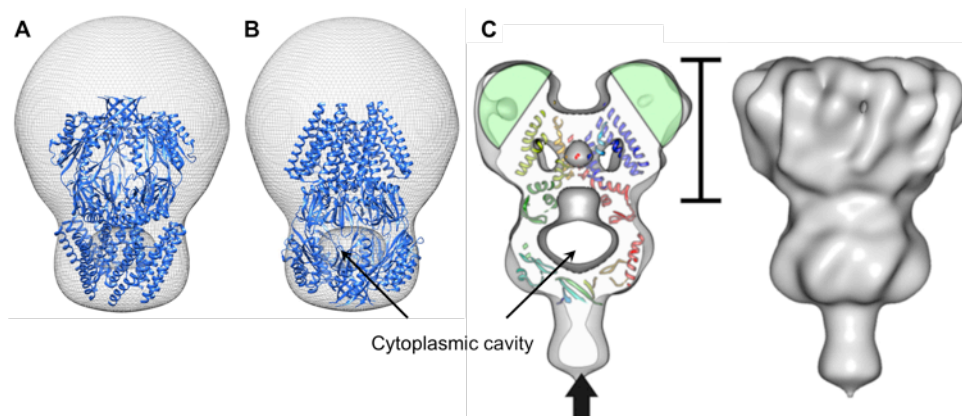


Figure 32: Putative domain organization of Neq198.

Fitting of the model from *EcMscS* (2oau.pdb) into the final 3D refinement volume A, surface representation as mesh. Two different possible orientations are displayed: (A) incorrect orientation, (B) correct orientation, (C) comparison to YnaI from *E. coli*, surface representations, slice along the central long axis of the side view with fitted *EcMscS* (2oau.pdb) (left), side view (right), green areas highlight the likely position of the detergent micelle, scale bar represents 7.5 nm and highlights the length of the membrane part of YnaI, arrow indicates the major contact site in aggregates (modified from Böttcher *et al.*, 2015).

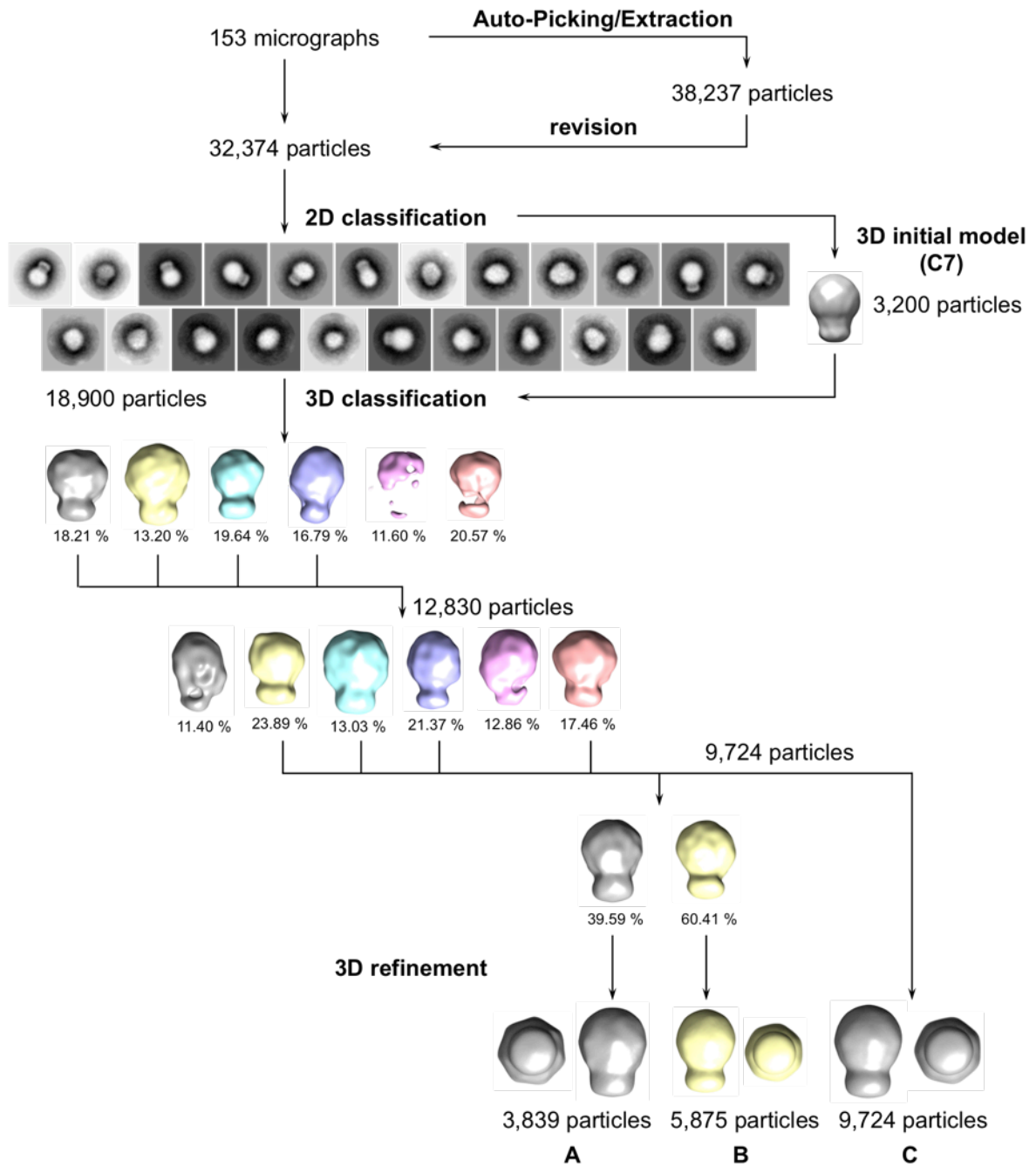


Figure 33: RELION-2.1 workflow overview of Neq198 reconstituted into APol in negative stain.

During 3D classification C1 symmetry, for refinement C7 symmetry was applied. 3D negative stain volumes were visualized with Chimera 1.12 (Pettersen *et al.*, 2004); final 3D refinements are represented as side and bottom views; final resolution (without masking): A - 26.25 Å; B - 24.71 Å; C - 24.71 Å.

2.3.2 Neq531 reconstituted into amphipol A8-35

In amphipol reconstituted Neq531 was negative-stained and the micrographs were recorded on a JEOL F2100 transmission electron microscope equipped with a 4k x 4k F416 camera with CMOS chip/detector, TVIPS.

From 60 micrographs 27,453 particles were manually picked, extracted, successively cleaned during 2D classification, and further processed in 3D following the RELION-2.1 workflow (Scheres, 2012b). Compared to other negative stain data sets, the Neq531 protein sample displays a much higher level of heterogeneity. This is either caused by the channel's significantly lower stability as it was already observed during purification (III.1), thus the data may represent channels in various oligomeric states or aggregates, or an excess of amphipol molecules might be mistaken for channel particles. A relative high amount of aggregates is observed. Yet, during 2D classification good class-averages are easily identified. Most 2D class-averages represent side views of the channel (Figure 34). Moreover, aggregates or channels of different oligomeric state are isolated by 2D classification (Figure 34, red boxes) and subsequently excluded from further processing. The cytoplasmic domain and the membrane part of the channels are differentiated analogous to Neq198, as "mushroom-like" foot and head. Additionally, dark areas that correlate with the negative stain entered into cavities confirm the cytoplasmic vestibule. In several 2D class-averages a structural feature at the bottom of the cytoplasmic domain is observed (Figure 34, red arrows). This feature may represent the cytoplasmic β -barrel that is also found for *EcMscS* (Figure 30). Moreover, an additional helix downstream of the β -strand is predicted for Neq531 (Figure 28A) explaining why this structural feature is more pronounced and is not observed for Neq198. The membrane domain of the channel appears blurry, which is in line with results obtained from the Neq198-APol data.

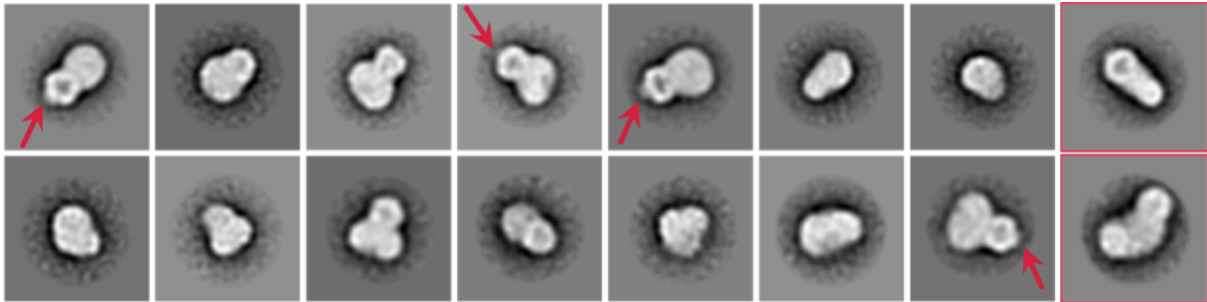


Figure 34: Representative 2D class-averages of Neq531 reconstituted into APol.

Negative stain micrographs with a pixel size of 3.7 Å, particle mask diameter 240 Å, 2D class-averages ordered from higher to lower classes, showing different orientations of particles, predominantly side views, red arrows: β -barrel of cytoplasmic domain; red marked boxes: channels of questionable quality or aggregates.

Only ~32.5 % of all picked particles served as input for 3D classification (Figure 35). Again, an initial model was generated *de novo* from the data set on a subset of 3,296 particles with applied C7 symmetry. The initial model was subsequently low-pass filtered to 40 Å. The reliability of the initial model was dependent on the selected 2D class-averages, the total number of particles, and especially the particle mask diameter also in this case. A mask diameter of 240 Å was used to avoid a too small mask.

The Neq531-APol data was processed similar to the Neq198-APol data. For 3D classification C1 symmetry was applied and the number of particles was further reduced by one run of 3D classification with four classes followed by a second run with only two classes. For the second 3D classification the best classes that also exhibited the structural feature at the bottom of the cytoplasmic domain (β -barrel) were selected after evaluating the densities in Chimera, arriving at 7,155 particles. These particles were processed in two classes, serving as input for 3D refinement. In 3D refinement the C7 symmetry was applied that resulted in a final resolution (without masking) of 21.53 Å for density C and D (Figure 35). In a second approach, only one 3D classification with two classes was performed. Each class served as input for 3D refinement and resulted in a final resolution (without masking) of 22.55 Å for volume A and 21.53 Å for volume B (Figure 35). This data is limited to a resolution of 21.53 Å highlighting that the resolution limit in negative stain of 20 Å (Ohi *et al.*, 2004; Cheng *et al.*, 2015) is already achieved with only few particles.

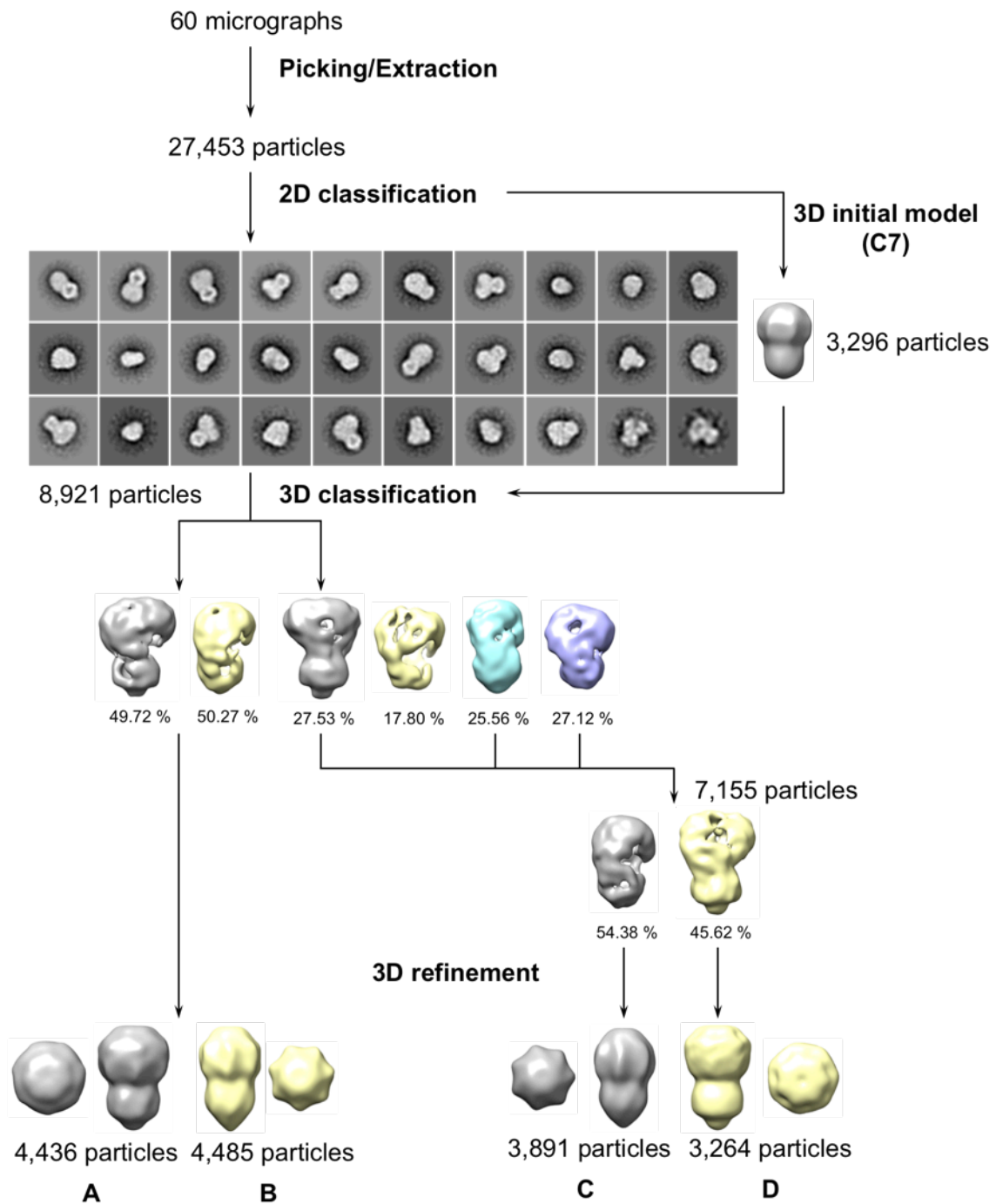


Figure 35: RELION-2.1 workflow overview of Neq531 reconstituted into APol in negative stain.

During 3D classification C1 symmetry, for refinement C7 symmetry was applied. 3D negative stain volumes were visualized with Chimera 1.12 (Pettersen *et al.*, 2004); final 3D refinements are represented as side and top views; final resolution (without masking): A - 22.55 Å; B, C and D - 21.53 Å.

The membrane part and therefore the amphipol bound part as well as the cytoplasmic domain are easily identified. The 3D volumes A and B suggest the location of single helices in the membrane domain as well as in the cytoplasmic domain. Moreover, distinctive structural extensions at the bottom of the cytoplasmic domain indicate the presence of the β -barrel. However, the β -barrel is better resolved in density A and D (Figure 35). Furthermore, the question arises whether two different conformations of the channel are isolated since the volumes A/D or B/C (Figure 35) differ significantly with respect to their overall dimensions and the shape of the β -barrel (Figure 36A). The 3D volumes reveal cavities in the transmembrane as well as in the cytoplasmic domain (Figure 36).

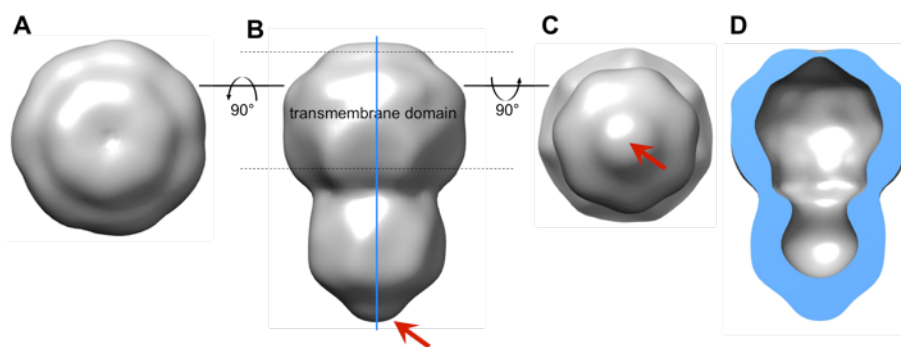


Figure 36: Surface representation of Neq531 reconstituted into APol.

3D refinement of volume A visualized in different orientations, surface representation: (A) top view, (B) side view, (C) bottom view, (D) slice along the central long axis through the side view, capped surface is visualized in blue; red arrow indicates the distinctive β -barrel at the C-terminal cytoplasmic domain; the transmembrane region is enclosed by dashed lines; volumes were visualized in Chimera 1.12 (Pettersen *et al.*, 2004).

The comparison of the Neq198-APol data set with the Neq531-APol data set, reveals an intriguing detail, at the position of the putative β -barrel, already observed in 2D classification: assuming that it represents a structural feature, it is much more pronounced in Neq531 than in Neq198. The heterogeneity of the protein sample as already noticed during purification is also observed in single particle analysis. However, the degree of heterogeneity can be handled and controlled in 2D classification and further processing.

2.3.3 Neq198 reconstituted into nanodiscs

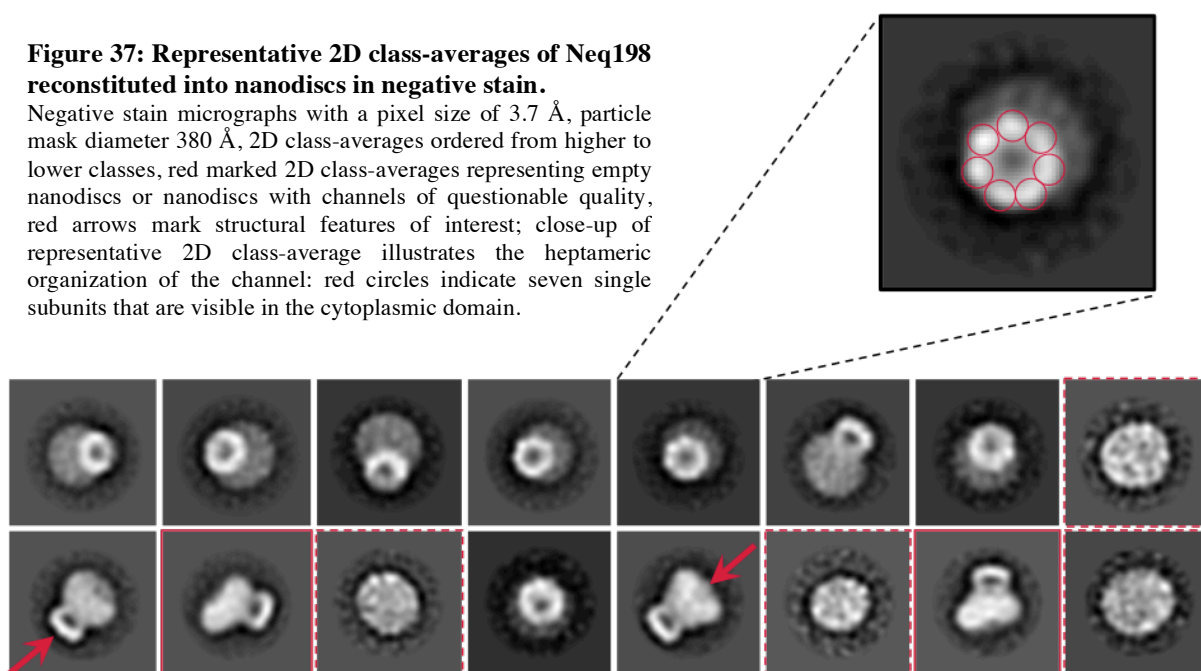
Neq198 reconstituted into nanodiscs was negative-stained and the micrographs were recorded on a JEOL F2100 transmission electron microscope equipped with a 4k x 4k F416 camera with CMOS chip/detector, TVIPS.

In total 8,923 particles were manually picked from 37 micrographs, extracted, successively cleaned during 2D classification, and further processed in 3D following the RELION-2.1 workflow (Scheres,

2012b). Particles of different orientations are classified in 2D. The 2D class-averages represent predominantly tilted views and only few side views. A distinct top or bottom view is difficult to identify (Figure 37). Again, the “mushroom-like” head of the particles corresponds to the membrane domain of the channel, while the “mushroom-like” foot represents the cytoplasmic domain. Moreover, dark areas containing the negative stain identify a hollow part of the channel similar to the previously described results.

Figure 37: Representative 2D class-averages of Neq198 reconstituted into nanodiscs in negative stain.

Negative stain micrographs with a pixel size of 3.7 Å, particle mask diameter 380 Å, 2D class-averages ordered from higher to lower classes, red marked 2D class-averages representing empty nanodiscs or nanodiscs with channels of questionable quality, red arrows mark structural features of interest; close-up of representative 2D class-average illustrates the heptameric organization of the channel: red circles indicate seven single subunits that are visible in the cytoplasmic domain.



In contrast to the amphipol samples, the cytoplasmic domain already provides relatively detailed information; even single subunits in the cytoplasmic domain are identified (Figure 37, close-up). However, the membrane part enclosed by the nanodiscs appears comparatively blurry.

Approximately 10 % of the manually picked particles are represented by empty nanodiscs or nanodiscs with incorporated channels that exhibited top or bottom views (Figure 37, red dashed boxes). Since these two categories are not distinguishable, those classes are handled as empty nanodiscs. Another roughly 10 % is identified as nanodiscs with incorporated channels of minor quality either not properly folded or missing one or more promoters (Figure 37, red boxes). Here, the membrane part looks irregular compared to other 2D class-averages. Those particles are excluded from further processing.

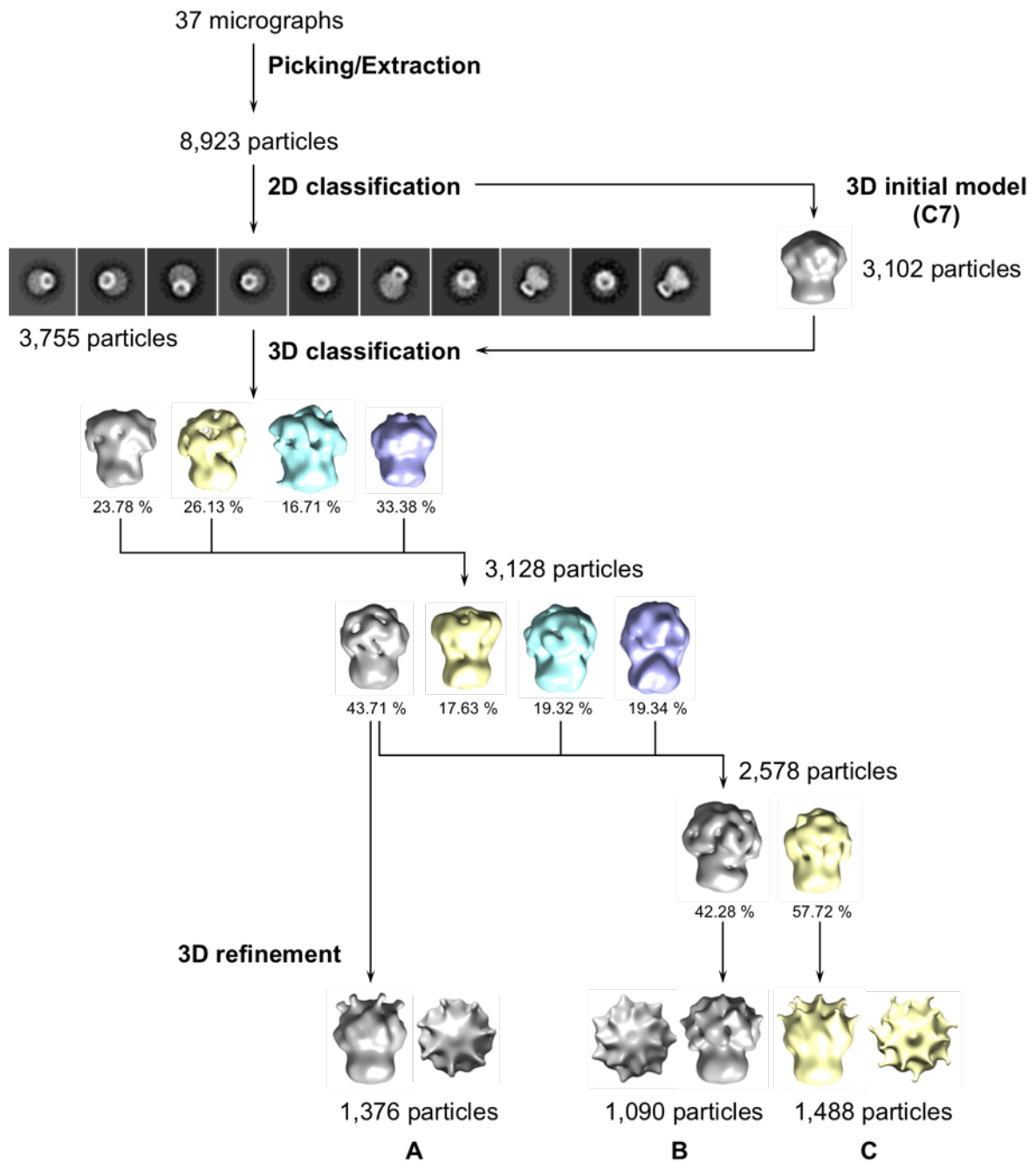


Figure 38: RELION-2.1 workflow overview of Neq198 reconstituted into nanodiscs in negative stain.

During 3D classification C1 symmetry, for refinement C7 symmetry was applied. 3D negative stain volumes were visualized with Chimera 1.12 (Pettersen *et al.*, 2004); final 3D refinements are represented as side and top views; final resolution (without masking): A + B - 23.68 Å; C - 24.93 Å.

In total, about 42 % of all particles, representing the best 2D class-averages, were used for 3D classification and further processing (Figure 38). The particles were classified twice with four classes in 3D, which was followed by another 3D classification with only two classes. The final refined 3D volumes originate only from approximately 12-17 % of the total number of particles. Compared to both amphipol data sets (III2.3.1 and III2.3.2), the nanodiscs data provides structural features of the membrane domain. The increase of the nanodisc size appears to be beneficial.

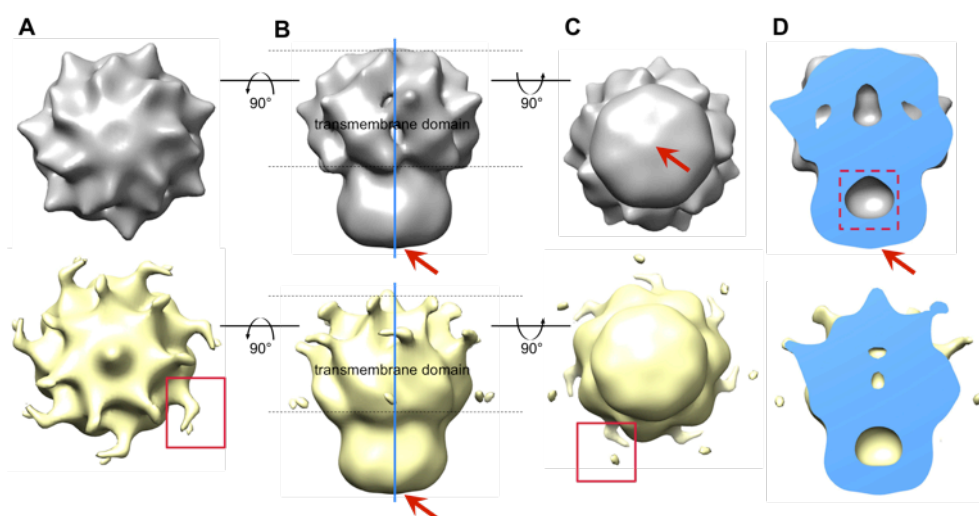


Figure 39: Surface representation of Neq198 reconstituted into nanodiscs.

3D refinement volume B (grey) and C (yellow) shown in different orientations, surface representation: (A) top view, (B) side view and (C) bottom view, (D) perpendicular cross-section through reconstructed 3D density; red boxes indicate representative densities that possibly originated from the nanodisc; dashed box identifies the cytoplasmic domain cavity, arrows indicate the β -barrel; the transmembrane region is enclosed by dashed lines; volumes were visualized in Chimera 1.12 (Pettersen *et al.*, 2004).

The refined 3D volume B and C with only approximately 1,000 particles and 1,400 particles respectively, provide basic insights into the transmembrane domain (Figure 39). Here, the volumes likely indicate the approximate arrangement and localization of single transmembrane helices. The refined 3D volume C (Figure 39, yellow) shows structural extensions in the transmembrane domain (Figure 39, red boxes), which may be also attributed to the nanodiscs themselves. The expected cavity of the cytoplasmic domain is visualized. However, for the β -barrel only a broad and featureless density appears at the bottom of the cytoplasmic domain (Figure 39, red arrows). This stands in contrast to the well-defined C-terminal structural element seen for the Neq531-APol data (Figure 36, III2.3.2). With final resolutions of ~ 23 - 25 Å (without masking), the resolution limit is almost achieved, although with only very few particles ($\sim 1,000$ - $1,500$) contributing to the final 3D volumes.

2.4 Single particle analysis of a cryo-EM data set

In nanodiscs reconstituted Neq198 was plunge-frozen in liquid ethane using a Leica EM Grid Plunger. Cryo-EM micrographs were recorded on a FEI Tecnai F30 Polara transmission electron microscope operated at 300 kV and equipped with a Gatan K2 summit direct electron detector.

A number of data sets were collected differing in grid preparation with respect to protein concentration and blotting time. For the two main data sets, grids were blotted for 1.2 s, 1.5 s, 1.7 s, 1.9 s, and 2.2 s as well as for 2.5 s, 3.0 s, 3.5 s, 4.0 s, and 4.5 s. By this, a reasonable screening was possible. The experimental set-up of these data sets (“Feb2017” and “Jun2017”) is stated in the appendix (VI2). Electron beam-induced sample motion in cryo-EM images was corrected with MotionCor2 (Zheng *et al.*, 2017). If sample motion was not satisfactorily corrected, micrographs were excluded from the data set. The CTF was estimated using CTFFIND3 (Mindell and Grigorieff, 2003) or CTFFIND4 (Rohou and Grigorieff, 2015). Micrographs, for which the CTF estimation showed astigmatism or the thin rings of the model did not converge, were removed from the data set. Moreover, micrographs that were contaminated with crystalline or hexagonal ice were also excluded.

In the first large data set (data set “Feb2017”), micrographs were recorded from grids that have been blotted for 1.2s, 1.5s, 1.7s, 1.9s, and 2.2s. The micrographs exhibit low contrast and the particles are hardly identified (low signal to noise ratio, SNR) (Figure 40A and B). To obtain micrographs with higher contrast (high SNR) and to increase the number of side views, micrographs were recorded from grids that have been blotted for 3.5 s or 4.0 s in a second data set (data set “Jun2017”). Moreover, the total electron dose was increased to $70 \text{ e}^-/\text{\AA}^2$ over 50 frames. Compared to the first large data set, here the signal-noise contrast is higher and particles can easily be identified (Figure 40C and D).

For the data set “Feb2017” 122,464 particles were picked from 229 micrographs using the autopicking option in RELION-1.4 (Scheres, 2012b). The picking threshold was set to 0.3 (0 = pick everything to 1 = pick very few particles) and the minimum inter-particle distance was optimized to 120 Å. After control and revision of all autopicked particles, only 96,521 particles were finally extracted. The particle number was further reduced to 73,286 and served as input for 2D classification. In 2D classification the particles collapse into only few classes and do not exploit the total given number of classes (Figure 41A). Collapsed classes are featureless and occur continuously upon processing although the number of particles was constantly decreasing. The collapsed classes contain all variations of particles that are not properly aligned (Figure 41A and B).

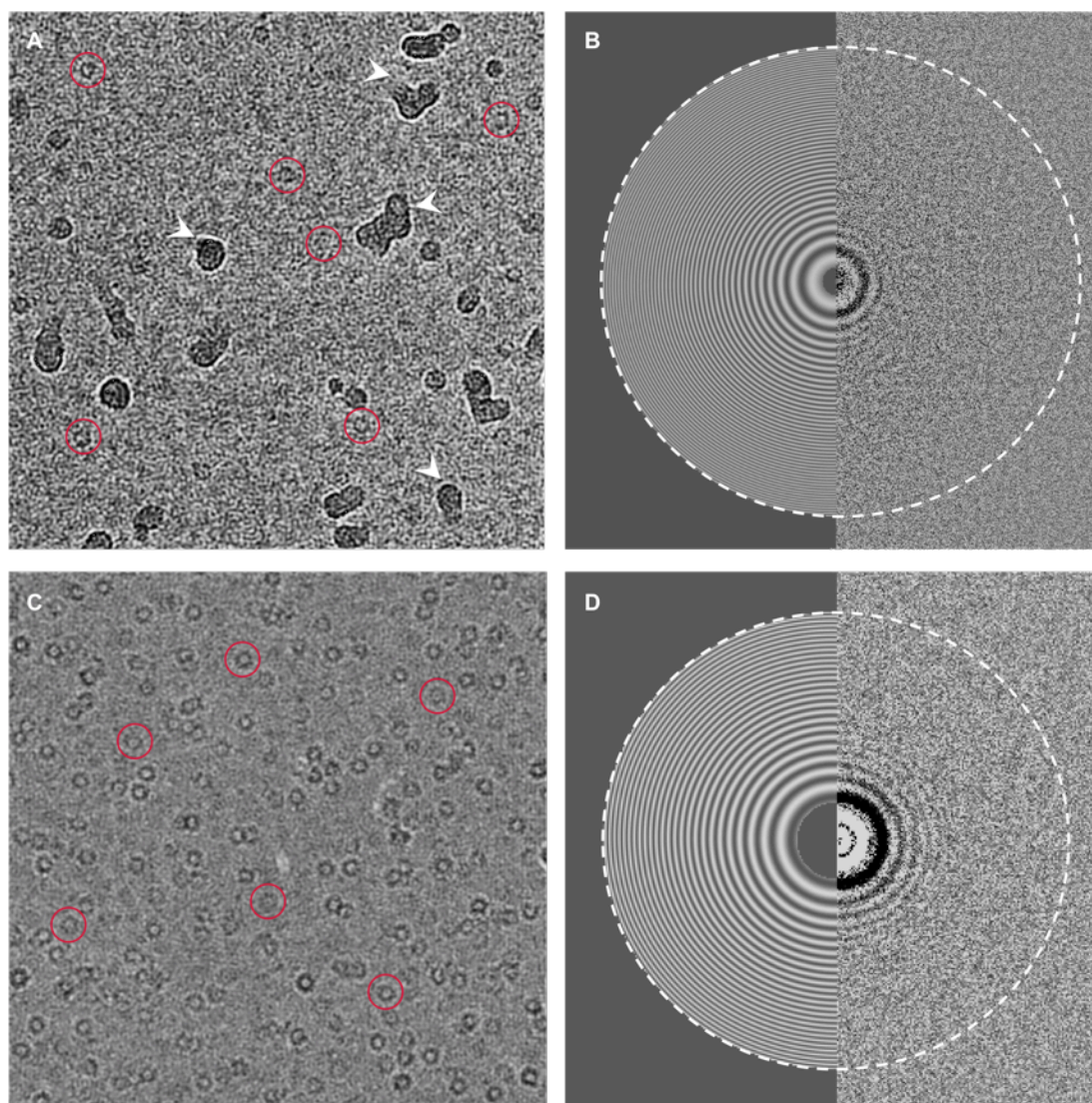


Figure 40: Cryo-EM micrographs of Neq198 reconstituted into nanodiscs.

Data were recorded on a FEI Tecnai F30 Polara (300 kV), K2 summit, 31,000x, 1.273 Å/px; (A) representative micrograph section from data set “Feb2017”: blotting time 1.2 s, 40 frames with a total electron dose of 33.59 $e/\text{Å}^2$; (B) motion-corrected sums (MotionCor2, Zheng *et al.*, 2017) with dose-weighting were used for CTF correction using CTFFIND3 (Mindell and Grigorieff, 2003), CTF estimation 2D power spectrum of (A); (C) representative micrograph section from data set “Jun2017”: blotting time 4 s, 50 frames with a total electron dose of 70.89 $e/\text{Å}^2$; (D) motion-corrected sums (MotionCor2, Zheng *et al.*, 2017) with dose-weighting were used for CTF correction using CTFFIND3 (Mindell and Grigorieff, 2003), CTF estimation 2D power spectrum of (C); white triangles mark putative ice and ethane contaminations; red circles highlight single particles in each micrograph.

By successive 2D classifications, other 2D class-averages with potential top views are identified (Figure 41B). Those 2D class-averages already provide first insights in secondary structure features. Though, no acceptable side views are detected. Besides collapsed classes, several classes that

represent potential top views of the channel show stalks, a well-known phenomenon arising from overfitting.

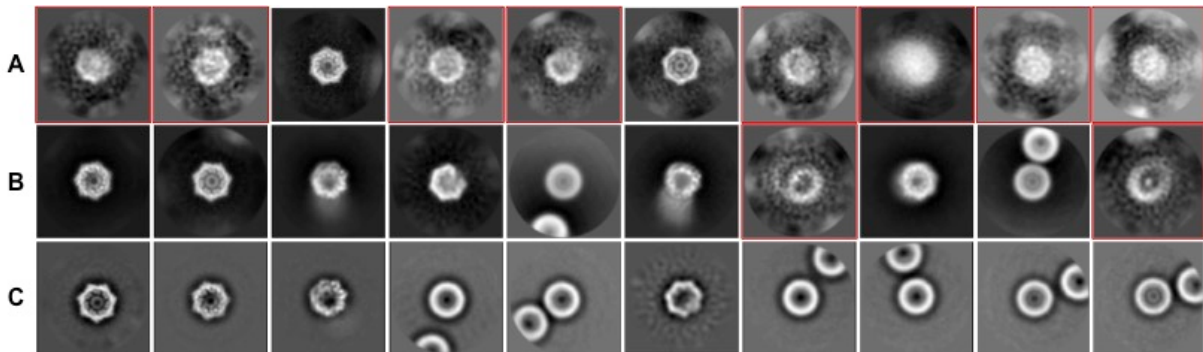


Figure 41: Comparison of different data sets during 2D classification in RELION-2.1.

Representative 2D class-averages of the first 2D classification run of different data sets, showing the first ten classes, ordered from larger (containing more particles) to smaller (containing less particles) classes, particle mask diameter 240 Å, classes that collapsed are boxed in red; **(A)** data set „Feb2017“, input: 73,286 particles, 200 classes, 12 degree angular sampling, 25 iterations, almost all classes are collapsed; **(B)** data set „Jun2017“, input: 169,657 particles, 200 classes, 12 degree angular sampling, 25 iterations, only few classes are collapsed, potential side views can be identified (class 3, 6, 8); **(C)** data set „Jun2017“, input: 169,657 particles, 200 classes, 12 degree angular sampling, 25 iterations, ignoring CTF until first peak (CTF tab), using subsets for initial updates (optimization tab), no classes collapsed, classes with neighboring particles dominated the first 10 classes.

These observations lead to the conclusion that the channel does not adopt random orientation but preferred orientation to top views, which is directly influenced by the thickness of the vitreous ice. In order to reduce the ice thickness, the grids were blotted longer to generate the second main data set. For the data set “Jun2017” 169,657 particles were manually picked from 524 micrographs, extracted and further processed in RELION-2.1 (Scheres, 2012b). Since the grids are contaminated with ice and probably ethane (Figure 40, cf. Thompson *et al.*, 2016), auto-picking did not succeed. Based on the experience gained by processing the first data set, particles were manually picked. 2D class collapses was less severe (Figure 41B). Numerous classes are identified that already show a high degree of details and potential side and top views in different orientations.

By variation of different parameters that are provided during the RELION-2.1 workflow, the output of 2D and 3D classification was optimized. 2D classification is significantly improved when the CTF is ignored until the first peak (CTF tab) and subsets are used (optimization tab). To prevent overfitting, the option “Limit resolution E-step” is set to 12 Å, optionally. The particle mask diameter is adjusted to 240 Å. During 2D classification the 169,657 manually picked particles were reduced to 42,758 particles. Finally, only ~25 % of the originally picked particles served as input for 3D classification. The particles were successfully cleaned from “defective” particles: neighboring particles that

interfered with alignment, empty nanodiscs, and putative top views that exhibited lower oligomers were excluded (Figure 42).

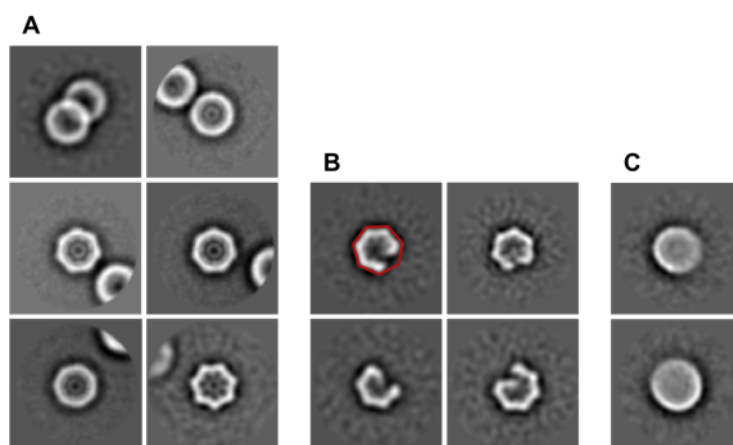


Figure 42: Representative 2D class-averages showing “defective” particles.

2D class-averages show different types of particles that were subsequently excluded from the data set: **(A)** particles with neighboring particles, **(B)** particles of different oligomeric state of the channel, red heptagon indicates the heptameric fold of Neq198 **(C)** potential empty nanodiscs.

An initial *de novo* model was generated from the data set with 2,772 particles of the best 2D class-averages of side and tilted views of the particles. For the generation of the initial model, C7 symmetry was applied, because the C1 model did not provide satisfying feature degree. To prevent that the data was biased the initial model was always low pass filtered to 60 Å. For the following 3D classifications no symmetry operators were used, whereas for 3D refinements the C7 symmetry was applied. 2D class-averages that served as input for 3D classification comprise to high proportions of the putative top views (Figure 43). These putative top views provide already detailed secondary structure elements. Tilted and side views show details, which allow the membrane domain of the channel and the cytoplasmic domain to be clearly identified. The membrane domain appears blurry. Moreover, some side view 2D class-averages contain particles that probably miss single subunits (last class, Figure 43). In contrast, the cytoplasmic domain provides more detail. The large cavity inside the cytoplasmic domain and the β -barrel are easily identified (Figure 43). In a first attempt 42,748 particles were subjected to a first 3D classification with 10 classes. After evaluation of each resulting 3D volume in Chimera, the best 3D classes (class 2, 3, 5, 9) were merged resulting in 11,305 particles. These particles were subjected to another 2D classification with 50 classes. This step helps to identify classes that induce poor 3D volumes. Particularly 2D class-averages of putative top views are excluded from

the data set in this first 3D classification (Figure 43, boxed 2D class-averages). Those top view 2D class-averages result in spherical 3D volumes suggesting that only parts of the channel are represented. The 3D classification reduced the initial 42,758 particles to 11,305 particles indicating that the putative top views contributed by ~74 % (Figure 43).

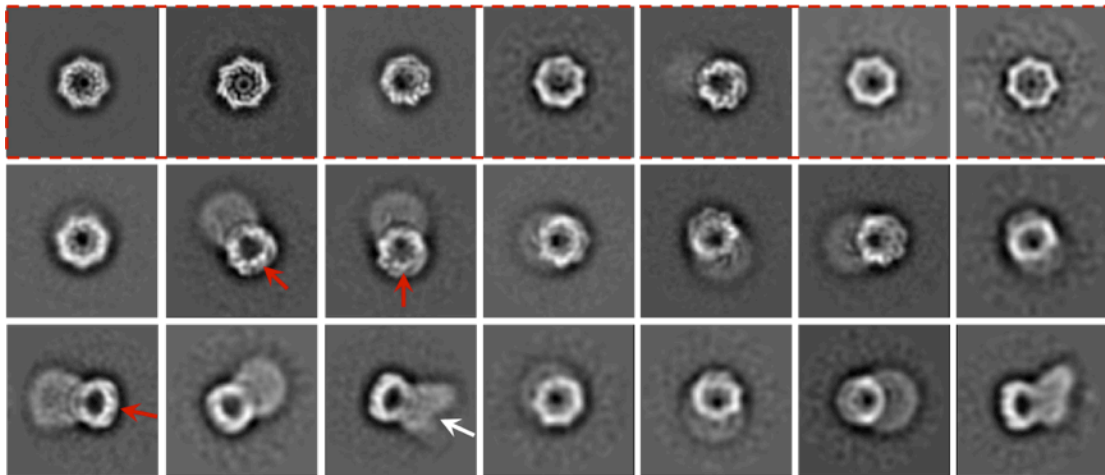


Figure 43: Representative 2D class-averages.

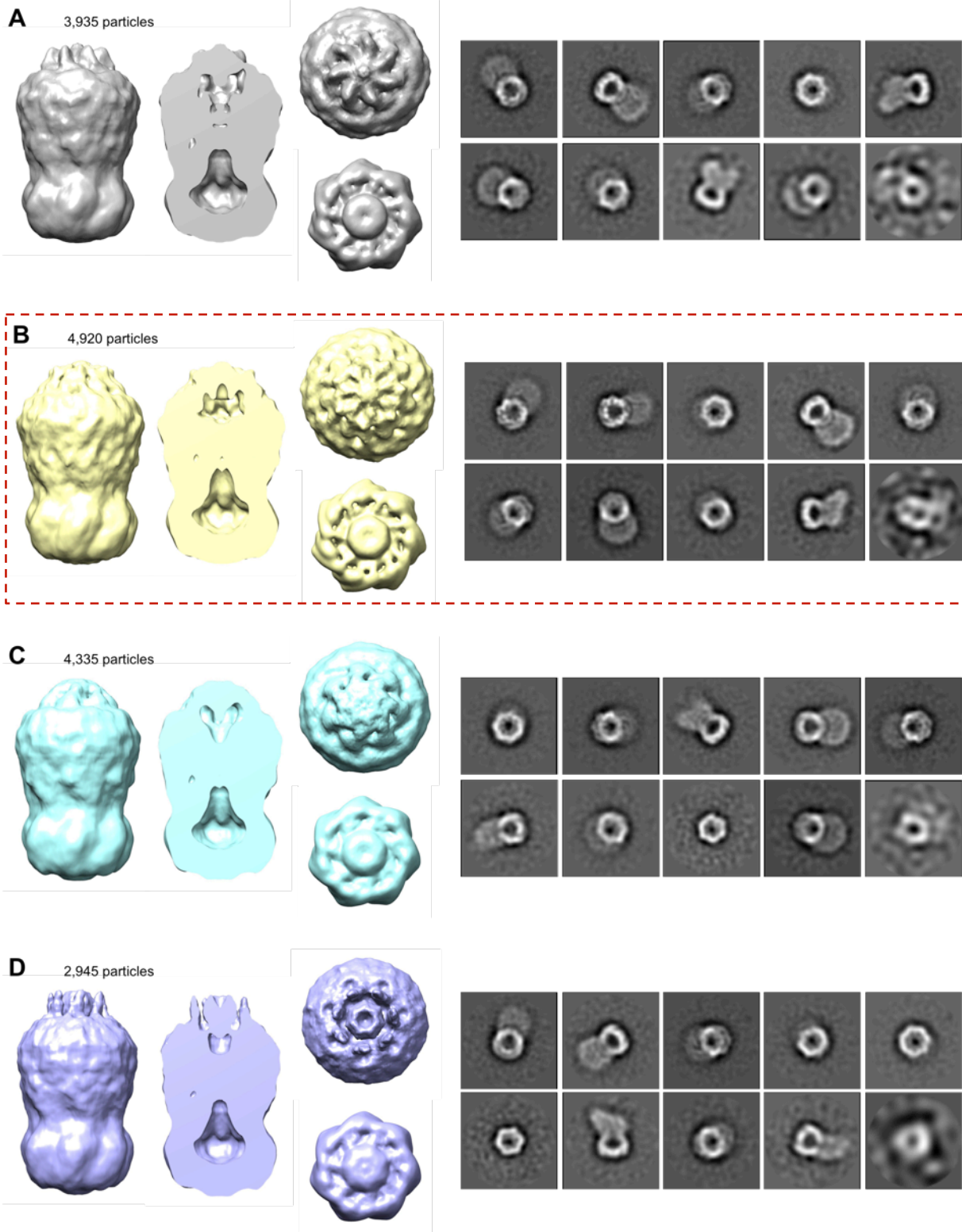
Representative 2D class-averages ordered from higher (containing more particles) to lower (containing less particles) classes that served as input for 3D classification; upper line shows classes of putative top views of the particles, lower lines show side views or tilted views of the particles; red arrows indicate the β -barrel of the cytoplasmic domain, white arrow indicates putative membrane pore in membrane domain; classes that do not contribute to the final cryo-EM density and are excluded from the data set during 3D classification are highlighted by a red dashed line.

Only the best 2D classes were selected from the following 2D classification resulting in 10,852 particles. Subsequently, the particles were classified in 6 classes in 3D. After evaluation of each 3D volume, the classes 1, 2, 3, 5 and 6 were merged resulting in 10,252 particles and subjected to another 2D classification with 25 classes. Again, the best 2D class-averages were selected for further processing. 9,767 particles served as input for a 3D refinement with a single class resulting in a reliable 3D volume. Processing was repeated in order to prevent anisotropy. 2D class-averages show that putative top views are highly over-represented in the data. Moreover, the cytoplasmic domain and the membrane domain in side or tilted views exhibit different SNR. The focus is set on the cytoplasmic domain. Therefore, it is beneficial if all classes contribute equally to the final volume. This minimizes the over-interpretation of the channel feature. Therefore, 2D class-averages were limited by setting an upper limit of contributing particles of each class. Here, the number of particles of the smallest class selected determines the maximum number of particles for each class. The refined

3D volume that was generated previously served as reference model and was low-pass filtered to 60 Å. The data were re-processed in different ways:

(A) 43 2D class-averages of the final 2D classification were selected for further processing. Those 2D class-averages were limited to 160 particles per class resulting in 6,880 particles, which served as input for the 3D classification with two classes. Both 3D classes were further processed in 3D refinement, but only 3D class 2 with 3,935 particles resulted in a reliable 3D volume (Figure 44A). **(B)** Only the best 2D class-averages of the final 2D classification were further processed. 36 2D class-averages were limited to 264 particles per class resulting in 9,375 particles. Processing these particles as a single class in 3D classification and refinement generated a corrupt 3D volume. Therefore, the particles were processed in 3D classification with two classes and each served as input for 3D refinement. Only 3D class 2 comprising 4,920 particles resulted in a reasonable 3D volume (Figure 44B). **(C)** The final 2D classification was followed by a 3D classification with 10 classes. After evaluating each 3D volume, the best 3D volumes were merged and subjected to another 2D classification with 50 classes (as mentioned before). Subsequently, 17 2D class-averages were selected and limited to 255 particles per class resulting in 4,335 particles. The 3D classification was repeated with these particles. The 3D classification and refinement with a single class resulted in a reliable 3D volume (Figure 44C). **(D)** Following a 3D classification with two classes (cf. C), only 3D class 1 with 2,945 particles resulted in a reliable 3D volume in refinement (Figure 44D). **(E)** The first 3D classification with 10 classes and subsequent 2D classification was followed by 3D classification with six classes and subsequent 2D classification with 25 classes (as mentioned before). 13 2D class-averages were selected and limited to 262 particles per class resulting in 3,406 particles. These particles were processed with a single class in 3D classification and refinement resulting in a reliable 3D volume. The 3D classification with two classes led to corrupted 3D volumes (Figure 44E). If the angular accuracy was less than 10 degree in 3D refinement, the particles were not aligned and resulted in corrupted 3D volumes. This was observed either when too few particles served as input for 3D refinement or when putative top views contributed a portion of input particles. After 3D refinement, particles that contributed to a refined 3D volume were re-classified in 2D. This step allowed for the final volumes to be additionally compared and evaluated. The 3D volumes basically look the same. The changes of the cytoplasmic domain are marginable for each volume but slight differences for the transmembrane domain are identified. Since the 3D volume B with 4,920 particles contains the highest number of particles and additionally the best 2D class-averages, this 3D volume is favored for further analysis.

III Results



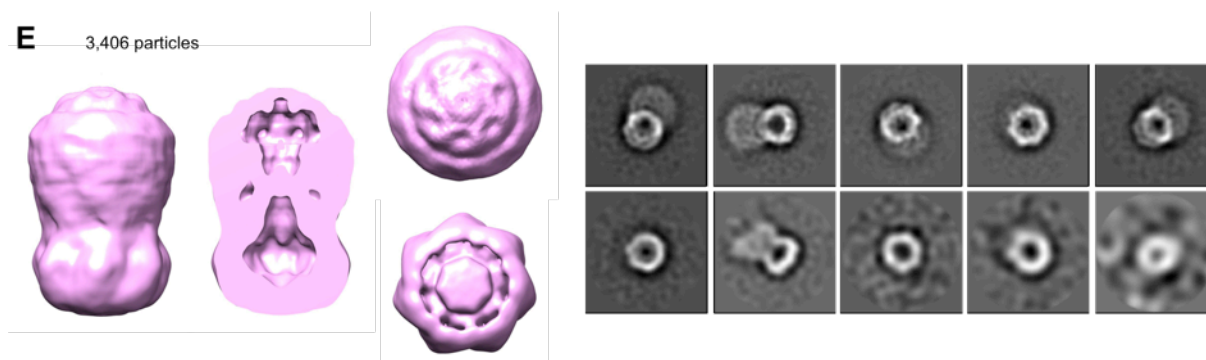


Figure 44: Representative final 3D volumes.

Comparison of final 3D volumes with respect to the number of particles and 2D class-averages that contributed to the final volume and the overall shape. 3D volumes were visualized with Chimera 1.12 (Pettersen *et al.*, 2004), showing side view (left), perpendicular cut through the side view (middle) and top (right top panel) and bottom (right lower panel) view. 2D class-averages are ordered from higher (containing more particles) to lower (containing less particles) classes.

In summary, the cryo-EM data set of Neq198 comprised several challenges, which had to be overcome during processing:

(1) Particle picking: The grids were contaminated with ice and/or ethane. Due to these contaminations the parameters for autopicking are difficult to define. The revision of FOM (figure of merit) maps highlights that on one hand the contaminations as well as the carbon film are likely to be picked due to their high SNR. On the other hand, clearly separated and distinct particles are not picked. Revision of all autopicked particles in addition with re-picking is evaluated to be more time consuming than manual picking. Manual picking provides more high quality particles.

(2) Mask diameter: A suitable mask diameter is difficult to define, since the particle's dimensions must be considered. The particle mask diameter should be as small as possible to minimize the noise around the particle but as large as necessary in order to not cut off real signal. The overall length of the particle (side view) is at least twice as large as the diameter of the particle (top view). Therefore, a mask diameter of 240 Å is chosen. Smaller particle mask diameters result in signal loss for the membrane domain of the particles with side or tilted views.

(3) Neighboring particles: Upon processing various degrees of neighboring particles cause problems since they are difficult to separate (Figure 42A). Moreover, the background signal is strongly impaired. If convergence is not slowed down in 2D classification, neighboring particles are aligned and partially misinterpreted as putative channel side views. In that case, they still appear in 3D classification and therefore complicate the cleaning procedure of the data set.

(4) Heterogeneity/polydispersity: The data contains a certain degree of heterogeneity. During 2D classification empty nanodiscs and particles missing one or two subunits can easily be identified (Figure 42B and C). Moreover, 3D classification emphasizes that putative top views result in spherical 3D volumes. Therefore, those 2D class-averages describe damaged channels, which exhibit only one domain, either membrane or cytoplasmic, of the channels.

(5) Empty nanodiscs: A relatively small percentage of empty nanodiscs is identified. In 2D classification three distinct classes with 1,560 particles are separated, corresponding to ~1 % of the total manually picked particles. They are successfully excluded from the data set during 2D classification (Figure 42C). The absolute percentage of empty nanodiscs is difficult to estimate but it might be in the order of 1-10 %.

(6) Preferred orientation and dominating types of particles: The picked particles exhibit a preferred orientation. Most particles represent putative top views of the channel, only few represent tilted views or side views. 2D and 3D classification highlight that only 10-20 % of all picked particles are side views and tilted views (Figure 43).

(7) Low SNR of the particle's membrane domain: The particles exhibit different signal intensities. Whereas the cytoplasmic domain displays a high SNR, the transmembrane domain exhibits a low SNR. Therefore the particles are centered on the basis of the high SNR of the cytoplasmic domain instead of the center of channel (Figure 43). This in turn influences the choice of the mask diameter and the degree of background noise.

In total, only 1.7-2.9 % of all manually picked particles (169,657 particles) contribute to final 3D volumes (Figure 44).

2.5 Neq198: Fitting of atomic coordinates into cryo-EM density

The atomic coordinates of Neq198 were fitted into the finite cryo-EM density (Volume B, Figure 44) in collaboration with Dr. M. Gregor Madej (Institute of Biophysics and Physical Biochemistry, University of Regensburg). For this purpose a homology model based on the crystal structure of the MscS from *E. coli* (2oau.pdb, Bass *et al.*, 2002) was generated and served as an initial model for fitting. This model missed the two additional helices that are predicted for Neq198. Those helices were modelled independently using ROSETTA (<https://www.rosettacommons.org>) and fitted manually into the cryo-EM density. By combining the two approaches a final model for Neq198 was generated.

The 3D volume of vitrified Neq198 shows distinct densities above the membrane domain that are not covered by the *EcMscS* homology model (Figure 45A). Although during processing no masking was

applied, the finite map of Neq198 is free of excessive background noise. This indicates that densities that are seen represent structural features of the vitrified protein. In general, the helices of the membrane domain are not resolved to high resolution in the cryo-EM density, which makes it difficult to allocate single helices. There is not enough density to assume that the helices are similarly staged and tilted as in *EcMscS*. The density on top of the membrane domain more likely indicates the additional helices to be located there. This channel organization, representing the final model for Neq198, accounts for almost all of the observed cryo-EM density (Figure 45A, B, C and D).

Although the periplasmic densities do not provide detailed information, the approximate localization of the additional helices is recognized. However, there is not enough density to fit two continuous helices. The helices build a cap-like structure on top of the transmembrane domain reaching into the periplasm (Figure 45A and B, slice 1). The nanodisc cannot be explicitly assigned. In proximity to the transmembrane domain additional density is available, which is not accounted by the model of Neq198 (Figure 45A and B, slice 2). This space is more likely to be filled with lipids and surrounded by the membrane scaffold protein of the nanodisc. This leads to the hypothesis that the MSP tightly encircles the channel and thus can not be clearly identified in the cryo-EM density. The approximate localization of the nanodisc can be compared with the channel embedded into a model bilayer (Figure 45E). The helices TM1, TM2 and TM3a are tightly packed, which results in a large pore through the channel also observed for *EcMscS* (Figure 45B, slice 2). The location of the TM3b helix, which is located proximal to the cytoplasmic membrane surface is confirmed. The kink in helix TM3 marks the membrane boundary (Figure 45B, slice 3). Particularly, the cytoplasmic domain fits very well. The pore through the β -barrel is clearly identified (Figure 45B, slice 4). Back projections (Figure 45F and G) evaluate the model and the final cryo-EM density of Neq198, respectively. They can be compared to 2D class-averages (Figure 43). The back projections confirm the heptameric fold of the channel that is already observed in 2D classification. Thus, the applied C7 symmetry in 3D refinement does not introduce artefacts.

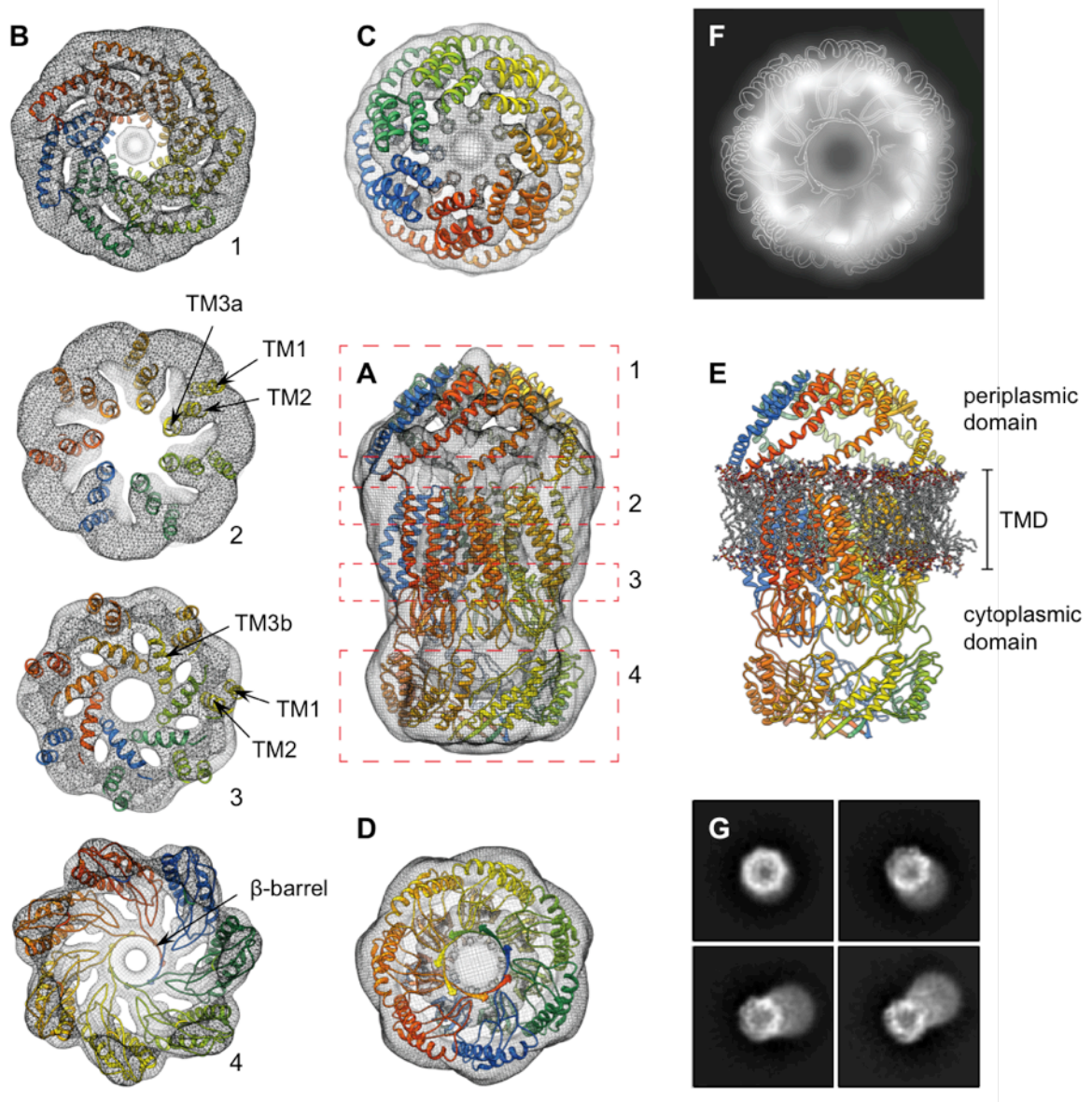


Figure 45: Surface representation of cryo-EM density with fitted atomic model of Neq198.

(A) Side view of the channel, ribbon diagram of Neq198 is fitted into EM density of vitrified Neq198, surface representation as mesh, (B) slices through the channel, approximate positions of the slices are indicated in (A), TM = transmembrane helix, (C) top view of the channel, (D) bottom view of the channel, (E) side view of the channel embedded in a model membrane, TMD = transmembrane domain, (F) back projection of the Neq198 model in Chimera 1.12 (Pettersen *et al.*, 2004), (G) representative back projections of the final refined 3D volume of vitrified Neq198 using the relion_project command in RELION-2.1 (Scheres, 2012b) with random orientation.

The ion permeation pathway through the channel was analyzed using the HOLE script (Smart *et al.*, 1996) (Figure 46). Compared to the closed and open conformation of the *EcMscS*, the channel Neq198 from *N. equitans* more likely adopts an open conformation. In *E. coli* the ion pathway is

constricted to ~ 2.4 Å in the membrane domain in the closed conformation (2oau.pdb; Bass *et al.*, 2002), in contrast to ~ 6 Å in the open conformation (2vv5.pdb; Wang *et al.*, 2008). The ion pathway in Neq198 is only constricted to ~ 6.8 Å (Figure 46B), resulting in a membrane pore that is even larger than that of an open *EcMscS*. A second constriction site is created by the C-terminal β -barrel and ranges from ~ 1.75 Å to ~ 2.19 Å in closed and open conformation in *EcMscS*, respectively (Bass *et al.*, 2002; Wang *et al.*, 2008). Regardless of the conformation, the cytoplasmic domain for *EcMscS* remains essentially unchanged (Figure 46B). Unlike in *EcMscS*, for Neq198 a constriction to only ~ 6 Å for the β -barrel is predicted (Figure 46B). Lateral portals are not assessed in the analysis by HOLE. The overall dimension of Neq198 parallel to the sevenfold axis can be assigned to ~ 160 Å (Figure 46B).

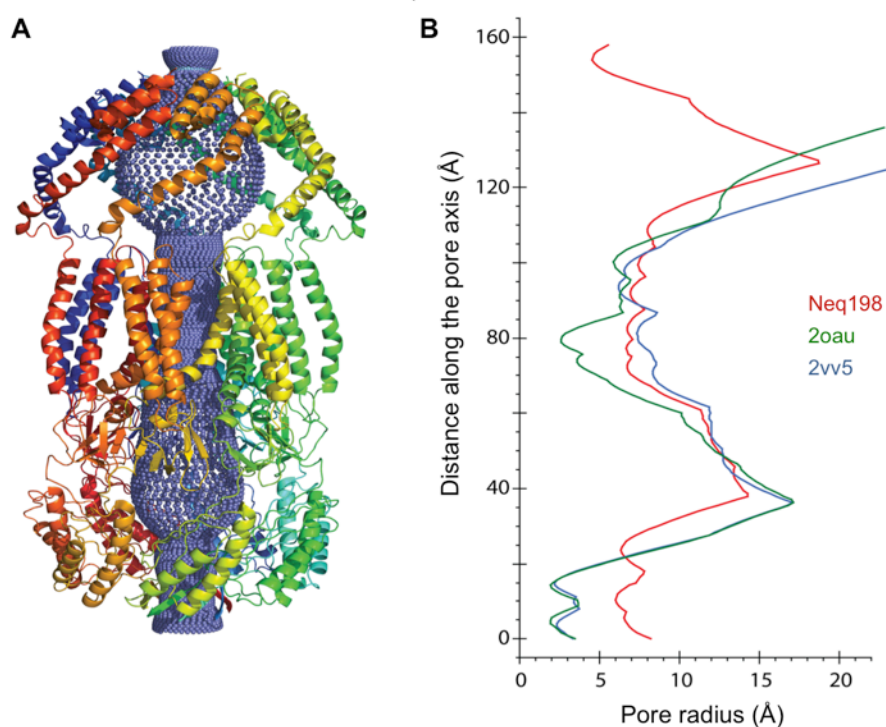


Figure 46: Profile of ion permeation pathway.

(A) Ribbon diagram of Neq198 superposed on probe spheres (blue) outlining the ion permeation pathway, the channel is shown normal to the sevenfold axis, pore profile generated by the HOLE script (Smart *et al.*, 1996); (B) comparison of the pore radii along the pore axis for Neq198 (red) with the crystal structures of *EcMscS* in closed (green) conformation (2oau.pdb; Bass *et al.*, 2002) and open (blue) conformation (2vv5.pdb; Wang *et al.*, 2008).

3 Functional analysis of Neq198 and Neq531

3.1 Hypoosmotic down-shock assay

To evaluate whether the purified mechanosensitive channels exhibit functionality, a hypoosmotic down-shock assay was performed. These experiments were carried out in cells lacking endogenous MscL as well as MscS. The *mscS* gene alone has shown to rescue bacteria from hypoosmotic down-shock (Levina *et al.*, 1999). The MJF465 *E. coli* cells (*MscL*⁻, *MscS*⁻, *MscK*⁻) containing the MscL gene (positive control), the Neq198 gene and no gene (negative control), were grown under hyperosmotic conditions for 9-10 h. After induction the cells were transferred to hypoosmotic media (shock). Roughly 97 % of the cells containing the *mscL* gene survive the hypoosmotic shock, whereas less than 2 % of the MJF465 cells lacking the *mscL*, *mscS* and *mscK* genes survive (Figure 47). Approximately 8 % of cells expressing the MscS-like channel Neq198 from *N. equitans* survive the hypoosmotic down-shock. The efficiency of MscS-like channel of *N. equitans* in *E. coli* is about 12-fold lower compared to the MscL from *E. coli*.

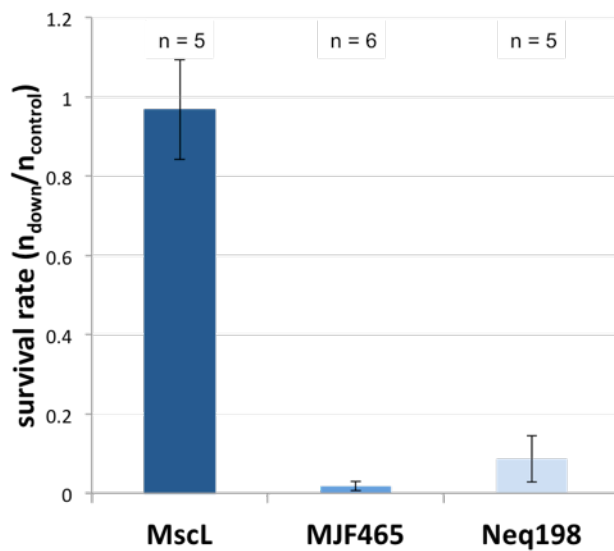


Figure 47: Hypoosmotic down-shock assay of Neq198 in MJF465 *E. coli* cells.

The survival rate ($n_{\text{down}}/n_{\text{control}}$) was calculated by counting the number of colony forming units (cfu) of cells that experienced the osmotic down-shock (n_{down}) compared to those that did not experience the down-shock (n_{control}); MscL represented the positive control, the MJF465 cells without any plasmid represented the negative control; n = number of mean values \pm standard deviation.

Taken together, Neq198 rescues cells from hypoosmotic down-shock to some significant degree. Although not yet tested for both MscS-like channels from *N. equitans*, the results for Neq198 already indicate that the channel is functional.

3.2 Patch clamp analysis

For the patch clamp analysis the DDM-solubilized and -purified protein (Neq198 and Neq531) was reconstituted into liposomes. Protein solubilized with and purified in Fos14 was also tested and it exhibits channel activity. Since negative effects of Fos14 on the channel activity can not be excluded, protein in DDM is preferred. Optionally, the N-terminal histidine tag was cleaved off with thrombin during purification to test whether the tag has an effect on channel activity. Neq198 was reconstituted without histidine tag. In contrast, Neq531 was reconstituted with and without histidine tag. In a standard procedure (Delcour *et al.*, 1989; Häse *et al.*, 1995) azolectin was used for reconstitution. Azolectin is a crude mixture of phospholipids and neutral lipids that comprises to ~25 % of phosphatidylcholine (Letters, 1964). In addition, various lipids in different combinations were tested like PC, PC-20, PE, PG. Moreover, cholesterol was optionally added. The channels were reconstituted in protein-lipid ratios ranging from 1:200-1:1000 (Table III.1).

In summary, a protein concentration of 1:1000 is favored for both channels. A negative effect of the histidine tag on channel activity is not confirmed - channels with and without histidine tag show spontaneous channel activity. During patch clamping both channels are constitutively active, i.e. spontaneous opening and closing events are observed, although no pressure is applied. Constitutive channel activity is observed for Neq198 reconstituted into azolectin liposomes and azolectin:PC20 (50:50) liposomes. Opening and closing events are observed with Neq531 reconstituted into azolectin and azolectin:cholesterol (80:20) liposomes. Moreover, Neq531 shows channel activity in the lipid composition of PE:PC20 (70:30) (Table III.1). For other lipid compositions either blisters (unilamellar liposomes budding from multilamellar proteoliposomes) are not formed, a seal is not established or no channel activity is observed at all. These observations need careful interpretation. The lipid composition directly influences the formation of blisters. In case that the blisters are not formed either the lipid composition hampers the formation of the blisters (e.g. PE:PC:cholesterol) or the incubation time in the bath solution is not sufficient for the blisters to be formed. Incubation time differs significantly from few (100% Azolectin) to more than 90 minutes (100 % PC20). No channel activity is contributed to the fact that in these cases the blister formation might be influenced negatively or a tight seal can not be established. The question is whether under these conditions enough channels are reconstituted and subsequently can be detected in patch clamping. The lipid composition influences the seals to be established. In particular, blisters consisting of pure PC20 or a percentage of cholesterol are more difficult to patch. In general, the seals are weak due to the constitutive activity of the channels. Strong seals are obtained when constitutive channel activity is (mostly) missing.

Table III.1: Liposome preparations

Protein	Protein-lipid ratio	Lipid composition	Observations
Neq198 w/o his-tag	1:1000	Azolectin	Many blisters
	1:500		→ Channel activity
	1:1000	50:50	→ Blisters, Channel activity
	1:500	Azolectin:PC20	
	1:1000	80:20	Blisters
		Azolectin:Cholesterol	
	1:1000	50:30:20	No channel activity
		Azolectin:PC20:Cholesterol	
Neq531 w/ his-tag	1:1000	Azolectin	Many blisters
	1:200		→ Channel activity
	1:1000	80:20	→ Few blisters
	1:200	Azolectin:Cholesterol	
	1:1000	60:20:20	No blisters
		PE:PC:Cholesterol	
	1:200	70:20:10	Few blisters
		PE:PC:PG	
1:50	85:15	Blisters	
	Azolectin:Cholesterol		No channel activity
Neq531 w/o his-tag	1:1000	PC20	Blisters
	1:500		No channel activity
	1:1000	70:30	Blisters
	1:500	PE:PC20	→ Channel activity

As several parameters such as the lipid composition of the liposomes were modified, the constitutive activity should be hampered and the channels should be forced into a closed conformation. Only closed channels that can be activated by applying pressure guarantee a correct characterization with respect to mechanosensitivity, conductance, activation threshold, and selectivity. The tested lipid compositions do not prevent the constitutive channel activity. Therefore, the channels were additionally treated with gadolinium - a known and widely used blocker for mechanosensitive channels (Ermakov *et al.*, 2010). Gadolinium (Gd^{3+}) is known to block mechanosensitive channels by reducing their capability to sense mechanical stimuli (Oliet and Bourque, 1996). The mechanisms itself is not fully understood. It is assumed that Gd^{3+} intercalates into lipid membranes and therefore alters the packing and lateral pressure of anionic lipids (Ermakov *et al.*, 2010). Ermakov *et al.*, 2010 demonstrated that Gd^{3+} effectively blocked the MscL from *E. coli* only when the channel was reconstituted into liposomes composed of negatively charged lipids. It was concluded that Gd^{3+} binds

with high affinity to anionic lipids in such a way that the lateral pressure is increased as tens of mN/m. As a consequence, the channel is compressed and forced into a closed conformation. High concentrations of gadolinium (500 mM) resulted in blocking of both channels. However, the channels could not be reactivated. Hence, gadolinium was titrated in order to find the optimal concentration that blocks the channel but allows a reactivation by pressure application and therefore indicates mechanosensitivity. Re-hydrated liposomes were incubated in bath solution to allow unilamellar blisters to be formed. These blisters were used to establish a giga- Ω -seal between micropipette and membrane. Here, an inside-out-patch was already obtained by just contacting the membrane with the pipette. After a seal was established, gadolinium was added step-wise with increasing concentrations directly into the bath solution. Pipetting directly into the bath solution disturbed the system and frequently resulted in a loss of the seal. Therefore a genuine titration was not achieved. It was concluded that the lipid environment was not favorable for both MscS-like channels from *N. equitans* in patch clamp experiments.

Careful analysis of the data obtained with azolectin liposomes indicates that both channels are constitutively active. If channel activity is observed, it occurs spontaneously while the channels mostly adopt an open conformation with only rare closing events. Moreover, both channels exhibit a degree of voltage dependence. For Neq198 more opening and closing events at applied negative voltages are observed. Yet, at applied positive voltages numerous gating events occur. In general long opening and closing events are noticed. Moreover, the channel probably shows modest inactivating behaviour (Figure 48). In contrast, Neq531 preferably shows gating events at applied positive voltages. At applied negative voltages only very few events are noticed. Gating events for Neq531 or closing of the channel occur rarely. Here, more likely a partial closing to sub-conducting states is observed frequently at higher voltages (Figure 49). In general it is problematic to identify full closing and opening events for both channels. Probably, openings to 2/3 conductance are abundant as it was already observed for *EcMscS* (Booth *et al.*, 2007). Due to these issues a detailed characterization with respect to single channel conductances was not possible. Here, a genuine reconstitution system is needed for the characterization of distinct single channel events.

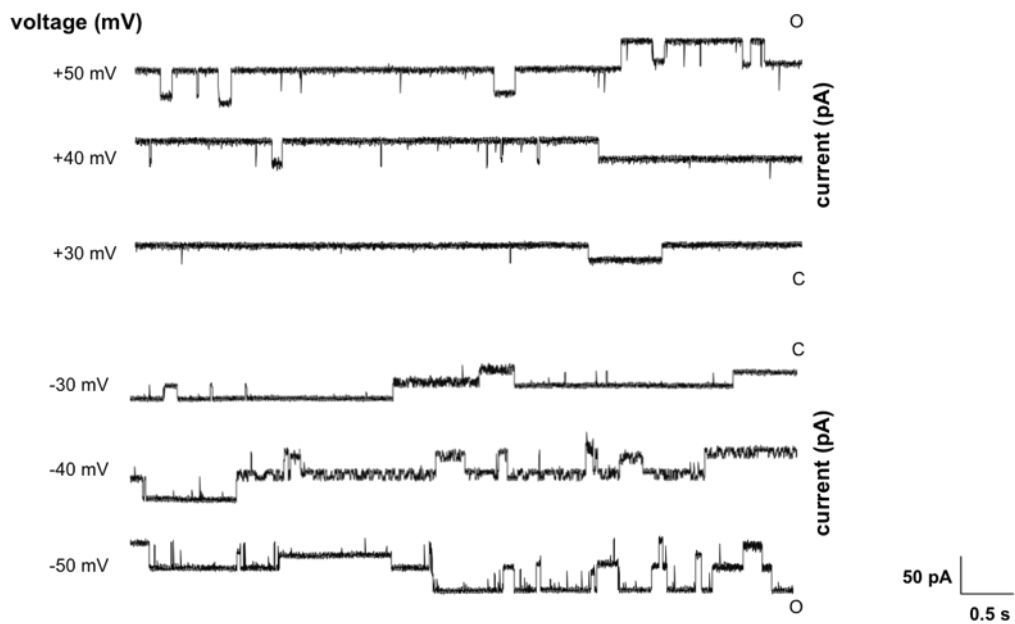


Figure 48: Patch clamp currents of Neq198 reconstituted into azolectin liposomes. Currents at applied positive and negative voltages; O – open conformation, C – closed conformation of channels at positive and negative voltages.

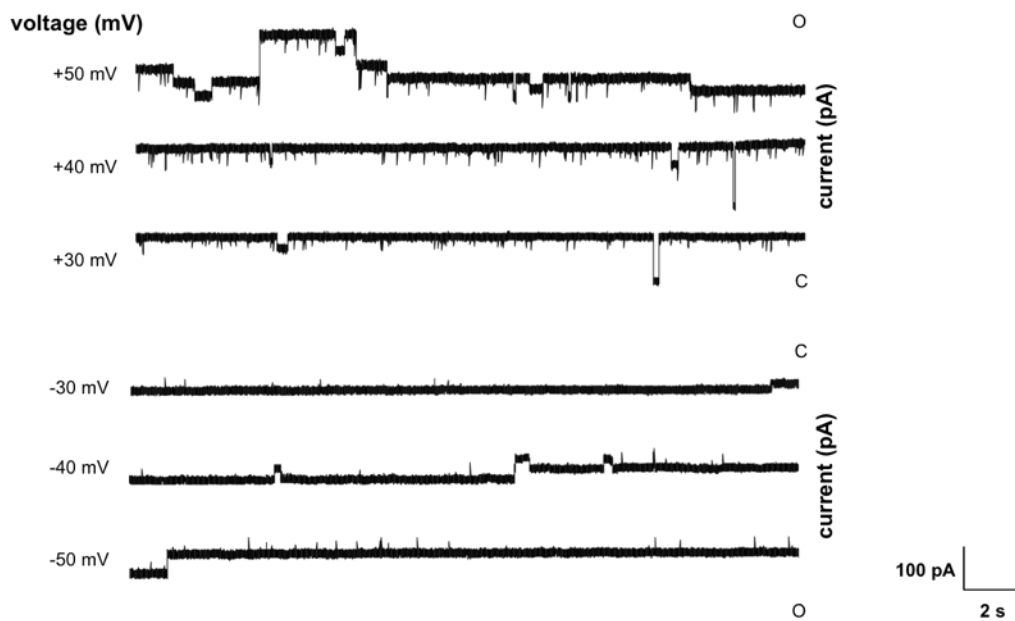


Figure 49: Patch clamp currents of Neq531 reconstituted into azolectin liposomes. Currents at applied positive and negative voltages; O – open conformation, C – closed conformation of channels at positive and negative voltages.

As alternative to the artificial system of liposomes, a more native-like environment was tested with the reconstitution into *E. coli* spheroplasts. Although various conditions for the expression in *E. coli* spheroplasts were tested, no channel activity is observed in patch clamp experiments (Table III.2). However, this can be attributed to a failure of the spheroplast reconstitution. After induction with arabinose the cells were regularly checked visually in the microscope. It was noticed that the filaments degraded to some extent. They got transparent and exhibited dark inclusions. This was mainly observed when the channel without histidine tag was expressed. For the expression of Neq198 with histidine tag the filamentous *E. coli* looked healthier although few transparent filaments were also observed. Six different conditions were finally tested in patch clamp experiment. The formed spheroplasts turned out to be hardly patchable. Only for spheroplasts from two conditions, stable seals were obtained but no channel activity was observed. As positive control MscL from *E. coli* was expressed. The formation of spheroplasts for 2:00 min and 5:30 min results in patchable spheroplasts where channel activity is observed. Patch clamping of *E. coli* spheroplasts was only tested for Neq198. Due to the aforementioned challenges this system is not further considered.

Table III.2: Reconstitution of Neq198 into *E. coli* spheroplast

#	Expression conditions	Formation of spheroplasts [min]	Patch clamping
1	w/o 6his elongation for ~1:45 h	3:00	Not tested
2	1:20 h induction with 0.02 % arabinose, 37 °C	4:50	Not tested
3	w/o 6his elongation for ~1:45 h	5:00	Seals, channel activity?
4	3 h induction with 0.02 % arabinose, 37 °C	7:30	No seals
5	w/ 6his elongation for ~1:45 h	3:00	Not tested
6	3 h induction with 0.02 % arabinose, 37 °C	6:00	Not tested
7	w/ 6his elongation for ~1:30 h, stored at 4°C for 4-5 h	4:20	No seals
8	induction o/N with 0.01 % arabinose, 20 °C (15-16 h)	7:30	Not tested
9	w/ 6his elongation for ~1:15 h	3:00	Seals, no channel activity
10	1 h induction with 0.02 % arabinose, 37 °C	6:00	No seals

IV DISCUSSION

1 Heterologous expression and purification of MscS-like channels from *N. equitans*

The heterologous expression of MscS-like channels from the symbiotic archaeon *N. equitans* in the mesophilic *E. coli* was very successful resulting in a relatively high quantity of target protein when expression was carried out in TB media overnight and at low temperatures. The high expression yield was somewhat surprising as previous attempts to express membrane proteins from the host *I. hospitalis* in *E. coli* had all failed and *Pichia pastoris* was used as an expression system (Wiegmann, 2014; Daxer, 2016). Ma and co-workers already reported expression and purification of archaeal membrane transport proteins in *E. coli*. They presented an efficient strategy for small-scale screening testing 15 integral membrane transport proteins. 13 transporters from MFS and LeuT superfamilies were successfully expressed, seven could be purified and six of those resulted in quantities suitable for functional and structural studies (Ma *et al.*, 2013). Moreover, the archaeal mechanosensitive channels T1 and T2 from *Thermoplasma volcanium* have been successfully expressed in *E. coli* and purified as well (L w *et al.*, 2013). Surprisingly, chemical crosslinking experiments proposed a pentameric fold for T1 and T2 in contrast to the heptameric arrangement of *E. coli* MscS. T2 served as a target for nanobody mediated crystallization (L w *et al.*, 2013) and as model protein for the reconstitution in a saposin-lipoprotein nanoparticle system (Salipro) (IV3.2) (Frauenfeld *et al.*, 2016).

Interestingly, the location of the histidine tag was most crucial. The entire cytoplasmic domain of MscS-like channels is important for oligomerization and stabilization. Deletion experiments have

shown that a loss of the β -barrel did not influence channel assembly or gating mechanisms but severely impaired stability (Schumann *et al.*, 2004; Rasmussen *et al.*, 2007). Most probably, the C-terminal location of the histidine tag caused destabilization of the homo-heptameric complex and led to aggregation as it was observed for Neq531, initially. This is further supported by observations made for the mechanosensitive channels from *T. volcanium*: high expression levels and homogeneous protein samples after purification were only obtained using a N-terminally tagged construct. Although T1 and T2 lack the C-terminal beta strand that forms a seven stranded β -barrel in the heptameric complex, these observations implicated that C-terminal tags might interfere with correct folding and oligomeric assembly of the channels (L w *et al.*, 2013). In literature, examples for successfully expressed and purified MscS with N-terminal and C-terminal tags can be found: MscS from *T. tengcongensis* and *E. coli* were tagged N-terminally (Zhang *et al.*, 2012; Wang *et al.*, 2008), MscS from *H. pylori* was tagged with a N-terminal histidine tag in addition to a C-terminal FLAG tag (Wang *et al.*, 2008), whereas the YnaI from *E. coli* contained a C-terminal histidine tag (B ttcher *et al.*, 2015). Switching the C-terminal histidine tag to N-terminal considerably influenced channel stability for Neq531. Single particle analysis of negative-stained Neq531 highlighted a pronounced β -barrel or C-terminal structural feature that was not observed for Neq198 so far.

In general, Neq531 was much more difficult to purify and stabilize than Neq198. Solubilization with detergent destabilized Neq531 most likely due to the lack of bulk lipids or the loss of specific lipids that may be essential for stability and/or activity of the protein. Although Neq531 could be stabilized to some extent by the reconstitution into amphipols, the protein sample was very heterogeneous as judged from negative stain micrographs. For Neq531 a direct reconstitution into nanodiscs without previous solubilization and purification (Shirzad-Wasei *et al.*, 2015) was tested. So far, this procedure was not successful and requires further optimization. Direct reconstitution into nanodiscs or purification in the presence of lipids might help to stabilize the protein Neq531. The specific lipid requirements of membrane proteins have proven to present a putative bottleneck in heterologous expression (Opekarova and Tanner, 2003). TLC highlighted that Neq198 and Neq531 have bound a different set of lipids that likewise supports the hypothesis Neq531 might be stabilized by the addition of lipids during purification. Lipid content and compositions represent important parameters, that require control during membrane protein preparations to optimize activity and stability (Hunte, 2005; Hunte and Richers, 2008). For example, structure determination of wild-type LacY was only obtained by the addition of polar phospholipid extracts from *E. coli* to de-lipidated LacY before crystallization (Guan *et al.*, 2006; Guan *et al.*, 2007).

A reconstitution into nanodiscs according to the previously used protocol (Bayburt and Sligar, 2003; Denisov *et al.*, 2004) might pose some challenges for Neq531. So far, Neq531 requires 10 % (v/v) glycerol during purification. However, high glycerol concentrations in the buffer should be avoided, since concentrations above 4 % interfere with the reconstitution process (Ritchie *et al.*, 2009). The self-assembly of nanodiscs is initiated by the addition of hydrophobic beads, which have been shown to absorb lipids along with the detergent (Lévy *et al.*, 1999). Therefore, care should be taken that not too excessive amounts of Bio-beads are used, considering also the potential positive effect of lipids on the channel's stability.

Negative stain and Blue Native Page represented valuable tools for quality control of the protein samples. By Blue Native Page the reconstitution into stabilizing environments was evaluated. Comparing the protein in detergent, reconstituted into amphipols, and into nanodiscs or empty nanodiscs, respectively, the shift in size of the protein sample indicated a proper reconstitution. This size shift was also observed in size exclusion chromatography. Moreover, the degree of higher oligomers or aggregates was checked. It has been shown that mechanosensitive channels tend to dimerize (Edwards *et al.*, 2012). Dimerization of MscS-like channels was observed in size exclusion chromatography as well as Blue Native Page (Edwards *et al.*, 2012) and is most likely triggered by de-lipidation during purification due to high detergent concentrations. For the channels Neq198 and Neq531, solubilized in detergent or stabilized in amphipols, dimerization was observed in Blue Native Page and size exclusion chromatography as well. In size exclusion chromatography a shoulder in front of the main peak indicated dimerization. Concerning the stabilization in amphipols, higher oligomers might be additionally triggered by the amphipol particles itself. A8-35 particles might aggregate due to their negative charges or their protonation or complexation of carboxylate groups, which makes them less hydrophilic. Moreover, multivalent cations can bridge particles leading to non-physiological oligomerization or even to precipitation (Zoonens *et al.*, 2014b). Here, bridging by multivalent cations can be neglected since the buffer comprised only of monovalent cations. Still, this fact elucidates the sensitivity of amphipol reconstitution to buffer conditions. For single particle analyses, dimerization or aggregation of the particles was tolerated to some extent, because those particles can be filtered out in the classification step during processing. In summary, negative staining allows to judge the heterogeneity of protein samples under optimal conditions with respect to protein concentration and staining procedure and under taking into account that buffer compositions and added detergents might influence the quality of the negative stain considerably.

2 The role of lipids in mechanosensation

Recent high resolution structures have revealed that protein-lipid interactions for MscS channels are important for tension sensing (I1.2.3). Pliotas and co-workers proposed an universal model for tension sensing, in which cavities in the protein's surface are reversibly filled with lipids (lipid interdigitation) and therefore enable the direct interaction with the surrounding bulk lipid bilayer. The lipid interdigitation affects the open-close-transition of the channel; upon opening the number of lipids in the voids decreases (Pliotas *et al.*, 2015; Pliotas and Naismith, 2017). Mechanosensitive channels in archaea and their lipid-protein interactions have been extensively discussed in Balleza, 2011.

2.1 Bacteria and archaea: membranes and lipids

Lipids in archael membranes differ significantly from bacterial ones (Figure 50). Lipids of bacteria and eukarya bind fatty acids via ester bonds to the glycerol backbone (1,2-*sn* position). In archaea, the hydrophobic side chains are connected via ether bonds at the 2,3-*sn* position to the glycerol instead.

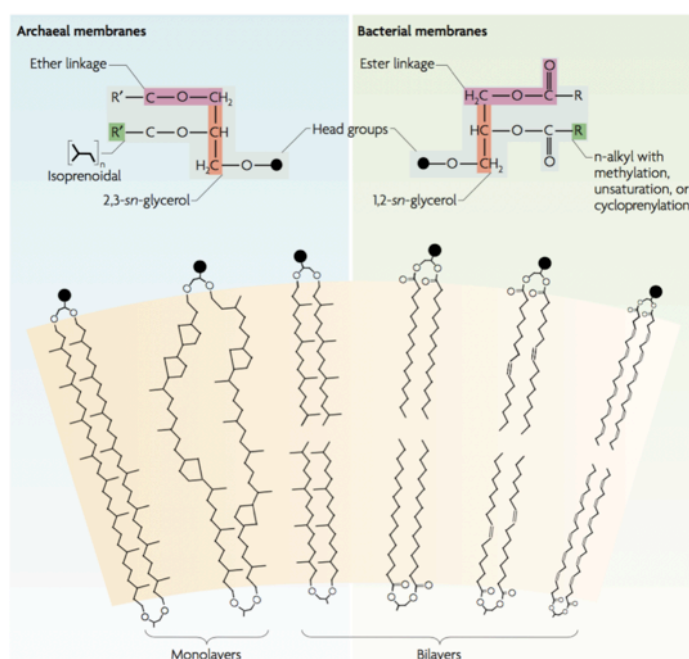


Figure 50: Comparison of archaeal and bacterial lipids and membranes.

The basic archael (left) and bacterial (right) membrane lipids are shown (modified from Valentine, 2007).

The hydrophobic side chains are comprised of repetitive isoprenyl subunits (Kates, 1992; Valentine, 2007; Albers and Meyer, 2011). The archaeal core lipids are glyceroldiether (phytanyl) and glyceroltetraether (diphytanyl); also termed as archaeol and caldarchaeol. Archaeols represent archaea's homolog of diacylglycerol (DAG). Glyceroldiethers result in lipid bilayers, whereas glyceroltetraether form lipid monolayers. These monolayers are considered to be more stable and are found in hyperthermophilic archaea and other prokaryotes that grow at high

temperatures (Figure 50) (Valentine, 2007; van de Vossenberg *et al.*, 1998).

Most archaea comprise an additional cell envelope that is located just on top the cell membrane consisting of a pseudo-crystalline proteinaceous layer, the so-called S-layer (surface layer) (Kandler and König, 1993; Albers and Meyer, 2011; Klingl, 2014). Archaeal S-layers are composed mostly of a single (glyco)protein species with an apparent relative molecular mass of 40-200 kDa (Albers and Meyer, 2011). They are associated by stalk like structures with the cytoplasmic membrane creating a quasi-periplasmic space (Klingl, 2014). The potential functions of S-layer proteins were thoroughly discussed (e.g. Beveridge and Graham, 1991; Messner and Sleytr, 1992; Beveridge *et al.*, 1997; Sleytr *et al.*, 1993) and range from protection against high temperatures, salinity (osmoprotection), and low pH to maintenance of cell shape as an exoskeleton. Moreover, S-layers may contribute to interactions with the environment as e.g. ion trap, metal binding, protein immobilization, specific contacts, and adhesion to surfaces (Engelhardt, 2007a; Engelhardt, 2007b).

The role of S-layers is particularly intriguing in the context of mechanosensitivity affecting the internal pressure on the lipid membrane. For cells without any cell wall component high internal pressure (ΔP), as a result of hydrophobic down-shock, stretches the cell membrane evenly. Thus, the cell radius increases and the membrane curvature decreases, accordingly (Figure 51). In contrast, for cells that are covered by an S-layer, the S-layer anchors define smaller membrane patches, where the interacting membrane lipids are hold in place. When the intracellular pressure increases, membrane bulges between the anchors are created. Thus, the membrane curvature increases locally (Engelhardt, 2007b).

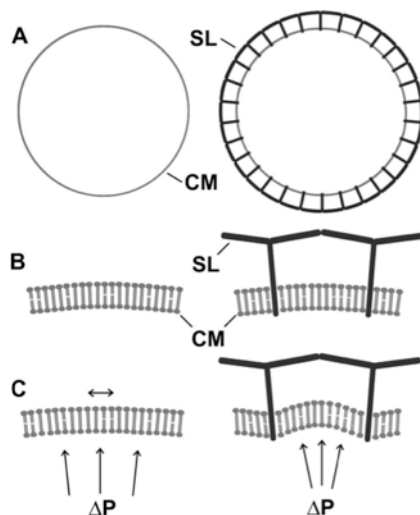


Figure 51: Effect of internal pressure on the lipid membrane.

Model cells without any additional cell wall component (left) and covered with an S-layer (right). (A) Cell models, (B) cell membrane (CM) section and the anchoring S-layer (SL) at low internal pressure, (C) high internal pressure (ΔP) dilates the cell membrane of the uncovered cell, increases the cell radius and decreases the membrane curvature globally. The S-layer anchors holds interacting membrane lipids in place. Increasing internal pressure result the membrane to bulge between the anchors so that the membrane curvature is increased locally (Engelhardt, 2007b).

Comparing the native membrane of *N. equitans* with that in the model system *E. coli*, differences become evident. The question arises, whether *E. coli* is suitable for functional assays of archaeal membrane proteins, e.g. the mechanosensitive channels from *N. equitans*. The differences of *N. equitans* to *E. coli* with respect to membrane and lipids will without any doubt affect mechanosensitivity. Analyses of *N. equitans* membranes revealed qualitatively and quantitatively identical lipid compositions to *I. hospitalis* as they were obtained for the inner membrane of *I. hospitalis* cells; i.e archaeol and cardiolipin (Jahn *et al.*, 2004). Moreover, *N. equitans* exhibits an S-layer with sixfold symmetry and a lattice constant of 15 nm creating a periplasmic space of 20 nm (Huber *et al.*, 2002; Huber *et al.*, 2003). In *E. coli* the cytoplasmic membrane is composed of phosphatidylethanolamine (~74-79 %), phosphatidylglycerol (~18 %) and cardiolipin (~4-8 %) (Dowhan, 1997; Romantsov *et al.*, 2009). The lipid composition is relatively invariant under a broad spectrum of growth conditions. When cells enter the stationary phase, CL levels rise at the expense of PG (Hiraoka *et al.*, 1993). Furthermore, the optimal growth temperatures of both organisms differ significantly. Whereas the mesophilic *E. coli* grows optimally at 37 °C (Doyle and Schoeni, 1984), *N. equitans* exclusively grows in co-culture with *I. hospitalis*, which exhibits optimal growing temperatures of ~90 °C (Huber *et al.*, 2002).

On a first glance, the characteristic structure of archaeal lipids seems to have an impact via altered protein-lipid interactions on the tension sensing mechanism suggesting that it will be very different to the one reported for *EcMscS*. The established model for tension sensing is based on the reversible lipid interdigitation into hydrophobic cavities on the protein's surface (Pliotas *et al.*, 2015; Pliotas and Naismith, 2017), which would not be possible when the channels are expressed in the potentially occurring lipid monolayers in *N. equitans*. Assuming that the channels of *N. equitans* cluster in areas of archaeols that form lipid bilayers, the S-layer on top might still affect channel activity and thereby the tension sensing mechanism. However, other archaeal mechanosensitive channels of organisms that exhibit S-layers (*M. jannashii* and *H. volcanii*) have been successfully characterized using patch clamp technique (Le Dain *et al.*, 1998; Kloda and Martinac, 2001c; Kloda and Martinac, 2001d). These observations seem to emasculate the role of the S-layer in proper channel function, but the final impact of the S-layer is still open for debate.

In summary, the functional characterization of MscS-like channels is affected by the chosen cellular or *in vitro* reconstitution system. The MS channel of *H. volcanii*, for instance, showed a higher activation threshold in native membranes compared to azolectin liposomes (Le Dain *et al.*, 1998).

2.2 Towards a functional understanding of Neq198 and Neq531

The functional analysis by patch clamp and hyperosmotic down-shock assay highlighted the importance of lipid-protein interactions for both channels from *N. equitans*. Although down-shock assays indicated that Neq198 shows characteristics of mechanosensitivity in a non-archaeal membrane environment, the *E. coli* cells were rescued only to a small percentage.

Archaeal MS channels have already been successfully reconstituted into azolectin liposomes and subsequently characterized electrophysiologically, e.g. MscMJ and MscMJLR from *M. janashii* (Kloda and Martinac, 2001b; Kloda and Martinac, 2001d), MscTA from *T. acidophilum* (Kloda and Martinac, 2001a), MscA1 and MscA2 from *H. volcanii* (Le Dain *et al.*, 1998). Patch clamp experiments of Neq198 and Neq531 reconstituted into azolectin liposomes also demonstrated that both channels were constitutively active, although an electrophysiological characterization of the activation threshold and conductance was inconclusive. Inconclusive results in channel characterization are not unusual and apparently a problem for MS channel functional assays in general. The MscTV from *T. volcanium* was previously reported as mechanosensitive channel due to channel-characteristic electrophysiological properties (Kloda and Martinac, 2001a). Upon structural analysis, however, this hypothetical channel was identified as a MarR-like protein (multiple antibiotic resistance regulator family). The protein turned out to be water soluble and moreover failed in functional assays to rescue the triple knockout (*mscL*⁻, *mscS*⁻, and *mscK*⁻) of *E. coli* from hypoosmotic down-shock (Liu *et al.*, 2010).

Interestingly, in patch clamp experiments of MscCG from *C. glutamicum* a similar behavior as for Neq198 was observed. MscCG Δ 110, a truncated construct missing 110 aa downstream the helix TM4 (Nakamura *et al.*, 2007), exhibited spontaneous channel activity although no membrane pressure was applied. Here, only few low giga- Ω -seals were obtained. The addition of Gd³⁺ resulted in a stabilization of the membrane patch and therefore prevented spontaneous channel activity. Compared to the full-length channel Gd³⁺ did not influence the conductance of the truncated construct (Becker, 2013). However, a stabilization of the membrane patch by the addition of Gd³⁺ for Neq198 and Neq531 was not obtained. A genuine titration of gadolinium failed. Nevertheless, an inhibitory effect of high concentrations of Gd³⁺ on both channels from *N. equitans* was observed.

In another approach, cholesterol was added to the reconstitution mixture. Cholesterol changes the physical properties of the lipid bilayer by (1) reducing the bilayer fluidity and thus increasing the membrane stiffness (Cooper, 1978), (2) decreasing the membrane permeability that goes along with increasing the acyl-chain orientational order of phospholipids and thus affecting bilayer thickness (Ipsen *et al.*, 1990), and (3) affecting the transbilayer pressure profile (Cantor, 1999). Cholesterol have

been shown to influence the activity of numerous membrane proteins including ion channels (Levitan *et al.*, 2010). The activation threshold of MscS/MscL from *E. coli* was dramatically decreased when co-reconstituted into cholesterol-containing liposomes (Nomura *et al.*, 2012). Here, cholesterol concentrations up to 30 % were used. Channels could not be activated anymore at cholesterol concentrations above 30 %. For the MscS-like channels from *N. equitans* 20 % cholesterol have been tested. Spontaneous activity was still detected for Neq531. For Neq198 applying pressure did not lead to activation in a stabilized membrane patch. These observations implicate that the channels might have slight different sensitivities with respect to cholesterol concentrations and membrane stiffness suggesting different activation thresholds. Nevertheless, further optimization and fine-tuning of cholesterol concentrations in the liposomes will be required to draw a conclusive picture.

Single channel events could not be identified in patch clamp experiments for both *N. equitans* channels. It was questionable whether channel events represented fully openings/closings or only openings/closings to subconducting states. MscS channels exhibit up to eight subconducting states considering their heptameric fold. Upon patch clamp analysis various possible subconducting states could be observed, particularly eye-catching when the channels were flickering (between two subconducting states). Furthermore, the effect of cooperative gating might play an important role (Ursell *et al.*, 2007). It was elusive whether only one channel or multiple channels contributed simultaneously to an opening/closing event. Bilayer thickness and by this the hydrophobic mismatch play an additional role on channel activity. Hydrophobic mismatch arises from the fact that the membrane-spanning part of integral membrane proteins and the hydrophobic part of the lipid bilayer differ in thickness (Killian *et al.*, 1998). Most models assume that lipids in close proximity adjust their acyl chain length to match the hydrophobic thickness of the protein, while the protein moves as rigid body in the membrane to adjust (Fattal and Ben-Shaul, 1993; Lee, 2004). If a distortion of the surrounding lipids does not provide full hydrophobic match, proteins might oligomerize or aggregate in order to minimize the exposed hydrophobic area. Often the structure of the protein is altered by the hydrophobic thickness of the lipid bilayer. Such structural adaptations might include changes in the tilt and the packing of transmembrane helices as well as backbone conformational changes (Killian, 1998; Lee, 2004). Consequences of hydrophobic mismatch were demonstrated e.g. for the model ion channel Gramicidin A (Martinac and Hamill, 2002; Kim *et al.*, 2012) and the Ca²⁺-activated K⁺ channels (BK) (Yuan *et al.*, 2004; Yuan *et al.*, 2007). Small changes in phospholipid acyl chain length converted Gramicidin A from a stretch-activated to a stretch-inactivated channel highlighting its sensitivity to bilayer thickness (Martinac and Hamill, 2002). The presence of brain sphingomyelin, which is known

to increase bilayer thickness, significantly reduced the conductance of the BK channel (Yuan *et al.*, 2004). Other examples how hydrophobic mismatch influenced the activity of membrane proteins are e.g. Ca²⁺ Mg²⁺ ATPase (Caffrey and Feigenson, 1981; East and Lee, 1982), human erythrocyte hexose transporter (Carruthers and Melchior, 1984), rhodopsin (Baldwin and Hubbell, 1985), melibiose permease MelB from *E. coli* (Dumas *et al.*, 2000), diacylglycerol kinase from *E. coli* (Pilot *et al.*, 2001), and Na⁺ K⁺ ATPase (Cornelius *et al.*, 2003).

Besides the effect of lipids, bilayer thickness and cooperative gating, the experimental procedure itself bears several challenges that should be kept in mind. Ideally, one would expect a planar bilayer that is uniformly stretched and in which the tension is evenly distributed between the two monolayers. In practice, a stretched membrane in a glass pipette as for patch clamping does not provide this uniformity. In patch clamp experiments a tight giga-Ohm (GΩ) seal between a membrane and a patch pipette is established. Those tight seals reduce background noise and enable the recording of single channel events. In this context, the patch adhesion to the glass pipette is significant and the resulting lipid bilayer mechanics have been extensively studied (Suchyna *et al.*, 2009; Ursell *et al.*, 2011; Slavchov *et al.*, 2014; Nakayama *et al.*, 2016). The resting tension of the patch, i.e. in the absence of transmembrane pressure when the patch is flat, ranges from ~1 to 5 mN/m (Opsahl and Webb, 1994). The lytic tension of a bilayer is determined to ~10 mN/m (Kwok and Evans, 1981). Thus, patch experiments are conducted under substantial and permanent resting tension that may alter channel kinetics (Suchyna *et al.*, 2009; Ursell *et al.*, 2011). The resting tension of the patch might be sufficient to activate the channels suggesting them to be extremely sensitive to membrane tension. Thus, Neq198 and Neq531 may exhibit a relatively small activation threshold compared to the *E. coli* MscS.

Furthermore, the transmembrane pressure gradient (Δp) causes the patch to bulge and the tension T increases according to Young-Laplace's law: $T = (\Delta p \times r) / 2$. Still, the radius of curvature (r) is rarely known (Ursell *et al.*, 2011). In addition an adhesion-driven creep of the patch is observed in glass pipettes that can not be neglected. Moving of the patch upwards the pipette changes the patch curvature radius, which directly influences the activation threshold (Slavchov *et al.*, 2014; Nakayama *et al.*, 2016). Therefore, activation thresholds should always be investigated in direct comparison to other MS channels. For example, MscSP from *S. pomeroyi* was characterized to exhibit an activation threshold that is between MscS and MscL of *E. coli* (Petrov *et al.*, 2013).

3 Single particle analysis using RELION

The MscS-like channels from *N. equitans* turned out to be difficult targets for processing using RELION. Both proteins are relatively small with sizes of 260-270 kDa. RELION - **RE**gularised **L**ikelihood **O**ptimisation - was developed by Sjors Scheres (Scheres, 2012a; Scheres, 2012b). It was written for and tested on well-defined data sets of macromolecular complexes, i.e. a rotavirus (VP7 recoated particle 7RP, ~60 MDa, Chen *et al.*, 2009), a hepatitis-B capsid (human Hepatitis B virus (HBV) capsid T=4, ~4.8 MDa, Böttcher *et al.*, 1997), a ribosome (70 S ribosome from *E. coli* with ~2.3 MDa, Scheres *et al.*, 2007), a groEL (798 kDa, Stagg *et al.*, 2006), and a β -galactosidase (450 kDa, Scheres and Chen, 2012). Therefore, data sets that provide e.g. preferred orientations or low signal to noise ratio (SNR) might not be dealt with optimally.

3.1 Protein quality and sample preparation challenges

The MscS-like channels have been purified in the detergent Fos14 and reconstituted into amphipols or lipid nanodiscs. Besides stability aspects of the protein in a more native environment like lipid nanodiscs, buffer compositions considerably influence grid preparation and quality in negative stain and cryo-EM. Sample preparation methods are considered as one of the most significant limitations in cryo-EM (Glaeser, 2015). For cryo-EM single particle analysis the specimen is embedded in a thin layer of amorphous ice (Dubochet *et al.*, 1982; Dubochet *et al.*, 1988). Several reagents are incompatible with cryo-EM. For example, high concentrations of glycerol (≤ 10 % (v/v)) that are often used to stabilize proteins prevent the acquisition of high-quality images. Glycerol would immediately bubble in the electron beam and therefore reduce contrast. Contrast in cryo-EM images relies on the density differences between the vitrified buffer (~ 0.93 g/cm³ for vitrified water) and the protein (~ 1.36 g/cm³) (Rubinstein, 2007). It is recommended to keep the buffer as simple as possible to avoid increasing the density of the buffer and by this decreasing the contrast. These effects are particularly problematic for small proteins (Rubinstein, 2007; Cheng *et al.*, 2015). Here, buffer composition of only 20 mM Tris and 100 mM NaCl were favored, which was only enabled by the reconstitution into nanodiscs (or amphipols). Neq531 needed to be stabilized with 10 % (v/v) glycerol so far. To avoid sample preparation issues with Neq531 in cryo-EM, a stabilizing environment like lipid nanodiscs and different buffer compositions are required. Moreover, detergents must be used at levels above their critical micelle concentration to prevent protein precipitation and/or aggregation and to ensure that the

protein remains in solution in a mono-disperse state. Such high detergent concentrations might interfere with cryo-EM sample preparation. Detergents reduce the surface tension of water so that the ice thickness is difficult to control, which in turn results in a loss of contrast. Moreover, detergent micelles might be mistaken for protein particles (Rubinstein, 2007; Schmidt-Krey and Rubinstein, 2011). Still, high resolution structures can be obtained in detergent, e.g. for the rabbit ryanodine receptor RyR1 in Tween20 (Yan *et al.*, 2015) or for the rotary H⁺-ATPase/synthase from *Thermus thermophilus* in LMNG (Nakanishi *et al.*, 2018). Alternative approaches such as amphipols and nanodiscs avoid these problems.

As a key requirement, particles must adopt random orientations to finally generate a 3D reconstruction of the protein. Moreover, sufficient image contrast is necessary. Image quality, i.e. image contrast, is critical to prevent model-induced bias. Low-dose images are extremely noisy. Especially for smaller particles it is difficult to validate the results since small molecules might not contain sufficient structural information for image alignment (Henderson, 2013).

The freezing conditions and consequently the ice thickness turned out to be essential for the analysis of Neq198. Reducing the ice thickness by longer blotting times in combination with an increased total electron dose resulted in higher signal to noise ratios. Moreover, side views of the particle were visualized and quantitatively detected during data processing. However, the thinnest ice does not necessarily imply that those are preferred conditions for the protein. In this context, the protein must be protected from the air-water interface. Brownian motion causes the protein to collide multiple times with the air-water interface between blotting and freezing. Some proteins are prone to stick to the air-water interface. Others may be partially or completely denatured (Glaeser, 2015, Cheng *et al.*, 2015). Data processing indicated that a high percentage of particles represented only one domain of the protein - either only the cytoplasmic domain or the membrane domain. The protein has fallen apart. It was assumed that the domains were sheared off during grid preparation as a result of reducing the ice thickness. Additionally, the protein might be already destabilized during protein purification. There are several approaches to stabilize proteins and prevent them to interact with the air-water interface. One trick is to add detergent in low concentrations to the buffer just before freezing.

Data processing revealed that the grids were contaminated with ice or crystalline ethane (Thompson *et al.*, 2016). Due to these contaminations manual picking was highly favored over auto-picking. For this MscS project automated picking was more model-based and prone to model-induced bias (“Einstein-from-noise”) (Henderson, 2013).

3.2 Nanodiscs versus amphipol reconstitution

Since the use of buffer compositions and detergents comprises challenges in negative stain and cryo-EM sample preparation (IV3.1), a reconstitution into amphipols and lipid nanodiscs was favored. Especially Neq198 was successfully stabilized in amphipols and nanodiscs. Neq531 could only be reconstituted into amphipols due to a lack of time and amphipol stabilized Neq531 still exhibited severe stability issues. Comparing the negative stain data for amphipols (Neq198 and Neq531) and nanodiscs (Neq198), it was noticed that the amphipol data showed less detail. The channels reconstituted into amphipols offered a general idea of the channel's overall structure and the cytoplasmic and membrane domain could be distinguished. Exclusively the lipid nanodiscs allowed to identify single subunits and confirmed the heptameric fold of Neq198 in negative stain and cryo-EM. The results obtained from nanodiscs in negative stain and cryo-EM will be discussed in more detail.

The reconstitution into amphipols (Popot *et al.*, 2003; Popot *et al.*, 2011) is relatively straightforward compared to that in nanodiscs. Moreover, the optimization is less laborious. But one of the major disadvantages of detergents and amphipols is that these systems do not provide additional lipids. The use of hydrophobic biobeads for the removal of detergents during the reconstitution procedure can even result in an additional loss of lipids due to their likewise interaction with the beads (Lévy *et al.*, 1999). This aspect might play an important role for Neq531, in particular. Its partially insufficient stabilization might be explained with a simultaneous loss of lipids, which compensates the positive stabilizing effect of the reconstitution into amphipols. It was already speculated that a purification in the presence of lipids might solve this problem. Additionally, a reconstitution into nanodiscs is favored here. Nanodiscs represent a more native environment than detergent micelles, bicelles, and amphipols. Currently, lipid nanodiscs describe the best-characterized and best-understood method (Efremov *et al.*, 2017). For nanodiscs, screening of the optimal reconstitution ratios of lipid:MSP:protein requires large amounts of protein and a considerable quantity of protein is lost during the reconstitution procedure. Whether a reconstitution was successful is sometimes difficult to evaluate for some proteins.

In literature, successfully solved structures in amphipols and nanodiscs are reported. High-resolution structures of TRPV1 (Liao *et al.*, 2013) and γ -secretase (Bai *et al.*, 2015) reconstituted into amphipols have been solved to resolutions of 3.4 Å. Furthermore, the human TRPA1 (Paulsen *et al.*, 2015) and the human sodium-bicarbonate cotransporter NBCe1 (Huynh *et al.*, 2018) reconstituted into amphipol PMAL-C8 were solved to ~ 4 Å and 3.9 Å by cryo-EM, respectively. But particularly nanodiscs gained

popularity in the last couple of years and were used to solve several medium- to high-resolution structures in cryo-EM (Table IV.1).

Table IV.1: Representative membrane proteins that have been reconstituted into nanodiscs for structure determination in cryo-EM

Protein	Protein size	MSP construct	Lipids	Resolution (Å)	Reference/EMDB
Vascular ATPase V _o proton channel <i>S. cerevisiae</i>	~320 kDa	MSP1E3D1	EPL	3.5	Roh <i>et al.</i> , 2018 n/a
TRPM4 <i>Homo sapiens</i>	540 kDa	MSP2N2	Soy-PL	3.1	Autzen <i>et al.</i> , 2018 7132
TRPML1 <i>Mus musculus</i>	260 kDa	MSP1	POPC:POPG:POPE (3:1:1)	3.59	Chen <i>et al.</i> , 2017 8883
NOMPC <i>Drosophila melanogaster</i>	~760 kDa	MSP2N2	Soy-PC	3.55	Jin <i>et al.</i> , 2017 8702
MsbA <i>E. coli</i>	~130 kDa	MSP1D1	<i>E. coli</i> PL	4.2	Mi <i>et al.</i> , 2017 8469
TRPV1 <i>Rattus norvegicus</i>	330 kDa	MSP1E3, MSP2N2	Soy-PL	3.28	Gao <i>et al.</i> , 2016 8118
CorA <i>Thermotoga maritima</i>	~200 kDa	MSP1D1	POPC POPG	3.8	Matthies <i>et al.</i> , 2016 6551
PKD2 <i>Homo sapiens</i>	340 kDa	MSP2N2	Soy-PL	3.0	Shen <i>et al.</i> , 2016 8354
RyR1 <i>Oryctolagus cuniculus</i>	2.3 MDa	MSPD1E3	POPC	6.1	Efremov <i>et al.</i> , 2015 2751
Ribosome- SecYE complex <i>E. coli</i>	SecYEG 74 kDa, bound to <i>E. coli</i> 70S ribosome (2.4 MDa)	MSP1D1	<i>E. coli</i> total lipids extract	7.1	Frauenfeld <i>et al.</i> , 2011 1858

If several structures for a protein are deposited in EMDB, only one representative accession number is provided. The structure of the vascular ATPase V_o proton channel was not deposited yet in EMDB (n/a).

Since the negative stain data of Neq198 reconstituted into nanodiscs already provided relatively detailed information about the protein, nanodiscs as a stabilizing native-like environment are highly favored over amphipols. Moreover, recent publications highlight the extensive use and broad application of nanodiscs in structure analysis.

Nanodiscs were first described by Sligar and co-workers (Bayburt *et al.*, 1998; Bayburt *et al.*, 2002). Initially, the lipid nanodisc system aimed at functional studies of membrane proteins but then emerged as a valuable tool for stabilizing membrane proteins for structure analysis. For single particle analysis of nanodiscs a large extra-membrane domain is favored; otherwise the alignment is prone to errors. With their large cytoplasmic domain, MscS-like channels reconstituted into nanodiscs constitute excellent targets for single particle analysis in cryo-EM. As mentioned before, the nanodisc data set comprised much more detail than the one with protein reconstituted into amphipol. Examining the data set for negative stain, in 2D class-averages seven single subunits were identified in the cytoplasmic domain of the protein. However, the membrane domain did not provide much detail. Especially in cryo-EM, the membrane domain showed low signal-to-noise ratios. Surprisingly, additional density of

Table IV.2: Commonly used membrane scaffold protein constructs (Ritchie *et al.*, 2009)

MSP construct	Disc size in nm
MSP1	9.7 ^a /9.8 ^b
MSP1D1	9.5 ^a /9.7 ^b
MSP1E1D1	10.5 ^a
MSP1E2D1	11.1 ^a
MSP1E3D1	12.1 ^a
MSP2N2	15.0 ^a /16.5 ^b
MSP2N3	15.2 ^a /17.0 ^b

^a Stokes hydrodynamic diameter, determined by SEC; ^b diameter determined by SAXS (Denisov *et al.*, 2004)

lipids from the nanodiscs were never clearly visible for Neq198 in single particle analysis. Neither the negative data nor the cryo-EM data showed a density as it would have been expected. The size of the nanodisc is essential for a successful reconstitution. Many different MSP constructs are available that result in different disc sizes (Table IV.2). The MSP construct should be chosen adequate for the incorporated protein. The MSP construct used for the reconstitution into nanodiscs of Neq198 from discs with a size of ~12 nm in diameter. The channel fits in this size but might be encircled by the MSP belt too tight that causes the protein to be embedded in only few lipids. This might explain why the lipid belt around the channel in nanodiscs was never observed in single particle analysis. A similar

observation was made by Cheng and co-workers, who determined the TRPV1 structure in lipid nanodiscs to a resolution of 3.28 Å (Table IV.1) (Gao *et al.*, 2016). Two different MSP constructs were tested: MSP1E3 and MSP2N2, resulting in nanodiscs with ~12 nm and ~15-16.5 nm in diameter, respectively. Finally, the smaller nanodiscs were dropped since the encircling MSP belt could not be clearly identified in 2D classification. Therefore, structure analysis was focused on the MSP2N2 construct (Gao *et al.*, 2016). The protein might be exposed to structural constraints and might be forced into non-native conformations if the membrane scaffold protein encircles the embedded membrane

protein too tight. The nanodiscs should be just large enough to accommodate the incorporated protein, but keep at least two layers of lipids between the encircling MSP and the protein. By this, unwanted interactions with the MSP are avoided (Efremov *et al.*, 2017). Molecular dynamics simulations have shown that the lipid bilayer that is in direct contact with the encircling MSP is perturbed due to hydrophobic mismatches between MSP and lipids. However, two layers of lipid molecules between MSP and incorporated protein (15-20 Å) are sufficient to ensure lipid properties similar to those in lipid bilayers (Shih *et al.*, 2005; Schuler *et al.*, 2013). How nanodisc size considerably influences the incorporated protein, was shown e.g. for the ABC transporter MsbA, whose activity is higher in larger nanodiscs containing more lipids (Kawai *et al.*, 2011). Recently, other scaffold systems for the stabilization of membrane proteins in lipid environments were published: (1) a styrene maleic acid copolymer (SMA) lipid particle system, referred to as SMALPs (Knowles *et al.*, 2009) and (2) a saposin-lipoprotein nanoparticle system, namely Salipro (Frauenfeld *et al.*, 2016). The latter was successfully used for the reconstitution of various membrane proteins. Their application for structure determination has been demonstrated (Frauenfeld *et al.*, 2016; Lyons *et al.*, 2017). Amongst others, the archaeal mechanosensitive channel T2 from *Thermoplasma volcanium* (Lów *et al.*, 2013) was successfully reconstituted as a model protein. The channel adopted random orientation in negative stain. In 2D class-averages the membrane and cytoplasmic domain were identified (Frauenfeld *et al.*, 2016). These results were similar to those found for Neq198, here. Saposin A demonstrates its advantage over nanodiscs by its ability to adopt to the size of the membrane proteins. Therefore, it is applicable to a wide range of membrane proteins without the need to screen for various membrane scaffold protein constructs. However, saposin A indicated a preference for certain lipids. Saposin A incubated with phosphatidylethanolamine and *E. coli* total lipids extract did not result in the formation of soluble saposin-lipoprotein particles (Frauenfeld *et al.*, 2016). On the other hand, SMALPs hold great potential since this system allows the detergent-free isolation of membrane proteins, while the local lipid environment is preserved (Lee *et al.*, 2016). Their application to structure analysis has been proven for the multidrug efflux pump subunit AcrB from *E. coli*. Here, SMALPs were successfully used for structure studies in negative stain electron microscopy (Postis *et al.*, 2015) and structure determination to 8.8 Å in cryo-EM (Parmar *et al.*, 2018). So far, nanodiscs seems to be preferred for structure determination of membrane proteins but SMALPs and Salipros represent valuable alternatives.

3.3 Preferred orientation and neighbouring particles

Upon processing the cryo-EM data, it was noticed that most of the particles showed a preferred orientation. Most of the particles represented top views and only very few of them side views or tilted views. The orientation was profoundly influenced by the ice thickness. For the first data sets, the grids were blotted for only 1.2-2.2 s resulting in ice that was too thick. The resulting micrographs exhibited a low signal to noise ratio and particles could hardly be identified. Increasing the blotting time resulted in micrographs with a higher signal to noise ratio and resulted in a detectable portion of different side and tilted views.

Besides ice thickness, different orientations of the particles can be triggered by additives supplemented to sample preparation buffers before plunge freezing. Especially the addition of detergents in low concentrations is favored here. For example, Zhao *et al.*, 2015 screened multiple detergents to change the preferred orientation of the 20S supercomplex. The addition of Noidet P-40 successfully resulted in more side views, although these buffer conditions dramatically reduced the particle densities in the vitreous ice (Zhao *et al.*, 2015).

Another issue was caused by neighbouring particles. The negative effect of neighbouring particles on structure analysis was shown for YnaI from *E. coli*. Here, contact sides between particles became evident from 2D classification to final 3D refinement and resulted in extra densities in the final 3D reconstruction (Böttcher *et al.*, 2015). Unless the 2D classification was not slowed down, it was almost impossible to separate neighbouring particles from the data set. They interfered with the alignment. If particles were too close or overlapping, they were even misinterpreted as side views of the protein. Neighbouring particles still popped up in 3D classification and had to be removed manually from the data set. Analysis highlighted that a large amount of particles represented neighbouring particles that were not eligible for structure analysis. This can be seen as another indication that more time should be spent on optimization of sample preparation. Nevertheless, neighbouring particles were successfully controlled by modifying processing parameters.

During processing of the different data sets “Feb2017” and “Jun2017” it could be observed that the particles collapsed into only few classes during 2D classification. This was manifested by the fact that not all of the given classes were filled. Instead only half of the given classes or in extreme cases only three out of 100 classes were filled. Collapsed classes were undefined lacking any details and showed spikes. This well-known problem is also described as the “attraction problem”. Classification depends on the similarity to the reference class. If the data consists of dominating types of particles, the similarity is mostly driven by noise rather than the signal itself (Sorzano *et al.*, 2010). Classification

relies on (1) differentiation and (2) accumulation. Classes need to first become as different as possible, and then data needs to be accumulated in significant enough proportions for the class to be recognized. 2D classification can tend to miss out on the differentiation step, simply because the convergence is too fast. This results in detection of only the most dominating type of data. To avoid this, convergence needs to be slowed down. There are a few ways during the RELION workflow to deal with this issue: (1) ignoring CTFs until first peak (CTF tab), (2) setting up an additional argument in the running tab of 2D classification with `--maxsig 5`, (3) using small subsets with ~ 100 particles per class (10,000 particles input/100 classes) in the optimization tab. If 2D class-averages look too similar, one has to re-pick the data in an objective way.

The cryo-EM data of Neq198 showed a preferred orientation of particles. Top views that dominated the data set caused the aforementioned RELION processing issues. To actively influence that the particles are picked in a more objective way, manual picking was - besides other reasons - preferred over auto-picking. Following the aforementioned suggestions, collapsing of classes was avoided. As a positive side effect, classes showing neighboring particles could be continuously and effectively separated from the data set.

3.4 Heterogeneity within a data set

Both channel protein preparations exhibited a certain degree of heterogeneity. Neq531 was difficult to purify and its propensity to aggregate or degrade was also reproduced and confirmed in negative stain single particle analysis. Heterogeneity to a minor degree can be tolerated since during data processing “defective” particles can be excluded. How heterogeneity was successfully dealt with was shown e.g. for U4/U6.U5 tri-snRNP, a sustanital part of the spliceosome from *S. cerevisiae*, that was solved to 3.7 Å (Nguyen *et al.*, 2016; Scheres, 2016). In the case of Neq531 in negative stain only $\sim 32\%$ of all picked particles served as input for 3D classification. These particles were further reduced prior to refinement to $\sim 15\%$. Compared to the negative stain data set of Neq198, the data set quality of Neq531 was therefore relatively poor. Particle picking and cleaning the data set from “defective” particles is one of the most time-consuming steps in data processing. Moreover, it is not always obvious how the cryo-preservation influenced protein quality. Cryo-EM sample preparations have already been shown to introduce artefacts and impair protein quality. Since the channel Neq531 already revealed stability and aggregation issues, in cryo-EM these would possibly get even worse. To improve resolution it is often better to invest all efforts in an optimization of protein quality, instead of re-picking and cleaning the data set. The experience with the Neq198 cryo-EM data set has shown that

heterogeneity to a minor degree can be tolerated. Particularly for Neq198, top view particles missing one or two subunits were easily identified during 2D classification and were excluded from further processing. Particles that showed irregularities in the membrane domain due to missing subunits or preparation artefacts were tolerated since missing subunits are averaged out due to the applied sevenfold symmetry in 3D classification. Particles that showed major preparation artefacts were excluded by 3D classification. The ability to identify and separate heterogeneous particle populations depends critically on the signal to noise ratio of the images and on the magnitude of differences among the populations (Sigworth, 2016). Actually, reconstitution into nanodiscs was shown to result in homogeneous, monodisperse and high-yield preparations (Denisov *et al.*, 2004) (Bayburt *et al.*, 2006). However, obtaining completely homogeneous nanodisc preparations in practice is difficult and a certain degree of inhomogeneity has to be taken into account usually (Nasr *et al.*, 2017; Efremov *et al.*, 2017). The negative effect of inhomogeneity of nanodiscs was highlighted in the case of CorA, the magnesium channel from *T. maritima*. Here, heterogeneity interfered with particle alignment and therefore hindered a high-resolution 3D reconstruction (Matthies *et al.*, 2016).

Serious consequences for data processing were brought up by the putative top views of Neq198. 3D classification identified those particles to result in spherical 3D reconstructions suggesting that only one domain of the protein was represented. The protein domains were probably sheared off upon sample preparation for cryo-EM (IV3.1). If about 75 % of the particles that serve as input for 3D classification are represented by protein that only consists of one domain while the second domain is missing, sample preparation should be seriously revisited. Those particles did not interfere with final 3D volumes or were successfully isolated, but consumed work load and were misleading as they were assumed to represent top views of the protein.

4 Structure of the first archaeal MscS-like channel

Single particle analysis in cryo-EM led to a first structure of Neq198. Neq198 exhibits a similar sevenfold symmetric organization as it was observed for other members of the MscS family in *E. coli*, *H. pylori* and *T. tencongensis* (Bass *et al.*, 2002; Wang *et al.*, 2008; Zhang *et al.*, 2012; Lai *et al.*, 2013). The cytoplasmic domain, especially the lateral portals and the C-terminal opening through the β -barrel are almost identical to that in *EcMscS*. The cytoplasmic vestibule was shown to provide

stability (Schumann *et al.*, 2004; Rasmussen *et al.*, 2007) and selectivity (Zhang *et al.*, 2012; MaksaeV and Haswell, 2013; Cox *et al.*, 2014).

Interestingly, single particle analysis of negative-stained Neq198 and Neq531 revealed minor structural differences between both MscS-like channels. Sequence analysis already indicated differences in the cytoplasmic domain, which is slightly larger for Neq531. Besides the C-terminal β -strand that forms a β -barrel in the heptameric complex, an additional short helix following the β -strand is predicted. In negative stain evident differences with respect to the β -barrel could be observed. Whereas the β -barrel can hardly be identified in 2D class-averages of Neq198, it represents an eye-catching structural feature for Neq531. In addition to structure prediction, single particle analysis confirmed that the β -barrel constitutes a larger and important structural feature for Neq531. A larger β -barrel or the additional C-terminal helices of Neq531 might indicate a different selectivity mechanism in contrast to Neq198 and *EcMscS* as well.

The N-terminal extension of Neq198 resulted in a significantly larger channel that protrudes into the periplasm and builds a cap-like structure. The central pore in Neq198 agrees with the pore diameter in an open *EcMscS*. The overall dimension of Neq198 with ~ 160 Å parallel to the sevenfold axis of the channel exceeds the dimensions of *EcMscS* that is 120 Å in length (Bass *et al.*, 2002). Comparing *EcMscS* in closed (2oau.pdb; Bass *et al.*, 2002) and open (2vv5.pdb; Wang *et al.*, 2008) conformation with the structure model of Neq198, the cytoplasmic vestibule and helix TM3 remain essentially unchanged. However, there are major changes for the membrane domain. The helices TM1 and TM2 move as a rigid paddle and increase their tilt with respect to the sevenfold axis of the channel (Figure 52). The paddle moves in the opposite direction than for the opening of *EcMscS* (2vv5.pdb) (cf. I1.2.2). The movement of the paddle for Neq198 should be evaluated with care, since structural constraints due to the tight membrane scaffold protein from the lipid nanodiscs can not be excluded.

The cap-like structure on top of the membrane domain of the channel represents a new feature that was not yet observed for other mechanosensitive channels. For *EcMscS* the first N-terminal 26 amino acids and the last C-terminal six residues have not been modelled in the crystal structure due to a lack of well-defined density corresponding to these sequences (Bass *et al.*, 2002; Vázquez *et al.*, 2008). Therefore it remains elusive whether *EcMscS* exhibits a similar periplasmic extra-domain structure as observed for *N. equitans*. If not, this structure might represent a unique feature of archaeal mechanosensitive channels or of organisms that exhibit an S-layer. It possibly enables the fixation in and interaction with the S-layer of *N. equitans*. The role of S-layers in transmitting tension and therefore its role in channel function was not investigated for any mechanosensitive channel so far,

leaving it open for speculation. The *E. coli* homologues YbiO, YjeP and MscK, which belong to the larger topological class of channels, are predicted to exhibit larger periplasmic domains as well (II.2.1).

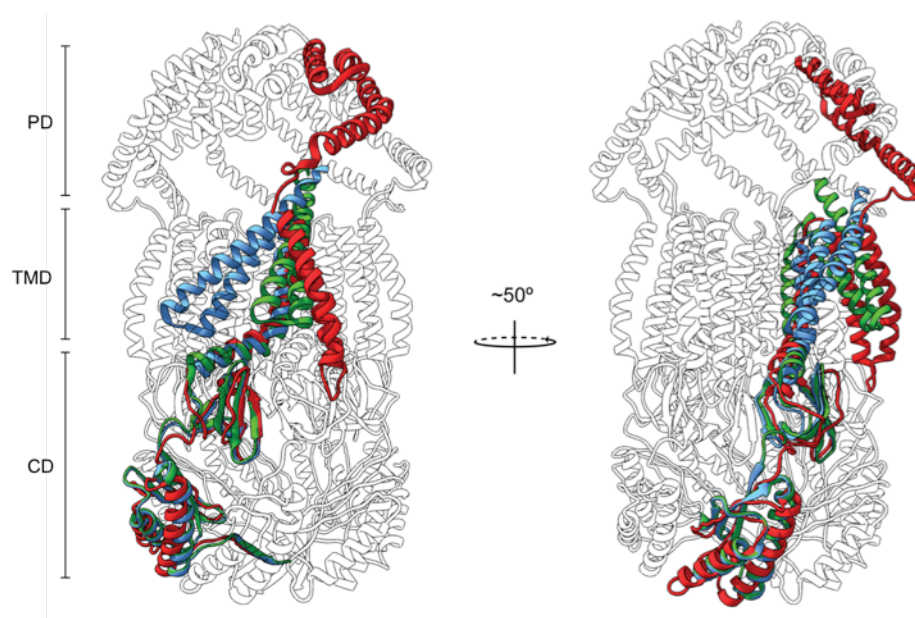


Figure 52: Structural comparison of Neq198 and *EcMscS*.

Neq198 is superposed on *EcMscS* in two different conformations; one protomer is highlighted: Neq198 (red), *EcMscS* in open (blue) (2oau.pdb, Bass *et al.*, 2002) and closed (green) (2vv5.pdb, Wang *et al.*, 2008) conformation. The heptamer of Neq198 is shown in white; PD – periplasmic domain, TMD - transmembrane domain, CD - cytoplasmic domain.

EcMscS exhibits a slight preference for anions over cations ($P_{Cl}/P_K \sim 1.2-3.0$) (Martinac *et al.*, 1987; Sukharev *et al.*, 1993). According to a proposed selectivity mechanism, negatively charged regions at the bottom of the cytoplasmic vestibule trap cations that enter through the lateral portals, resulting in an easier transit of anions (II.2.2; Cox *et al.*, 2014). Neq198 shows regions of high electronegativity at the bottom of the cytoplasmic vestibule (Figure 53A). Moreover, the β -barrel is negatively charged in Neq198 in contrast to the positively charged β -barrel in *EcMscS* (Figure 53B). This might result in higher anion selectivity in Neq198. Higher anion selectivity in contrast to *EcMscS* was already observed for *TtMscS*. Here, the β -barrel region mainly confers the anion selectivity since the lateral portals are significantly smaller in *TtMscS* than *EcMscS* (Zhang *et al.*, 2012; Song *et al.*, 2017). In Neq198 the β -barrel is likely to contribute to anion selectivity as well. How the aforementioned additional C-terminal helical bundle of Neq531 influences the selectivity mechanism, is open for speculation and will be addressed in future analyses.

The periplasmic domain of Neq198 is mostly uncharged. Only the very top of the cap-like structure exhibits highly positive charges, which possibly aims at an interaction with the surrounding S-layer of *N. equitans*.

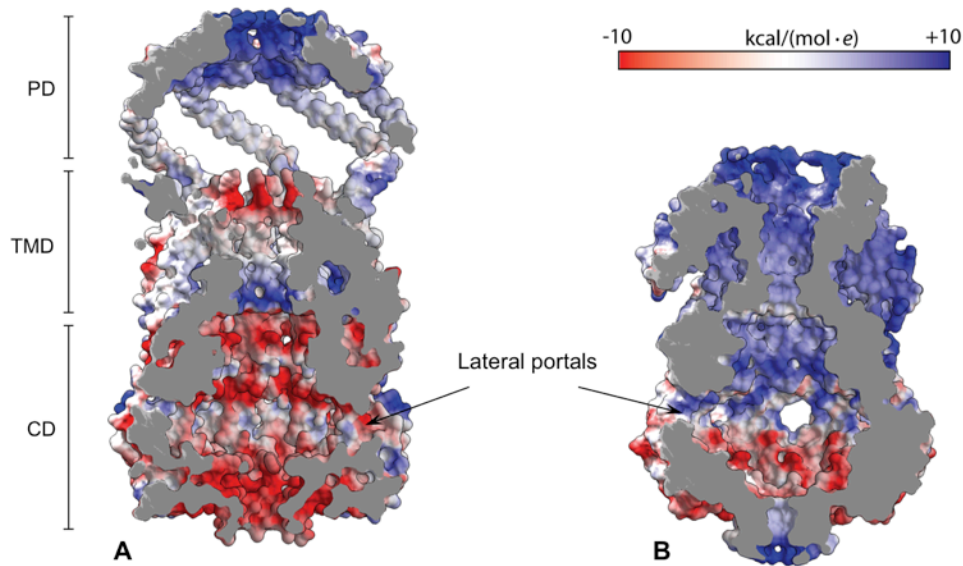


Figure 53: Electrostatic potential surface of Neq198 and EcMscS.

Comparison of the electrostatic potential surface in Neq198 (left) and EcMscS (right) (2oau.pdb, Bass *et al.*, 2002); the channel is shown normal to the sevenfold axis, slice along the central long axis through the side view, capped surface is visualized in grey; the lateral portals, through which ions enter the cytoplasmic vestibule, are indicated; PD - periplasmic domain, TMD - transmembrane domain, CD - cytoplasmic domain.

5 Conclusions and future directions

Two MscS-like channels from *N. equitans*, Neq198 and Neq531, have been structurally and functionally analyzed. Isolated Neq198 was much more stable compared to Neq531 due to a different set of associated lipids. Purification in the presence of lipids and immediate reconstitution into lipid nanodiscs is recommended for future high-resolution structural and more conclusive functional work with Neq531. A direct reconstitution into nanodiscs (Shirzad-Wasei *et al.*, 2015) might be beneficial as well. Our knowledge on cryo-preservation and data processing of Neq198 will be beneficial for the further analysis of Neq531. One future aim will be to compare both channels structurally at resolutions better than 5 Å.

At the present resolution the membrane domain of Neq198 was only poorly resolved. Still, 2D class-averages provided structural information that would have been expected to result in more details in the final 3D reconstruction of the protein. Loss in detail is attributed to too tight MSP interactions and shortcomings in data processing. Since the cytoplasmic domain was dominant, particle alignment was highly focussed on this domain rather than the center of the protein. Here, masking of the membrane domain might be constructive. As discussed, the size of the encircling membrane scaffold protein is highly relevant for a structural analysis (IV3.2). Since negative effects with respect to structural constraints in nanodiscs, which are too small, are not conceivable, a larger MSP for reconstitution is favored. A new preparation in larger MSP2N2 (Denisov *et al.*, 2004; Ritchie *et al.*, 2009) followed by single particle analysis in cryo-EM addresses this issue.

In general, RELION might not optimally deal with small particles. Therefore, data processing with alternative programs or a complementary use might be beneficial for this project. Up to date, there are various different softwares available for cryo-EM data processing such as EMAN2 (Ludtke *et al.*, 1999; Tang *et al.*, 2007), FREALIGN (Grigorieff, 2007), IMAGIC (van Heel *et al.*, 1996), cryoSPARC (Punjani *et al.*, 2017), SPARX (Hohn *et al.*, 2007) or SPHIRE (SPARx for High Resolution Electron Microscopy) (Moriya *et al.*, 2017), and SPIDER (System for Processing Image Data from Electron microscopy and Related fields) (Frank *et al.*, 1996; Shaikh *et al.*, 2008).

Particle picking is assumed as a bottleneck in cryo-EM data processing. Manual picking of cryo-EM particles of Neq198 turned out to be tedious and time-consuming. This approach was favored over the auto-picking option implemented in RELION. Particularly contaminations and the carbon areas complicated optimizing of the parameters (inter-particle distance and picking threshold) and the picking procedure. Of course, auto-picking is appealing because of suspected time saving. Nonetheless, the final output can be doubted when thoroughly revising is necessary. Thus, an alternative to the auto-picking in RELION should be evaluated. The program Gautomatch was developed by Dr. K. Zhang at MRC Laboratory of Molecular Biology and provides an accurate, fast, flexible, and fully automatic particle picking from cryo-EM micrographs with or without templates (<http://www.mrc-lmb.cam.ac.uk/kzhang/>). It is compatible with RELION and EMAN. Especially the implemented feature of automatically detecting non-particle areas such as ice and carbon and rejecting them, addresses the aforementioned issues. Recently, Gautomatch was used in various studies relating e.g. ryanodine receptors (Wei *et al.*, 2016), haemoglobin (Khoshouei *et al.*, 2017), triheteromeric NMDA receptor (Lü *et al.*, 2017), human cytoplasmic dynein (Zhang *et al.*, 2017), and the human SLC4A4 Na⁺-coupled acid-base transporter NBCe1 (Huyhn *et al.*, 2018).

With respect to channel functionality several questions need to be addressed in future. To test whether Neq531 also exhibits characteristics of mechanosensitivity, a hypoosmotic down shock assay should be performed as well. Although the test system in *E. coli* might not be ideal, the results offer indications with respect to mechanosensitivity at least. If the hypoosmotic down-shock assay for Neq198 had been negative, the capability of the channels to react to mechanical stimuli would have been seriously doubted, as well as in context with observed difficulties in patch clamp experiments.

The test systems in liposomes and *E. coli* spheroplasts created several challenges in patch clamp analysis. Therefore, native lipids of *N. equitans* should be extracted for a reconstitution of both channels into liposomes comprised of archaeal lipids (archaeosomes). Probably, an electrophysiological characterization by patch clamp technique is rendered possible by this approach. The structure in hand of Neq198 in combination with a homology model of Neq531 might allow assumptions with respect to ion selectivity. For this, the cytoplasmic domain and in particular the electrostatic potential surface in close proximity to the lateral portals and at the bottom of the cytoplasmic domain is compared to other MscS such as *EcMscS* and *TtMscS*. For example, Cox *et al.*, 2013 provided a ranking of several MscS channels with respect to cation and anion selectivity. Finally, a proper characterization with respect to activation threshold, inactivation and ion selectivity is sought. By this, it might be partially explained why *N. equitans* possesses two MscS-like channels although its genome is highly reduced and only a limited set of transporters and channels is available.

Furthermore, the physiological role of the MscS-like channels might be of interest for the intimate association with *I. hospitalis* as well. Previous studies concerning the interaction of both organisms have shown that a direct transport of e.g. amino acids and lipids must take place (Jahn *et al.*, 2004). Moreover, a fusion of both cell membranes and a partial degradation of the S-layer from *N. equitans* at the contact site were observed (Heimerl *et al.*, 2017). MscS-like channels might have crucial roles in regulating and fine-tuning intracellular ion concentrations resulting from the direct contact to the *I. hospitalis* cell and transport activities. A localization of the channels in the cell membrane of *N. equitans* would elucidate their distribution. The generation of antibodies against the purified proteins followed by TEM immunogold labelling addresses these considerations.

With high-resolution structures in hand and in combination with a localization of both channels in the host-symbiont association of *N. equitans* with *I. hospitalis*, important questions on additional functions of archaeal MS channels can be answered in future.

V REFERENCES

- Adams, DW, Errington, J (2009).** Bacterial cell division: assembly, maintenance and disassembly of the Z ring. *Nat Rev Microbiol* **7**, 642-653.
- Akitake, B, Anishkin, A, Sukharev, S (2005).** The “dashpot” mechanism of stretch-dependent gating in MscS. *J Gen Physiol* **125**, 143-154.
- Albers, S-V, Meyer, BH (2011).** The archaeal cell envelope. *Nat Rev Microbiol* **9**, 414-426.
- Anishkin, A, Sukharev, S (2004).** Water dynamics and dewetting transitions in the small mechanosensitive channel MscS. *Biophys J* **86**, 2883-2895.
- Árnadóttir, J, Chalfie, M (2010).** Eukaryotic mechanosensitive channels. *Annu Rev Biophys* **39**, 111-137.
- Autzen, HE, Myasnikov, AG, Campbell, MG, Asarnow, D, Julius, D, Cheng, Y (2018).** Structure of the human TRPM4 ion channel in a lipid nanodisc. *Science* **359**, 228-232.
- Bai, X-c, Yan, C, Yang, G, Lu, P, Ma, D, Sun, L, Zhou, R, Scheres, SHW, Shi, Y (2015).** An atomic structure of human γ -secretase. *Nature* **525**, 212-217.
- Baldwin, PA, Hubbell, WL (1985).** Effects of lipid environment on the light-induced conformational changes of rhodopsin. 2. Roles of lipid chain length, unsaturation, and phase state. *Biochemistry* **24**, 2633-2639.
- Balleza, D, Gómez-Lagunas, F (2009).** Conserved motifs in mechanosensitive channels MscL and MscS. *Eur Biophys J* **38**, 1013-1027.
- Balleza, D (2011).** Mechanosensitive channels in archaea: roles, lipid-protein interactions and future questions, in *Archaea: Structure, Habitats and Ecological Significance*, chap. 6, pp. 143-161.

- Bass, RB, Strop, P, Barclay, M, Rees, DC (2002).** Crystal structure of *Escherichia coli* MscS, a voltage-modulated and mechanosensitive channel. *Science* **298**, 1582-1587.
- Bayburt, TH, Carlson, JW, Sligar, SG (1998).** Reconstitution and imaging of a membrane protein in a nanometer-size phospholipid bilayer. *J Struct Biol* **123**, 37-44.
- Bayburt, TH, Grinkova, YV, Sligar, SG (2002).** Self-assembly of discoidal phospholipid bilayer nanoparticles with membrane scaffold proteins. *Nano Lett* **2**, 853-856.
- Bayburt, TH, Sligar, SG (2003).** Self-assembly of single integral membrane proteins into soluble nanoscale phospholipid bilayers. *Protein Sci* **12**, 2476-2481.
- Bayburt, TH, Grinkova, YV, Sligar, SG (2006).** Assembly of single bacteriorhodopsin trimers in bilayer nanodiscs. *Arch Biochem Biophys* **450**, 215-222.
- Bayburt, TH, Sligar, SG (2010).** Membrane protein assembly into Nanodiscs. *FEBS Lett* **584**, 1721-1727.
- Becker, M (2013).** Biochemische und elektrophysiologische Charakterisierung der dualen Funktion des Kanals MscCG aus *Corynebacterium glutamicum*. Dissertation, Universität zu Köln.
- Becker, M, Börngen, K, Nomura, T, Battle, AR, Marin, K, Martinac, B, Krämer, R (2013).** Glutamate efflux mediated by *Corynebacterium glutamicum* MscCG, *Escherichia coli* MscS, and their derivatives. *Biochim Biophys Acta - Biomembr* **1828**, 1230-1240.
- Belyy, V, Anishkin, A, Kamaraju, K, Liu, N, Sukharev, S (2010).** The tension-transmitting 'clutch' in the mechanosensitive channel MscS. *Nat Struct Mol Biol* **17**, 451-458.
- Berrier, C, Coulombe, A, Houssin, C, Ghazi, A (1989).** A patch-clamp study of ion channels of inner and outer membranes and of contact zones of *E. coli*, fused into giant liposomes. *FEBS Lett* **259**, 27-32.
- Berrier, C, Besnard, M, Ajouz, B, Coulombe, A, Ghazi, A (1996).** Multiple mechanosensitive ion channels from *Escherichia coli*, activated at different thresholds of applied pressure. *J Membr Biol* **151**, 175-187.
- Bertani, G (1951).** Studies on lysogenesis I.: The mode of phage liberation by lysogenic *Escherichia coli*. *J Bacteriol* **62**, 293-300.
- Beveridge, TJ, Graham, LL (1991).** Surface layers of bacteria. *Microbiol Rev* **55**, 684-705.
- Beveridge, TJ, Pouwels, PH, Sára, M, Kotiranta, A, Lounatmaa, K, Kari, K, Kerosuo, E, Haapasalo, M, Egelseer, EM, Schocher, I, Sleytr, UB, Morelli, L, Callegari, M-L, Nomellini, JF, Bingle, WH, Smit, J, Leibovitz, E, Lemaire, M, Miras, I, Salamiou, S, Béguin, P, Ohayon, H, Gounon, P, Matuschek, M, Sahm, K, Bahl, H, Grogono-Thomas, R, Dworkin, J, Blaser, MJ, Woodland, RM, Newell, DG, Kessel, M, Koval, SF (1997).** V. Functions of S-layers. *FEMS Microbiol Rev* **20**, 99-149.

- Bezanilla, F, Perozo, E (2002).** Force and voltage sensors in one structure. *Science* **298**, 1562-1563.
- Blake, MS, Johnston, KH, Russell-Jones, GJ, Gotschlich, EC (1984).** A rapid, sensitive method for detection of alkaline phosphatase-conjugated anti-antibody on Western blots. *Anal Biochem* **136**, 175-179.
- Blount, P, Sukharev, SI, Schroeder, MJ, Nagle, SK, Kung, C (1996).** Single residue substitutions that change the gating properties of a mechanosensitive channel in *Escherichia coli*. *Proc Natl Acad Sci USA* **93**, 11652-11657.
- Bondos, SE, Bicknell, A (2003).** Detection and prevention of protein aggregation before, during, and after purification. *Anal Biochem* **316**, 223-231.
- Booth, IR, Edwards, MD, Black, S, Schumann, U, Miller, S (2007).** Mechanosensitive channels in bacteria: signs of closure? *Nat Rev Microbiol* **5**, 431-440.
- Booth, IR, Rasmussen, T, Edwards, MD, Black, S, Rasmussen, A, Bartlett, W, Miller, S (2011).** Sensing bilayer tension: Bacterial mechanosensitive channels and their gating mechanisms. *Biochem Soc Trans* **39**, 733-740.
- Booth, IR, Blount, P (2012).** The MscS and MscL families of mechanosensitive channels act as microbial emergency release valves. *J Bacteriol* **194**, 4802-4809.
- Booth, IR, Miller, S, Müller, A, Lehtovirta-Morley, L (2015).** The evolution of bacterial mechanosensitive channels. *Cell Calcium* **57**, 140-150.
- Börngen, K, Battle, AR, Möker, N, Morbach, S, Marin, K, Martinac, B, Krämer, R (2010).** The properties and contribution of the *Corynebacterium glutamicum* MscS variant to fine-tuning of osmotic adaptation. *Biochim Biophys Acta - Biomembr* **1798**, 2141-2149.
- Böttcher, B, Wynne, SA, Crowther, RA (1997).** Determination of the fold of the core protein of hepatitis B virus by electron cryomicroscopy. *Nature* **386**, 88-91.
- Böttcher, B, Prazak, V, Rasmussen, A, Black, Susan S, Rasmussen, T (2015).** The structure of YnaI implies structural and mechanistic conservation in the MscS family of mechanosensitive channels. *Structure* **23**, 1705-1714.
- Bradford, MM (1976).** A rapid and sensitive method for the quantitation of microgram quantities of protein utilizing the principle of protein-dye binding. *Anal Biochem* **72**, 248-254.
- Brohawn, SG, Campbell, EB, MacKinnon, R (2014).** Physical mechanism for gating and mechanosensitivity of the human TRAAK K⁺ channel. *Nature* **516**, 126-130.
- Buchan, DWA, Minnici, F, Nugent, TCO, Bryson, K, Jones, DT (2013).** Scalable web services for the PSIPRED Protein Analysis Workbench. *Nucleic Acids Res* **41**, W349-W357.
- Buddelmeijer, N, Beckwith, J (2002).** Assembly of cell division proteins at the *E. coli* cell center. *Curr Opin Microbiol* **5**, 553-557.

- Burghardt, T, Nather, DJ, Junglas, B, Huber, H, Rachel, R (2007).** The dominating outer membrane protein of the hyperthermophilic Archaeum *Ignicoccus hospitalis*: a novel pore-forming complex. *Mol Microbiol* **63**, 166-176.
- Burghardt, T, Saller, M, Gurster, S, Muller, D, Meyer, C, Jahn, U, Hochmuth, E, Deutzmann, R, Siedler, F, Babinger, P, Wirth, R, Huber, H, Rachel, R (2008).** Insight into the proteome of the hyperthermophilic Crenarchaeon *Ignicoccus hospitalis*: the major cytosolic and membrane proteins. *Arch Microbiol* **190**, 379-394.
- Caffrey, M, Feigenson, GW (1981).** Fluorescence quenching of model membranes. 3. Relationship between calcium adenosinetriphosphatase enzyme activity and the affinity of the protein for phosphatidylcholines with different acyl chain characteristics. *Biochemistry* **20**, 1949-1961.
- Cantor, RS (1999).** Lipid composition and the lateral pressure profile in bilayers. *Biophys J* **76**, 2625-2639.
- Carruthers, A, Melchior, DL (1984).** Human erythrocyte hexose transporter activity is governed by bilayer lipid composition in reconstituted vesicles. *Biochemistry* **23**, 6901-6911.
- Casanueva, A, Galada, N, Baker, GC, Grant, WD, Heaphy, S, Jones, B, Yanhe, M, Ventosa, A, Blamey, J, Cowan, DA (2008).** Nanoarchaeal 16S rRNA gene sequences are widely dispersed in hyperthermophilic and mesophilic halophilic environments. *Extremophiles* **12**, 651-656.
- Chang, G, Spencer, RH, Lee, AT, Barclay, MT, Rees, DC (1998).** Structure of the MscL homolog from *Mycobacterium tuberculosis*: a gated mechanosensitive ion channel. *Science* **282**, 2220-2226.
- Chen, JZ, Settembre, EC, Aoki, ST, Zhang, X, Bellamy, AR, Dormitzer, PR, Harrison, SC, Grigorieff, N (2009).** Molecular interactions in rotavirus assembly and uncoating seen by high-resolution cryo-EM. *Proc Natl Acad Sci USA* **106**, 10644-10648.
- Chen, Q, She, J, Zeng, W, Guo, J, Xu, H, Bai, X-c, Jiang, Y (2017).** Structure of mammalian endolysosomal TRPML1 channel in nanodiscs. *Nature* **550**, 415-418.
- Cheng, Y, Grigorieff, N, Penczek, PA, Walz, T (2015).** A primer to single-particle cryo-electron microscopy. *Cell* **161**, 438-449.
- Clingenpeel, S, Kan, J, Macur, RE, Woyke, T, Lovalvo, D, Varley, J, Inskip, WP, Neilson, K, McDermott, TR (2013).** Yellowstone Lake Nanoarchaeota. *Front Microbiol* **4**, 274.
- Cooper, R (1978).** Influence of increased membrane cholesterol on membrane fluidity and cell function in human red blood cells. *J Supramol Struct* **8**, 413-430.
- Cornelius, F, Turner, N, Christensen, HRZ (2003).** Modulation of Na,K-ATPase by phospholipids and cholesterol. II. Steady-state and presteady-state kinetics. *Biochemistry* **42**, 8541-8549.

- Cox, CD, Nomura, T, Ziegler, CS, Campbell, AK, Wann, KT, Martinac, B (2013).** Selectivity mechanism of the mechanosensitive channel MscS revealed by probing channel subconducting states. *Nat Commun* **4**, 2137.
- Cox, CD, Wann, KT, Martinac, B (2014).** Selectivity mechanisms in MscS-like channels: From structure to function. *Channels* **8**, 5-12.
- Cox, CD, Nakayama, Y, Nomura, T, Martinac, B (2015).** The evolutionary ‘tinkering’ of MscS-like channels: generation of structural and functional diversity. *Pfluegers Arch - Eur J Physiol* **467**, 3-13.
- Daxer, S (2016).** Untersuchungen der Expression, Funktion und Struktur archaeeller Membrantransportproteine. Dissertation, Universität Regensburg.
- Delcour, AH, Martinac, B, Adler, J, Kung, C (1989).** Modified reconstitution method used in patch-clamp studies of *Escherichia coli* ion channels. *Biophys J* **56**, 631-636.
- Denisov, IG, Grinkova, YV, Lazarides, AA, Sligar, SG (2004).** Directed self-assembly of monodisperse phospholipid bilayer nanodiscs with controlled size. *J Am Chem Soc* **126**, 3477-3487.
- Denisov, IG, Baas, BJ, Grinkova, YV, Sligar, SG (2007).** Cooperativity in cytochrome P450 3A4: linkages in substrate binding, spin state, uncoupling, and product formation. *J Biol Chem* **282**, 7066-7076.
- Dörr, JM, Scheidelaar, S, Koorengel, MC, Dominguez, JJ, Schäfer, M, van Walree, CA, Killian, JA (2016).** The styrene–maleic acid copolymer: a versatile tool in membrane research. *Eur Biophys J* **45**, 3-21.
- Dorwart, MR, Wray, R, Brautigam, CA, Jiang, Y, Blount, P (2010).** *S. aureus* MscL is a pentamer *in vivo* but of variable stoichiometries *in vitro*: implications for detergent-solubilized membrane proteins. *PLoS Biol* **8**, e1000555.
- Dowhan, W (1997).** Molecular basis for membrane phospholipid diversity: why are there so many lipids? *Annu Rev Biochem* **66**, 199-232.
- Doyle, MP, Schoeni, JL (1984).** Survival and growth characteristics of *Escherichia coli* associated with hemorrhagic colitis. *Appl Environ Microbiol* **48**, 855-856.
- Dubochet, J, Lepault, J, Freeman, R, Berriman, JA, Homo, JC (1982).** Electron microscopy of frozen water and aqueous solutions. *J Microsc* **128**, 219-237.
- Dubochet, J, Adrian, M, Chang, J-J, Homo, J-C, Lepault, J, McDowell, AW, Schultz, P (1988).** Cryo-electron microscopy of vitrified specimens. *Q Rev Biophys* **21**, 129-228.
- Dumas, F, Tocanne, J-F, Leblanc, G, Lebrun, M-C (2000).** Consequences of hydrophobic mismatch between lipids and melibiose permease on melibiose transport. *Biochemistry* **39**, 4846-4854.

- Dumon-Seignovert, L, Cariot, G, Vuillard, L (2004).** The toxicity of recombinant proteins in *Escherichia coli*: a comparison of overexpression in BL21(DE3), C41(DE3), and C43(DE3). *Protein Expression Purif* **37**, 203-206.
- East, JM, Lee, AG (1982).** Lipid selectivity of the calcium and magnesium ion dependent adenosine triphosphatase, studied with fluorescence quenching by a brominated phospholipid. *Biochemistry* **21**, 4144-4151.
- Edwards, MD, Li, Y, Kim, S, Miller, S, Bartlett, W, Black, S, Dennison, S, Iscla, I, Blount, P, Bowie, JU, Booth, IR (2005).** Pivotal role of the glycine-rich TM3 helix in gating the MscS mechanosensitive channel. *Nat Struct Mol Biol* **12**, 113-119.
- Edwards, MD, Black, S, Rasmussen, T, Rasmussen, A, Stokes, NR, Stephen, T-L, Miller, S, Booth, IR (2012).** Characterization of three novel mechanosensitive channel activities in *Escherichia coli*. *Channels* **6**, 272-281.
- Efremov, RG, Leitner, A, Aebersold, R, Raunser, S (2015).** Architecture and conformational switch mechanism of the ryanodine receptor. *Nature* **517**, 39-43.
- Efremov, RG, Gatsogiannis, C, Raunser, S (2017).** Lipid nanodiscs as a tool for high-resolution structure determination of membrane proteins by single-particle cryo-EM, in *Methods in Enzymology*, vol. 594, chap. 1, pp. 1-30.
- Elbourne, Liam D H, Tetu, SG, Hassan, KA, Paulsen, IT (2017).** TransportDB 2.0: a database for exploring membrane transporters in sequenced genomes from all domains of life. *Nucleic Acids Res* **45**, D320-D324.
- Emsley, P, Lohkamp, B, Scott, WG, Cowtan, K (2010).** Features and development of Coot. *Acta Crystallogr D Biol Crystallogr* **66**, 486-501.
- Engelhardt, H (2007a).** Are S-layers exoskeletons? The basic function of protein surface layers revisited. *J Struct Biol* **160**, 115-124.
- Engelhardt, H (2007b).** Mechanism of osmoprotection by archaeal S-layers: A theoretical study. *J Struct Biol* **160**, 190-199.
- Ermakov, YA, Kamaraju, K, Sengupta, K, Sukharev, S (2010).** Gadolinium ions block mechanosensitive channels by altering the packing and lateral pressure of anionic lipids. *Biophys J* **98**, 1018-1027.
- Fattal, DR, Ben-Shaul, A (1993).** A molecular model for lipid-protein interaction in membranes: the role of hydrophobic mismatch. *Biophys J* **65**, 1795-1809.
- Frank, J, Radermacher, M, Penczek, P, Zhu, J, Li, Y, Ladjadj, M, Leith, A (1996).** SPIDER and WEB: processing and visualization of images in 3D electron microscopy and related fields. *J Struct Biol* **116**, 190-199.

- Frauenfeld, J, Gumbart, J, van der Sluis, EO, Funes, S, Gartmann, M, Beatrix, B, Mielke, T, Berninghausen, O, Becker, T, Schulten, K, Beckmann, R (2011). Cryo-EM structure of the ribosome-SecYE complex in the membrane environment. *Nat Struct Mol Biol* **18**, 614-621.
- Frauenfeld, J, Löving, R, Armache, J-P, Sonnen, AFP, Guettou, F, Moberg, P, Zhu, L, Jegerschöld, C, Flayhan, A, Briggs, JAG, Garoff, H, Löw, C, Cheng, Y, Nordlund, P (2016). A saposin-lipoprotein nanoparticle system for membrane proteins. *Nat Methods* **13**, 345-351.
- Gamini, R, Sotomayor, M, Chipot, C, Schulten, K (2011). Cytoplasmic domain filter function in the mechanosensitive channel of small conductance. *Biophys J* **101**, 80-89.
- Gao, Y, Cao, E, Julius, D, Cheng, Y (2016). TRPV1 structures in nanodiscs reveal mechanisms of ligand and lipid action. *Nature* **534**, 347-351.
- Giannone, RJ, Huber, H, Karpinets, T, Heimerl, T, Küper, U, Rachel, R, Keller, M, Hettich, RL, Podar, M (2011). Proteomic characterization of cellular and molecular processes that enable the *Nanoarchaeum equitans*-*Ignicoccus hospitalis* relationship. *PLoS One* **6**, e22942.
- Giannone, RJ, Wurch, LL, Heimerl, T, Martin, S, Yang, Z, Huber, H, Rachel, R, Hettich, RL, Podar, M (2015). Life on the edge: functional genomic response of *Ignicoccus hospitalis* to the presence of *Nanoarchaeum equitans*. *ISME J* **9**, 101-114.
- Gill, SC, von Hippel, PH (1989). Calculation of protein extinction coefficients from amino acid sequence data. *Anal Biochem* **182**, 319-326.
- Glaeser, RM (2015). How good can cryo-EM become? *Nat Methods* **13**, 28.
- Glück, JM, Koenig, BW, Willbold, D (2011). Nanodiscs allow the use of integral membrane proteins as analytes in surface plasmon resonance studies. *Anal Biochem* **408**, 46-52.
- Goujon, M, McWilliam, H, Li, W, Valentin, F, Squizzato, S, Paern, J, Lopez, R (2010). A new bioinformatics analysis tools framework at EMBL-EBI. *Nucleic Acids Res* **38**, W695-W699.
- Grigorieff, N (2007). FREALIGN: High-resolution refinement of single particle structures. *J Struct Biol* **157**, 117-125.
- Guan, L, Smirnova, IN, Verner, G, Nagamori, S, Kaback, HR (2006). Manipulating phospholipids for crystallization of a membrane transport protein. *Proc Natl Acad Sci USA* **103**, 1723-1726.
- Guan, L, Mirza, O, Verner, G, Iwata, S, Kaback, HR (2007). Structural determination of wild-type lactose permease. *Proc Natl Acad Sci USA* **104**, 15294-15298.
- Guzman, LM, Belin, D, Carson, MJ, Beckwith, J (1995). Tight regulation, modulation, and high-level expression by vectors containing the arabinose pBAD promoter. *J Bacteriol* **177**, 4121-4130.

- Hamill, OP, Marty, A, Neher, E, Sakmann, B, Sigworth, FJ (1981).** Improved patch-clamp techniques for high-resolution current recording from cells and cell-free membrane patches. *Pfluegers Arch - Eur J Physiol* **391**, 85-100.
- Hamill, OP, Martinac, B (2001).** Molecular basis of mechanotransduction in living cells. *Physiol Rev* **81**, 685-740.
- Hanahan, D (1983).** Studies on transformation of *Escherichia coli* with plasmids. *J Mol Biol* **166**, 557-580.
- Häse, CC, Le Dain, AC, Martinac, B (1995).** Purification and functional reconstitution of the recombinant large mechanosensitive ion channel (MscL) of *Escherichia coli*. *J Biol Chem* **270**, 18329-18334.
- Haswell, ES (2007).** MscS-like proteins in plants, in *Current Topics in Membranes*, vol. 58, pp. 329-359.
- Haswell, ES, Phillips, R, Rees, DC (2011).** Mechanosensitive channels: what can they do and how do they do it? *Structure* **19**, 1356-1369.
- Heimerl, T, Flechsler, J, Pickl, C, Heinz, V, Salecker, B, Zweck, J, Wanner, G, Geimer, S, Samson, RY, Bell, SD, Huber, H, Wirth, R, Wurch, L, Podar, M, Rachel, R (2017).** A complex endomembrane system in the archaeon *Ignicoccus hospitalis* tapped by *Nanoarchaeum equitans*. *Front Microbiol* **8**.
- Henderson, R (2013).** Avoiding the pitfalls of single particle cryo-electron microscopy: Einstein from noise. *Proc Natl Acad Sci USA* **110**, 18037-18041.
- Hiraoka, S, Matsuzaki, H, Shibuya, I (1993).** Active increase in cardiolipin synthesis in the stationary growth phase and its physiological significance in *Escherichia coli*. *FEBS Lett* **336**, 221-224.
- Hoffmann, K, Stoffel, W (1993).** TMbase-a database of membrane spanning protein segments. *Biol Chem Hoppe-Seyler* **347**.
- Hohn, M, Tang, G, Goodyear, G, Baldwin, PR, Huang, Z, Penczek, PA, Yang, C, Glaeser, RM, Adams, PD, Ludtke, SJ (2007).** SPARX, a new environment for Cryo-EM image processing. *J Struct Biol* **157**, 47-55.
- Hohn, MJ, Hedlund, BP, Huber, H (2002).** Detection of 16S rDNA sequences representing the novel phylum "Nanoarchaeota": indication for a wide distribution in high temperature biotopes. *Syst Appl Microbiol* **25**, 551-554.
- Huber, H, Burggraf, S, Mayer, T, Wyschkony, I, Rachel, R, Stetter, KO (2000).** *Ignicoccus* gen. nov., a novel genus of hyperthermophilic, chemolithoautotrophic Archaea, represented by two new species, *Ignicoccus islandicus* sp nov and *Ignicoccus pacificus* sp nov. *Int J Syst Evol Microbiol* **50**, 2093-2100.

- Huber, H, Hohn, M, Rachel, R, Fuchs, T, Wimmer, V, Stetter, K (2002).** A new phylum of Archaea represented by a nanosized hyperthermophilic symbiont. *Nature* **417**, 63 - 67.
- Huber, H, Hohn, MJ, Stetter, KO, Rachel, R (2003).** The phylum Nanoarchaeota: present knowledge and future perspectives of a unique form of life. *Res Microbiol* **154**, 165-171.
- Huber, H, Gallenberger, M, Jahn, U, Eylert, E, Berg, IA, Kockelkorn, D, Eisenreich, W, Fuchs, G (2008).** A dicarboxylate/4-hydroxybutyrate autotrophic carbon assimilation cycle in the hyperthermophilic Archaeum *Ignicoccus hospitalis*. *Proc Natl Acad Sci USA* **105**, 7851-7856.
- Huber, H, Küper, U, Daxer, S, Rachel, R (2012).** The unusual cell biology of the hyperthermophilic Crenarchaeon *Ignicoccus hospitalis*. *Antonie van Leeuwenhoek* **102**, 203-219.
- Hunte, C (2005).** Specific protein–lipid interactions in membrane proteins. *Biochem Soc Trans* **33**, 938-942.
- Hunte, C, Richers, S (2008).** Lipids and membrane protein structures. *Curr Opin Struct Biol* **18**, 406-411.
- Huynh, KW, Jiang, J, Abuladze, N, Tsirulnikov, K, Kao, L, Shao, X, Newman, D, Azimov, R, Pushkin, A, Zhou, ZH, Kurtz, I (2018).** CryoEM structure of the human SLC4A4 sodium-coupled acid-base transporter NBCe1. *Nat Commun* **9**, 900.
- Inoue, H, Nojima, H, Okayama, H (1990).** High efficiency transformation of *Escherichia coli* with plasmids. *Gene* **96**, 23-28.
- Ipsen, JH, Mouritsen, OG, Bloom, M (1990).** Relationships between lipid membrane area, hydrophobic thickness, and acyl-chain orientational order. The effects of cholesterol. *Biophys J* **57**, 405-412.
- Jahn, U, Summons, R, Sturt, H, Grosjean, E, Huber, H (2004).** Composition of the lipids of *Nanoarchaeum equitans* and their origin from its host *Ignicoccus* sp. strain KIN4/I. *Arch Microbiol* **182**, 404-413.
- Jahn, U, Huber, H, Eisenreich, W, Hugler, M, Fuchs, G (2007).** Insights into the autotrophic CO₂ fixation pathway of the archaeon *Ignicoccus hospitalis*: comprehensive analysis of the central carbon metabolism. *J Bacteriol* **189**, 4108-4119.
- Jahn, U, Gallenberger, M, Paper, W, Junglas, B, Eisenreich, W, Stetter, KO, Rachel, R, Huber, H (2008).** *Nanoarchaeum equitans* and *Ignicoccus hospitalis*: new insights into a unique, intimate association of two archaea. *J Bacteriol* **190**, 1743-1750.
- Jin, P, Bulkley, D, Guo, Y, Zhang, W, Guo, Z, Huynh, W, Wu, S, Meltzer, S, Cheng, T, Jan, LY, Jan, Y-N, Cheng, Y (2017).** Electron cryo-microscopy structure of the mechanotransduction channel NOMPC. *Nature* **547**, 118-122.
- Jones, DT (1999).** Protein secondary structure prediction based on position-specific scoring matrices. *J Mol Biol* **292**, 195-202.

- Junglas, B, Briegel, A, Burghardt, T, Walther, P, Wirth, R, Huber, H, Rachel, R (2008).** *Ignicoccus hospitalis* and *Nanoarchaeum equitans*: ultrastructure, cell-cell interaction, and 3D reconstruction from serial sections of freeze-substituted cells and by electron cryotomography. *Arch Microbiol* **190**, 395 - 408.
- Kakuda, T, Koide, Y, Sakamoto, A, Takai, S (2012).** Characterization of two putative mechanosensitive channel proteins of *Campylobacter jejuni* involved in protection against osmotic downshock. *Vet Microbiol* **160**, 53-60.
- Kandler, O, Konig, H (1993).** Cell envelopes of archaea: structure and chemistry, in *New Comprehensive Biochemistry*, vol. 26, chap. 8, pp. 223-259.
- Kates, M (1992).** Archaeobacterial lipids: structure, biosynthesis and function. *Biochem Soc Symp* **58**, 51-72.
- Kawai, T, Caaveiro, JMM, Abe, R, Katagiri, T, Tsumoto, K (2011).** Catalytic activity of MsbA reconstituted in nanodisc particles is modulated by remote interactions with the bilayer. *FEBS Lett* **585**, 3533-3537.
- Khoshouei, M, Radjainia, M, Baumeister, W, Danev, R (2017).** Cryo-EM structure of haemoglobin at 3.2 Å determined with the Volta phase plate. *Nat Commun* **8**, 16099.
- Killian, JA (1998).** Hydrophobic mismatch between proteins and lipids in membranes. *Biochim Biophys Acta - Biomembr* **1376**, 401-416.
- Killian, JA, de Planque, MRR, van der Wel, PCA, Salemink, I, de Kruijff, B, Greathouse, DV, Koeppe II, RE (1998).** Modulation of membrane structure and function by hydrophobic mismatch between proteins and lipids. *pac* **70**, 75-82.
- Killmann, H, Benz, R, Braun, V (1996).** Properties of the FhuA channel in the *Escherichia coli* outer membrane after deletion of FhuA portions within and outside the predicted gating loop. *J Bacteriol* **178**, 6913-6920.
- Kim, T, Lee, Kyu I, Morris, P, Pastor, Richard W, Andersen, Olaf S, Im, W (2012).** Influence of hydrophobic mismatch on structures and dynamics of gramicidin A and lipid bilayers. *Biophys J* **102**, 1551-1560.
- Klingl, A (2014).** S-layer and cytoplasmic membrane – exceptions from the typical archaeal cell wall with a focus on double membranes. *Front Microbiol* **5**, 624.
- Kloda, A, Martinac, B (2001a).** Mechanosensitive channel of *Thermoplasma*, the cell wall-less archaea. *Cell Biochem Biophys* **34**, 321-347.
- Kloda, A, Martinac, B (2001b).** Mechanosensitive channels in archaea. *Cell Biochem Biophys* **34**, 349-381.
- Kloda, A, Martinac, B (2001c).** Molecular identification of a mechanosensitive channel in archaea. *Biophys J* **80**, 229-240.

- Kloda, A, Martinac, B (2001d)**. Structural and functional differences between two homologous mechanosensitive channels of *Methanococcus jannaschii*. *EMBO J* **20**, 1888-1896.
- Kloda, A, Martinac, B (2002)**. Mechanosensitive channels of bacteria and archaea share a common ancestral origin. *Eur Biophys J* **31**, 14-25.
- Knowles, T, Finka, R, Smith, C, Lin, Y, Dafforn, T, Overduin, M (2009)**. Membrane proteins solubilized intact in lipid containing nanoparticles bounded by styrene maleic acid copolymer. *J Am Chem Soc* **131**, 7484-7485.
- Koprowski, P, Grajkowski, W, Balcerzak, M, Filipiuk, I, Fabczak, H, Kubalski, A (2015)**. Cytoplasmic domain of MscS interacts with cell division protein FtsZ: a possible non-channel function of the mechanosensitive channel in *Escherichia coli*. *PLoS One* **10**, e0127029.
- Kreuter, L (2014)**. Isolierung, Charakterisierung und Lokalisierung der ATP-Synthasen der archaeellen Genera *Ignicoccus* und *Nanoarchaeum*. Dissertation, Universität Regensburg.
- Krogh, A, Larsson, B, von Heijne, G, Sonnhammer, ELL (2001)**. Predicting transmembrane protein topology with a hidden Markov model: application to complete genomes. *J Mol Biol* **305**, 567-580.
- Kung, C, Saimi, Y, Martinac, B (1990)**. Mechanosensitive ion channels in microbes and the early evolutionary origin of solvent sensing, in *Current Topics in Membranes and Transport*, vol. 36, chap. 12, pp. 145-153.
- Kung, C (2005)**. A possible unifying principle for mechanosensation. *Nature* **436**, 647-654.
- Küper, U, Meyer, C, Müller, V, Rachel, R, Huber, H (2010)**. Energized outer membrane and spatial separation of metabolic processes in the hyperthermophilic Archaeon *Ignicoccus hospitalis*. *Proc Natl Acad Sci USA* **107**, 3152-3156.
- Kwok, R, Evans, E (1981)**. Thermoelasticity of large lecithin bilayer vesicles. *Biophys J* **35**, 637-652.
- Laemmli, UK (1970)**. Cleavage of structural proteins during the assembly of the head of bacteriophage T4. *Nature* **227**, 680-685.
- Lai, JY, Poon, YS, Kaiser, JT, Rees, DC (2013)**. Open and shut: crystal structures of the dodecylmaltoside solubilized mechanosensitive channel of small conductance from *Escherichia coli* and *Helicobacter pylori* at 4.4 Å and 4.1 Å resolutions. *Protein Sci* **22**, 502-509.
- Lange, M (2009)**. Neue Hochtemperatur-Organismen von Lesbos und dem Ostpazifischen Rücken. Zulassungsarbeit, Universität Regensburg.
- Larkin, MA, Blackshields, G, Brown, NP, Chenna, R, McGettigan, PA, McWilliam, H, Valentin, F, Wallace, IM, Wilm, A, Lopez, R, Thompson, JD, Gibson, TJ, Higgins, DG (2007)**. Clustal W and Clustal X version 2.0. *Bioinformatics* **23**, 2947-2948.

- Le Dain, AC, Saint, N, Kloda, A, Ghazi, A, Martinac, B (1998).** Mechanosensitive ion channels of the archaeon *Haloferax volcanii*. *J Biol Chem* **273**, 12116-12119.
- Lebendiker, M, Danieli, T (2014).** Production of prone-to-aggregate proteins. *FEBS Lett* **588**, 236-246.
- Lee, AG (2004).** How lipids affect the activities of integral membrane proteins. *Biochim Biophys Acta - Biomembr* **1666**, 62-87.
- Lee, SC, Knowles, TJ, Postis, VLG, Jamshad, M, Parslow, RA, Lin, Y-p, Goldman, A, Sridhar, P, Overduin, M, Muench, SP, Dafforn, TR (2016).** A method for detergent-free isolation of membrane proteins in their local lipid environment. *Nat Protoc* **11**, 1149-1162.
- Letters, R (1964).** The application of a two-dimensional paper-chromatographic technique to the analysis of phospholipids. *Biochem J* **93**, 313-316.
- Levina, N, Töttemeyer, S, Stokes, NR, Louis, P, Jones, MA, Booth, IR (1999).** Protection of *Escherichia coli* cells against extreme turgor by activation of MscS and MscL mechanosensitive channels: identification of genes required for MscS activity. *EMBO J* **18**, 1730-1737.
- Levitan, I, Fang, Y, Rosenhouse-Dantsker, A, Romanenko, V (2010).** Cholesterol and ion channels. *Subcell Biochem* **51**, 509-549.
- Lévy, D, Mosser, G, Lambert, O, Moeck, GS, Bald, D, Rigaud, J-L (1999).** Two-dimensional crystallization on lipid layer: a successful approach for membrane proteins. *J Struct Biol* **127**, 44-52.
- Li, J, Guo, J, Ou, X, Zhang, M, Li, Y, Liu, Z (2015).** Mechanical coupling of the multiple structural elements of the large-conductance mechanosensitive channel during expansion. *Proc Natl Acad Sci USA* **112**, 10726-10731.
- Li, Y, Moe, PC, Chandrasekaran, S, Booth, IR, Blount, P (2002).** Ionic regulation of MscK, a mechanosensitive channel from *Escherichia coli*. *EMBO J* **21**, 5323-5330.
- Liao, M, Cao, E, Julius, D, Cheng, Y (2013).** Structure of the TRPV1 ion channel determined by electron cryo-microscopy. *Nature* **504**, 107-112.
- Liu, Z, Gandhi, CS, Rees, DC (2009).** Structure of a tetrameric MscL in an expanded intermediate state. *Nature* **461**, 120-124.
- Liu, Z, Walton, TA, Rees, DC (2010).** A reported archaeal mechanosensitive channel is a structural homolog of MarR-like transcriptional regulators. *Protein Sci* **19**, 808-814.
- Löw, C, Yau, YH, Pardon, E, Jegerschöld, C, Wählin, L, Quistgaard, EM, Moberg, P, Geifman-Shochat, S, Steyaert, J, Nordlund, P (2013).** Nanobody mediated crystallization of an archeal mechanosensitive channel. *PLoS One* **8**, e77984.

- Lü, W, Du, J, Goehring, A, Gouaux, E (2017).** Cryo-EM structures of the trimeric NMDA receptor and its allosteric modulation. *Science* **355**.
- Ludtke, SJ, Baldwin, PR, Chiu, W (1999).** EMAN: semiautomated software for high-resolution single-particle reconstructions. *J Struct Biol* **128**, 82-97.
- Lyons, JA, Bøggild, A, Nissen, P, Frauenfeld, J (2017).** Saposin-lipoprotein scaffolds for structure determination of membrane transporters, in *Methods in Enzymology*, vol. 594, chap. 3, pp. 85-99.
- Ma, P, Varela, F, Magoch, M, Silva, AR, Rosário, AL, Brito, J, Oliveira, TF, Nogly, P, Pessanha, M, Stelter, M, Kletzin, A, Henderson, PJF, Archer, M (2013).** An efficient strategy for small-scale screening and production of archaeal membrane transport proteins in *Escherichia coli*. *PLoS ONE* **8**, e76913.
- Maksaev, G, Haswell, ES (2013).** Recent characterizations of MscS and its homologs provide insight into the basis of ion selectivity in mechanosensitive channels. *Channels* **7**, 215-220.
- Malcolm, Hannah R, Heo, Y-Y, Elmore, Donald E, Maurer, Joshua A (2011).** Defining the role of the tension sensor in the mechanosensitive channel of small conductance. *Biophys J* **101**, 345-352.
- Malcolm, HR, Maurer, JA (2012).** The mechanosensitive channel of small conductance (MscS) superfamily: not just mechanosensitive channels anymore. *ChemBioChem* **13**, 2037-2043.
- Martinac, B, Buechner, M, Delcour, AH, Adler, J, Kung, C (1987).** Pressure-sensitive ion channel in *Escherichia coli*. *Proc Natl Acad Sci USA* **84**, 2297-2301.
- Martinac, B, Adler, J, Kung, C (1990).** Mechanosensitive ion channels of *E. coli* activated by amphipaths. *Nature* **348**, 261-263.
- Martinac, B, Hamill, OP (2002).** Gramicidin A channels switch between stretch activation and stretch inactivation depending on bilayer thickness. *Proc Natl Acad Sci USA* **99**, 4308-4312.
- Martinac, B, Kloda, A (2003).** Evolutionary origins of mechanosensitive ion channels. *Prog Biophys Mol Biol* **82**, 11-24.
- Martinac, B (2004).** Mechanosensitive ion channels: molecules of mechanotransduction. *J Cell Sci* **117**, 2449-2460.
- Matthies, D, Dalmas, O, Borgnia, Mario J, Dominik, Pawel K, Merk, A, Rao, P, Reddy, Bharat G, Islam, S, Bartesaghi, A, Perozo, E, Subramaniam, S (2016).** Cryo-EM structures of the magnesium channel CorA reveal symmetry break upon gating. *Cell* **164**, 747-756.
- Mayer, F, Küper, U, Meyer, C, Daxer, S, Müller, V, Rachel, R, Huber, H (2012).** AMP-forming acetyl coenzyme a synthetase in the outermost membrane of the hyperthermophilic crenarchaeon *Ignicoccus hospitalis*. *J Bacteriol* **194**, 1572-1581.

- McCliment, EA, Voglesonger, KM, O'Day, PA, Dunn, EE, Holloway, JR, Cary, SC (2006).** Colonization of nascent, deep-sea hydrothermal vents by a novel Archaeal and Nanoarchaeal assemblage. *Environ Microbiol* **8**, 114-125.
- Messner, P, Sleytr, UB (1992).** Crystalline bacterial cell-surface layers, in *Advances in Microbial Physiology*, vol. 33, pp. 213-275.
- Meyer, C, Heimerl, T, Wirth, R, Klingl, A, Rachel, R (2014).** The Iho670 fibers of *Ignicoccus hospitalis* are anchored in the cell by a spherical structure located beneath the inner membrane. *J Bacteriol* **196**, 3807-3815.
- Mi, W, Li, Y, Yoon, SH, Ernst, RK, Walz, T, Liao, M (2017).** Structural basis of MsbA-mediated lipopolysaccharide transport. *Nature* **549**, 233-237.
- Miller, S, Bartlett, W, Chandrasekaran, S, Simpson, S, Edwards, M, Booth, IR (2003).** Domain organization of the MscS mechanosensitive channel of *Escherichia coli*. *EMBO J* **22**, 36-46.
- Mindell, JA, Grigorieff, N (2003).** Accurate determination of local defocus and specimen tilt in electron microscopy. *J Struct Biol* **142**, 334-347.
- Miroux, B, Walker, JE (1996).** Over-production of proteins in *Escherichia coli*: mutant hosts that allow synthesis of some membrane proteins and globular proteins at high levels. *J Mol Biol* **260**, 289-298.
- Moe, PC, Levin, G, Blount, P (2000).** Correlating a protein structure with function of a bacterial mechanosensitive channel. *J Biol Chem* **275**, 31121-31127.
- Moriya, T, Saur, M, Stabrin, M, Merino, F, Voicu, H, Huang, Z, Penczek, PA, Raunser, S, Gatsogiannis, C (2017).** High-resolution single particle analysis from electron cryo-microscopy images using SPHIRE. *J Vis Exp* **123**, e55448.
- Müller, DW, Meyer, C, Gürster, S, Küper, U, Huber, H, Rachel, R, Wanner, G, Wirth, R, Bellack, A (2009).** The Iho670 Fibers of *Ignicoccus hospitalis*: a new type of archaeal cell surface appendage. *J Bacteriol* **191**, 6465-6468.
- Mullis, KB, Faloona, FA (1987).** Specific synthesis of DNA *in vitro* via a polymerase-catalyzed chain reaction, in *Methods in Enzymology*, vol. 155, chap. 21, pp. 335-350.
- Munson-McGee, JH, Field, EK, Bateson, M, Rooney, C, Stepanauskas, R, Young, MJ (2015).** Nanoarchaeota, their Sulfolobales host, and Nanoarchaeota virus distribution across Yellowstone National Park Hot Springs. *Appl Environ Microbiol* **81**, 7860-7868.
- Naismith, JH, Booth, IR (2012).** Bacterial mechanosensitive channels—MscS: evolution's solution to creating sensitivity in function. *Annu Rev Biophys* **41**, 157-177.
- Nakamura, J, Hirano, S, Ito, H, Wachi, M (2007).** Mutations of the *Corynebacterium glutamicum* NCgl1221 gene, encoding a mechanosensitive channel homolog, induce L-glutamic acid production. *Appl Environ Microbiol* **73**, 4491-4498.

- Nakanishi, A, Kishikawa, J-i, Tamakoshi, M, Mitsuoka, K, Yokoyama, K (2018).** Cryo EM structure of intact rotary H(+)-ATPase/synthase from *Thermus thermophilus*. *Nat Commun* **9**, 89.
- Nakayama, Y, Yoshimura, K, Iida, H (2012).** Organellar mechanosensitive channels in fission yeast regulate the hypo-osmotic shock response. *Nat Commun* **3**, 1020.
- Nakayama, Y, Slavchov, RI, Bavi, N, Martinac, B (2016).** Energy of liposome patch adhesion to the pipet glass determined by confocal fluorescence microscopy. *J Phys Chem Lett* **7**, 4530-4534.
- Nasr, ML, Baptista, D, Strauss, M, Sun, Z-YJ, Grigoriu, S, Huser, S, Plückthun, A, Hagn, F, Walz, T, Hogle, JM, Wagner, G (2017).** Covalently circularized nanodiscs for studying membrane proteins and viral entry. *Nat Methods* **14**, 49-52.
- Näther, DJ, Rachel, R (2004).** The outer membrane of the hyperthermophilic archaeon *Ignicoccus*: dynamics, ultrastructure and composition. *Biochem Soc Trans* **32**, 199-203.
- Neher, E, Sakmann, B (1976).** Single-channel currents recorded from membrane of denervated frog muscle fibres. *Nature* **260**, 799-802.
- Nguyen, THD, Galej, WP, Bai, X-c, Oubridge, C, Newman, AJ, Scheres, SHW, Nagai, K (2016).** Cryo-EM structure of the yeast U4/U6.U5 tri-snRNP at 3.7 Å resolution. *Nature* **530**, 298-302.
- Nomura, T, Sokabe, M, Yoshimura, K (2006).** Lipid-protein interaction of the MscS mechanosensitive channel examined by scanning mutagenesis. *Biophys J* **91**, 2874-2881.
- Nomura, T, Sokabe, M, Yoshimura, K (2008).** Interaction between the cytoplasmic and transmembrane domains of the mechanosensitive channel (MscS). *Biophys J* **94**, 1638-1645.
- Nomura, T, Cranfield, CG, Deplazes, E, Owen, DM, Macmillan, A, Battle, AR, Constantine, M, Sokabe, M, Martinac, B (2012).** Differential effects of lipids and lyso-lipids on the mechanosensitivity of the mechanosensitive channels MscL and MscS. *Proc Natl Acad Sci USA* **109**, 8770-8775.
- Ohi, M, Li, Y, Cheng, Y, Walz, T (2004).** Negative staining and image classification - powerful tools in modern electron microscopy. *Biol Proced Online* **6**, 23-34.
- Oliet, SHR, Bourque, CW (1996).** Gadolinium uncouples mechanical detection and osmoreceptor potential in supraoptic neurons. *Neuron* **16**, 175-181.
- Opekarová, M, Tanner, W (2003).** Specific lipid requirements of membrane proteins - a putative bottleneck in heterologous expression. *Biochim Biophys Acta - Biomembr* **1610**, 11-22.
- Opsahl, LR, Webb, WW (1994).** Lipid-glass adhesion in giga-sealed patch-clamped membranes. *Biophys J* **66**, 75-79.

- Osanai, T, Sato, S, Tabata, S, Tanaka, K (2005).** Identification of PamA as a PII-binding membrane protein important in nitrogen-related and sugar-catabolic gene expression in *Synechocystis* sp. PCC 6803. *J Biol Chem* **280**, 34684-34690.
- Paper, W, Jahn, U, Hohn, MJ, Kronner, M, Nather, DJ, Burghardt, T, Rachel, R, Stetter, KO, Huber, H (2007).** *Ignicoccus hospitalis* sp. nov., the host of '*Nanoarchaeum equitans*'. *Int J Syst Evol Microbiol* **57**, 803-808.
- Parey, K, Fielding, AJ, Sörgel, M, Rachel, R, Huber, H, Ziegler, C, Rajendran, C (2016).** In meso crystal structure of a novel membrane-associated octaheme cytochrome c from the Crenarchaeon *Ignicoccus hospitalis*. *FEBS J* **283**, 3807-3820.
- Parmar, M, Rawson, S, Scarff, CA, Goldman, A, Dafforn, TR, Muench, SP, Postis, VLG (2018).** Using a SMALP platform to determine a sub-nm single particle cryo-EM membrane protein structure. *Biochim Biophys Acta - Biomembr* **1860**, 378-383.
- Paulsen, CE, Armache, J-P, Gao, Y, Cheng, Y, Julius, D (2015).** Structure of the TRPA1 ion channel suggests regulatory mechanisms. *Nature* **520**, 511-517.
- Perozo, E, Cortes, DM, Sompornpisut, P, Kloda, A, Martinac, B (2002).** Open channel structure of MscL and the gating mechanism of mechanosensitive channels. *Nature* **418**, 942-948.
- Perozo, E, Kloda, A, Cortes, DM, Martinac, B (2002).** Physical principles underlying the transduction of bilayer deformation forces during mechanosensitive channel gating. *Nat Struct Biol* **9**, 696-703.
- Perozo, E, Rees, DC (2003).** Structure and mechanism in prokaryotic mechanosensitive channels. *Curr Opin Struct Biol* **13**, 432-442.
- Perozo, E (2006).** Gating prokaryotic mechanosensitive channels. *Nat Rev Mol Cell Biol* **7**, 109-119.
- Petrov, E, Palanivelu, D, Constantine, M, Rohde, Paul R, Cox, Charles D, Nomura, T, Minor, Daniel L, Martinac, B (2013).** Patch-clamp characterization of the MscS-like mechanosensitive channel from *Silicibacter pomeroyi*. *Biophys J* **104**, 1426-1434.
- Petterson, EF, Goddard, TD, Huang, CC, Couch, GS, Greenblatt, DM, Meng, EC, Ferrin, TE (2004).** UCSF Chimera - A visualization system for exploratory research and analysis. *J Comput Chem* **25**, 1605-1612.
- Pilot, JD, East, JM, Lee, AG (2001).** Effects of bilayer thickness on the activity of diacylglycerol kinase of *Escherichia coli*. *Biochemistry* **40**, 8188-8195.
- Pivetti, CD, Yen, M-R, Miller, S, Busch, W, Tseng, Y-H, Booth, IR, Saier, JMH (2003).** Two families of mechanosensitive channel proteins. *Microbiol Mol Biol Rev* **67**, 66-85.
- Pliotas, C, Ward, R, Branigan, E, Rasmussen, A, Hagelueken, G, Huang, H, Black, SS, Booth, IR, Schiemann, O, Naismith, JH (2012).** Conformational state of the MscS

- mechanosensitive channel in solution revealed by pulsed electron-electron double resonance (PELDOR) spectroscopy. *Proc Natl Acad Sci USA* **109**, E2675-E2682.
- Pliotas, C, Dahl, ACE, Rasmussen, T, Mahendran, KR, Smith, TK, Marius, P, Gault, J, Banda, T, Rasmussen, A, Miller, S, Robinson, CV, Bayley, H, Sansom, MSP, Booth, IR, Naismith, JH (2015).** The role of lipids in mechanosensation. *Nat Struct Mol Biol* **22**, 991-998.
- Pliotas, C, Naismith, JH (2017).** Spectator no more, the role of the membrane in regulating ion channel function. *Curr Opin Struct Biol* **45**, 59-66.
- Podar, M, Anderson, I, Makarova, KS, Elkins, JG, Ivanova, N, Wall, MA, Lykidis, A, Mavromatis, K, Sun, H, Hudson, ME, Chen, W, Deciu, C, Hutchison, D, Eads, JR, Anderson, A, Fernandes, F, Szeto, E, Lapidus, A, Kyrpides, NC, Saier, MH, Richardson, PM, Rachel, R, Huber, H, Eisen, JA, Koonin, EV, Keller, M, Stetter, KO (2008).** A genomic analysis of the archaeal system *Ignicoccus hospitalis*-*Nanoarchaeum equitans*. *Genome Biol* **9**, R158.
- Podar, M, Makarova, KS, Graham, DE, Wolf, YI, Koonin, EV, Reysenbach, A-L (2013).** Insights into archaeal evolution and symbiosis from the genomes of a nanoarchaeon and its inferred crenarchaeal host from Obsidian Pool, Yellowstone National Park. *Biol Direct* **8**, 9.
- Popot, JL, Berry, EA, Charvolin, D, Creuzenet, C, Ebel, C, Engelman, DM, Flötenmeyer, M, Giusti, F, Gohon, Y, Hervé, P, Hong, Q, Lakey, JH, Leonard, K, Shuman, HA, Timmins, P, Warschawski, DE, Zito, F, Zoonens, M, Pucci, B, Tribet, C (2003).** Amphipols: polymeric surfactants for membrane biology research. *Cell Mol Life Sci* **60**, 1559-1574.
- Popot, JL, Althoff, T, Bagnard, D, Banères, JL, Bazzacco, P, Billon-Denis, E, Catoire, LJ, Champeil, P, Charvolin, D, Cocco, MJ, Crémel, G, Dahmane, T, de la Maza, LM, Ebel, C, Gabel, F, Giusti, F, Gohon, Y, Goormaghtigh, E, Guittet, E, Kleinschmidt, JH, Kühlbrandt, W, Le Bon, C, Martinez, KL, Picard, M, Pucci, B, Sachs, JN, Tribet, C, van Heijenoort, C, Wien, F, Zito, F, Zoonens, M (2011).** Amphipols from A to Z. *Annu Rev Biophys* **40**, 379-408.
- Postis, V, Rawson, S, Mitchell, JK, Lee, SC, Parslow, RA, Dafforn, TR, Baldwin, SA, Muench, SP (2015).** The use of SMALPs as a novel membrane protein scaffold for structure study by negative stain electron microscopy. *Biochim Biophys Acta* **1848**, 496-501.
- Punjani, A, Rubinstein, JL, Fleet, DJ, Brubaker, MA (2017).** cryoSPARC: algorithms for rapid unsupervised cryo-EM structure determination. *Nat Methods* **14**, 290-296.
- Rachel, R, Wyszchony, I, Riehl, S, Huber, H (2002).** The ultrastructure of *Ignicoccus*: evidence for a novel outer membrane and for intracellular vesicle budding in an archaeon. *Archaea* **1**, 9-18.
- Rasmussen, A, Rasmussen, T, Edwards, MD, Schauer, D, Schumann, U, Miller, S, Booth, IR (2007).** The role of tryptophan residues in the function and stability of the mechanosensitive channel MscS from *Escherichia coli*. *Biochemistry* **46**, 10899-10908.

- Ritchie, TK, Grinkova, YV, Bayburt, TH, Denisov, IG, Zolnerciks, JK, Atkins, WM, Sligar, SG (2009).** Reconstitution of membrane proteins in phospholipid bilayer nanodiscs, in *Methods of Enzymology*, vol. 464, chap. 11, pp. 211-231.
- Robert, X, Gouet, P (2014).** Deciphering key features in protein structures with the new ENDscript server. *Nucleic Acids Res* **42**, W320-W324.
- Roh, S-H, Stam, NJ, Hryc, CF, Couoh-Cardel, S, Pintilie, G, Chiu, W, Wilkens, S (2018).** The 3.5-Å cryoEM structure of nanodisc-reconstituted yeast vacuolar ATPase Vo proton channel. *Mol Cell* **69**, 993-1004.
- Rohou, A, Grigorieff, N (2015).** CTFFIND4: Fast and accurate defocus estimation from electron micrographs. *J Struct Biol* **192**, 216–221.
- Romantsov, T, Guan, Z, Wood, JM (2009).** Cardiolipin and the osmotic stress responses of bacteria. *Biochim Biophys Acta* **1788**, 2092-2100.
- Rubinstein, JL (2007).** Structural analysis of membrane protein complexes by single particle electron microscopy. *Methods* **41**, 409-416.
- Saiki, RK, Gelfand, DH, Stoffel, S, Scharf, SJ, Higuchi, R, Horn, GT, Mullis, KB, Erlich, HA (1988).** Primer-directed enzymatic amplification of DNA with a thermostable DNA polymerase. *Science* **239**, 487-491.
- Šali, A, Blundell, TL (1993).** Comparative protein modelling by satisfaction of spatial restraints. *J Mol Biol* **234**, 779-815.
- Schägger, H, Cramer, WA, Vonjagow, G (1994).** Analysis of molecular masses and oligomeric states of protein complexes by blue native electrophoresis and isolation of membrane protein complexes by two-dimensional native electrophoresis. *Anal Biochem* **217**, 220-230.
- Scheres, SHW, Núñez-Ramírez, R, Gómez-Llorente, Y, San Martín, C, Eggermont, PPB, Carazo, JM (2007).** Modeling experimental image formation for likelihood-based classification of electron microscopy data. *Structure* **15**, 1167-1177.
- Scheres, SHW, Chen, S (2012).** Prevention of overfitting in cryo-EM structure determination. *Nat Methods* **9**, 853-854.
- Scheres, SHW (2012a).** A Bayesian view on cryo-EM structure determination. *J Mol Biol* **415**, 406-418.
- Scheres, SHW (2012b).** RELION: implementation of a Bayesian approach to cryo-EM structure determination. *J Struct Biol* **180**, 519-530.
- Scheres, SHW (2016).** Processing of structurally heterogeneous cryo-EM data in RELION, in *Methods in Enzymology*, vol. 579, chap. 6, pp. 125-157.

-
- Schmidt-Krey, I, Rubinstein, JL (2011).** Electron cryomicroscopy of membrane proteins: specimen preparation for two-dimensional crystals and single particles. *Micron* **42**, 107-116.
- Schuler, M, Denisov, I, Sligar, S (2013).** Nanodiscs as a new tool to examine lipid-protein interactions, in *Lipid-Protein Interactions*, vol. 974, chap. 18, pp. 415-433.
- Schumann, U, Edwards, MD, Li, C, Booth, IR (2004).** The conserved carboxy-terminus of the MscS mechanosensitive channel is not essential but increases stability and activity. *FEBS Lett* **572**, 233-237.
- Schumann, U, Edwards, MD, Rasmussen, T, Bartlett, W, van West, P, Booth, IR (2010).** YbdG in *Escherichia coli* is a threshold-setting mechanosensitive channel with MscM activity. *Proc Natl Acad Sci USA* **107**, 12664-12669.
- Shaikh, S, Cox, CD, Nomura, T, Martinac, B (2014).** Energetics of gating MscS by membrane tension in azolectin liposomes and giant spheroplasts. *Channels* **8**, 321-326.
- Shaikh, TR, Gao, H, Baxter, WT, Asturias, FJ, Boisset, N, Leith, A, Frank, J (2008).** SPIDER image processing for single-particle reconstruction of biological macromolecules from electron micrographs. *Nat Protoc* **3**, 1941-1974.
- Shen, PS, Yang, X, DeCaen, PG, Liu, X, Bulkley, D, Clapham, DE, Cao, E (2016).** The structure of the polycystic kidney disease channel Pkd2 in lipid nanodiscs. *Cell* **167**, 763-773.
- Shih, AY, Denisov, IG, Phillips, JC, Sligar, SG, Schulten, K (2005).** Molecular dynamics simulations of discoidal bilayers assembled from truncated human lipoproteins. *Biophys J* **88**, 548-556.
- Shirzad-Wasei, N, van Oostrum, J, Bovee-Geurts Petra, HM, Kusters Lianne, JA, Bosman Giel, JCGM, DeGrip Willem, J (2015).** Rapid transfer of overexpressed integral membrane protein from the host membrane into soluble lipid nanodiscs without previous purification. *Biol Chem* **396**, 903-915.
- Sievers, F, Wilm, A, Dineen, D, Gibson, TJ, Karplus, K, Li, W, Lopez, R, McWilliam, H, Remmert, M, Söding, J, Thompson, JD, Higgins, DG (2011).** Fast, scalable generation of high-quality protein multiple sequence alignments using Clustal Omega. *Mol Syst Biol* **7**, 539.
- Sigworth, FJ (2016).** Principles of cryo-EM single-particle image processing. *Microscopy* **65**, 57-67.
- Slavchov, RI, Nomura, T, Martinac, B, Sokabe, M, Sachs, F (2014).** Gigaseal mechanics: creep of the gigaseal under the action of pressure, adhesion, and voltage. *J Phys Chem B* **118**, 12660-12672.
- Sleytr, UB, Messner, P, Pum, D, Sára, M (1993).** Crystalline bacterial cell surface layers. *Mol Microbiol* **10**, 911-916.

- Smart, OS, Neduelil, JG, Wang, X, Wallace, BA, Sansom, MSP (1996).** HOLE: A program for the analysis of the pore dimensions of ion channel structural models. *J Mol Graph* **14**, 354-360.
- Smith, PK, Krohn, RI, Hermanson, GT, Mallia, AK, Gartner, FH, Provenzano, MD, Fujimoto, EK, Goeke, NM, Olson, BJ, Klenk, DC (1985).** Measurement of protein using bicinchoninic acid. *Anal Biochem* **150**, 76-85.
- Song, Y, Zhang, B, Guo, F, Yang, M, Li, Y, Liu, Z-Q (2017).** Identification of intracellular β -barrel residues involved in ion selectivity in the mechanosensitive channel of *Thermoanaerobacter tengcongensis*. *Front Physiol* **8**, 832.
- Sonnhammer, ELL, Heijne, Gv, Krogh, A,** paper presented at the Proceedings of the 6th International Conference on Intelligent Systems for Molecular Biology, 1998.
- Sorzano, COS, Bilbao-Castro, JR, Shkolnisky, Y, Alcorlo, M, Melero, R, Caffarena-Fernández, G, Li, M, Xu, G, Marabini, R, Carazo, JM (2010).** A clustering approach to multireference alignment of single-particle projections in electron microscopy. *J Struct Biol* **171**, 197-206.
- Stagg, SM, Lander, GC, Pulokas, J, Fellmann, D, Cheng, A, Quispe, JD, Mallick, SP, Avila, RM, Carragher, B, Potter, CS (2006).** Automated cryoEM data acquisition and analysis of 284742 particles of GroEL. *J Struct Biol* **155**, 470-481.
- Steinbacher, S, Bass, R, Strop, P, Rees, DC (2007).** Structures of the prokaryotic mechanosensitive channels MscL and MscS, in *Current Topics in Membranes*, vol. 58, chap. 1, pp. 1-24.
- Suchyna, TM, Markin, VS, Sachs, F (2009).** Biophysics and structure of the patch and the gigaseal. *Biophys J* **97**, 738-747.
- Sukharev, S (2002).** Purification of the small mechanosensitive channel of *Escherichia coli* (MscS): the subunit structure, conduction, and gating characteristics in liposomes. *Biophys J* **83**, 290-298.
- Sukharev, SI, Martinac, B, Arshavsky, VY, Kung, C (1993).** Two types of mechanosensitive channels in the *Escherichia coli* cell envelope: solubilization and functional reconstitution. *Biophys J* **65**, 177-183.
- Sukharev, SI, Blount, P, Martinac, B, Blattner, FR, Kung, C (1994).** A large-conductance mechanosensitive channel in *E. coli* encoded by *mscL* alone. *Nature* **368**, 265-268.
- Sukharev, SIB, Paul; Martinac, Boris; Kung, Ching (1997).** Mechanosensitive channels of *Escherichia coli*: The MscL gene, protein, and activities. *Annu Rev Physiol* **59**, 633-657.
- Tang, G, Peng, L, Baldwin, PR, Mann, DS, Jiang, W, Rees, I, Ludtke, SJ (2007).** EMAN2: An extensible image processing suite for electron microscopy. *J Struct Biol* **157**, 38-46.
- Tartoff, K, Hobbs, C (1987).** Improved media for growing plasmid and cosmid clones. *Berthesda Res Lab Focus* **9**.

- Teng, J, Loukin, S, Anishkin, A, Kung, C (2015).** The Force-From-Lipid (FFL) principle of mechanosensitivity, at large and in elements. *Pfluegers Arch - Eur J Physiol* **467**, 27-37.
- Thompson, RF, Walker, M, Siebert, CA, Muench, SP, Ranson, NA (2016).** An introduction to sample preparation and imaging by cryo-electron microscopy for structural biology. *Methods* **100**, 3-15.
- Topf, M, Lasker, K, Webb, B, Wolfson, H, Chiu, W, Sali, A (2008).** Protein structure fitting and refinement guided by cryoEM density. *Structure* **16**, 295-307.
- Towbin, H, Staehelin, T, Gordon, J (1979).** Electrophoretic transfer of proteins from polyacrylamide gels to nitrocellulose sheets: procedure and some applications. *Proc Natl Acad Sci USA* **76**, 4350-4354.
- Tribet, C, Audebert, R, Popot, J-L (1996).** Amphipols: polymers that keep membrane proteins soluble in aqueous solutions. *Proc Natl Acad Sci USA* **93**, 15047-15050.
- Tsirigos, KD, Peters, C, Shu, N, Käll, L, Elofsson, A (2015).** The TOPCONS web server for consensus prediction of membrane protein topology and signal peptides. *Nucleic Acids Res* **43**, W401-W407.
- Ursell, T, Huang, KC, Peterson, E, Phillips, R (2007).** Cooperative gating and spatial organization of membrane proteins through elastic interactions. *PLoS Comput Biol* **3**, e81.
- Ursell, T, Agrawal, A, Phillips, R (2011).** Lipid bilayer mechanics in a pipette with glass-bilayer adhesion. *Biophys J* **101**, 1913-1920.
- Valentine, DL (2007).** Adaptations to energy stress dictate the ecology and evolution of the Archaea. *Nat Rev Microbiol* **5**, 316-323.
- van de Vossenberg, JLCM, Driessen, AJM, Konings, WN (1998).** The essence of being extremophilic: the role of the unique archaeal membrane lipids. *Extremophiles* **2**, 163-170.
- van Heel, M, Harauz, G, Orlova, EV, Schmidt, R, Schatz, M (1996).** A new generation of the IMAGIC image processing system. *J Struct Biol* **116**, 17-24.
- Vásquez, V, Sotomayor, M, Cortes, DM, Roux, B, Schulten, K, Perozo, E (2008).** Three dimensional architecture of membrane-embedded MscS in the closed conformation. *J Mol Biol* **378**, 55-70.
- Viklund, H, Elofsson, A (2008).** OCTOPUS: improving topology prediction by two-track ANN-based preference scores and an extended topological grammar. *Bioinformatics* **24**, 1662-1668.
- Wang, W, Black, SS, Edwards, MD, Miller, S, Morrison, EL, Bartlett, W, Dong, C, Naismith, JH, Booth, IR (2008).** The structure of an open form of an *E. coli* mechanosensitive channel at 3.45 Å resolution. *Science* **321**, 1179-1183.

- Wang, Z, Wang, X, Lu, P, Ni, C, Li, Y, van der Veen, S (2018).** Identification and characterization of the *Neisseria gonorrhoeae* MscS-like mechanosensitive channel. *Infect Immun*, pii: IAI.00090-00018.
- Ward, R, Pliotas, C, Branigan, E, Hacker, C, Rasmussen, A, Hagelueken, G, Booth, Ian R, Miller, S, Lucocq, J, Naismith, James H, Schiemann, O (2014).** Probing the structure of the mechanosensitive channel of small conductance in lipid bilayers with pulsed electron-electron double resonance. *Biophys J* **106**, 834-842.
- Waters, E, Hohn, MJ, Ahel, I, Graham, DE, Adams, MD, Barnstead, M, Beeson, KY, Bibbs, L, Bolanos, R, Keller, M, Kretz, K, Lin, X, Mathur, E, Ni, J, Podar, M, Richardson, T, Sutton, GG, Simon, M, Soll, D, Stetter, KO, Short, JM, Noordewier, M (2003).** The genome of *Nanoarchaeum equitans*: insights into early archaeal evolution and derived parasitism. *Proc Natl Acad Sci USA* **100**, 12984-12988.
- Wei, R, Wang, X, Zhang, Y, Mukherjee, S, Zhang, L, Chen, Q, Huang, X, Jing, S, Liu, C, Li, S, Wang, G, Xu, Y, Zhu, S, Williams, AJ, Sun, F, Yin, C-C (2016).** Structural insights into Ca²⁺-activated long-range allosteric channel gating of RyR1. *Cell Res* **26**, 977-994.
- Wiegmann, P (2014).** Heterologe Expression von Membranproteinen des hyperthermophilen Crenarchaeons *Ignicoccus hospitalis* sowie Expression und Aufreinigung eines mechanosensitiven Kanals aus *Nanoarchaeum equitans*. Masterarbeit, Universität Regensburg.
- Wilson, ME, Jensen, GS, Haswell, ES (2011).** Two mechanosensitive channel homologs influence division ring placement in *Arabidopsis* chloroplasts. *Plant Cell* **23**, 2939-2949.
- Wilson, ME, Haswell, ES (2012).** A role for mechanosensitive channels in chloroplast and bacterial fission. *Plant Signaling Behav* **7**, 157-160.
- Wittig, I, Braun, H-P, Schagger, H (2006).** Blue native PAGE. *Nat Protoc* **1**, 418-428.
- Wittig, I, Schagger, H (2009).** Native electrophoretic techniques to identify protein-protein interactions. *Proteomics* **9**, 5214-5223.
- Wurch, L, Giannone, RJ, Belisle, BS, Swift, C, Utturkar, S, Hettich, RL, Reysenbach, A-L, Podar, M (2016).** Genomics-informed isolation and characterization of a symbiotic Nanoarchaeota system from a terrestrial geothermal environment. *Nat Commun* **7**, 12115.
- Yan, Z, Bai, X-c, Yan, C, Wu, J, Li, Z, Xie, T, Peng, W, Yin, C-c, Li, X, Scheres, SHW, Shi, Y, Yan, N (2015).** Structure of the rabbit ryanodine receptor RyR1 at near-atomic resolution. *Nature* **517**, 50-55.
- Yuan, C, O'Connell, RJ, Feinberg-Zadek, PL, Johnston, LJ, Treistman, SN (2004).** Bilayer thickness modulates the conductance of the BK channel in model membranes. *Biophys J* **86**, 3620-3633.

-
- Yuan, C, O'Connell, RJ, Jacob, RF, Mason, RP, Treistman, SN (2007).** Regulation of the gating of BKCa channel by lipid bilayer thickness. *J Biol Chem* **282**, 7276-7286.
- Zhang, K, Foster, HE, Rondelet, A, Lacey, SE, Bahi-Buisson, N, Bird, AW, Carter, AP (2017).** Cryo-EM reveals how human cytoplasmic dynein is auto-inhibited and activated. *Cell* **169**, 1303-1314.
- Zhang, X, Wang, J, Feng, Y, Ge, J, Li, W, Sun, W, Iscla, I, Yu, J, Blount, P, Li, Y, Yang, M (2012).** Structure and molecular mechanism of an anion-selective mechanosensitive channel of small conductance. *Proc Natl Acad Sci USA* **109**, 18180-18185.
- Zhao, M, Wu, S, Zhou, Q, Vivona, S, Cipriano, DJ, Cheng, Y, Brunger, AT (2015).** Mechanistic insights into the recycling machine of the SNARE complex. *Nature* **518**, 61-67.
- Zheng, SQ, Palovcak, E, Armache, J-P, Verba, KA, Cheng, Y, Agard, DA (2017).** MotionCor2 - anisotropic correction of beam-induced motion for improved cryo-electron microscopy. *Nat Methods* **14**, 331-332.
- Zoonens, M, Popot, J-L (2014a).** Amphipols for each season. *J Membr Biol* **247**, 759-796.
- Zoonens, M, Zito, F, Martinez, KL, Popot, J-L (2014b).** Amphipols: a general introduction and some protocols, in *Membrane Proteins Production for Structural Analysis*, pp. 173-203.

VI APPENDIX

1 Protein characteristics

1.1 General characteristics of Neq198 and Neq531

Characteristics	Neq198	Neq531
Length (aa)	337	323
Molecular weight (kDa)	38.596 (monomer) 270 (heptamer)	37.245 (monomer) 260 (heptamer)
pI (isoelectric point)	6.23	8.79
Signal peptides (length)	No	No
Predicted TM helices	5	5
Number of Cys residues	0	0
Number of Met residues	3	3
Number of Trp residues	3	6
Number of Tyr residues	16	12
Number of Phe residues	23	24
Extinction coefficient ($M^{-1} cm^{-1}$)	40,340	50,880
Homologs in PDB	9	9

1.2 Protein sequences of relevant MS channels

Protein	Sequence in fasta-format
<i>N. equitans</i> Neq198	<pre>>tr Q74MQ0 Q74MQ0_NANEQ NEQ198 OS=Nanoarchaeum equitans (strain Kin4-M) GN=NEQ198 PE=4 SV=1 MKS LIAFIAFIITGFLATKILSYFLEGIHKKLVIDSNTKIDDIIYNSLRLPLLLIVFL IFLYIGILLAPIQIDINFNVNFVKFVSILVGTYAIVNFVDGIFEYYIIPWAEKTET KLDEHLIKPLRKLIRLLIIVFGLLTALSSVGYDITILAGLGIGGLAFALAMQD TIKNFIAGVLLIDKPFITIGDWIRVGDLEGIIEEVGIRSTRIRTFDQSLITVANSY LLERPIENFSERTKRRVVLINIGITYETPVEKIEKAKQIIKEILSSNPMVVGPIRVH FYSFGDWSLNIRVEYYVKNTNFDEFDLDTVDYINKEIKRRFDLEGIEFAYPTYT IYQK</pre>
<i>N. equitans</i> Neq531	<pre>>tr Q74M35 Q74M35_NANEQ NEQ531 OS=Nanoarchaeum equitans (strain Kin4-M) GN=NEQ531 PE=4 SV=1 MLEIWEKLIPIIVSFAIILLDKFFFKDDKAFILLRKNLYLGGFIGTIYAVLYFFN LKILGDLVAIIYAAKLLDNIIVYIRRVGFEFFKTKETEFAILIARTFLWLTA VH MVLSSFGIDIAPLLTSLGIGSIVIGLALQSTLSNFFSGMAIASEGILKEGDIIELP ELGIRGTIIDITWRGVHIKTISDTIAIPFNYINNNIINKTKHWPWYWGRI NFGI SYYSDDLKAKQLIRTIKKEKGLGVDVRFNFGDNNIEGVVIFKVVYNILDELKY KDELIREIKRRFDREGIEISFPNRNIYLRPEGLDKVLDIIRKRLQ</pre>
<i>H. pylori</i> MscS	<pre>>tr E8QGV2 E8QGV2_HELP7 Mechanosensitive channel MscS OS=Helicobacter pylori (strain India7) OX=907238 GN=HPIN_05000 PE=1 SV=1 MDEIKTLLVDFFPQAKHFGIILIKAVIVFCIGFYFSSFLRNKTMKLLSKKDEIL ANFVAQVTFILILITIIALSTLGVQTTSIITVLGTVGIAVALALKDYLSIAGGI ILIIHHPFKKGDIIISGLEGKVEALNFFNTSLRLHDGR LAVLPNRSVANSNIIN SNNTACRRIEWVCGVGYGSDIELVHKTIKDVIDAMDKIDKNMPTFIGITDFGS SSLNFTIRVWAKIEDGIFNVR SELIERIKNALDANHIEIPFNKLDIAIKNQDSSK</pre>
<i>M. jannashii</i> MJ0170 = MscMJ	<pre>>sp Q57634 MSMJS_METJA Small-conductance mechanosensitive channel MscMJ OS=Methanocaldococcus jannaschii (strain ATCC 43067 / DSM 2661 / JAL-1 / JCM 10045 / NBRC 100440) GN=MJ0170 PE=1 SV=1 MNMEIFGNSISNILIFVVITLLGIFIGKIVDKIVRNYLKKIHDKTKTKFDDIILESI DLPIIVLVVTLFFYFGLRFLILPDYILKLIDEAVKVVVILSATYFAVKFIDGIFE HYLIPLTEKTETELDEHIIKPLKKVVKILTILLGILTALSSVGYDITALLAGLVG GGLALALAMQDTIKNFIAGILILIDKPFSLGHVVKVKAEGIVEEIGIRSTRIR TFDYTLITIPNSELDSAIENLTVRDRRRVLMTIGLTYNTPVEKIKRAKEIIEI VENHPATLPPYRVHFREYGDWSLNL RVEYFVRNMGFDYYLNAVDEINLKIK EEFEKEGIEMAFPTYTVYLEKDN</pre>
<i>M. jannashii</i> MJ1143 = MscMJLR (MscL)	<pre>>sp Q58543 MSMJL_METJA Large-conductance mechanosensitive channel MscMJLROS=Methanocaldococcus jannaschii (strain ATCC 43067 / DSM 2661 / JAL-1 / JCM 10045 / NBRC 100440) GN=MJ1143 PE=1 SV=1 MTITQMISEILMHNTVYNYILSLISIILFIVIGKYANALIERLADKLHKKSGIEL DELLIRALSPLVAIAIILSGFYFGVNFLLYLLPSLKTAVNEGILTAFILCVVVFDD RFLNELVERYLALTISKTKKDDVDDQIVVLT KKL VRLV VVVVGLLLILSNLG YDIKTL LAGLGIGGLAVALASQNLVSNLIAGLIILTDKPFKIGNWITFSGGSGI VEDIGIRSTKIRATDNSIIVPNSKLIDEIIQNVPSKNKWKVSTTIGVTYNTPVE KIRKAEIKNILLEHPNVEDEPITVYFKEFGDWSLNIQVVVYIKNSRYNGYQ KYISTINEVNLKIKEEFDRKGIEFAFPTYTLYLKRDD</pre>

<i>E. coli</i> MscS	<p>>sp P0C0S1 MSCS_ECOLI Small-conductance mechanosensitive channel OS=Escherichia coli (strain K12) GN=mscS PE=1 SV=1 MEDLNVVDSINGAGSWLVANQALLLSYAVNIVAALAIIVGLIARMISNAVN RLMISRKIDATVADFLSALVRYGIIAFTLIAALGRVGVQTASVIAVLGAAGLA VGLALQGSLSNLAAGVLLVMFRPFPRAGEYVDLGGVAGTVLSVQIFSTTMRT ADGKIIVIPNGKIIAGNIINFSREPVRNEFIIGVAYDSDIDQVKQILTNIQSED RILKDREMTVRLNELGASSINFVVRVWSNSGDLQNVYWDVLERIKREFDAA GISFPYPQMDVNFKRVKEDKAA</p>
<i>E. coli</i> YnaI	<p>>sp P0AEB5 YNAI_ECOLI Low conductance mechanosensitive channel YnaI OS=Escherichia coli (strain K12) OX=83333 GN=ynaI PE=1 SV=1 MIAELFTNNALNLVIIFGSCAALILMSFWFRRGNRKRKGFHFHAVQFLIYTIIS AVGSIINYVIENYKLFITPGVIDFICTSLIAVILTIKLFLINQFEKQQIKKGRDI TSARIMSRIIKITIIIVVLVLLYGEHFGMSLSGLLTFGGIGGLAVGMAGKDILSN FFSGIMLYFDRPFSIGDWIRSPDRNIEGTVAEIGWRITKITTFDNRPLYVPNSLF SSISVENPGRMTNRRITTTIGLR YEDA AKVGVIVEAVREMLKNHPAIDQRQT LLVYFNQFADSSLNIMVYCFKTTVWAEWLAAQQDVYLKIIDIVQSHGADF AFPSQTLYMDNITPPEQGR</p>
<i>T. tengcongensis</i> MscS	<p>>sp Q8R6L9 MCS_CALS4 Small-conductance mechanosensitive channel OS=Caldanaerobacter subterraneus subsp. tengcongensis (strain DSM 15242 / JCM 11007 / NBRC 100824 / MB4) OX=273068 GN=mscS PE=1 SV=1 MWADIYHKLVEIYDIKAVKFLLDVLKILIIAFIGIKFADFLIYRFYKLYSKSKIQ LPQRKIDTLTSLTKNAVRYIIYFLAGASILKLFNIDMTSLLAVAGIGSLAIGFG AQNLVKDMISGFFIIFEDQFSVGDYVTINGISGTVEEIGLRVTKIRGFSDGLHII PNGEIKMVTNLTKDSMMAVVNIAFPIDEDVDKIIIEGLQEICEEVKKSRRDDLIE GPTVLGITDMQDSKLVIMVYAKT QPMQKWAVERDIRYRVKMKMFDQKNISFPYPRTTVILSEKKTN</p>

1.3 Accession numbers of relevant MS channels

Protein	NCBI	Uniprot	PDB/EMDB
<i>E. coli</i> MscS	NP_417399.1	P0C0S1	2vv5, 2oau, 3agf, 4age, 5aji
<i>E. coli</i> YnaI	NP_415846.1	P0AEB5	EMD-3035
<i>H. pylori</i> MscS	WP_000343461.1	E8QGV2	4hwa, 4hw9
<i>N. equitans</i> Neq198	AAR39052.1	Q74MQ0	-
<i>N. equitans</i> Neq531	AAR39371.1	Q74M35	-
<i>M. jannashii</i> MJ1143 = MscMJLR (MscL)	WP_010870654.1	Q58543	-
<i>M. jannashii</i> MJ0170 = MscMJ	WP_064496414.1	Q57634	-
<i>T. tengcongensis</i> MscS	AAM25887.1	Q8R6L9	3udc, 3t9t

1.4 Sequence alignments

Sequence alignments were performed with Clustal O (1.2.4) (Sievers *et al.*, 2011) and visualized with ESPript 3.0 (Robert and Gouet, 2014). A column is framed in blue if more than 70 % of its residues are similar according to physico-chemical properties, identical residues are marked red.

Neq198-Neq531: sequence identity 30.43 %

	1	10	20	30	40	50	60	70																																														
Neq198	MKSLIA	FAFIITGF	LA	TKILSY	FLEGI	IKKLVIDSNTKI	DDI	IYNSLR	LPLLLIVFLIF	LYT	GILLAP	IQ	IDINE																																									
Neq531	MLE..	IW.....	EKLII	PIIVSFA	IIILL	DKFFF.....	KDD	KAFILR	KN	LYL	GFFI	GTIYAVLYE																																									
	80	90	100	110	120	130	140																																															
Neq198	VNNVFKFVSI	LVGTYAI	...VNF	VDGTFEY	YIIPWAE	.KTE	TKLDEH	IKPLRK	LIRLLI	IVFG	LLT	ALSSV	GVD																																									
Neq531	FN.....	LKILGLD	LVAII	YAAKLL	LDNI	IVIVY	RRIV	GFEFK	TKETE	FAT	...IL	IAR	TFLWITAVHMLSSFGID																																									
	150	160	170	180	190	200	210	220																																														
Neq198	ITTI	LAGL	GTGL	AFAL	LAMQD	TIK	NFI	AGV	LLID	KPFTI	GDW	IR	VGD	..E	GITE	EVGI	RST	RIR	TFDQ	SLIT	VA																																	
Neq531	IAP	LLTS	LGIG	SIV	IGL	ALOST	ILSN	FSC	MAIAS	EGIL	KEGD	I	ELPE	GIR	GTI	IDI	TW	RGV	H	IKT	ISD	TIA	IIP																															
	230	240	250	260	270	280	290																																															
Neq198	NSY	LLERP	IEN	FS	.ERT	KRRVI	IN	IGI	YET	PVEK	TE	KAKO	IT	KE	IL	SSN	PM	VV	GP	IR	V	H	F	S	F	G	D	W	SL	NIR	VE	Y																						
Neq531	FNY	INNNI	I	INK	TK	HW	PY	WGR	IN	F	G	S	Y	S	..	LD	KAKO	IT	KE	IL	REK	GL	.E	C	..	D	V	R	F	T	N	F	G	D	N	I	E	G	V	I	..	E												
	300	310	320	330																																																		
Neq198	V	N	T	N	F	D	E	F	I	D	T	V	D	Y	I	N	K	E	I	K	R	R	F	D	L	E	G	I	E	F	A	Y	P	T	Y	I	Y	Q	R														
Neq531	F	K	V	N	I	L	D	E	I	K	Y	K	D	E	L	I	R	E	I	K	R	R	F	D	R	E	G	I	E	I	S	F	N	R	N	I	Y	L	R	P	E	G	L	D	K	V	L	D	I	K	R	G	L	Q

Neq198-MscMJ: sequence identity 54.6 %

```

Neq198      . . . . . 1      10     20     30     40     50     60
MscMJ      MNMEIFGNSISNILIFVVTLLGIFIGKIVDKIVRNYLKKIIDKTKKFDIILESIDLPILVVTLEFYGLRF

Neq198      70     80     90     100    110    120    130    140
MscMJ      APTLQIDINFNVNNVFKFVSVLVGTYAVNFDGIFYYIIPWAEKTEKLDDEHLKPLKLRLLITVGLITALS
MscMJ      LILPDYIKLIDEAVKVVVLSATYFAVKFDGIFHYLIPLTKETEELDEHLKPLKRVKILTLGLITALS

Neq198      150    160    170    180    190    200    210
MscMJ      SVGYDITITLAGLGGGLAFALAMQDTIKNFIAGLVLLIDKPFITIGDWIRVGDLEGIIEEVGIRSTRIRTFDQSLI
MscMJ      SVGYDITITLAGLGGGLAFALAMQDTIKNFIAGLVLLIDKPFSLGHWVVKVKGREGIVEEVGIRSTRIRTFDITLI

Neq198      220    230    240    250    260    270    280    290
MscMJ      TVANSYLLERP IENFSERTKRRVLINIGITYETPVEKIEKAKI IKEIISNPMVVGPIRVHFYSFGDWSLNRVE
MscMJ      TIPNSELLSAL IENLTVRDRRRVLMITIGITYNTPVEKIKRAK I IKEI IENHPATLPPYRVHFREYFGDWSLNRVE

Neq198      300    310    320    330
MscMJ      YVVKNTNFD EFLD TVDYINKEIKRRFDLEGIFFAVPTTYTYQK...
MscMJ      YVVRNMGFDYVYLNADV E INLKEEFEREGIEMAFPTTYTYVLEKDN
    
```

Neq531-MscMJ: sequence identity 27.72 %

```

Neq531      1      10     20     30
MscMJ      .MLEIWE.....KLIIPPIVVSFAITILLDKFFFKDDKA
MscMJ      MNMEIFGNSISNILIFVVTLLGIFIGKIVDKIVRNYLKKIIDKTKKFDIILESIDLPILVVTLEFY.....

Neq531      40     50     60     70     80     90
MscMJ      FILLRKNLYLGF FFICTIYAVLYFN LKILGDL.....VAIIYAAKLDNIIVIYIRRVGVEFFKTEFAI..
MscMJ      .....FYFGLRFLILPDYILKLEDEAVKVVVILSATYFAVKFDGIFEFHYLIPLTE...KTELEDEHI

Neq531      100    110    120    130    140    150    160    170
MscMJ      ...ILIAR TFLWLTAVHMLSSFGIDIAPLLTSLGIGSIVIGLALOSTISNFFSGMAIASGILKECDITELPEL
MscMJ      IKPLKRVKILTI LGLTALSSVGYDITALLAGLGVGLALALAMQDTIKNFIAGILILIDKPFSLCHWVVKV...

Neq531      180    190    200    210    220    230    240
MscMJ      GTRGTITDITWRGVFKTISDTAIPFNNTNNNINKTKHWPWYWGRI NFGISYSDLDK...AKQIRTIKE
MscMJ      GAREGIVEEIGIRSTRIRTFDYTLITIPNSELLSAL IENLTV.RDRRRVLMITIGLTYNTPVEKIKRAKEI IKEI IEN

Neq531      250    260    270    280    290    300    310
MscMJ      KGL...EGDVRFNF GDN NIEGVIF...KVYNILDE LKYKDEI IREIKRRFDREGIEISFPNRNIYLRPEGLDKVL
MscMJ      HPA TLPPYRVHFREYGDWLSILNLRVEYFVRNMGFDYVYLNADV E INLKEEFEREGIEMAFPTTYTYVLEKDN.....

Neq531      320
MscMJ      DIIKRG LQ
MscMJ      .....
    
```

Neq198-MscMJLR: sequence identity 43.67 %

```

Neq198      .....KSLIAFIAFIITGFLATKILSYFLEGIKKLVIDSNTKIDDIYNSIRLPPLLLIV
MscMJLR    MTITQMISEILMHNTVYNYILSLISILFIVIGKYANALIERLADKLHKKSGIEDELLIRATSLPVAIAI

          60          70          80          90          100          110          120
Neq198      FLIFLYIGILLAPTIQIDINF.VN.NVFKFVSTIVGTYAIVNFVVDGTF.EYIIPWAEKTEKLDLHLLKPLKLLI
MscMJLR    ILSGFYFGVNFVYLLPSLKTAVNEGILT.AFILLCVVVFDFRFLNEIVERYLALITISKKTKKDVDDQIVVLTKKLV

          130         140         150         160         170         180         190         200
Neq198      RLIIIVFGLLTALSSVGYDITILAGLGIGGLAFALAMODTIKNFTAGVLLITDKPFTICDWINRVGDLEGIIEV
MscMJLR    RLIVVWVGLLILSNIGYDITLLAGLGIGGLVVALASQNLVSNLTAGLIIITDKPFTICDWINVITFSGGSGIVEEDI

          210         220         230         240         250         260         270
Neq198      GIRSTRIRTFDQSIITVANSYLLERTEINFSERTKRRLVNLNIGITYETPVEKTEKAKQIIEKILSSNPMV.VGPI
MscMJLR    GIRSTRIRATDNSIIVVNSKILIDEIIONVPSKKNKWKVSTIGVTYNTFVEKIRKAEIIEKILLEHPNVEDEBPI

          280         290         300         310         320         330
Neq198      RVHFYSFGDWSLNIQVYYVYKNTNFDE...FLDTVDYINKEIKRRFDLEGIEFAYPTYTYLQK...
MscMJLR    TVYFKEFGDWSLNIQVYYVYKNSRYNGYQKYISTINEVNLKIKEEFDKRGIEFAYPTYTYLKRDD

```

Neq531-MscMJLR: sequence identity 27.30 %

```

Neq531      .....MDEIWEKLIIPITIVSFAIIILDK
MscMJLR    MTITQMISEILMHNTVYNYILSLISILFIVIGKYANALIERLADKLHKKSGIEDELLIRATSLPVAIAIISG

          30          40          50          60          70          80          90
Neq531      FFFKDDKAFILLR..KNLYIGFFIGTYAVLYFNLKILGDLVAIIYAAKLDNIIVYVRRIVGEFFKTKETB.
MscMJLR    RYFGVNFVYLLPSLKTAVNEGILTAFILCVVVF.....FDRFLNEIVERYLALITISKTKKDVDDQ

          100         110         120         130         140         150         160
Neq531      ..FAIILIARTFLWLTAVHMLVSSFGIDIAPLITSLGIGSIVIGLALQSTLSNFFSGMAIASEGIRKEDIHELP
MscMJLR    IVVLTKKLVRLVWVVGILLILSNLGYDIKTLTAGLGIGLAVALASQNLVSNLIALGLIILTDKPFKIGNWITFS

          170         180         190         200         210         220         230         240
Neq531      ELGIRGTIIDITWRGVHKTISDTIAIIPFNYNINNIINIKTKHPWPYWGRIKFGISYSDLDK...AKQLRITL
MscMJLR    ..GGSGIVEEDIGIRSTKIRATDNSIIVVPSKILIDEIIONVPSKKNKWKV.STIGVTYNTFVEKIRKAEIIEKNI

          250         260         270         280         290         300
Neq531      LKEKGLE...GDVRFNTNIEGVTFKYYN..I...LDELYKYDELIREIKRRFDRREGIEISFPNRIYLR
MscMJLR    LLEHPNVEDEPITVYFKEFGDWSLNIQVYYVYKNSRYNGYQKYISTINEVNLKIKEEFDRKRGIEFAYPTYTYLKR

          310         320
Neq531      PELGDKVLDIIKRGLO
MscMJLR    RDD.....

```

Neq198-YnaI: sequence identity 30.19 %

```

Neq198  1 10 20 30 40 50 60 70
        .MKSII...AFIAFITGFLA.TKILSYFLEGIKKLVIDSNTKIDDIYNSLRPLLLIVFLIFLYIGILLAPIQ
YnaI    MIAELFTNNALNLVITFGSCAALILMSFWFR.....RGNRKRKGFLEHAVQ.....FLIYTIISAVG

Neq198  80 90 100 110 120 130 140
        IDINFNVNVFKFVSLVGTYS.AIVNFVD...GIFYYIIPWAEKTEETKLDE..HLTKPLRKLIRLITVFGLLTA
YnaI    SIINYPNIENYKLFKFTPGVIDFICTSLIAVILTIKLFLINQFEKQIKKGRDITSARIMSRIKITITVVLVLY

Neq198  150 160 170 180 190 200 210
        LSSVGYDITILAGIGIGGLAFALAMQDITKNFIAGVLLIDKPFITGDWIRVGD..LEGITEVGIKRSRTRITFD
YnaI    GEHFGMSLSGLITFGIGGLAVGMAGKDIISNFFSGIMLYFDKPFISGDWIRSDRNIECTVAEIGWRITKIITFD

Neq198  220 230 240 250 260 270 280
        QSLITVANSYLLERPENFSERTKRRVLLINIGITYPETPVEKIEKAKOIKEILSSNPMVVG..PIRVHFYSFGDWS
YnaI    NRPILYVNSLFSISVENPGRMTNRRITITIGLRYEADAKV.GVIVEAVREMLKNHPAIDQRQTLLVYENQFADSS

Neq198  290 300 310 320 330
        LNI RVEYVVKNTNDFEFLDTVDYINKEIKRRFDLFGIEFAYPTTYTIYK.....
YnaI    LNI MVYCETKITVVAEWLAAQQDVYLYKIIDIVQSHGADFAPSSQTIYMDNITPPEQGR
    
```

Neq531-YnaI: sequence identity 21.82 %

```

Neq531  1 10 20 30 40 50 60
        .MLEIWEKLIIPIT..IVSFAIILLDKFFKDDKAFILLRKNLYLGFFIGTITYAVLYFFNKKILGLDLVAIT...Y.
YnaI    MIAELFTNNALNLVITFGSCAALILMSFWFRGNR.....KRKGFLEHAVQFLIYTIISAVGSIINYPNIENYK

Neq531  70 80 90 100 110 120
        .....AAKLDLNDIIVIYIRRVLGEFFKKE...TEF..AII..LIARTFLWLTAVHMLVSSSFGIDIAFL
YnaI    LKFITPGVIDFICTSLIAVILITIKLFLINQFEKQIKKGRDITSARIMSRITKITIIVVILVLYGEHFGMSLSGL

Neq531  130 140 150 160 170 180 190 200
        LITSLGIGSIVIGLALQSTLSNFFSGMAIASEGILKEGDIIELELPELGIKCTIIDITWRGVHITKISDITAIIPFNYYI
YnaI    LITFGIGGLAVGMAKGDILSNFFSGIMLYFDKPFISGDWIRSDRNIECTVAEIGWRITKITITFDNRPILYVNSLFS

Neq531  210 220 230 240 250 260
        NNNIITINKTKHWPWYWGRIKFTSYSDIDKAK...QLIRITLKEKGL....EGDVRFNTNFGDNNIEGVIFFK..
YnaI    SSISVENPG.RMTNRRITITIGLRYE.DAKVGVIVEAVREMLKNHPAIDQRQTLLVYFNQFADSSLNIMVYCFK

Neq531  270 280 290 300 310 320
        VYNI LDELKYKDELIREIKRRFDREGISFPNRYL RPEGLDKVLDI I KRG LQ
YnaI    TTVVAEWLAAQQDVYLYKIIDIVQSHGADFAPSSQTIYMDNITPPEQGR.....
    
```

2 Single particle data sets

2.1 Negative stain data sets

- APol Neq198: 153 micrographs, 38,237 particles (auto-picking)
- APol Neq531: 60 micrographs, 27,453 particles (manual picking)
- ND Neq198: 37 micrographs, 8,923 particles (manual picking)

2.2 Cryo-EM data sets

- ND Neq198 Sept 2016: 31 micrographs, 1,721 particles (manual picking)
- ND Neq198 Feb 2017: **229 micrographs, 122,464 particles (auto-picking)**
- ND Neq198 Jun 2017: **524 micrographs, 169,657 particles (manual picking)**
- ND Neq198 Nov 2017: 54 micrographs, 10,615 particles (manual picking)

3 Cryo-EM data sets: experimental set-up

3.1 Experimental set-up for “Feb2016” data set

Sample preparation	
Sample	Neq198 in nanodiscs (MSP1E3D1); 0.2:1:45 (Neq198:MSP:POPC)
Concentration	~120 mAU (concentrated)
Buffer	20 mM Tris, 100 mM NaCl (pH 7.5)
Freezing conditions	
Grids	Quantifoil R2/4, 400 mesh, Cu
Sample volume	4 μ l
Temperature	25 °C
Humidity	95 %
Pre-blotting exp.	15 s
Blotting time (s)	1.2/1.5/1.7/1.9/2.2 s
Post blotting exp. (s)	-
Microscope settings	
Microscope (kV)	FEI Tecnai F30 Polara Helium (300 kV)
Magnification	31,000x
Defocus range	-2.0 - -2.5 μ m
Spot size/CA/OA	8/ C2 70 μ m 50.57 %/ 100 μ m
Spherical aberration (Cs)	2.0
Amplitude contrast	0.1
Acquisition software	Serial EM (+ Digital Micrograph)
Camera settings	
Camera (mode)	K2 summit (counting mode, dose fractionating)
Image pixel size (\AA /px)	1.273
Pixel size on detector (μ m)	5
Number of frames	40
Exposure time	8 s (total); 0.2 s per frame
Electron dose	33.59 $e^-/\text{\AA}^2$ (total); 0.84 $e^-/\text{\AA}^2$ per frame
Data format	*.mrc stacks

3.2 Experimental set-up for “Jun2016” data set

Sample preparation	
Sample	Neq198 in nanodiscs (MSPE3D1); 0.1:1:50 (Neq198:MSP:POPC)
Concentration	~370 mAU (not concentrated)
Buffer	20 mM Tris, 100 mM NaCl (pH 7.5)
Freezing conditions	
Grids	Quantifoil R2/4, 400 mesh, Cu
Sample volume	3 μ l
Temperature	25 °C
Humidity	88 %
Pre-blotting exp.	15 s
Blotting time (s)	3.5/4.0 s
Post blotting exp. (s)	1 s
Microscope settings	
Microscope (kV)	FEI Tecnai F30 Polara Helium (300 kV)
Magnification	31,000x
Defocus range	-2.0 - -2.5 μ m
Spot size/CA/OA	8/ C2 70 μ m 50.57 %/ 100 μ m
Spherical aberration (Cs)	2.0
Amplitude contrast	0.1
Acquisition software	Serial EM (+ Digital Micrograph)
Camera settings	
Camera (mode)	K2 summit (counting mode, dose fractionating)
Image pixel size (\AA /px)	1.273
Pixel size on detector (μ m)	5
Number of frames	50
Exposure time	10 s (total); 0.2 s per frame
Electron dose	70.89 $e^-/\text{\AA}^2$ (total); 1.4178 $e^-/\text{\AA}^2$ per frame
Data format	*.mrc stacks

ACKNOWLEDGMENTS

First of all, I want to thank my supervisor **Prof. Dr. Christine Ziegler** for introducing me to the world of membrane proteins and structure analysis. I always thought I would never end up with electron microscopy, but still I did. Thank you for the patience and the confidence, the support and discussions that helped me to improve my thesis. And finally, I am deeply grateful for the chance to go on a research stay to Sydney. I deeply thank my first mentor **Dr. Harald Huber** for his constant support throughout the last couple of years. I sort of grew up in the microbiology department so that the microbiology will always hold a special place. Thank you for your discussions, your motivations, and your interest in my thesis. I very much thank my second mentor **Prof. Dr. Boris Martinac** from the Victor Chang Cardiac Research Institute in Sydney. I am very grateful that he gave me the opportunity to become a member of his group for three months. His interest in my thesis and his never-ending enthusiasm were inspiring. I have learned a lot in this short time. I thank **Prof. Dr. Reinhard Rachel** for collaboration and support concerning all electron microscopy matters. A big “THANK YOU” goes to **Dr. M. Gregor Madej** for the homology model, his magic structure modeling skills and for critical reading the manuscript! I thank **Dr. Rebecca Richter** for her support in the laboratory, for critical reading the manuscript, and beyond that her friendship. Special thanks go to **Elisabeth Nagelfeld** and **Claudia Pauer** for their administrative and organizational support. A big “thank you” goes to the **microbiology department** and the **Huber lab** for their great atmosphere and, especially to Gabi Leichtl and Dr. Lydia Kreuter (I loved working with you!), for their constant support. I deeply thank all members of the **Ziegler lab**: Barbara Kellerer, Claudia Georgi, Sabine Ruppel, Robert Boppart, Katharina Koßmann, and the numerous student that joined us. Special thanks go to **Veronika Heinz**,

who recorded the electron micrographs, for her help, patience and discussions concerning electron microscopy and single particle analysis.

I deeply thank my boys' lab in Sydney with Navid Bavi, Dr. Charles D. Cox, **Dr. Yoshitaka Nakamura**, Yury Nikolaev, **Pietro Ridone**, and **Paul Rohde** for their sincere welcome to their group. Yoshi and Pietro introduced me to the world of patch clamping. Paul always kept an eye on my experiments and took care of cloning. I miss you guys a lot! I further want to thank my **students** Georg Horn, Michaela Raab, Kristina Plobner, Johanna Schaubächer, Judith Thomas, and Karolin Kapustij, who did great work in the lab. I thank **Thomas Heuser** from the VBCF in Vienna for his support and the opportunity to record cryo-electron micrographs for my project. I very much thank the international PhD program at the University of Regensburg (**iPUR**) for their financial support of my research stay in Sydney.

Ganz besonders danke ich **Dr. Stefanie Stelzer** dafür, dass unsere gemeinsame Zeit im Labor einfach unvergesslich war und dadurch eine einzigartige und innige Freundschaft gewachsen ist.

Meiner **Mama Regine Wiegmann** möchte ich von Herzen für ihre bedingungslose Unterstützung danken und die zahlreichen aufmunternden Worte in allen Lebenslagen. Ihr unbrechbarer Glaube in mich hat mich immer wieder gestärkt!

Nicht zuletzt gilt mein ganz besonderer liebevoller Dank meinem Mann **Maximilian Berlik**, der mich auch in schweren Zeiten ertragen, mir unglaubliche Geduld und Rückhalt entgegen gebracht, das ein oder andere Mal ordentlich den Kopf gewaschen und das Selbstvertrauen gestärkt hat.

